Studies of supernovae and their remnants based on gamma-ray observations with H.E.S.S.

Simoni, R.C.

Publication date
2022

Document Version
Final published version

Citation for published version (APA):
Simoni, R. C. (2022). *Studies of supernovae and their remnants based on gamma-ray observations with H.E.S.S.* [Thesis, fully internal, Universiteit van Amsterdam].

Studies of supernovae and their remnants based on gamma-ray observations with H.E.S.S.

RACHEL SIMONI

contact email : simonirachel1@gmail.com

Cover credits :
Photo : Vikas Chandler.
Design : Federico D'Ambrosio — Céline Serrad.

Imprimé aux Presses Universitaires de Bruxelles

The work presented in this thesis has been carried out at the Anton Pannekoek Institute of Astronomy (API) with the group for Gravitation and Astroparticle Physics Amsterdam (GRAPPA) of the University of Amsterdam. And partly at the Inter-University Institute For High Energies (IIHE) at Université libre de Bruxelles, which kindly provided a guest status and a desk.

Studies of supernovae and their remnants based on gamma-ray observations with H.E.S.S.

ACADEMISCH PROEFSCHRIFT

ter verkrijging van de graad van doctor
aan de Universiteit van Amsterdam
op gezag van de Rector Magnificus
prof. dr. K.I.J Maex
ten overstaan van een door het College voor Promoties ingestelde
commissie, in het openbaar te verdedigen in de Agnietenkapel
op maandag 24 januari 2022, te 14:00

door

Rachel Christianne Simoni

geboren te Strasbourg, France

Promotiecommissie :

Promotores :	dr. J. Vink	Universiteit van Amsterdam
	prof. dr. D. Berge	Humbold Universität zu Berlin
Copromotor :	prof. dr. R.A.M.J. Wijers	Universiteit van Amsterdam

Overige leden :	prof. dr. S. Markoff	Universiteit van Amsterdam
	prof. dr. R.A.D. Wijnands	Universiteit van Amsterdam
	prof. dr. J.W.T Hessels	Universiteit van Amsterdam
	prof. dr. A.L. Watts	Universiteit van Amsterdam
	dr. A. Oklopčić	Universiteit van Amsterdam
	prof. dr. S. Wagner	Universität Heidelberg
	prof. dr. N. Komin	University of Witwatersrand

Faculteit der Natuurwetenschappen, Wiskunde en Informatica

A mes enfants, Paolina et Luciano.

A la mémoire de mon père, Hubert Simoni.

Table des matières

1

Introduction

The research described in this thesis is motivated by one persistent question : which are the sources of cosmic rays (CRs) ? Answering this question was the main motivation to develop gamma-ray astronomy in the TeV (1 TeV=10^{12} eV) domain, although the results obtained go beyond the concerns of CR physics, allowing numerous source detection and studies. Gamma-ray observations may indeed be the key to clearing up this long-unsolved mystery in astrophysics, as the only established source of CRs so far are supernova remnants (SNR), and this was established by gamma-ray observations. But the SNR can account for only a part of the CR spectrum, at energies below 10^{15} eV, where CRs are believed to be of Galactic origin. Above 10^{15} eV the CRs sources remain unknown, and above $\sim 3 \times 10^{18}$ eV CRs are firmly of extragalactic origin.

The High Energy Stereoscopic System (H.E.S.S.) is observing the sky in gamma-rays at TeV energies. Its location in the southern hemisphere, close to the tropic of Capricorn, allows the observation of the southern celestial sphere. A large part of the Galactic plane, including the Galactic center region, can be observed from there, harboring many astrophysical sources such as SNR or pulsar wind nebulae (PWNe). The contribution of H.E.S.S. is important, as almost half of the currently known TeV gamma-ray sources have been discovered by the H.E.S.S. Collaboration.

This introduction will first give a brief insight into CR physics, and gamma-ray astronomy (Section 1.1). Section 1.2 will present supernova remnants and supernovae (SNe) from the gamma-ray perspective, with an explanation of the underlying mechanisms in play to produce gamma-ray emission. Finally, in Section 1.3, our instrument, the H.E.S.S. telescope, will be presented, with the challenges of the imaging air shower technique and some data analysis steps used to obtain our results.

1.1 Cosmic-rays

Cosmic rays (CRs) is a term that refers to energetic charged particles (protons, nuclei, and electrons) originating from space, which constantly bombard Earth. They were discovered by balloon experiments conducted by Viktor Hess, an Austrian-American physicist, from 1911-1913. Hess' discovery was preceded by pioneer experiments such as Eifel tower radiation measurements (Wulf - 1909) and underwater measurements (Pacini - 1911) (De Angelis et al. 2010). During balloon flights, Hess observed ionizing radiation increasing with height, which could not be due to radioactivity on Earth, but originate from a "penetrating radiation from outer space". This radiation was named by Millikan "cosmic rays" in 1925. These discoveries somehow marked the beginning of the Astroparticle physics "era", as space could be used as an incredibly powerful lab for testing particle physics. Indeed, in the 30s, experiments permitted the discovery of the positron by Anderson in 1932 (Anderson 1932), the muon in 1936 (Anderson & Neddermeyer 1936), and pions and kaons in 1947 (Lattes et al. 1947; Rochester & Butler 1947). Carl David Anderson and Viktor Hess received the Nobel prize in 1936 for their discoveries. The second part of the 20th century was marked by the development of accelerator physics, with groundbreaking discoveries. But even nowadays, like the Large Hadron Collider (LHC) can accelerate protons up to 13 TeV ($\sim 10^{13}$ eV), cosmic accelerators in the Galaxy can reach PeV (10^{15} eV) energies, two orders of magnitude higher than the LHC.

Nowadays, CR physics is a whole field in high energy astrophysics gathering direct and indirect observations. The main observatories dedicated to the observation of CR particles are the Pierre Auger Observatory (Abraham et al. 2004) and the Telescope Array (Abu-Zayyad et al. 2013). Open issues are the composition of CRs at high energies, the behavior of the CR spectrum at $\sim 10^{20}$ eV, as recently the origin of a cut-off is challenged, and the origin of CRs above 10^{14} eV, which remains unknown. The latter is a central issue for this thesis.

1.1.1 Cosmic-ray spectrum

Figure 1.1 shows the energy spectrum of all particle CRs measured by different experiments. The spectrum extends over more than 12 orders of magnitude in energy and 32 orders of magnitude in flux. As a first approximation, the spectrum can be described by a power-law, $dN/dE \propto E^{-\Gamma}$, but main features can be observed corresponding to changes in the power-law index :

- The low energy cut-off : below 1 GeV, the spectrum does not follow a power law. CRs being charged particles, they are deviated by the heliospheric magnetic fields. This suppression varies according to the solar modulation, which has a period of 11 years.
- The "knee" designates a break observed at $\sim 10^{15}$ eV and corresponds to a

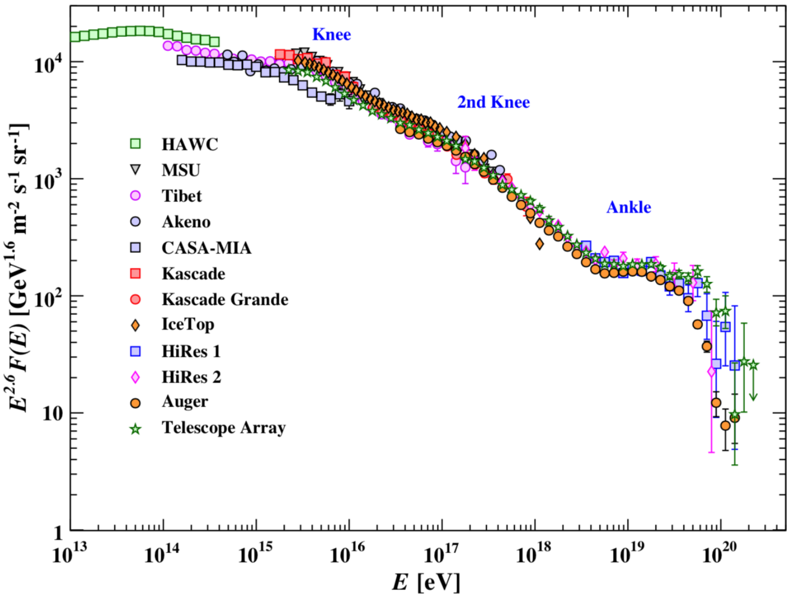

Figure 1.1 – Proton and all particle CR spectrum as measured at the Earth by different experiments. The spectrum is scaled by $E^{2.6}$, enhancing the features (from Zyla et al. 2020).

steepening in the index of the CR spectrum from ~ 2.7 to ~ 3.1. Likely the "knee" corresponds to the maximum energy proton CRs are accelerated to by Galactic sources. The existence of a second knee at $\sim 4 \times 10^{17}$ eV is under discussion.

- The "ankle" : at $\sim 6 \times 10^{18}$ eV the spectrum gets harder, following a power-law with index $\Gamma \sim 2.7$. Beyond the Ankle, the origin of the CR particles is extragalactic.
- The GZK cut : CR particles have been recorded up to $\sim 10^{20}$ eV. A cut at high energy is predicted at $\sim 5 \times 10^{19}$ eV by Greisen Zatsepin and Kuzmin, called the "GZK cut" (Zatsepin & Kuzmin 1966). This suppression is due to the interaction of CR particles with the diffuse Cosmic Microwave Background (CMB) : the proton or nuclei interacting with CMB photon will produce pions and neutrino through the production of a baryon Δ^+ (also called the Δ resonance). However, recently, evidence has emerged that a more likely origin is that the cut-off marks the maximum energy protons are accelerated to by extragalactic sources.

The CRs are charged particles consisting of 99% hadrons (protons, helium, and heavier nuclei) and 1% leptons (electrons and positrons). The transition between the Galactic and extragalactic origin of CRs is dependant on the inferred magnetic-field strength in our Galaxy. The particles gyration radius follows $r_g \propto E\ /\ ZB$, where r_g is the gyro-radius in pc, E the particle's energy in PeV (1 PeV $= 10^{15}$ eV), B the magnetic field in μG, and Z the atomic number. When r_g reaches the Galactic scale height ($\sim$104 pc) the particles can escape. The strength of the magnetic field is estimated at $\sim 3\mu$G on average in the Galactic interstellar medium, implying that CRs are confined in the Milky Way up to $\sim 3 \times 10^{17}$ eV. This corresponds approximately to the position of the second knee : it would then be explained by the transition between a Galactic CR component and a harder spectrum of extragalactic origin. Similarly, below the knee at 10^{15} eV, $r_g(B = 3\mu\mathrm{G}) < 0.3\,\mathrm{pc}$, CR particles are of Galactic origin. Between the knee and the ankle, the origin of CRs could be both Galactic or extragalactic, depending on the source. Beyond 10^{18} eV (ankle) the origin of CR is extragalactic. Hillas was using similar arguments to constrain some parameters for the CRs sources, as the size and magnetic field, with the idea that a CR particle should stay confined a while in a source to be accelerated (see Hillas 1984, 2006). In this scheme, SNR are predicted to be Galactic CRs source candidates, with moderate magnetic field strength ($B \simeq 1 - 100\,\mu$G) and rather big size ($r_g \simeq 1 - 20\,$pc). In reality, based on gamma-ray observations, SNR seems to accelerate CRs up to 10^{14} eV, as no gamma-ray signal beyond has been observed from individual SNRs. However, it could be that the highest energy CRs are accelerated in the earliest phase of SNR development, or in star-forming regions with multiple SNRs and stellar winds acting together. Extragalactic CRs source candidates are active galactic nuclei (AGN), galaxy clusters, or gamma-ray bursts.

Fermi acceleration The power-law (PL) shape of the CR spectrum can be well explained with the shock acceleration mechanism initially developed by Enrico Fermi (Fermi 1949).

In the first-order Fermi acceleration, the particle is crossing a magnetized plasma, with a jump in velocity : multiple elastic interactions on either side of the jump result in a Lorentz boost of the order of 1% of the energy of the particle. After many crossings, the particles can obtain highly relativistic energies. The first-order Fermi acceleration predicts an index of 2 for the differential flux of the accelerated particles $dN/dE \propto E^{-\Gamma}$ with $\Gamma \geq 2$. The PL dependency is the result of exponential growth of the energy of the particle at each crossing cycle, but also an exponential decline in the number of particles that participate in the acceleration process, as each cycle, a few percent of the particles are advected too far away from the shock to be able to recross the velocity jump and escape. For a detailed derivation of the Fermi acceleration (see e.g Section 21 in Longair 2011).

The first-order Fermi acceleration at strong shock can explain particle acceleration by SNRs, the shock front playing the role of the accelerator, although the presence of accelerated particles may make the shock structure itself more complicated (e.g. Bell 1978a,b; Blandford & Eichler 1987; Drury et al. 1994; Malkov & Drury 2001).

The difference between the spectrum of particles accelerated by the first-order Fermi mechanism and that observed on Earth can be explained by the effects of CR propagation in the Galaxy. These effects include spallation, energy losses, and the escape of particles from the Galaxy. Calculations show that they retain the spectral shape in power law but incur an increase in the spectral index, which can go up to 0.7. The measurement of the cosmic ray spectrum with $\Gamma \sim 2.7$ before the knee is therefore compatible with the theory of Fermi acceleration.

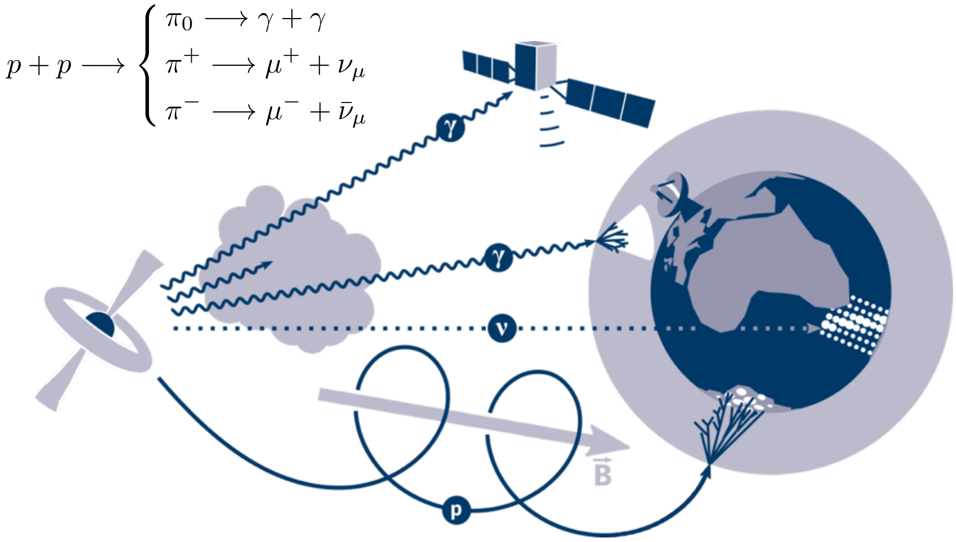

$$p + p \longrightarrow \begin{cases} \pi_0 \longrightarrow \gamma + \gamma \\ \pi^+ \longrightarrow \mu^+ + \nu_\mu \\ \pi^- \longrightarrow \mu^- + \bar{\nu}_\mu \end{cases}$$

Figure 1.2 – Cartoon of multi-messenger signals, here from an active galactic nucleus. CR protons are deflected by magnetic fields, gamma-rays, and neutrinos travel in straight lines. Gamma-rays are recorded by satellite or ground observatories. Some absorption of gamma-rays can take place in the intergalactic medium. Neutrinos travel in straight lines, without absorption (adapted from Figure 1.8 in Raab 2021).

1.1.2 Gamma-ray astronomy

As CRs consist of ultra-relativistic charged particles, they are deflected by the solar system, Galactic or extragalactic magnetic fields and lose information about their origin. In general, the CRs sources must be traced by neutral messengers that can travel to Earth without deflection, such as gamma rays and neutrinos. In the case of hadronic CRs, gamma-ray and neutrino are produced on the same acceleration site where inelastic proton-proton interactions take place, leading to neutral and charged pion decays as described in Figure 1.2. Hadronic gamma-ray signals are produced in the shells of SNRs. However, no source was detected with neutrinos so far, as the neutrino sky appears quite uniform. A near-simultaneous signal in neutrinos and gamma-rays was observed only once for the Blazar TXS 0506+056 (IceCube Collaboration et al. 2018), confirming the idea that AGNs are extragalactic CR sources, although they can not account for the entire CR spectrum beyond the knee.

Gamma-rays can be produced by CR hadrons, but also by CR leptons through inverse Compton scattering ; high gamma-ray is thus expected in the GeV-TeV domain from regions with enhanced CR densities, such as near CR acceleration sites. The gamma-ray sky was explored by three generations of instruments since the first detection of the Crab Nebula in 1989 by the Whipple Collaboration (see Weekes et al. 1989; Holder 2012, for a review).

At GeV energies, gamma-ray flux is large enough for satellites to detect gamma rays. AGILE and Fermi-LAT are the currently operational satellites, scanning the sky in an energy range from 0.2 to 300 GeV. At TeV energies, the flux becomes much lower, and larger effective areas are needed. Ground-based observatories can not directly measure the incoming gamma-ray photons as they interact with nuclei in the atmosphere. For that reason, indirect detection techniques were developed.

The third generation telescopes using the Imaging Atmospheric shower Cherenkov Technique (IACT) have been in operation for almost two decades. The H.E.S.S. telescope [1], is located in Namibia and will be described in details in Section 1.3, MAGIC [2] is an array of two large telescopes located on the Island of La Palma, and VERITAS [3] is in Arizona. The next generation, the Cherenkov Telescope Array (CTA) [4], is partly operating on its Northern site on La Palma. Besides IACTs, new generation of water Cherenkov ground observatories, HAWC [5], LHAASO [6] and Tibet AS-γ [7] are operating, resulting in new source catalogues (Albert et al. 2020) and unidentified TeV sources, emitting beyond 10 TeV, and even to PeV energies (PeVatrons)(Cao et al. 2021; Amenomori et al. 2021a).

The map of all observed TeV sources is shown in Figure 1.3. The TeV catalog (`http://tevcat2.uchicago.edu/` currently contains up to 240 sources, from which 129 sources have been observed by H.E.S.S. (95 discoveries, see `https://www.mpi-hd.mpg.de/hfm/HESS/pages/home/sources/`). $\sim$ 24 SNRs, $\sim$40 PWNe (Abdalla et al.

---

[1] `https://www.mpi-hd.mpg.de/hfm/HESS/`
[2] `https://magic.mpp.mpg.de/`
[3] `https://veritas.sao.arizona.edu/`
[4] `https://www.cta-observatory.org/about/`
[5] `https://www.hawc-observatory.org/`
[6] `http://english.ihep.cas.cn/lhaaso/`
[7] `https://www.icrr.u-tokyo.ac.jp/em/index.html/`

2018b) are populating the region near the Galactic plane or in the Large Magellanic Cloud (LMC). Note that some SNRs are cataloged as "composite" as it is still unclear if the gamma-ray emission comes from the PWN in the center of the remnant or from the SNR shell. Tens of Galactic binaries emitting in gamma-rays have also been identified.

Extragalactic observations are numerous and concern other types of sources (for a review, see Prandini 2017) : AGN (Blazar, BL lac, ...), and starburst galaxies. More recently, H.E.S.S. and MAGIC were discovering for the first time TeV emission from transient events, such as Gamma-Ray Bursts (GRBs) (e.g. Acciari et al. 2021; Abdalla et al. 2019, 2021) and TeV emission was reported by H.E.S.S. from the nova RS Ophiuchi (Wagner & H. E. S. S. Collaboration 2021). $\sim$ 75 sources are still unidentified (UNID), and more detective work is needed to identify them (e.g. Ahnen et al. 2019).

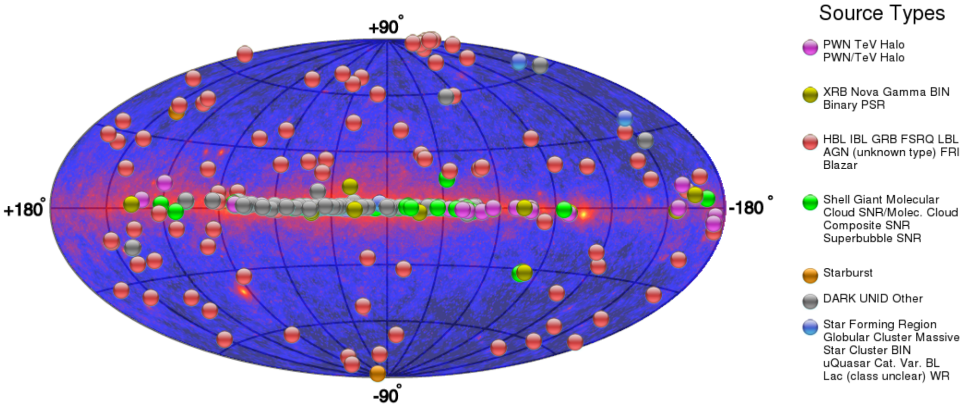

Figure 1.3 – Map of the galaxy showing the detected TeV sources, as catalogued in TeVCat. SNR and PWN are located in the Galaxy, along the Galactic plane and in the nearby galaxy LMC. The *Fermi-LAT* sky is map also shown in the background.

Finally, an important component of the gamma-ray sky is the diffuse background emission, which can be seen on the Fermi-LAT sky map in Figure 1.3. The diffuse gamma-ray background is visible, especially in the GeV domain in the Galactic-plane region. It is detected by H.E.S.S. in a region near the Galactic center (Abramowski et al. 2014a). Its origin is the propagation of CR in the Galaxy interacting with the interstellar medium, leading to the production of gamma-rays. The dominant process is neutral pion decays. The spectrum of diffuse gamma-rays follows the spectrum of cosmic rays with an index of 2.7. In addition, it is very well correlated with the distribution of baryonic matter, as probed by molecular line-emission maps tracing cold gas. But among these TeV gamma-ray sources, SNRs remain the only firmly identified accelerators of hadronic CRs.

1.2 Supernova remnants as cosmic-ray sources

SNRs are believed to be responsible for the bulk of Galactic CRs. SNRs are the structures created by the explosion of a star, an event called a supernova (SN). About 70–80% of the SNe in the Galaxy are caused by the explosions of massive stars—the so-called core collapse SNe—and about 20–30% are caused by thermonuclear explosions of white dwarfs (Type Ia SNe), either caused by mass transfer in a binary, or by merging of two white dwarfs. Apart from the activity from supermassive black holes in galaxies, perhaps responsible for the Fermi Bubble (see Chapter 6), SNe are the most energetic phenomena in galaxies. Supernovae were first predicted to be responsible for CRs by Baade & Zwicky (1934b,a).

The main arguments for SNRs to be CR sources are the following :

1. The energy released by the explosion of $\sim 10^{51}$ erg is enough to explain the energy of CRs,
2. the SN rate in the Galaxy of 2-3 per century is high enough to sustain the CR flux below the knee,
3. SNRs exhibit a gamma-ray spectrum consistent with the Fermi acceleration process.

For the first two points, simple arguments can be established comparing the CR power in the Galaxy to the power released by Galactic SNRs and the rate of one SN occuring in the Galaxy (e.g. Ginzburg & Syrovatskii 1964). Assuming the CR density at $n_{\mathrm{CR}} \sim 1\,\mathrm{eV\ cm^3} = 1.6 \times 10^{12}\ \mathrm{erg\,cm^3}$ considering the Galaxy as a cylindrical volume V with a radius of 15 kpc and a height of 300 pc, then the Galactic cosmic rays power is : $L_{\mathrm{CR}} = V\ n_{\mathrm{CR}} \simeq 3 \times 10^{40}\mathrm{erg\,s^1}$. On the other hand, SNe occurring every 30 years can deliver a power of $L_{\mathrm{SNR}} = 10^{51}\mathrm{erg/30yr} \simeq 10^{42}\mathrm{erg\,s^{-1}}$. Thus if each SNR transmits a few percent of its initial energy to CRs, it is enough to explain the Galactic CR density.

The third argument is linked with the first-order Fermi acceleration, also called diffusive shock acceleration, which is well confirmed by observational evidence. Indeed, the prediction of an SNR gamma-ray spectrum following a power-law with index in the range $\sim 2.0 - 2.7$ is confirmed in many cases (see Table 1.1). Diffusive shock acceleration is thoroughly explained in Schure et al. (2012), (see also Section 21 in Longair (2011), Section 11 in Vink (2020)).

These arguments motivated the search for some observational proof which can be given by a spectrum exhibiting a "pion bump" feature in the gamma-ray band, establishing the hadronic origin of the gamma-ray.

1.2.1 Notions of Supernova evolution

To understand CR acceleration at the SNR shock front, we need to know how an SN is created and evolves. Details for this Section can be found in Chapter 5 of Vink (2020). Both core-collapse SNRs (i.e., caused by type Ib/c, and type II supernovae) and SNRs created by thermonuclear SNe (type Ia) are CR accelerators. Core collapse SNe are explosions of massive stars with masses of more than 8 $M_\odot$ at the main sequence. During their lives, they successively burn hydrogen (protons) into helium, then helium into carbon by nuclear fusion, the subsequent burning cycles are shorter and shorter, and result in neon/magnesium, oxygen, silicon/sulfur, and finally in an iron-rich core, with burning shells of lighter elements on top. The fusion of Iron does not result in energy production, and as the core shrinks, electron capture by iron nuclei results in rapid loss of pressure support, therefore the core collapses within a second. In the process $\sim 10^{53}$ erg of gravitational energy is liberated, mainly in the form of energetic neutrinos. About 1% of that energy is used to explode the remainder of the star, which results in the supernova. The ages of massive stars range from 3 to ~50 million years, depending on the star's mass. In that time, stellar winds have been able to remove some of the hydrogen-rich outer layers of the stars, in particular of stars that started with masses above ~ 15 solar masses. After the supernova explosion, the core of the progenitor remains as a neutron star. However, if the neutron degeneracy can not resist the gravitational force, it collapses further into a black hole.

For type Ia supernovae, the explosion is the result of a thermonuclear runaway explosion happening in the core of an carbon-oxygen white dwarf, the end-product of a star less massive than ~ 6 solar masses. The trigger of the explosion is either due to the accretion from a companion star increasing the mass of the white dwarf or by the merging of two white dwarfs. The white dwarf mass reaches the Chandrasekhar limit of 1.4 $M_\odot$, at which it becomes unstable, and the pressure in the core becomes very high. The energy of the explosion is thermonuclear, first by the fusion of carbon/oxygen in iron-group elements, and then from the outer layers in silicon, sulfur, argon, and calcium. The resulting supernova explosion has an explosion energy of 10^{51} erg, similar to core-collapse SNe. An important source of energy, which makes type Ia SNe bright, is the radioactive decay of ^{56}Ni into ^{56}Co, which further decays into ^{56}Fe.

The stellar material is ejected into space in all directions with very high velocities, of the order of 20,000 km s^{-1}.This matter, referred to as ejecta, acts like a piston in the circumstellar medium (CSM), leading to the creation of a supersonic shock wave, which heats and sweeps up the CSM into a hot shell : the SNR. On the inside of the shell the ejecta are shocked by a reverse shock, as the ejecta are relatively cool after a few months to years, due to expansion. A young SNR, therefore, consists of an outer layer of hot, shocked CSM, a hot layer of shocked ejecta, and an inner layer of ejecta that is cool, and not easily visible, in the center. See Figure 1.4 for an X-ray image of a young SNR.

Initially, the energy of the explosion is mainly carried out by the SN ejecta material, and in the SNR, the energy is redistributed from the shocked ejecta to the whole SNR shell. This early phase is usually referred to as the free-expansion phase, or the ejecta-dominated phase.

However, after typically a few hundred years, most of the mass in the shell and the explosion energy resides in the shock-heated, swept-up CSM.

The shell becomes self-propagating. The so-called Sedov-Taylor phase is reached. The Sedov Taylor phase typically lasts $\sim 10^4$ years, during which the remnant reaches a radius of $\sim$20 pc.

When radiative losses become important and the shock is weaker, the next phase is reached, corresponding to a denser shell expanding non-adiabatically into a constant density interstellar medium. This is called the "pressure-driven" or "snowplow" phase.

After $\sim 10^5$years, the remnant dissolves in its surrounding. The CR acceleration process is believed to be significant during the free-ejecta and Sedov-Taylor phases.

The morphology of the remnant is a shell when the shock develops into a relatively homogeneous and sparse medium. In some cases, the leftover stellar core turns into a pulsar, a fast-spinning neutron star whose outflows can fill and power the inside of the SNR. These remnants are synchrotron nebulae, known as pulsar wind nebulae (PWNe), such as the very bright Crab Nebula. A rare sub-type of SNRs/PWNe includes the so-called composite SNRs (Helfand & Becker 1987), which show distinct evidence of both a PWN surrounded by an SNR shell (e.g. Abramowski et al. 2014a).

In this work, we are interested in shell-shaped SNRs : several have been observed by H.E.S.S., and the efficiency of CR acceleration by these objects has been studied in multi-wavelengths.

1.2.2 Shock acceleration in multi-wavelength observations

The first evidence of CR acceleration by SNRs was formed by the radio detection of synchrotron emission from SNRs : signaling the presence of energetic electrons gyrating in the magnetic field of the SNR shells. Such signals were discovered already in the 1950s (Shklovskii 1953; Minkowski 1957) . Synchrotron emission in the X-ray band (discovery by Koyama et al. (1995)) provides a second evidence, for electrons of beyond energies of $\sim$10 TeV.

Observations of non-thermal X-rays with the current satellites imprint the outer shocks for some shells SNR (Helder et al. 2012). As an example, the remnant of Kepler's SN (SN 1604) observations are shown in Figure 1.4. This Type Ia SN was observed by a.o. Johannes Kepler in 1604. Its distance is estimated at $\sim$ 5 kpc (details in Chapter 3). The composite X-ray image by the satellite Chandra (see also Burkey et al. 2013a), the blue outer rims (energy range 1.7-8 keV) reveals the presence of relativistic electrons by their synchrotron emission in X-rays : this edge is delineating the SNR shock.

Inside the shell, the ejecta is visible by lower energy thermal X-rays, in red (0.3 - 0.72 keV) and green, (0.72 - 1.7 keV). This X-rays signal corresponds to line emission (here mostly Fe-L and Si-K emission), giving information about the SNR evolution and the nature of its progenitor.

The real challenge in establishing SNRs as CR sources is thus the modeling of the gamma-ray spectrum to answer the following question : which radiation mechanism is mainly responsible for the gamma-ray emission ? Either inverse Compton scattering associated with the electron CRs, or pion production and decay, caused by hadronic CRs ?

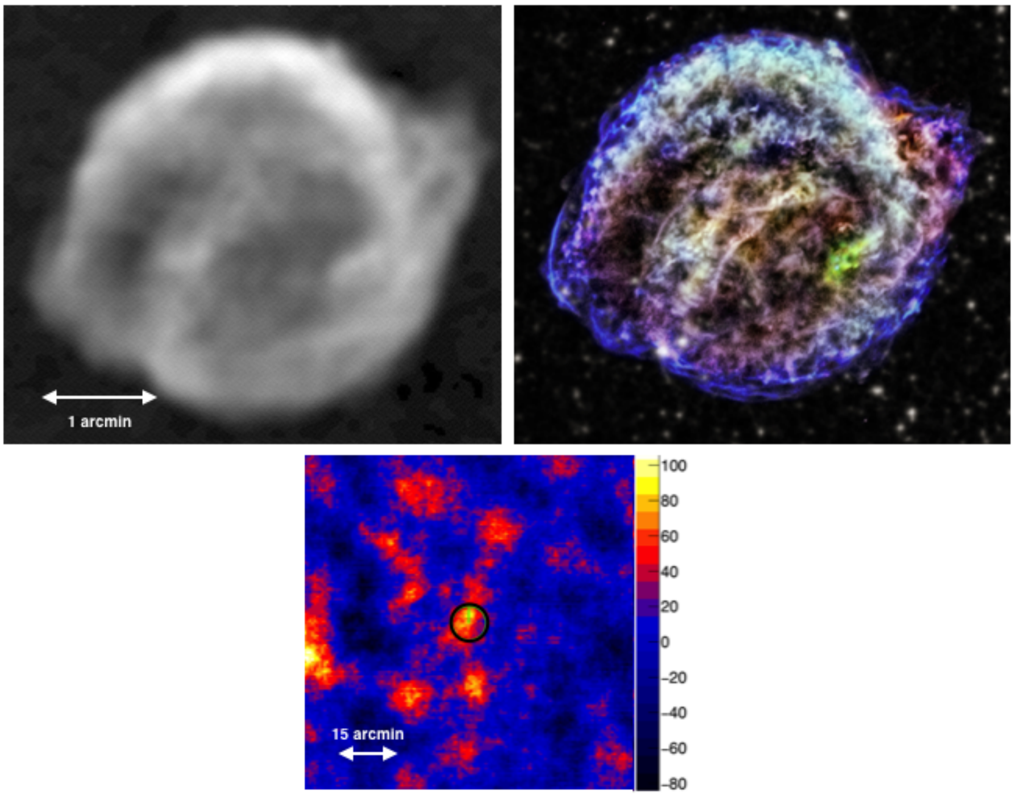

Figure 1.4 – Left : Kepler SNR with radio observation VLA (4.85 GHz) (DeLaney et al. 2002). Right : Kepler SNR as seen in composite X-rays by Chandra observatory (`https://chandra.harvard.edu/photo/2013/kepler/`) (Red : 0.3 – 0.72 keV ; green, 0.72 – 1.7 keV ; blue, 1.7 – 8 keV) (Burkey et al. 2013a). Notice the narrow filaments in blue, which is associated with X-ray synchrotron from multi-TeV electrons. Bottom : Kepler SNR TeV gamma-rays count map with H.E.S.S.

1.2.3 Emission mechanism leading to gamma-rays

Pion Decay emission

The pion decay process is the only radiative emission due to hadrons. It happens when hadronic CRs, atomic nuclei, and protons collide with atomic nuclei in the local gas, producing pi-mesons, better known as pions (π_0,$\pi^{\pm}$). The gamma-ray emission is due to the decay of the short-lived neutral pion, π_0, with a mass at 135 MeV and mean lifetime of $8.43{\times}10^{-17}$s[8]) The π_0 decays almost immediately into two photons, with a probability of 99%. Each photon takes half of the pion energy in its rest frame. Relativistic protons produce the π_0 ; its energy is then higher than just its rest mass, as some momentum is transferred from the protons. The minimal energy required for π_0 production is 279.66 MeV. This value is obtained by considering the two protons at rest. In reality, the incoming protons have a PL distribution in energy, producing π_0 spanning a whole range of energies that reflect into broad gamma-ray distribution in the GeV range up to TeV energies. The energy spectrum of photons produced in the pion decay process is estimated by taking many factors into consideration, such as the distribution of CR particles and the pion decay cross-section, including the p-p cross-section.

A semi-analytical approach is presented in Kelner et al. (2006) and Monte-Carlo simulations have been produced (Mori (1997), Hinton & Hofmann (2009a), Chapter 13.6 in Vink (2020)). These models show that the signature of π_0 decay in gamma-rays has a typical shape, commonly called a "pion bump", with a low energy suppression. The gamma-rays typically take away $\sim$ 10% of the parent proton energy, and both the gamma-ray and proton PL distribution have a similar PL slope.

To model the gamma-ray due to a pion decays, the main parameters to take into account are 1)the power-law distribution of the CR proton distribution (index, energy cut-off), 2) the total energy in the proton distribution (W_p)(which is unlikely to exceed 10 % of the SN explosion energy) 3)the density of the medium which accounts for the hadronic targets for an inelastic collision to take place. The mean density in the Galaxy is estimated at $n_p = 1\,\mathrm{cm}^{-3}$. The gamma-ray luminosity can be derived from W_p via the interaction time of π_0. $L_\gamma = W_p/\tau_{\pi_0} = 2.5\times10^{-16}(n_p/(1\,\mathrm{cm}^{-3})\times W_p$.

The clear hadronic spectral signature of the "pion bump" in the GeV regime has been established for the first time for two SNRs/molecular cloud associations, IC443 and W44, whose spectra are shown in Figure 1.5. This important result was established by AGILE in Giuliani et al. (2011) and *Fermi*-LAT Collaboration in Ackermann et al. (2013). Data fit with leptonic bremsstrahlung and hadronic emission models at GeV energies significantly favored hadronic interpretation. The data can be well fitted by assuming a broken power-law distribution for the CR hadrons. The spectral break in the gamma-emission is at $\sim$2 GeV for W44 and $\sim$ 20 GeV for IC 443. These breaks

---

[8] https://pdglive.lbl.gov/

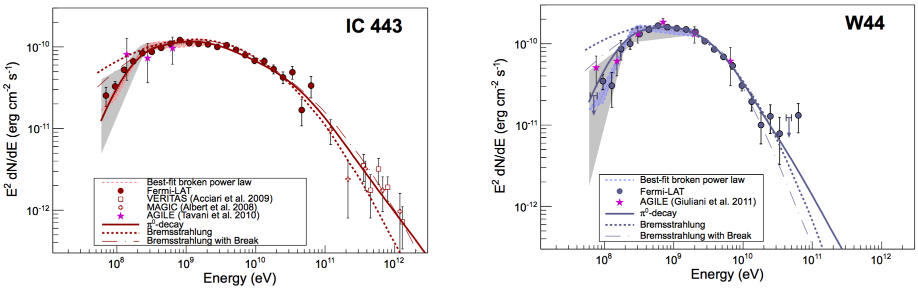

Figure 1.5 – *Fermi*-LAT spectrum of IC 443 (left) and W44 (right), for which a neutral pion decay emission model achieves the best fit. These SNRs are believed to interact with a nearby molecular cloud. The distribution of the parent CR hadrons follows a broken power law. These figures are taken from Ackermann et al. (2013)

are due to proton escape.

1.2.4 Leptonic emission

The non-thermal emission due to the CR relativistic leptons (electron and positrons[9]) relevant for SNRs are : synchrotron radiation, bremsstrahlung and inverse Compton scattering (hereafter IC). In general non-thermal radiation of high-energy relativistic electrons occurs when the electrons experience a change in momentum, deflected by magnetic or electric fields (synchrotron radiation or bremsstrahlung) or scattered by a photon field (IC scattering). All these processes involve the electromagnetic force.

In the GeV-TeV regime, the dominant leptonic process is usually IC scattering, which happens for the same energy range as pion decay. Determining which process, pion decay or IC scattering, is dominant is the main challenge in gamma-ray observations. Bremsstrahlung emission can also occur in the GeV range for very dense environments, but in those cases, usually, pion decay is the dominant mechanism.

Synchrotron emission This emission mechanism occurs when a charged particle in a magnetic field experiences a Lorentz force ($\vec{F} = q\,(\vec{v} \times \vec{B})$). The particle's trajectory is thus forced to be helical following the magnetic field direction.

Synchrotron emission in the radio band is due to electrons with few GeV. In the X-ray band, it is due to electrons of TeV energies. Synchrotron energy loss is directly linked to the magnetic strength being proportional to $U_{mag} \propto B^2$.

The energy loss caused by synchrotron emission is important for high energies

---

[9] Hereafter, whenever electrons are described, it also is valid for positrons.

electrons, with a characteristic time for the cooling of the electrons of :

$$\tau_{sync}\,(yr) \approx 1258 \left(\frac{E_e}{1\,\mathrm{TeV}}\right)^{-1} \left(\frac{B}{1\,\mu\mathrm{G}}\right)^{-2} \tag{1.1}$$

The time scale suggests that for radio synchrotron emitting electrons around a few GeV, radiative losses are not significant during typical lifetimes of SNRs ($\sim 10^5$ yr). However, radiative losses are important for X-ray synchrotron emitting electrons, which are typically 10 TeV.

This formula also predicts an "age break" or "cooling break" that can be observed in the synchrotron spectrum for some mature SNRs (Section 18 in Longair 2011). The break is expected for electron energies for which the cooling time is similar to the age of the SNR.

Assuming an electron energy distribution in $N(E)dE \propto E^{-q}dE$ and the resulting gamma-ray distributed as $N(E)dE \propto E^{-\Gamma}dE$, then $\Gamma = \alpha + 1 = \frac{q+1}{2}$, with α the radio spectral index.

Bremsstrahlung Bremsstrahlung is a "braking" emission of an electron deflected by the Coulomb force of an atomic nucleus ; the emission intensity heavily depends on the medium's density. Bremsstrahlung characteristic time in a medium of density n is $t_{Br} \approx 4 \times 10^7 \left(n_p/(1\,\mathrm{cm}^{-3})\right)^{-1}$ years. Bremsstrahlung emission could then be amplified if the CR electrons encounter dense regions, such as molecular clouds with proton densities of $\sim 10^3$ to $\sim 10^5 \mathrm{cm}^{-3}$. Bremsstrahlung can play a role in hard X-rays up to GeV band (for details of Section 13 in Vink 2020).

Inverse Compton scattering The inverse Compton effect is a process of interaction between an electron and a photon. The electron transfers part of its energy to a target photon which gains enough energy to emit at GeV and TeV energies. As an example, an electron with an energy of 1 TeV will upscatter a typical cosmic-microwave background (CMB) photon of 7×10^{-4} eV, to an energy of 2.7 GeV. The photon field provided by the diffuse cosmic background is a natural target for this process, and the star radiation fields as well. The power radiated by an electron in an isotropic photon field is : $\frac{dE}{dt} = \frac{4}{3}\sigma_T \gamma^2 U_{rad}$, with σ_T, the Thomson scattering cross-section in the case where the energy of the photon is $E_\gamma << 2mec^2$, or the Klein-Nishina cross-section otherwise. U_{rad} is the radiation energy density. An important component for the radiation energy density is the CMB, for which $U_{rad} \approx 0.26\,\mathrm{eV\,cm}^{-3}$. Other contributions come from the Galactic infrared emission and UV stellar light that may be as large as the CMB, depending on the local environment. The ratio of synchrotron peak compared to the peak of IC can provide some information on the ratio of magnetic field compared to background radiation field, as it scales like $U_{mag}/U_{rad} \propto B^2/(U_{rad})$.

Leptonic versus hadronic gamma-ray emission

In the so-called "leptonic scenario," the SNR non-thermal emission is well modeled with synchrotron radiation from radio to X-ray energies, and IC scattering and perhaps bremsstrahlung in the GeV–TeV band : a single population of CR electrons produces all these emission components.

In the hadronic scenario, the radiation model includes pion decay emission to explain the data in the GeV-TeV regime. Synchrotron emission from CR electrons still accounts for the low energy emission (radio to X-rays). IC scattering will be contributing to the gamma-ray emission but is sub-dominant.

Note that in the case of local high-magnetic field strength, the energy density in the population of electrons does not need to be energetic to produce the synchrotron emission. As a result, the IC contribution to the gamma-ray emission tends to be weak.

The magnetic field strength in the acceleration region is thus a critical value but may be challenging to estimate. It can be estimated from the radio luminosity using the assumption of equipartition between magnetic-field energy and particle energy density (Longair 2011). It is also possible to estimate it by the width of the filament of the non-thermal X-rays, which is the case for a few SNR, and the errors are important (Section 12 in Vink 2020). Finally, if the gamma-ray emission is assumed to be leptonic, the relative flux ratio of synchrotron radiation and IC scattering provides a magnetic-field strength estimate. However, this ignores the possibility of a hadronic gamma-ray component.

In principle, gamma-ray observations could be sufficient to prove that CR particles —electron and hadrons—are accelerated at the SNR shock fronts. Most of the time, the gamma-ray data by itself does not permit a firm interpretation of the energetics and nature of the particles, and even considering the broad electromagnetic spectrum, it is sometimes difficult to disentangle between the leptonic and hadronic origin of the gamma-ray. Multi-wavelength studies of thermal and non-thermal emission are essential to investigate plausible scenarios. In addition, observations across the electromagnetic spectrum can provide crucial information on the SNR properties, such as the age, composition, and evolutionary stages, and provide estimates of the magnetic field, radiation fields, and local proton densities. These ingredients help to build the multi-wavelength modeling and its interpretation.

1.2.5 Supernova remnants detected in TeV gamma-rays

Among 294 SNRs identified in Green (2019), 28 are seen at TeV energies and 30 at GeV (Acero et al. 2016), with 24 objects emitting both in the GeV and TeV regime. Table 1.1 (from table 12.4 in Vink 2020)) lists the 27 SNR detected at TeV energies, to which Kepler SNR should be added, as a 4 σ detection is reported in Chapter 3. Classification of these objects is difficult to make. However, one trend is apparent :

young shell-type SNRs (< 1000 years old) are bright in TeV, with moderate luminosity in GeV, but the nature of their emission remains ambiguous. For "middle-aged" and "mature" SNRs (3000-5000 years), GeV emission is bright, and TeV emission is weak : detected mature SNRs mostly seem to interact with dense matter, such as molecular clouds (MCs). The strong GeV emission is difficult to explain by the inverse Compton mechanism. It can be better explained by bremsstrahlung radiation of a lepton population or neutral pion decay (e.g. Abdalla et al. 2018c). An explanation is given by the fact that the shock acceleration is powerful for young SNRs, with high shock velocities and no CR escape. As a result, CR leptons and hadrons are accelerated in the TeV domain. When the remnant gets older, the acceleration gets weaker, CR particles can still reach the GeV domain, and the highest energy CRs have escaped. However, interaction with surrounding matters such as molecular clouds maintains some TeV emission. Of course, this is just a trend, and the origin of the TeV emission should be discussed on a case-by-case basis. In this Section we will mention a few examples.

A good example of totally different behavior among similar SNRs can be found for the $\sim 1000 - 3000$ years old, sometimes called middle-aged, SNRs LMC N132D and Puppis A. Both SNRs are oxygen-rich, N132D is located in the Large Magellanic Cloud at $\sim$ 50kpc, and Puppis A is at a Galactic distance at $\sim$ 2.5kpc. N132D is very bright in gamma-ray, as discussed in Chapters 2. Puppis A is very bright in X-rays and seen in the GeV regime, but its TeV emission has eluded us so far, which is surprising, as the SNR is in the vicinity of a molecular cloud, and its distance is much closer than N132D (Hewitt et al. 2012; Abramowski et al. 2015a).

The age of an SNR is not a trivial value to address. For some "historical" young SNRs, the associated SNe were recorded by astronomers or astrologers, such as the remnant of SN1604/Kepler's SNR (Aharonian et al. 2008c), SN185/RCW 86 (Abramowski et al. 2018), SN 1006 (Acero et al. 2010), and SN 1572/Tycho's SNR (Acciari et al. 2011). The SNR RX J1713.7-3946 (RX J1713 Abdalla et al. 2018d) is believed to be the remnant of SN 393 (Wang et al. 1997), and SNR Cassiopeia A is possibly associated with a nearby SN exploding around 1671, but which was not detected at the time. In other cases, the age estimates rely on the expected size evolution of SNRs, in addition to estimates of local densities or direct or indirect measurements of the shock velocities.

Some nearby SNRs detected in TeV gamma rays are extended enough—0.5–1 degree, to resolve their morphology in TeV gamma rays,

for example RX J1713, RCW86 (Abramowski et al. 2018), and SN1006 (Acero et al. 2010). This permits a detailed study of the gamma-ray and non-thermal X-rays in the shock region. See, for example, RX J1713 in Abdalla et al. (2018d). Among the brightest TeV SNR are RJX1713 and Vela Jr (Abdalla et al. 2018e), for which the origin of the gamma-ray emission is uncertain : both leptonic and hadronic models are fitting well the spectral data.

Cas A is a particular case of a young SNR ($\sim$ 340 years old) for which a cut-off at surprisingly low energy is observed at $\sim$3.5 TeV (Ahnen et al. 2017; Abeysekara et al. 2020). Note that the gamma-ray emission of Cassiopeia A is believed to be of hadronic origin (Ahnen et al. 2017).

The interaction of SNR with MCs is intensively discussed in Aharonian & Atoyan (1996); Gabici et al. (2009); Gabici & Aharonian (2014); Gabici (2017). The idea is that CRs escaping from the SNR shock front interact with the dense surrounding matter, leading to pion production and decay. As already mentioned, interaction with surrounding molecular clumps has been well-established for two SNRs, IC443, and W44 showing a clear signature of a pion decay. Furthermore, these SNRs have an estimated age of $\sim$ 10 000 years, which is the same order as the other SNR listed as SNR/MC, such as SNR W28, whose age is estimated at $\sim$3500-15 000 years. W28 is a particular SNR, surrounded by identified molecular clouds : TeV emission was detected by H.E.S.S. towards this system (Abramowski et al. 2008) with four emission peaks coincident with the position of the clouds showing that clouds illuminated by the CR escaped from the SNR can emit in the TeV regime. Evidence for SNRs interacting with MCs was also reported by H.E.S.S for W49B (Abdalla et al. 2018d), for CTB37B (Xin et al. 2016), and HESS J1457-303 (Aharonian et al. 2008b; Hayakawa et al. 2012), HESS J1640-465 (Abramowski et al. 2014b) and G349.7+0.2 (Abramowski, A. et al. 2015). Clear hadronic signatures have been established, besides IC443 and W44, for SNR W51C (Jogler & Funk 2016), and W49B (Abdalla et al. 2018d). Moreover, a recent search for pion decay signatures in the latest *Fermi*-LAT catalog established 13 SNRs as hadronic CR accelerators (Lemoine-Goumard & Ballet 2021), whose identification will be published soon.

Among all the listed SNRs, even for the brightest objects, spectra exhibit energy cut-offs, and no emission beyond 10^{14} eV is seen for any of these SNR, although a few objects are still under scrutiny for PeV emission (e.g. Amenomori et al. 2021b).

1.2.6 Supernovae as possible CR sources beyond the knee

The lack of evidence for any signal from SNRs above 10^{14} eV motivated the investigation of possible PeV emission at some earlier stages of the SNR evolution, i.e., the supernova (SN) stage itself.

When an SN event occurs, the shock velocity is at its maximum ($v_{sh} \approx 10000 - 20000\,\mathrm{km s^{-1}}$, and CR escape has not been experienced yet. The shock can happen on a scale of days after the star outburst, and acceleration is predicted to be very efficient quite early if the SN occurs in a very dense environment.

The dense environment provides a high-density medium for a proton-proton collision to take place and allows for substantial magnetic-field amplification (Bell 2004).

The best candidates are core-collapse SNe (ccSNe), for which dense environments have been observed, created by the progenitor's wind before the outburst, also known

Table 1.1 – List of supernova remnants and related sources detected in TeV gamma-rays. Taken from table 12.4 in Vink (2020), which established the list based on the TeVCat catalog (`http://tevcat.uchicago.edu`) and (Abdalla et al. 2018c), Abdalla et al. (2018e),

Name	Type	d (kpc)	$F(1-100\ \mathrm{GeV})$ $(10^{-10}\mathrm{erg\,cm^{-2}s^{-1}})$	Γ_{GeV}	$L(1-100\ \mathrm{GeV})$ $(10^{33}\mathrm{erg\,s^{-1}})$	$F(>1\ \mathrm{TeV})$ $(10^{-12}\mathrm{ergcm^{-2}s^{-1}})$	Γ_{GeV}	$L(>1\ \mathrm{TeV})$ $(10^{33}\mathrm{ergs^{-1}})$	X-ray synchrotron ?
W 28	SNR/Molec. Cloud	2	2.01 ± 0.19	2.64	96.3	1.82 ± 0.29	2.66	0.87	no
W 49B	SNR/Molec. Cloud	11.3	0.94 ± 0.15	2.36	1441.3	0.44 ± 0.10	3.14	6.72	no
W 51	SNR/Molec. Cloud	5.4	1.63 ± 0.21	2.3	568.7	2.70 ± 0.30	2.58	9.42	no
SNR G106.3+2.7	Shell	0.8	< 0.12	≡ 2	0.9	7.90 ± 3.43	2.29	0.61	no
Cassiopeia A	Shell	3.4	0.41 ± 0.10	2.09	57.2	3.30 ± 0.05	2.4	4.57	yes
Tycho	Shell	3.5	0.05 ± 0.01	2.14	7.3	0.38 ± 0.14	2.9	0.56	yes
IC 443	SNR/Molec. Cloud	1.5	2.86 ± 0.30	2.34	77.1	1.11 ± 0.50	3	0.30	no
RX J0852.0-4622	Shell	0.2	1.08 ± 0.27	1.87	0.5	100.00 ± 24.00	1.81	0.48	yes
RCW 86	Shell	2.5	0.11 ± 0.04	1.42	8.0	16.00 ± 3.86	1.6	11.97	yes
HESS J1457-593	SNR/Molec. Cloud	3.5	< 0.04	≡ 2	6.1	5.93 ± 0.77	2.52	8.69	no
HESS J1534-571	Shell					6.50 ± 2.12	2.51	0.00	no
SN 1006	Shell	2.2	0.02 ± 0.01	1.79	1.4	1.90 ± 0.40	2.3	1.10	yes
HESS J1614-518	Shell					20.00 ± 6.32	2.42	0.00	no
HESS J1640-465	SNR/Molec. Cloud	10	0.69 ± 0.07	2.19	825.2	6.50 ± 1.18	2.11	77.79	no
RX J1713.7-3946	Shell	1	0.40 ± 0.10	1.5	4.8	400.00 ± 6.25	2.2	47.87	yes
CTB 37A	SNR/Molec. Cloud	7.9	0.51 ± 0.10	2.64	378.8	4.60 ± 1.10	2.3	34.36	no
CTB 37B	Shell	13.2	< 0.42	≡ 2	873.7	16.00 ± 3.69	2.65	333.63	no
G349.7+0.2	SNR/Molec. Cloud	11.5	0.24 ± 0.10	2.19	371.9	0.44 ± 0.14	2.8	6.96	no
HESS J1731-347	Shell	3.2	0.06 ± 0.02	1.71	6.9	13.20 ± 2.60	2.32	16.18	yes
HESS J1745-303	SNR/Molec. Cloud		0.59 ± 0.19	2.6	0.0	6.45 ± 0.63	2.71	0.00	no
LMC N132D	SNR/Molec. Cloud ?	50	0.03 ± 0.02	1.4	861.7	0.50 ± 0.19	2.4	149.59	no
HESS J1813-178	Composite	4	0.47 ± 0.13	2.9	89.8	8.98 ± 1.80	2.09	17.19	
HESS J1833-105	Composite	4.6	< 0.09	≡ 2	22.3	1.80 ± 0.36	2.08	4.56	
W41/HESS J1834-087	Composite	5	0.70 ± 0.34	2.38	210.6	12.00 ± 2.00	2.5	35.90	
Kes 75/HESS J1846-029	Composite	11	< 0.13	≡ 2	191.7	3.81 ± 1.11	2.26	55.14	
MGRO J1908+06	Composite	3.4	< 0.08	≡ 2	11.2	34.00 ± 8.00	2.2	47.04	
G54.1+0.3	Composite	8.2	< 0.11	≡ 2	88.5	3.10 ± 1.50	2.39	24.95	

as the "wind bubble".

Some theoretical studies indeed predict gamma-ray emission from ccSNe up to PeV, on timescales of days to weeks (e.g. Murase et al. 2011; Cardillo et al. 2015; Marcowith et al. 2018; Katz et al. 2011).

Important parameters are the mass-loss rate before outburst, $\dot{M}$, and the wind velocity, u_w, as the medium density scales as $\rho_{env} = \dot{M}/(u_w r^{-2})$ (e.g. Dwarkadas 2013). Among ccSNe, the best candidates are type IIn , for which the $\dot{M}$ is predicted to be high ($10^{-2} - 10^{-4} M_{\odot}\,\mathrm{yr}^{-1}$) and wind velocities moderate ($u_w \simeq 10\,\mathrm{kms}^{-1}$. Type IIP , IIL, and Type Ib, are also potential candidates (details in Marcowith et al. 2014).

A prime example for CR acceleration is the nearby and bright radio source, SN 1993J. For this type IIb SN, a high magnetic field (1–100G) is estimated from radio observations (Fransson & Björnsson 1998; Tatischeff 2009) and very high shock speeds are observed ($\sim 20\,000\,\mathrm{kms}^{-1}$). TeV gamma-ray emission should have been detected on a timescale of weeks after the outburst, but sensitive IACTs were not present at the time (Tatischeff 2009; Marcowith et al. 2018).

These studies motivated the search for a TeV gamma-ray emission from ccSNe with H.E.S.S., presented in Chapters 4 and 5. A serendipitous search in H.E.S.S. data was conducted in the fall of 2014 (published in 2019), finding the location of 9 SNe in archival data (Chapter 4). In parallel, a proposal for triggered targets-of-opportunity observations (ToO) for ccSNe was accepted in 2016 and had been going on ever since. The ToO program is described in Chapter 5. A ToO was triggered for SN 2016adj in Centaurus A and AT2019krl in M74.

No TeV emission was found from any of the 11 observed SNe, and upper limits (UL) on the flux were reported. With H.E.S.S. ULs we can provide interesting constraints on the environment of the observed SNe and define better the detection horizons in terms of mass loss rate, wind velocity, and distance (see Figures 4.3, 4.4).

So far no SNe has been detected at TeV (see also Ahnen et al. 2017) But a possible GeV emission towards the peculiar H-rich super-luminous SN iPTF14hls at ~150 Mpc Yuan et al. (2018) and the nearby (~3.5 Mpc) type IIP SN 2004dj Xi et al. (2020) were reported.

The H.E.S.S. ToO program is ongoing. Since 2021, collaboration with external observatories have been developed : this permits alerts on a possible candidate and to gather information as early as possible on the SNe characteristics, such as the type, the environment, the progenitor properties, and radio signals of the SNe.

1.3 H.E.S.S. : the High Energy Stereoscopic System

The High Energy Stereoscopic System (H.E.S.S.) is an array of telescopes using the imaging air shower technique (IACT). H.E.S.S. began its observations in 2002 and was fully operational by 2004. The objective of the array is to detect gamma-ray radiation between $\sim$ 100 GeV and $\sim$ 100 TeV with unprecedented sensitivity and arcminute resolution.

The location of the telescopes ($23^\circ16'18''$ S,$16^\circ30'30''$ E) on the Khomas Highlands in Namibia is far from light pollution. The site is at an altitude of 1800m and benefits from a semi-desert climate.

The particular meteorology allows a long span of annual observation time. Apart from the rain season from January to March, most nights are clear and cloudless, allowing observations with high efficiency. The mean annual observation time is of $\sim$1000hrs. It is the only observatory in the TeV domain located in the southern hemisphere. Therefore, H.E.S.S. has a unique view in the southern sky, on the Galactic plane and, in particular, its central region. Since 2012, the experiment has entered a new phase with a fifth telescope, CT5, with a large collection area and improved camera, allowing the energy threshold to be lowered to a few tens of GeV. H.E.S.S. is managed by a collaboration of more than 40 institutes spread over more than 13 countries. This collaboration takes care of the construction, maintenance, data collection, and data analysis up to scientific production. H.E.S.S. operations were planned till the end of 2021, but recently, a three-year extension was agreed upon by the collaboration.

Figure 1.6 – The H.E.S.S. site in Namibia. CT5 is in the middle, from left to right are CT1 to CT4. In building in the front host the central computing and control room.

In every science Chapter of this thesis, the telescope and its performance are briefly described. Here I discuss more precisely the different steps leading to the analysis of astrophysical source data, from data-taking to source detection, with particular attention on the Imaging Atmospheric Cherenkov Technique and the analysis steps used in the work presented here.

The detection technique is indirect : the signal recorded is not from the astrophysical TeV gamma-ray, but from secondary particles belonging to the air shower induced by the primary TeV gamma-ray photon. These secondary particles emit Cherenkov light and the shower image is recorded on the telescopes' optical cameras.

From the shower images in the cameras we reconstruct the energy and the direction of the incoming gamma-ray. First, the Cherenkov light needs to be deduced from the electrical signal recorded by the camera. Secondly, from the Cherenkov light, the shower characteristics and the gamma-ray properties are derived, leading to reconstructed gamma-ray-like events. A few more steps are needed concerning the source detection from the reconstructed events, among which background estimation.

As a consequence, H.E.S.S. analysis involves complex techniques requiring good knowledge of the instruments, solid Monte Carlo simulations, and atmospheric simulations. That can be summarized in three main steps.

— From primary gamma-ray to camera image : this includes the air shower imaging technique, the telescope, and the data acquisitions (Sections 1.3.1 to 1.3.3).

— From camera image to gamma-ray events : this includes calibration of the camera signal and reconstruction of the gamma-ray events (Section 1.3.4 and 1.3.5).

— From gamma-rays events to results : including data quality selection, gamma-hadron separation, and source analysis (Section 1.3.5).

1.3.1 The Imaging Atmospheric Cherenkov Technique

In this first part, we describe the Cherenkov atmospheric imagery, the H.E.S.S. experimental settings, and briefly the data acquisition.

The shower begins with the interaction of the primary particle in the Earth' atmosphere, which produces secondary particles, spreading on large distances along the shower's axis. These charged particles emit Cherenkov light, as they travel faster than the speed of light in the atmosphere.

The atmosphere is used as an inhomogeneous calorimeter, with the density varying with altitude. The Cherenkov light density on the ground is proportional to the total number of charged particles at the gamma-ray shower maximum depth, which is proportional to the initial energy of the gamma-ray photon.

The detection technique is quite interesting and relies on solid air shower simulations (mainly CORSIKA (Heck et al. 1998) adapted to gamma rays (Bernlöhr 2008)), as well as atmospheric modeling. With this technique we reconstruct the primary particle's energy with a typical resolution of 15%, and and its direction with an angular resolution of $\simeq 0.06$ deg. In practice the following shower parameters are important : the shower zenith and azimuth angles, the shower size, the distance of the shower impact on the ground, with respect to the center of the telescope array, the first interaction depth, and if possible the nature of the primary particle : gamma-ray photon or background particle (electrons, positrons, protons...).

An Air Shower simulation example is represented in Figure 1.8. The maximal development of a shower of 1 TeV is typically at 8-10 km above the ground, at plane-cruising altitude. One uncertainty is the first point of interaction, which can vary by several kilometers, because of the interaction length in the top of the atmosphere.

The Cherenkov light is emitted as the charged particles travelling faster than the speed of light in the medium (Čerenkov 1937; Tamm & Frank 1937). On the ground, first the low latitude light is received then the high latitude particle light follows a few nanoseconds later. On a distance of less than 150 m the light emitted at every latitude is nearly isochronous : there is less than 2 ns delay between particles Cherenkov flashes.

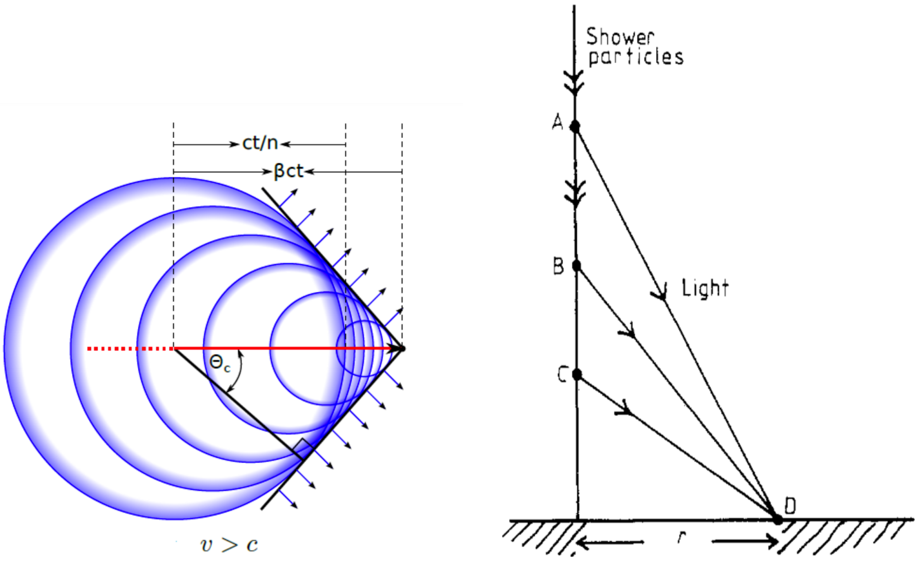

Figure 1.7 – Left :Shock front of Cherenkov light. The particle travels with a speed $\beta = v/c$, greater than the speed of light in the medium, $\frac{c}{n}$. The opening angle θ_c depends on the particle speed and the medium, as $cos\theta_c = \frac{1}{\beta n}$ (credit : Ömer Penek). Right : the Cherenkov light cone seen by a detector on the ground located on position D (Figure taken from Hillas (1982))

.

The Cherenkov light cone is represented in Figure 1.7. This cone is explained by the fact that the Cherenkov light ring angle is linked to the atmospheric refractive index, n, with $\cos\theta_c = 1/\beta n$ and the refractive index is linked to the atmosphere profile with $n - 1 = \rho(z)$ with $\rho(z)$ assumed exponential ($\rho(z) = \rho_0 \exp(-z/z_0)$). The Cherenkov light pool has a diameter of $\sim$ 120m, corresponding to the telescope distance and a typical opening angle of the cone of 1°. The Cherenkov light emission permits a large effective area ($\simeq 11300\,\mathrm{m}^2$), even with a modest installation.

The key parameter of the Cherenkov Atmospheric imagery is the time : the Cherenkov light pulses must be recorded within a few nanoseconds, typically less than five ns. During this small interval, the Cherenkov light outshines the night sky background.

Hadronic shower rejection capabilities : the discrimination between an electromagnetic (induced by a gamma-ray) and a hadronic shower (induced by a primary hadron particle) can be made using the shape of the shower. As shown in Figure 1.8, the gamma-ray induced shower is quite regular : the primary gamma-ray photon creates an electron-positron pair, which in turn emits photons by bremsstrahlung, these photons will be able to create a new electron-positron pair, etc., leading to the nearly exponential growth. Eventually, the rate of ionization energy losses dominates over that of bremsstrahlung, and the shower electrons/positrons lose their energy before being able to produce another secondary gamma-ray photon. These electromagnetic showers can be modeled semi-analytically.

The hadronic shower shape is more chaotic, as it involves pions and kaons production and subsequent electromagnetic showers created randomly at the edge of the secondary particle production. For details on showers (see e.g. Bernlöhr 2008; De Naurois 2012)).

The Cherenkov light pulse from an electromagnetic shower leads to an elliptical shape on the ground as recorded by the telescope camera. The image of a hadronic shower is not regular due to fluctuations in the initial nuclear interactions. Cherenkov light camera images from CR-generated muons are very typical, having a ring shape (see Figure 1.9).

These imprints of the Cherenkov light emitted by the particles of the atmospheric shower are the building blocks of the gamma-ray shower reconstruction. They are used to identify the primary particle and determine its properties with elaborate reconstruction methods.

1.3.2 H.E.S.S. experimental setting

The H.E.S.S. array consists of five telescopes : four small telescopes (CT1–4) are arranged in a square with a baseline of 120 m, and a fifth telescope in the center, CT5. The telescope separation length was chosen accordingly to the development size of a typical Cherenkov light cone on the ground, which is $\sim 100 - 150$m allowing a single shower to be observed within the cone. Imprints of the shower are recorded on more than one telescope allowing stereoscopic mode. In this Section, we will mainly present the CT1-4 telescopes, only mentioning CT5 when relevant.

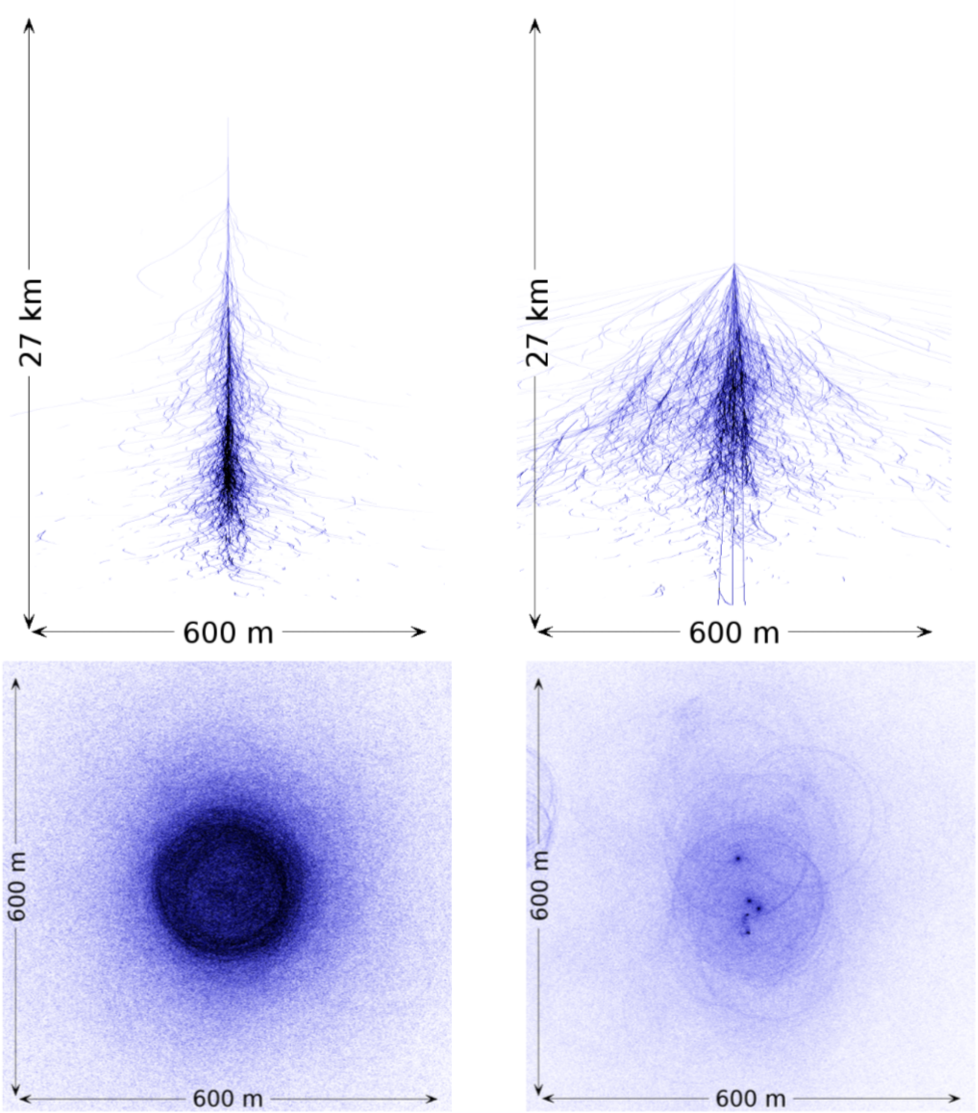

Figure 1.8 – Left : Monte-Carlo simulation of a gamma-ray photon-induced air shower. Right : Monte-Carlo simulation of a proton-induced air shower. Figures are taken from Balzer (2014)

.

The telescope

The telescopes consist of the mechanical structure, a mirror surface and a camera. Each of the four telescopes of 107 m^2 mirror area is equipped with a 960-pixel photomultiplier-tube camera. The steel structure rigidity allows avoiding any curva-

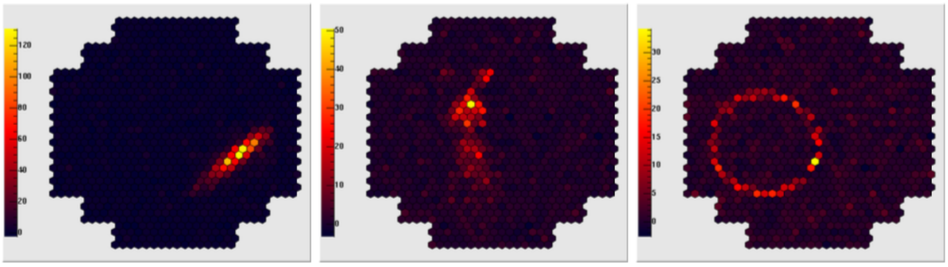

Figure 1.9 – Three different shower images as a H.E.S.S. camera could record them : Cherenkov light due to atmospheric showers from a gamma-ray photon and a proton (resp. left and middle), as well as a muon passing the detector (right). Each point is a camera pixel, with the color scale representing the intensity of Cherenkov photons in arbitrary units.

ture effect due to the weight of the camera or to strong winds. The telescope mount is of the alt-azimuth type, which offers the possibility of pointing in all directions and reverse mode. The travel speed is ∼ 100° per minute for CT1–4 (∼ 200° per minute for CT5). The pointing to a source location typically takes 2 minutes for CT1–4.

The reflecting surface is hexagonal (squared for CT5) with a diameter of 12 m for CT1–4 (28 m for CT5). It is made up of 380 circular mirrors of 60 cm in diameter, arranged in a Davies-Cotton frame (Davies & Cotton 1957). The alignment of the mirrors is carried out using three supports, two of which are motorized, located at the base of each mirror. For CT5, the mirrors are hexagonal facets of 90 cm size, and the mount is parabolic. Mirrors can be seen in Figure 1.10).

The alignment can affect the point spread function (PSF), which defines the angular resolution of the gamma-ray source reconstruction. The PSF is smaller than one pixel, but it can become more significant for large offsets and large zenith angles, which is due to the limits in mirror alignment (see Cornils et al. 2005).

The mirror alignment also affects pointing precision, leading to a systematic error estimated to be $\sim 20''$ in both right ascension and declination for the source position. The telescope pointing is calibrated using a database for telescope deformations, which is regularly updated and used during observations. The database is constituted using CCD cameras : one is located on the mirror surface, pointing to a bright star in the sky. Another is placed in the center of the reflecting surface, pointing towards a H.E.S.S. camera with its cover closed. This camera points to LEDs placed on the cover, lighting up in the direction of the CCD. The position of the star image relative to that of the LEDs permits estimation of the pointing deformation with respect to the pointing direction (zenith, azimuth). For pointing procedures, see also Gottschall (2018). Finally, mirror aging is a technical problem that needs to be taken into account for IACTs, as optical efficiency is degrading over the years as the mirror reflectivity declines (Bernlohr et al. 2003). The mirrors of CT1–4 were changed in 2013.

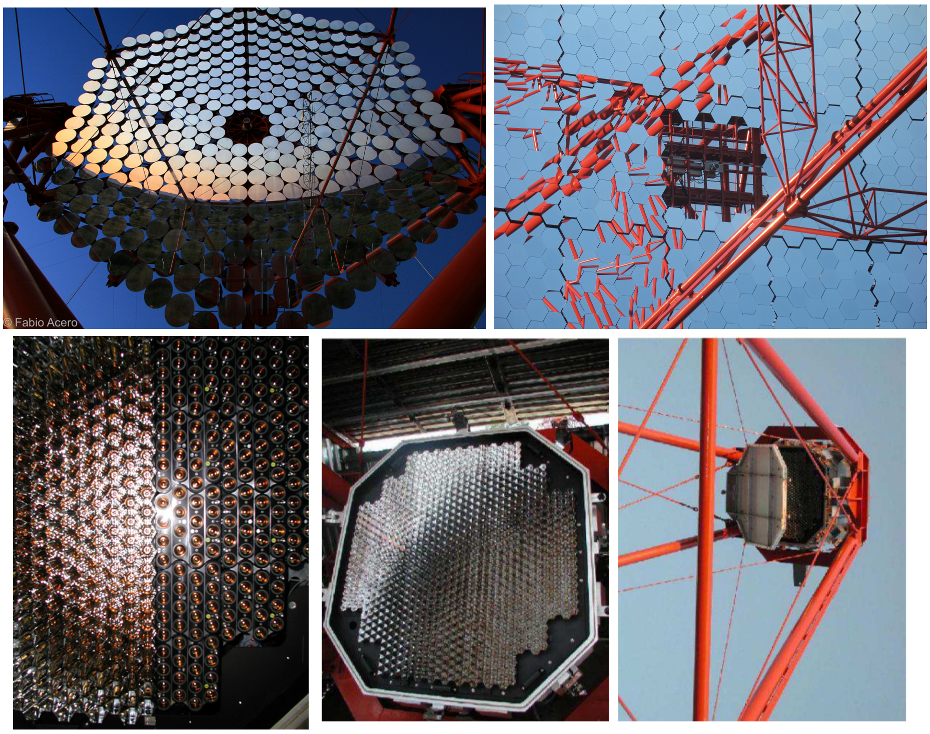

Figure 1.10 – Top : mirror surfaces for CT1-4 telescopes and CT5 (left). The CCD cameras are visible in the center. Bottom : views of CT1-4 camera, also mounted on the telescope structure with the lid opened (Hinton & HESS Collaboration 2004). The bottom left image shows the Winston cones partly placed on the upgraded camera.

The camera

The telescope camera is located 15 m from the reflector in the focal plane. They combine a fine pixelation with fast electronics. The fast recording limits noise from the sky background and noise recorded during the acquisition of the Cherenkov flash. The cameras consist of 960 photo-multiplier tubes (PMTs hereafter), also called pixels, distributed over 60 drawers. Each PMT is fitted with a Winston cone, which limits the mirror's field of view and reduces the dead space between each pixel. Each pixel has a field of view of 0.16° in the sky. The camera allows observing a field of view of 5° in diameter.

PMTs are made up of a photo-cathode converting light into electrons, called photo-electrons (pe). The conversion probability of a photon to a pe is called quantum efficiency. It depends on the wavelength and varies from one PMT to another. The quantum efficiency of H.E.S.S. PMTs is about 20% in the near UV, the dominant wavelength band for Cherenkov light. The Winston cones (see Figure 1.10) allow light to be guided directly onto the photo-cathode, which makes it possible to obtain a homogeneous efficiency with a transmission factor of $\sim 70 - 80\%$. The PMTs are grouped by 16 in units called drawers. Each drawer contains electronic cards managing the power supply, the output reading of the PMTs, and the communication with the camera backend electronics. For the CT1–4 camera see also Hinton & HESS Collaboration (2004) and (Bernlohr et al. 2003).

The CT5 camera consists of 2048 PMTs (128 drawers of 16 PMTs each). Each PMT has a field of view of 0.07° leading to a total field of view of 3.2° on the sky. Details can be found in Bolmont et al. (2014).

The CT1 telescope camera was upgraded during the summer of 2015, the other CT2–4 cameras during the fall of 2016. The upgrade is using new techniques with the NECTAr chips (Ashton et al. 2020a). CT5 camera was upgraded in 2019 with a FlashCam camera (Bi et al. 2021). Both NECTAr and FlashCam techniques will be used for CTA.

Weather and Atmosphere control

The air quality directly influences the amount of light received by the telescopes. The atmosphere modeling induces uncertainty in reconstructing the primary particle's energy. Therefore, it is essential to characterize with precision the quality of the air at the time of acquisition. Therefore, a series of instruments have been installed on the H.E.S.S. site to control the quality of the atmosphere. They also make it possible to secure data collection by allowing the night shift to anticipate the arrival of clouds, to control the humidity and the intensity of the wind.

The on-site instruments to monitor the weather are :

- A telescope radiometer pointing in the same direction makes it possible to probe the humidity of the atmosphere and, therefore, the presence of clouds in the field of view. Clouds are pretty visible in the evolution of the triggering rate, which drops as they pass through the field of view.
- A weather station provides temperature, pressure, air humidity, wind speed, and direction.
- A Lidar estimates the composition of aerosols in the atmosphere as a function of altitude (Devin et al. 2019). Aerosols lead to the extinction of the Cherenkov Light.

Systematic uncertainties due to simulation : the Air shower is quite well modeled by Monte Carlo simulation, leading to less than 1% systematic uncertainties. However, the main systematic error reported on the energy scale of the incoming gamma-ray comes from the atmospheric modeling. 1–4% uncertainties are due to atmospheric models not accounting for seasonal variations (which, of course, depend on the years) Moreover, $>5\%$ is due to aerosol models : aerosol in the atmosphere is, for example, dependant on periodical phenomena, such as biomass burning from agricultural activity, which is not included in the models.

1.3.3 Trigger and Data Acquisition

The telescope triggers on an event according to two criteria, one on the telescope level, the other considering the whole array.

1. For each telescope, the camera will trigger the signal acquisition when at least 3 pixels in an area exceeds the threshold of 4 pe in a 1.3 ns window. The trigger rate of each camera is $\sim$ 1.4 kHz.

2. The second level of triggering is at the network level. When a camera is triggered, it sends a signal to the central server. The signal is kept in memory for $\sim$ 80 ns. If at least one other telescope has also been triggered within this time, then the central server sends a confirmation signal to each camera that has triggered. The data stored at the camera level is sent to the servers that record the event. With this second level, the network trigger rate is $\sim$ 300Hz.

These two level trigger permits to exclude already background events, such as atmospheric muons, which are only imaged by one telescope. Also, all the selected triggered events have a stereoscopic resolution which helps in the reconstruction of the shower.

The triggered camera images, atmospheric conditions, and monitoring data are sent to the Central Data Acquisition System (DAQ). Once collected by the DAQ, real-time analysis is performed. Real-time results, although only informative, are sometimes helpful to evaluate the priorities in observation, especially in the case of the ToO program on transients. Data are stored locally on RAID servers, and tapes are used for distribution to Europe ; although nowadays, transmission through the Internet is enabled as well, which significantly limits the delay from data acquisition to final analysis results. For more details on Data Acquisition with H.E.S.S., see Balzer et al. (2014).

Data are collected during the dark time, with no moonlight and the Sun at more than 18° below the horizon. Recently moonlight and twilight observations were made possible, extending the annual available observation time. Observation sessions last for 28 minutes to limit the volume of data and variations in observation conditions, such as zenith angle and atmospheric conditions. These 28 minutes observations are called "runs". The data acquisition and telescope operation require human presence to monitor the operation of all sub-systems of the array. Two collaborators ("shifters") remain on-site for one month to perform night-shifts, helped by the local crew in Namibia.

1.3.4 Calibration

Calibration of the H.E.S.S. cameras, consists of mastering the camera response in order to convert the electrical signal into photo-electron accounting for the Cherenkov light : this is a crucial and complex step explained in Aharonian et al. (2004a). There are two independent calibration chains, the so-called *French* calibration (De Naurois 2012), and the *Heidelberg* calibration (Balzer 2010). Here we will only mention the main steps. It is important to note that the selected events stored on disk by the H.E.S.S. DAQ had their electrical signal converted into an analog-to-digital (ADC) count rate signal, and this is done for each concerned camera PMT in two gain channels.

The overall goal of the calibration is the measurement of ADC/pe conversion factor, the homogeneous response of the camera (flat-fielding), the camera gain (in two regimes : a high and low gain), the noise — consisting in electronic noise and night sky background (measured via the signal pedestal)— and finally converting pe to Cherenkov light.

The calibration challenges are summarized in these two formulas :

$$I_{HG} = \frac{ADC_{HG} - P_{HG}}{\gamma_{HG}} FF_{HG} \qquad I_{LG} = \frac{ADC_{LG} - P_{LG}}{\gamma_{HG}} \frac{HG}{LG} FF_{LG} \tag{1.2}$$

I is the intensity of the Cherenkov light in pe, seen in both high-gain (HG) and low-gain (LG) channels. P is the value of the pedestal, FF stands for the flat-field coefficient, used to correct for the different responses of the PMTs in one camera. γ_{HG} is the conversion factor from ADC counts to pe. For low gains, it can not be measured, then $\frac{1}{\gamma_{HG}} \frac{HG}{LG}$ is used.

There are two calibration phases : the first one uses various calibration devices on-site and dedicated calibration runs during the shifts. The second phase is offline, using the quantities recorded in the calibration session.

Dedicated calibration sessions are scheduled during the dark period to estimate the various parameters, using the following instruments :

1. A LED associated with an isotropic diffuser placed in the center of the mirror surface. It allows for uniform illumination of the camera, thus achieving a "flat field" to probe the homogeneity of the response of the camera's pixels. The FF factor is established with these measurements.
2. A LED, pulsed at 70 Hz, associated with a diffuser, is placed in the telescope shelter, 2 m from the camera. The LED's intensity is adjustable and allows a camera illumination with an average of 1 pe per pixel. This is used to estimate the γ_G factor (see details in Aharonian et al. (2004a)).

The pedestal factor P is measured during observations, as the noise can be significant over a 28-minute run. P is measured for each PMT and gain, using the camera's parts without showers.

The high-gain to low-gain ratios, $\frac{HG}{LG}$, are measured in observation runs by averaging the ADC counts from the PMTs in the high gain compared to the one in the low gain, substracted with the pedestal value.

The conversion from pe values for I to Cherenkov light is done using the ring-shaped shower image of atmospheric muons and applied to all cameras. The Cherenkov light emitted by a muon is similar to the light associated with primary gamma-ray events. The main difference is that the Cherenkov light from muons– muons being more penetrating–experiences fewer losses in the ultraviolet. The image of the Cherenkov light from an atmospheric muon forms a ring because the muons are highly relativistic, and the opening angle from the Cherenkov pulse is independent of their energy and only depends on their direction. The expected amount of radiation of a muon passing by at a given distance can be calculated analytically, which is then used as a standard reference light source to calibrate each camera (e.g. Chalme-Calvet et al. 2014). Calibration also deals with hardware problems, including broken pixels or loss of drawers caused by electronic problems.

Once the shower image is calibrated, the shower event can be reconstructed.

1.3.5 Data Analysis steps

In this Section, we describe data analysis steps leading to a possible source detection. There is two main analysis chain in H.E.S.S., one developed by the french part of the collaboration, which led to the *Model* reconstruction framework as described in de Naurois & Rolland (2009). The other was historically developed in Heidelberg and is called HAP (Heidelberg analysis package). For consistency and reliability, the policy of the H.E.S.S. Collaboration necessitates having both analysis chains used independently by two collaboration members : the shower models, calibrations, and reconstructions are done twice, independently. This crosscheck policy makes the results unequivocal, raises unseen problems, and leads to better handles of systematic errors.

Both analysis chains were then used in this thesis work, but I performed the analyses using HAP. I will, therefore, focus on its performance, mainly reported in Ohm et al. (2009) and in Parsons & Hinton (2014), concerning the ImPACT analysis.

Hillas reconstruction The primary gamma-ray photon's energy and direction are reconstructed from the calibrated events. This step involves MonteCarlo shower simulations. The so-called Hillas parameter-based reconstruction Hillas (1985) has been used in IACTs for the first decade. However, more advanced techniques are nowadays used using some 2D-3D template fitting methods.

Nevertheless, explaining the Hillas parameters is instructive for understanding the gamma-ray reconstruction. So we present here the basics of H.E.S.S. Hillas reconstruction as defined in Aharonian et al. (2006b) .

The method uses the regular ellipsoidal shape of the gamma-ray-induced shower image. A fit to the ellipse is performed on the camera images of all telescopes. Image cleaning is carried out prior to the fit to limit the contamination by the sky background noise. Pixels with at least 7 pe of measured intensity and at least one neighbor of at least 10 pe are selected.

Several variables resulting from the fit are extracted for analysis (see Figure 1.11) :

- the width and length of the ellipse,
- the distance the ellipse's center to the center of the field of view, called "nominal distance",
- the angle between the ellipse's main axis and the axis formed by the center of the camera and the center of the ellipse
- the total charge of PMTs in photoelectrons contained within the ellipse

Hillas reconstruction is very sensitive to the number of non-operational pixels (and their distribution in the camera image), resulting in erroneous direction estimates (and therefore energy). In addition, images at the edge of the field, only partly in the camera, can lead to very poorly reconstructed events. Therefore a selection on the nominal distance is generally applied to keep only the events with sufficient information in the camera.

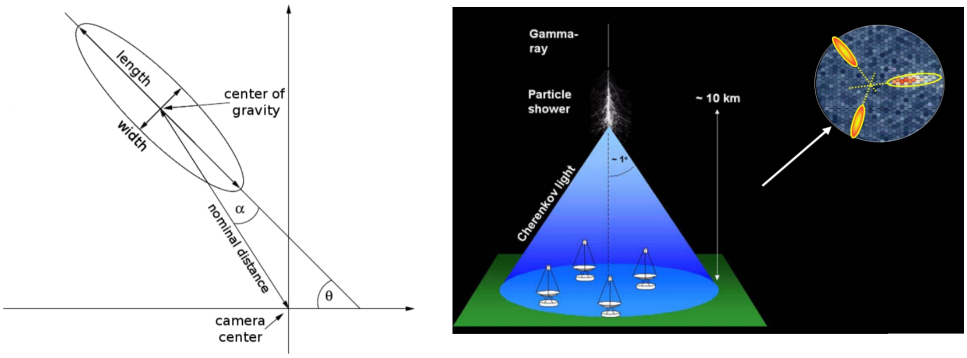

FIGURE 1.11 – Left : Schematic representation of a shower ellipse and the geometric Hillas parameters. Right : Schematic view of an atmospheric shower and its Cherenkov Light cone illuminating the telescope arrays. The superimposed camera image of the event as seen by three H.E.S.S of the CT1–4 telescopes is shown. The intersection of the different major axes of all ellipses is the source position.

The fit is applied to each camera individually. In principle, the Hillas parameters can be determined for a single camera shower, and this is the case for the "mono analysis" using only CT5 events. For the other analysis in H.E.S.S., a minimum of two camera showers are considered. The reconstruction performances, improving with the use of multiple telescopes, can be seen in the next Section in Figure 1.14.

The impact point of the shower on the ground and the height of maximum emission are used to reconstruct the primary particle direction (corresponding to the source position). However, that operation requires several coordinate transformations, which is done with the H.E.S.S. software, as detailed, for example, in Balzer (2014).

The energy reconstruction uses dedicated lookup tables obtained from MonteCarlo simulations. For each telescope, lookup tables are generated for different zenith and offset angle values. The tables list the size of the ellipse for different energies. The mean energy is obtained from the respective lookup table for each telescope triggered by the event, as well as en error on the energy. The final energy value is obtained using an average over all the telescopes, weighted by the errors.

The Hillas parameters are the pillars of IACTs reconstruction. However, nowadays, reconstruction techniques use multi-variate components to select the width and length parameters and two-dimensional fitting methods. The *Model* analysis framework (de Naurois & Rolland 2009) is based on a semi-analytical model, the ImPACT analysis framework (Parsons & Hinton 2014), is based on 2D MonteCarlo templates. The work presented in this thesis is mostly based on the ImPACT framework.

Gamma-hadron separation

CRs are mainly composed of protons and heavier nuclei. These particles constitute a background of hadron-induced showers that must be suppressed by several orders of magnitude in rate to be able to do TeV gamma-ray astronomy.

Some gamma-hadron separation procedure is applied, motivated by the differences between hadrons and gamma-rays-induced showers on the ground, and this is done using stereoscopic reconstruction. Indeed a hadronic air shower can look like a gamma-ray induced on one shower image. However, combining two shower images can reveal some asymmetry, revealing its hadronic origin. This procedure is done by establishing a discriminating variable, based on the "mean reduced scaled width" and "mean reduced scaled height" as described in Aharonian et al. (2006b). These values correspond to the averaged mean of the ellipse's width and height over all the telescopes compared to MonteCarlo simulations values stored in look-up tables. As shown in Figure 1.12, the discrimination variable permits to separate two clear distributions of gamma-ray-induced shower signals compared to the background of proton-induced showers. However, it also shows that a small contribution of proton background events will not be rejected, contaminating the selected gamma-ray events.

The gamma-hadron discrimination is performed nowadays with a boost decision tree for HAP (Ohm et al. 2009) or using a semi-analytical model together with a pixel-wise log-likelihood fit for the *Model analysis* (de Naurois & Rolland 2009).

Selection cuts Once the data has been calibrated, and the hadronic background rejection procedure has been applied, the data are ready for source analysis. First

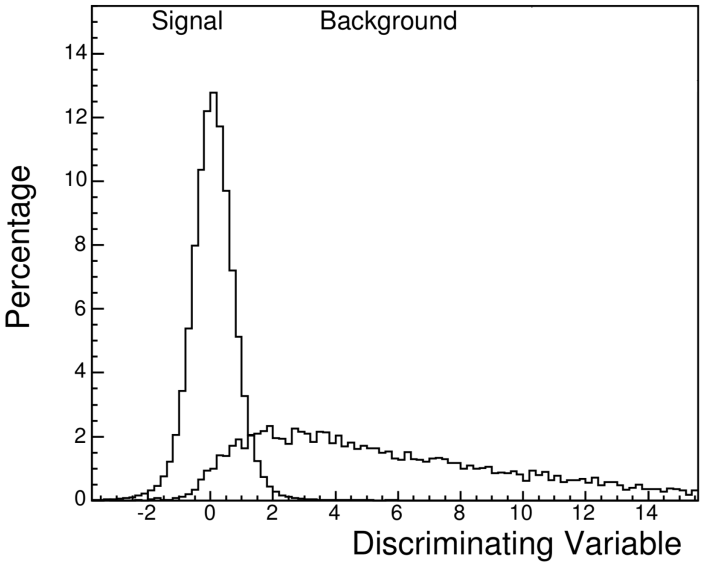

Figure 1.12 – Distribution of gamma-ray versus proton events, as function of the event discrimination parameter (Figure reproduced from De Naurois (2012)).

some cuts should be applied in order to select good quality data. Quality involves quantities such as the trigger rate, the run duration, and attenuation of the Cherenkov light by atmospheric phenomena (clouds and aerosols). A transparency coefficient is established for each shower and each telescope to address it. This coefficient also uses the muon efficiency (Chalme-Calvet et al. 2014). Data quality selection for HAP is described in Hahn et al. (2014), and for the transparency coefficient, see also Mariaud (2018).

Depending on the source and its environment, different configuration cuts can be chosen based on the minimal amount of pe contained in the shower and the distance from the reconstructed shower position to the source (Θ). These sets of cuts are more or less selective on the signal, and as a consequence, act on the residual background level (see Figure 1.12) ; the most selective ones reject more background but also more signal. There are four types of selection cuts : the "standard" cuts are used for bright point sources, the "loose" cuts could be used for very bright point sources, with well-handled background, the "hard" cuts are generally used for faint point sources with important diffuse background, and the "full enclosure" cuts for extended sources. These cuts are detailed in Table 2 in Aharonian et al. (2006b), and Table 1 in Parsons & Hinton (2014).

Background subtraction

The source analysis can begin once the gamma-ray showers are reconstructed and pass the selection cuts. It consists of extracting the source signal over the background level, mainly the diffuse gamma-ray emission, non-excluded hadron-induced showers, and some electron-induced showers. The source and background regions are generally selected in the same field of view (FOV).

A region around the source of interest is chosen : ON events will be extracted from this region. The standard ON radius for a point source analysis is 0.07°. After extraction of the ON events, the source region is excluded along with known gamma-ray sources in the FOV. The OFF events are selected with different background methods. We enumerate here the main background techniques used for source analysis in H.E.S.S. and used in the work presented in this thesis. The Ring background method is usually used for establishing the count maps. The Reflected background method is used to establish the spectrum.

The Ring background selects OFF events in a ring around the ON region (by default, the inner ring radius is 0.5° and ring thickness is 0.2°). The Reflected Background selects the OFF regions by central symmetry from the ON region on the observation position. It is important to remind here that observations are taken in the so-called "wobble mode" Aharonian et al. (2006b), at $\sim 0.5^\circ$ around the source changing direction for each observation run. The Reflected background method leads to OFF regions with the same radial offset as the ON region. Ring and Reflected Background regions are illustrated in Figure 1.13.

These methods and other interesting background techniques for IACTs are described in Berge et al. (2007). ON events, α value, and OFF events are selected on every runs ; then, the values are added to account for the whole data set. The excess number of events from the source can be evaluated by : $N_{\text{excess}} = N_{\text{ON}} - \alpha N_{\text{OFF}}$.

The significance of the source quantifies how much of the derived excess above the background level is statistically meaningful. The significance can be approximate by : $N_{\text{excess}}/\alpha\sqrt{N_{\text{OFF}}}$.

The complete computation uses a log-likelihood ratio of the hypothesis of no signal (the null hypothesis) and the hypothesis of a signal, as described in Li & Ma (1983). Note that a source detection should have a minimum of $5\,\sigma$ according to the standards adopted by the field of very-high-energy gamma-ray astronomy.

The normalization factor α is established to account for the difference of exposure from the OFF to the ON region by integrating the exposure, per azimuth, zenith, offset angles, energies, and duration, as shown in the following formula (Berge et al. 2007) :

$$\alpha = \frac{\int_{ON} A^{\gamma}_{ON}(\Psi_x, \Psi_y, \Psi_z, E, t) d\Psi_x d\Psi_y d\Psi_z dE dt}{\int_{OFF} A^{\gamma}_{OFF}(\Psi_x, \Psi_y, \Psi_z, E, t) d\Psi_x d\Psi_y d\Psi_z dE dt}. \tag{1.3}$$

A_{ON} and A_{OFF} are the acceptances of the detector in the source and background

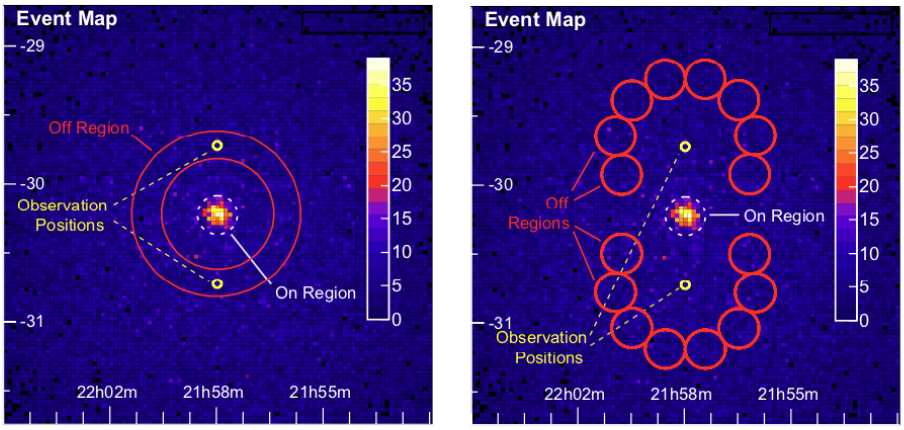

FIGURE 1.13 – Count map of gamma-ray-like events from 5hrs of H.E.S.S. observations of the active galaxy PKS 2155-304. The Ring (left) and Reflected background regions (right) are illustrated schematically (Figure from Berge et al. (2007)).

regions respectively. They depend on the position in the camera, Ψ_x, Ψ_y, on the zenith angle Ψ_z, on the energy, E, and on the observation time t.

For the Ring background method, the alpha factor is approximately the ratio of the solid angle of the source region to that of the ring region. It is typically chosen to be $\sim 1/7$, for a ring of radius 0.5°. For the Reflected background, as offset is conserved and the acceptance not considered, then the correction factor can be resumed to $1/N_{\text{offregion}}$.

The instrument response is taken into account to evaluate the selected OFF and ON events exposure. We call it the "acceptance" : it is crucial to estimate the background as explained in Berge et al. (2007). Over the 5° FOV, the coverage of the telescope is not uniform : there are more events in the center of the FOV than on the edges. This depends on the pointing parameters but also on the shower's energy.

For the Ring background, depending on the ring radius, the acceptance has small variations across the ring extraction region. Therefore, a small correction factor is added. However, for the Reflected background method, the variation in acceptance over the FOV is too considerable, and the Reflected background method is not used for maps.

The acceptance can be estimated from MonteCarlo generated look-up tables or from the data itself. The simulated tables are produced for zenith, offset, and azimuth angle ranges and for different energies. The advantage of these simulations is to master the instrument response, but the range can not be infinitely sampled. Acceptance can also be derived from the observations by subtracting the events maps from the exposure map. That is what is mainly used in the analyses presented in this thesis.

Look-up tables are radially generated in HAP even when generated from data, with a fit that smooths any asymmetrical effect in the FOV. This works well, as the observations are usually taken symmetrically with four positions around the source. However, a field of view is not perfectly symmetrical for two main reasons : the camera is not perfectly spherical, more critically at offsets larger than 2° and the zenith angle is not the same throughout the camera. This difference creates a trigger rate gradient not considered in the acceptance when pointing at large zenith angles. In the analysis presented in Chapter 6, the problem of asymmetrical effects due to the gradient of events is important.

Spectral analysis

Once an event excess is established, the energy spectrum can be built by determining the number of gamma-ray photons detected from the source regions and determining the distribution in reconstructed photon energy. The energy spectrum considers the detector effective area : it accounts for the surface of detection estimated from simulations and the exposure time recorded during the detection. The effective area simulations are organized in a series of tables produced for several energy values and zenith, azimuth, and offset angles. The spectrum energy results in a distribution, which in H.E.S.S. is usually regrouped within energy intervals, considering a minimum significance of $2\,\sigma$ per bin.

The energy of interest is the true energy of the photon, which is different from the reconstructed energy. So the instrument energy response has to be taken into account. The simulated acceptance reflects the detector response and is used to build tables dependent on the true energy and the zenith angle, the offset angle, and the optical efficiency. These tables are used to construct a response matrix, expressing the dependency between reconstructed energy and true energy. Finally, the spectrum is folded back with this matrix, which is mostly diagonal with some bias. In the present work, the spectra are expressed in terms of the reconstructed energy.

Light curves are built from the spectral data, assuming a fixed spectral shape, and binning the flux events with reference to time intervals. This permits monitoring temporal changes in the flux and characterizing temporal behavior of transient events.

Performances

To illustrate the source analysis performance, angular and energy resolution obtained for ImPACT analysis with standard cuts is shown in Figure 1.14. These distributions have been produced using simulated MonteCarlo events reconstructed using CT1–4 telescopes. The values are represented for different telescope multiplicities and two zenith angle values.

The angular resolution is evaluated with the PSF. It is measured with the distribution of events as a function of the distance to the pointing position (see Aharonian et al. 2006b, Figure 6), and corresponds to the radius that contains 68% of the events with respect to the source position. The energy resolution is usually evaluated by comparing reconstructed energy with simulations. For example, on the following plots, the energy resolution is $\Delta E/E$, with ΔE the rms of the reconstructed events for simulations with the same energy (similar as in Figure 5 in Parsons & Hinton (2014)).

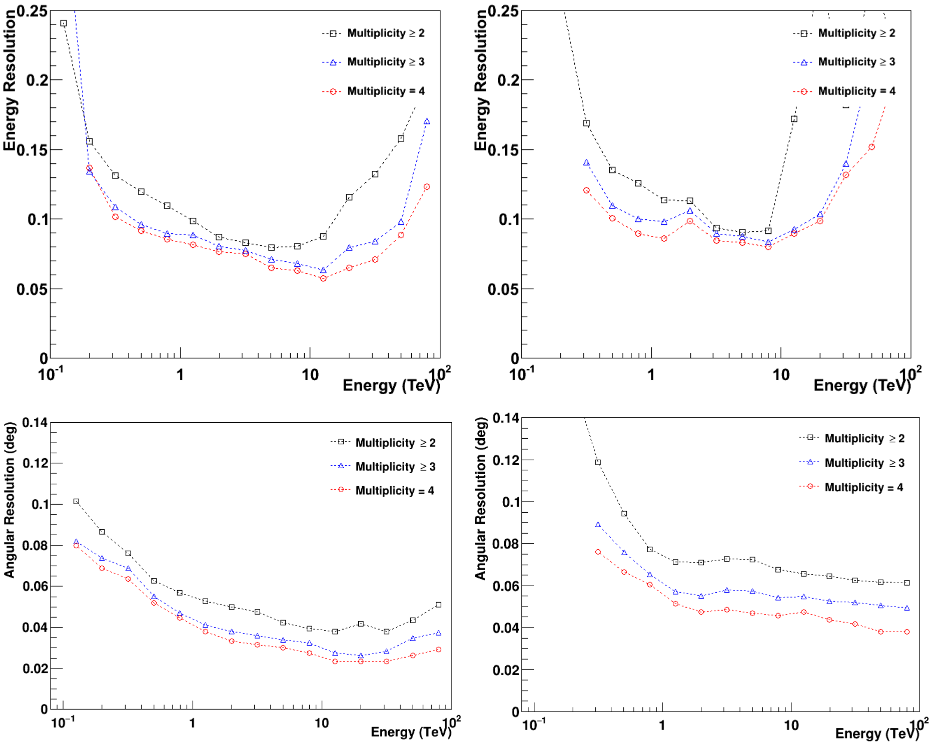

FIGURE 1.14 – MonteCarlo simulation showing the effect of telescope multiplicity on the angular and the energy resolution with respect to the shower energy. The simulation is for CT1-4 using the ImPACT analysis framework with standard cuts and showers generated at a zenith of 20° (left), and 45° (right) (courtesy of R.D.Parsons).

The left figures show that the CT1–4 telescopes are sensitive to gamma-ray photons with energies of ∼100 GeV - 100 TeV with an energy resolution varying from 0.08 to 0.25 and can reconstruct them with an angular resolution in the range ∼ 0.04 –0.1° with a minimum of two telescopes. As a comparison, an analysis with the same settings and using an Hillas based reconstruction method results in an energy resolution in the range 0.15–0.25. The angular and energy resolution are improved with a reconstruction involving a minimum of three camera showers on different telescopes. The figures on the right show that performances are sensitive to observations at large zenith angles : for observation at 45°, the energy range is reduced to (~200 GeV – 80 TeV), the angular resolution values in the range 1-10 TeV lie around 0.07–0.08° for a multiplicity ≥ 2, reaching 0.06° for a multiplicity ≥ 3. In Chapter 2, we report results obtained with observations at large zenith angles, which necessitated an analysis with a multiplicity ≥ 3. Due to its larger size, CT5 is more sensitive to low-energy gamma-ray events. It is optimized for gamma-ray energies of $\sim$ 30 GeV–10 TeV, an angular resolution of ~0.14° can be reached at 1 TeV with ImpACT mono with standard cuts, and 0.05° with ImPACT stereo. (Parsons et al. 2015).

1.3.6 Sensitivity

H.E.S.S. telescopes and IACTs reconstruction techniques were developed and optimized to achieve a 5σ point source detection with competitive sensitivity at 1 TeV. The sensitivities of actual IACTs are shown in Figure 1.15 compared to other IACTs and space-based telescopes like the Fermi-LAT and a water-Cherenkov observatory like HAWC. Predictions for both CTA North and CTA South are reported : at 1 TeV IACTs are the most sensitive instruments, and CTA in the future will improve that sensitivity by one order of magnitude, which will open new windows on the gamma-ray sky. Note that for IACTs, the sensitivity is given for 50 h of observation, as compared to 1–10 yr for HAWC and Fermi-Lat. This is not so important for persistent sources, as HAWC and Fermi-LAT are all-sky survey instruments, whereas IACTs are pointed telescopes. However, it does mean that IACTs greatly outperform water Cherenkov and space-based instruments for transient sources.

1.4 Summary : thesis outline

In the work presented in this thesis, we performed several H.E.S.S. data analyses aiming to study the gamma-ray emission of SNRs and their ability to be powerful CRs accelerators. First, we present the detection and study of the TeV emission of two well-known SNRs, N132D and Kepler's SNR. In addition, we searched for gamma-ray emission from SNe, i.e., from the very earliest stages of SNR evolution. A Chapter on the Fermi Bubbles does not entirely encompass the main topic of this thesis. Nevertheless, the Fermi Bubbles are a Galactic source of cosmic rays. It is still debated whether its formation is caused by energetic jets originating from the supermassive black hole in the center of the Milky Way or a past episode of star formation in the Galactic center. In the latter case, the Fermi Bubbles derive their energy still mostly from supernovae. Here is the outline of the scientific results published in this thesis :

- In Chapter 2, we present a 5.7 σ detection of LMC N132D, the only extra-galactic TeV SNR. N132D is a very particular middle-age SNR (2500 yrs), as it is very bright in gamma-ray, but non-thermal X-rays are not observed. We report a spectrum extending beyond 10 TeV that can be well fitted with a

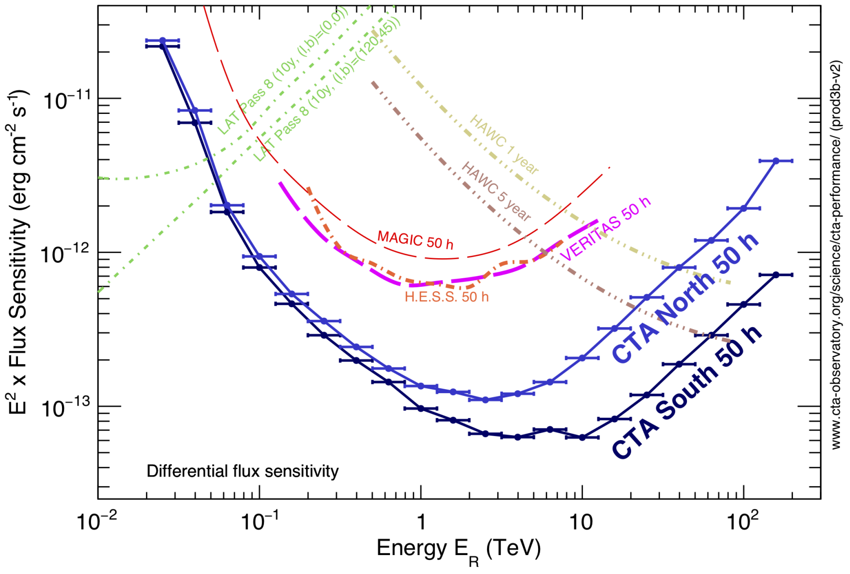

FIGURE 1.15 – Comparison of the differential energy flux sensitivities for several instruments observing the gamma-ray sky. The sensitivities are given for five standard deviation detection in five independent logarithmic bins per decade in energy. Note that the comparison is purely indicative as the method of sensitivity calculation and the criteria applied are different. Cherenkov Telescope Array Consortium (2019)

PL, with no evidence for an energy cut-off. We argue the gamma-ray emission could be of hadronic origin, although the leptonic nature can not be excluded.

— Chapter 3 is about SN1604, better known as Kepler's SNR. Kepler's SNR is the only historical SNR undetected so far in gamma-rays : we report strong evidence for a gamma-ray excess at a $4\,\sigma$ significance, both in the GeV (*Fermi*-LAT) and TeV (H.E.S.S.) regime. Some multi-wavelength modeling is presented in comparison with a model for Tycho's SNR, which suggests that the gamma-ray emission is of hadronic origin.

— In Chapters 4 and 5 we present two projects on the possible gamma-ray emission of SNe. A search for signals from 9 objects serendipitously observed with H.E.S.S. is presented along with analysis for two nearby SNe, SN2016apj and AT2019krl, which triggered dedicated observations. No significant excess is observed for any 11 objects, and UL on the flux is derived. These ULs are translated into constraints on the SNe environment. The ongoing observation program itself is presented along with AT2019krl results.

— A search for a signal at the edge of Fermi Bubbles at large Galactic latitude (b) is described in Chapter 6. The analysis aims to characterize the Fermi Bubbles signal at the edge of the H.E.S.S. observation dedicated to the blazar PKS2155-305. 304 h of good quality data are analyzed, and no significant signal is found. ULs on the Fermi Bubbles flux are computed and discussed in comparison with *Fermi*-LAT and HAWC spectra.

2

LMC N132D : A mature supernova remnant with a power-law gamma-ray spectrum extending beyond 8 TeV

H.E.S.S. Collaboration.
Corresponding authors : R.Simoni, D.Prokhorov, J.Vink & N.Komin.

Astronomy & Astrophysics, 2021 , 655, A7

Abstract

Supernova remnants (SNRs) are commonly thought to be the dominant sources of Galactic cosmic rays up to the knee of the cosmic-ray spectrum at a few PeV. Imaging Atmospheric Cherenkov Telescopes have revealed young SNRs as very-high-energy (VHE, >100 GeV) gamma-ray sources, but for only a few SNRs the hadronic cosmic-ray origin of their gamma-ray emission is indisputably established. In all these cases, the gamma-ray spectra exhibit a spectral cutoff at energies much below 100 TeV and thus do not reach the PeVatron regime. The aim of this work was to achieve a firm detection for the oxygen-rich SNR LMC N132D in the VHE gamma-ray domain with an extended set of data, and to clarify the spectral characteristics and the localization of the gamma-ray emission from this exceptionally powerful gamma-ray-emitting SNR. We analyzed 252 hours of High Energy Stereoscopic System (H.E.S.S.) observations towards SNR N132D that were accumulated between December 2004 and March 2016 during a deep survey of the Large Magellanic Cloud, adding 104 hours of observations to the previously published data set to ensure a $> 5\sigma$ detection. To broaden the gamma-ray spectral coverage required for modeling the spectral energy distribution, an analysis of *Fermi*-LAT Pass 8 data was also included. We unambiguously detect N132D at VHE with a significance of 5.7σ. We report the results of a detailed analysis

of its spectrum and localization based on the extended H.E.S.S. data set. The joint analysis of the extended H.E.S.S and Fermi-LAT data results in a spectral energy distribution in the energy range from 1.7 GeV to 14.8 TeV, which suggests a high luminosity of N132D at GeV and TeV energies. We set a lower limit on a gamma-ray cutoff energy of 8 TeV with a confidence level of 95%. The new gamma-ray spectrum as well as multiwavelength observations of N132D when compared to physical models suggests a hadronic origin of the VHE gamma-ray emission. SNR N132D is a VHE gamma-ray source that shows a spectrum extending to the VHE domain without a spectral cutoff at a few TeV, unlike the younger oxygen-rich SNR Cassiopeia A. The gamma-ray emission is best explained by a dominant hadronic component formed by diffusive shock acceleration. The gamma-ray properties of N132D may be affected by an interaction with a nearby molecular cloud that partially lies inside the 95% confidence region of the source position.

2.1 Introduction

Supernova remnants (SNRs) have long been thought to be the dominant sources of Galactic cosmic rays (CRs). If this is the case, then 5–10% of the explosion energy needs to be transferred to the CR particles to explain the CR energy budget (Ginzburg & Syrovatskii 1964). This concerns atomic nuclei (hadronic CRs) in particular, which make up ~99% of CRs that are detected on Earth. Gamma-ray observations provide a probe of energetic particles accelerated in SNRs. Accelerated electrons can produce gamma rays through their inverse Compton scattering and bremsstrahlung (the leptonic scenario), and accelerated hadrons can produce gamma rays through the production of short-lived neutral pions by proton-proton (or ion-ion) interactions (the hadronic scenario). In both cases, the gamma-ray photon energy is typically $\sim 10\%$ of the energy of the accelerated particle. The highest CR energies to be expected in SNRs are at least $10^{14} - 10^{15}$ eV (Lagage & Cesarsky 1983; Berezhko 1996), which should lead to gamma-ray emission in the TeV–sub PeV range.

To date, 25 sources associated with SNRs[1] have been firmly detected in the very-high-energy gamma-ray regime (VHE, 100 GeV $<$E$<$ 100 TeV, Abdalla et al. 2018c), some of which were even first discovered in VHE gamma rays (e.g., Abdalla et al. 2018e). These VHE gamma-ray detections were achieved with ground-based Imaging Atmospheric Cherenkov Telescope (IACT) arrays. Thirteen of these sources have been identified as Galactic shell-type SNRs, ten additional sources are SNRs interacting with molecular clouds, and a few remaining sources are composite SNRs, containing both a shock-dominated shell and a pulsar wind nebula (PWN).

In the high-energy regime (HE, 100 MeV $\lesssim$E$\lesssim$ 100 GeV), ~30 gamma-ray sources are classified as SNRs in the *Fermi*-LAT SNR catalog (Acero et al. 2016). These

---

[1] See `http://tevcat.uchicago.edu/`.

include the mature SNRs ($\gtrsim$5000 yr) IC443 and W44, whose gamma-ray spectra display a clear pion bump signature, which provides evidence for a hadronic origin of the gamma-ray emission (Ackermann et al. 2013). The outer shocks of these two SNRs are interacting with dense molecular clouds, which act as reservoirs of target material for pion production. Their gamma-ray spectra show spectral breaks, suggesting that the highest-energy accelerated protons have largely escaped the SNR shell. Further evidence that VHE emission in mature SNRs originates from CRs that have escaped the SNR is provided by VHE gamma-ray observations of W28, for which VHE emission was detected from a nearby molecular cloud situated outside the shell of the SNR (e.g., Abramowski et al. 2008; Gabici 2017).

In general, gamma-ray studies show that (i) several young SNRs ($\lesssim$1000 yr) have prominent VHE gamma-ray emission, but there is no evidence that the underlying CR spectrum extends to the CR knee at 3×10^{15} eV ; the bright young SNR, Cassiopeia A (Cas A, ~340 yr), exhibits a cutoff at a surprisingly low energy of 3.5 TeV in the gamma-ray spectrum (Ahnen et al. 2017) ; (ii) mature SNRs evolving in dense regions are bright GeV sources, but exhibit a cutoff and/or break in their HE spectra, and they are therefore not prominent VHE gamma-ray sources ; (iii) for some mature SNRs, it is suggested that the gamma-ray emission is caused by CRs that have escaped the SNR shell and are now colliding with dense nearby gas.

The SNR N132D is a remarkable object located in the Large Magellanic Cloud (LMC). At a distance of ~50 kpc (e.g., Pietrzyński et al. 2019), N132D is the only known extragalactic VHE emitting SNR (Abramowski et al. 2015b). SNR N132D was discovered in gamma rays in the HE and the VHE regimes (Abramowski et al. 2015b; Ackermann et al. 2016). Its gamma-ray luminosity was estimated to be about 10^{35} erg s^{-1} , making it one of the most luminous VHE gamma-ray SNRs detected so far. It is the brightest X-ray SNR in the LMC of 38 cataloged LMC SNRs (Maggi et al. 2016). However, unlike many other VHE-emitting shell-type SNRs, N132D shows only strong thermal X-ray emission (e.g., Mathewson et al. 1983; Hughes et al. 1998; Behar et al. 2001; Borkowski et al. 2007) without evidence for an X-ray synchrotron component (e.g., Bamba et al. 2018). It is also a luminous source in the radio (Dickel & Milne 1995) and infrared (IR) bands (Seok et al. 2013). There is evidence that N132D was caused by a powerful explosion with an energy of (3-5)$\times 10^{51}$ erg (Dickel & Milne 1995; Hughes et al. 1998), three to five times more than the canonical supernova explosion energy.

N132D has a peculiar horseshoe morphology in the X-ray band (see, e.g., Figure 2 in Borkowski et al. 2007) and also in the radio and IR bands, with a typical angular size of $1.4'$ by $1.8'$. This corresponds to a physical size of about 20 pc by 26 pc. The northeast region of the SNR is fainter than the southwest region, which suggests that the SNR interacts with denser material in the southwest. Molecular clouds are projected toward the southwestern region of the remnant (e.g., Braiding et al. 2018). HI emission also shows that N132D is surrounded by relatively dense HI gas, with a gradient toward the southwest. Sano et al. (2020) estimated an HI density as high as $n \approx 30$ cm^{-3}. It seems plausible that in the southern part of the shell, molecular cloud material has been swept up and heated by a high-speed shock, resulting in the peculiar morphology of N132D (see Williams et al. 2006; Tappe et al. 2007, 2012). Sano et al. (2020) also reported that there are small clouds in the south and in the center of N132D that shows signs of present or past interaction with the shock.

The age of N132D is estimated to be ~2500 years (Vogt & Dopita 2011). It is therefore one of the oldest VHE gamma-ray-emitting shell-type SNRs. It is much older than Cas A (~340 yr), to which it is often compared in other aspects : both SNRs probably have evolved in a wind-blown bubble, and both contain oxygen-rich ejecta, which suggest that their explosions were the result of core-collapse supernovae of massive stars ($\gtrsim 18$ M$_{\odot}$, at the zero-age main sequence). The age of another oxygen-rich SNR, Puppis A, is similar to that of N132D, but it has not yet been detected in VHE gamma rays although it is located only 1.3 kpc away (Abramowski et al. 2015a). The difference in VHE gamma-ray properties of N132D, Cas A, and Puppis A makes a detailed study of N132D relevant for the important question of the timescale on which the bulk of CRs are accelerated, and of the timescale on which the CRs eventually escape the shells as a function of CR energy.

Abramowski et al. (2015b) reported a gamma-ray excess from N132D at a statistical significance level of 4.7 σ and a spectrum extending up to 10 TeV, based on H.E.S.S. observations with an exposure time of 148 hours. Our goal is to update this result by reporting the analysis of H.E.S.S. observations with 252 hours of total exposure time. The HE gamma-ray counterpart of VHE emission is also studied with *Fermi*-LAT Pass 8 data. This joint study in the HE and VHE gamma-ray bands allows us to place new constraints on the mechanism of gamma-ray production and the underlying populations of accelerated particles responsible for the gamma-ray emission.

The content of this paper is structured as follows : In Section 2.2 the data analysis of both H.E.S.S. and *Fermi*-LAT observations are described. In Section 2.3 the H.E.S.S VHE spectrum and gamma-ray morphology are presented. In Section 2.4 a multiwavelength spectrum modeling is explained. These results are discussed in Section 2.5 in the context of the environment of N132D as well as in the context of the VHE-emitting SNR population. The conclusions of this study are presented in Section 2.6.

2.2 Observations and data analysis

2.2.1 H.E.S.S. experiment

The High Energy Stereoscopic System [2] (H.E.S.S.) is an array of five IACTs located in the Khomas Highland in Namibia at an altitude of 1800 m above sea level. It has been operating since December 2003. In its first phase ("H.E.S.S. I"), the array consisted of four identical 12m Cherenkov telescopes (CT1-4) placed at the corners of a square of 120m side length. CT1-4 are equipped with mirrors with a total area of 107 m^2 and cameras with 960 photo-multiplier tubes each. The stereoscopic IACT technique allows determining the energy and direction of VHE gamma rays through imprints of the Cherenkov light emitted by secondary charged particles of a shower initiated by a primary VHE photon entering the atmosphere. With the 5° field of view (FoV) of CT1-4, gamma rays can be reconstructed with a typical angular resolution of $\sim 0\overset{\circ}{.}1$ (68% containment radius). The energy threshold is ~100 GeV for small zenith angles and below 1 TeV for zenith angles up to 60°, and the energy resolution is ~15% (for further details, see Aharonian et al. 2006b). The fifth Cherenkov telescope (CT5) with a diameter of 28 m (mirror area of 614 m^2) was added in the center of the CT1-4 array in July 2012, initiating the second phase of the experiment, "H.E.S.S. II". This study mostly uses H.E.S.S. I observations because only about 5% of the data were taken by the full CT1-5 array, for the observations presented here. H.E.S.S. performance depends on the zenith angle, configuration cuts, and the number of telescopes considered in the reconstruction (for more details, see Sections 2.2.2 and 2.2.3).

2.2.2 Data set : LMC survey

Its location in the southern hemisphere makes H.E.S.S. the only currently operating IACT array able to observe the LMC in the VHE band. With its angular size of ~8°, the LMC galaxy is compact enough for the H.E.S.S. telescopes to perform a survey. Such a survey was conducted over 13 years, from 2004 to 2017, during which the full LMC galaxy was covered with over 325 hours of observations. The exposure of the LMC is rather inhomogeneous and mostly concentrated on the central region around the Tarantula nebula. H.E.S.S. observations from 2003 to 2012 led to the discovery of three individual VHE gamma-ray-emitting sources, including SNR N132D, along with the PWN of N 157B and the superbubble 30 Dor C (Abramowski et al. 2012, 2015b), as well as the detection of the gamma-ray binary LMC P3 (Abdalla et al. 2018f). The data set used for our analysis was taken between December 2004 and March 2016. It consists of 252 hours of total exposure time, adding 104 hours to the previously published data set. The zenith angle of these observations spans a

---

[2] https ://www.mpi-hd.mpg.de/hfm/HESS/

range of 45-57°, with a mean of 46°, and a mean azimuth angle of $182.^\circ5$. The data set was selected with a maximum offset of $2.^\circ5$ around the source to avoid observations with large offset angles with respect to the camera center. For N132D, the observation positions were mostly toward the east side of the SNR. This is due to the nature of the observations, which are part of a survey, instead of being dedicated to N132D : the pointings were mostly directed toward N157B in the Tarantula nebula, which is situated toward the east of N132D. This results in offset angles in the range of $0.^\circ16$ to $2.^\circ5$ and a mean offset angle for N132D of $1.^\circ13$. The observations are thus taken at rather large offset, for which the acceptance is reduced compared to sources located closer to the camera center. Observations at large zenith angles with IACTs in general result in a lower effective area at energies below 1 TeV, but an increase in effective area above 1 TeV (e.g., Acciari et al. 2020). Therefore these observations were particularly well suited for measuring the high-energy part of the N132D gamma-ray spectrum.

2.2.3 H.E.S.S. data analysis

Data corresponding to 252 hours were recorded in 28-minute exposures that are called runs. Each calibrated run that passed the quality criteria of a dead time shorter than 30% of the run duration, a low fluctuation in trigger rate, and acceptable weather conditions (see Aharonian et al. 2006b; Hahn et al. 2014) was analyzed using the ImPACT framework described by Parsons & Hinton (2014), which includes a boosted decision-tree-based event classification algorithm to distinguish gamma rays from the charged particle background (Ohm et al. 2009). This analysis was performed using a special configuration that selected events with a minimum of three shower images in different telescopes. Using this event selection cut allowed us to improve the signal-to-background ratio for this faint gamma-ray source in the presence of a strong diffuse component, or multiple unresolved sources constituting an astrophysical background, which may be present in the vicinity of N132D.

To compute the maps and statistics presented in Section 2.3, ON events were selected from a circle centered on the geometrical center of the X-ray emission (referred to as the “X-ray source position”) at RA $5^h25^m2.2^s$, Dec $-69°38'39''$. OFF events were selected according to a ring-background method (Berge et al. 2007). An additional cut on the energy of reconstructed gamma-rays was made above 1.3 TeV in order to improve the signal-to-background ratio for this hard gamma-ray source and keep only gamma-ray events from a well-determined direction because the angular resolution improves by 10% from 800 GeV to 1.3 TeV using the ImPACT shower reconstruction software. This resulted in a point spread function (PSF) of $0.^\circ06$, which corresponds to the 68% containment radius of the fit on the observation position. The event count excess was computed using $N_{excess}=N_{on} - \alpha N_{off}$, with α the normalization factor for the OFF area with respect to the ON area. The cumulative statistical significance was calculated using equation 17 of Li & Ma (1983). The excess map is shown in

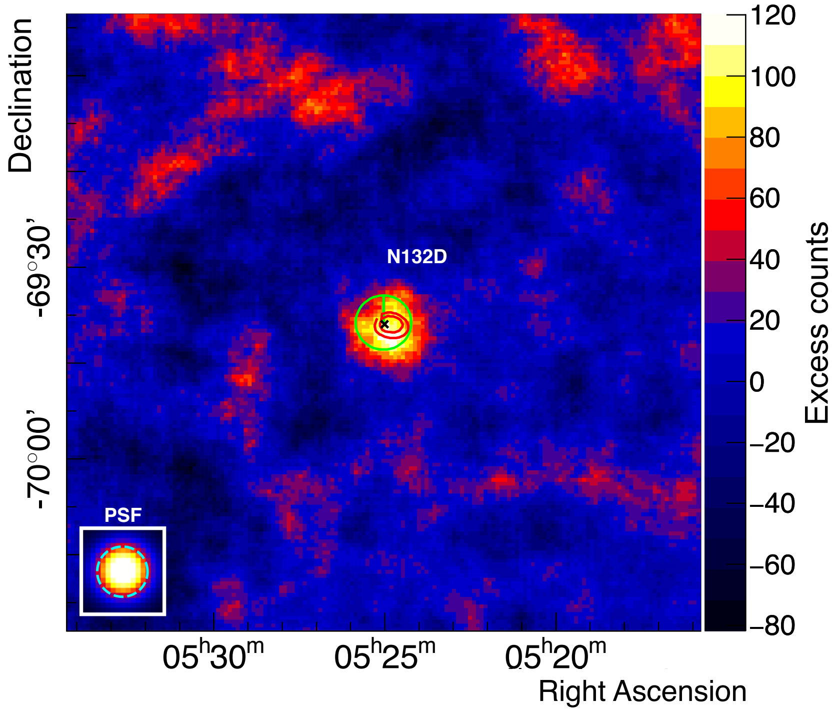

Figure 2.1 – H.E.S.S. excess map with a size of 1°.6, smoothed with a Gaussian of width 0°.1. The ON region with a radius of 0°.07, centered on the N132D X-ray source position, is shown in green, and the 2 and 3σ of the best-fit position (see Section 2.3.2) are represented in red.

Figure 2.1.

For the spectrum, the reflected-background method was applied with a three-telescope-image selection cut and a low-energy cut above 1.3 TeV. The spectral background was derived from background control regions that were defined run-wise and were chosen to have the same offset to the camera center as the source region to ensure a nearly identical spectral response. For maps and the spectrum, the sky areas with known sources or with excess events above a certain significance threshold were excluded. For reliability, the results were cross-checked with an independent analysis and calibration chain (de Naurois & Rolland 2009).

2.2.4 *Fermi*-LAT data analysis

The Large Area Telescope (*Fermi*-LAT) is a high-energy gamma-ray telescope installed on the Fermi spacecraft (Atwood et al. 2009). It uses a pair-conversion technique for gamma-ray photon detection, and has a large FoV of about 20% of the sky. The

Fermi-LAT has been scanning the entire sky since August 2008, recording astrophysical gamma rays with energies in the range 30 MeV to 300 GeV. Despite the uniform coverage of the entire LMC galaxy and the excellent spectral capabilities of *Fermi*-LAT, the previous analyses of *Fermi*-LAT observations were inconclusive regarding the origin of gamma-ray emission from N132D. In particular, different values of the photon spectral index were reported : $\Gamma = 1.4 \pm 0.3$ in Ackermann et al. (2016) and $\Gamma = 2.07 \pm 0.19$ in the LAT 8-year source catalog (the 4FGL catalog ; Abdollahi et al. 2020). In the latter work, the source 4FGL J0524.8-6938 was identified with N132D, and it was argued that the derived photon index of 2.07 supports the hypothesis of dominantly hadronic emission, while for SNRs exhibiting gamma-ray spectra with very hard photon indices, $\Gamma \leqslant 1.6$, the gamma-ray emission is most likely of leptonic origin (Abdollahi et al. 2020).

Pass 8 R3 `SOURCE` class photon data [3] (`evclass`=128) spanning 10.8 years between August 4, 2008, and May 15, 2019, with energies between 1 GeV and 250 GeV were selected. For the data analysis, the `FERMITOOLS` v1.0.7 package and `P8R3_SOURCE_V2` instrument response functions were used. Contamination from the gamma-ray-bright Earth limb was avoided by removing all events with zenith angle larger than 90°. The recommended quality cuts `(DATA_QUAL>0 && LAT_CONFIG==1)` were applied. The $10^\circ \times 10^\circ$ square region of interest with spatial bins $0\overset{\circ}{.}05$ in size was centered on the position of N132D. A *Fermi*-LAT count map in the range 3-250 GeV smoothed with a Gaussian kernel is shown in Figure 2.2. The choice of the low-energy limit at 3 GeV was made for illustration purposes because it provides a narrower point spread function. The central region of $1\overset{\circ}{.}6 \times 1\overset{\circ}{.}6$ in Figure 2.2 indicated with the dashed line corresponds to the H.E.S.S. excess map shown in Figure 2.1. Given the diameter of $\sim 1.6'$ of N132D in X-rays, a point-like source model for its counterpart in HE gamma rays was adopted. Gamma-ray sources from the 4FGL catalog within a 17° radius from N132D were included to model the data. To model the diffuse emission from the LMC, the spatial templates for four diffuse sources, LMC-FarWest, LMC-Galaxy, LMC-30DorWest, and LMC-North, provided by the *Fermi*-LAT collaboration (Ackermann et al. 2016), were used. These sources are outlined with circles in Figure 2.2. To model the Galactic and isotropic background diffuse emission, the standard templates `gll_iem_v07.fits` and `iso_P8R3_SOURCE_V2_v1.txt` were used. The spectral shapes of the sources were taken from the 4FGL catalog. The normalization and the photon index of N132D were derived from the likelihood analysis along with the normalizations of four strong point sources, including 4FGL J0537.8-6909 and 4FGL J0540.3-6920, and all diffuse sources, while the normalizations of fainter point sources were held fixed at the 4FGL catalog values. A binned likelihood analysis was applied to the data using the Fermi Science tool `gtlike`. To assess the goodness of fit, test-statistic and residual maps were produced showing some residuals at the position of

---

[3] https ://fermi.gsfc.nasa.gov/ssc/data/

SNR N63A. However, the inclusion of a new source corresponding to N63A in the model negligibly affects the derived spectrum of N132D. To extract a spectral energy distribution (SED), the photon index of N132D derived to be 1.86 ± 0.25 was fixed at the central value, the data were rebinned in four broad logarithmically spaced bands in energy, and a binned likelihood analysis was applied to the data in each of these bands.

The main analysis with all LMC templates was first performed, providing the best estimate of the SNR N132D HE emission. A second analysis was then launched to estimate the uncertainties related to the presence of a molecular cloud near N132D. For this purpose, LMC-Galaxy and LMC-30DorWest templates were modified by patching the area enclosing the molecular cloud, with constant intensities matching those in the nearby region and keeping their initial spectral shapes. Given the proximity of N132D and the molecular cloud, the alternative model predicts a stronger HE gamma-ray signal from N132D and leads to an expected VHE flux that is higher by about 30%, which is an estimate of the HE emission of SNR N132D plus the nearby molecular cloud. The data points obtained from the *Fermi*-LAT analysis are shown in Figure 2.3 for the main model.

2.3 Results

2.3.1 Statistics and spectral properties

The H.E.S.S analysis of N132D reveals an excess of 95 gamma-ray events above an energy of 1.3 TeV, corresponding to a significance of 5.7 σ for an exposure of 252 hours. The VHE gamma-ray emission from N132D is thus unambiguously detected, for which there was previous evidence from H.E.S.S. at a lower significance level of 4.7 σ (Abramowski et al. 2015b).

The excess corresponds to 337 ON events and 11179 OFF events, and a normalization parameter $\alpha = 0.0216$ established with the ring-background method with standard settings. ON events were extracted in a circle of radius $0\overset{\circ}{.}07$ centered on the X-ray source position. The corresponding excess map is shown in Figure 2.1.

Figure 2.3 shows the combined H.E.S.S. and *Fermi*-LAT photon energy spectrum spanning an energy range of 1 GeV to 40 TeV, where H.E.S.S. data points were chosen to start at 1.3 TeV. The H.E.S.S. spectrum was extracted using the same analysis cuts as for the maps and the reflected-background method. Spectral points between 1.3 and 40 TeV were binned in energy bands requiring a minimum of 2 σ significance per point. The H.E.S.S. spectrum exhibits a 2 σ significant spectral bin at $\sim$ 15 TeV.

The H.E.S.S. spectrum is well fit with a single power law ($dN/dE = \Phi_0 \times (E/1\mathrm{TeV})^{-\Gamma}$) with an index $\Gamma = 2.3 \pm 0.2$ and a differential flux normalization at 1 TeV of $\Phi_0 = (1.31 \pm 0.43) \times 10^{-13}$ TeV^{-1}cm^{-2}s^{-1}, with a χ^2 of 3.9 for 2 degrees of freedom. The derived photon index is consistent with the previous estimate by H.E.S.S.,

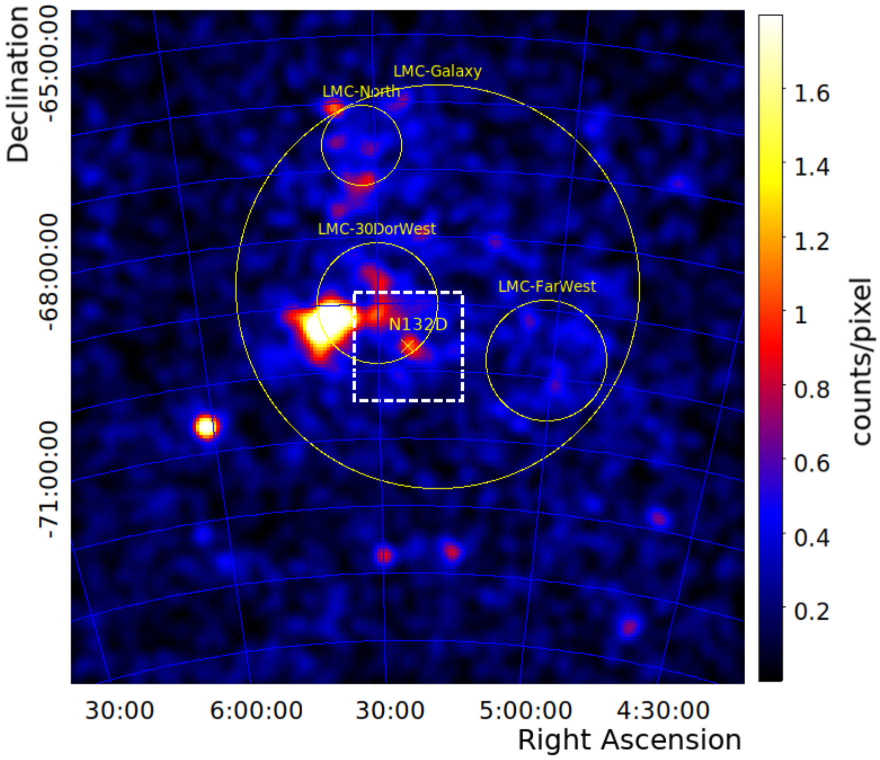

Figure 2.2 – Gaussian (σ=0°.2) kernel smoothed *Fermi*-LAT count map centered on the position of N132D for the energy range 3-250 GeV. The central dashed box corresponds to the FoV of the H.E.S.S. excess map shown in Figure 2.1. The bright *Fermi*-LAT sources at the eastern edge of the LMC-30 DorWest region are N157B and PSR B0540-69. Their emissions overlap at this resolution.

yielding $\Gamma = 2.4 \pm 0.3$ (Abramowski et al. 2015b). Systematic errors on the spectrum parameters are estimated to be ± 0.3 for Γ, and ± 30% for Φ_0. These systematic uncertainties arise because the data set spans 13 years and the LMC is mostly observed during the rainy season, leading to significant variations in atmospheric conditions (see Abramowski et al. 2012). The corresponding luminosity, assuming a distance $d = 50$ kpc to the source, is $L(1 - 10 \text{ TeV}) = (1.05 \pm 0.29) \times 10^{35} (d/50\text{kpc})^2$ erg s^{-1}. This value is consistent with previous results and is comparable to the luminosity of the brightest SNRs in the VHE band : N132D is as luminous as HESS J1640-465 (Abramowski et al. 2014b) and ~28 times more luminous than Cas A (Aharonian et al. 2001).

A combination of the H.E.S.S and *Fermi*-LAT data allowed us to investigate the spectral properties in a wide energy range. The fits were performed on H.E.S.S and Fermi-LAT eight spectrum points, as shown in Figure 2.3. The fit parameters are reported in Table 2.1. The combined spectrum can be perfectly fit with a single power law, resulting in a reduced χ^2 of 8.2 for 6 degrees of freedom (Figure 2.3 left). The derived photon index, $\Gamma = 2.13 \pm 0.05$, is consistent with the index obtained with the H.E.S.S. data alone. The fit model with a power law and an exponential cutoff (Figure 2.3 right), $dN/dE = \Phi_0 \times (E/1\text{TeV})^{-\Gamma} \exp(-E/E_\text{c})$, is not preferred over a fit with a simple power law as derived from this table by means of a likelihood ratio test (1.4σ, $\Delta\chi^2 = 1.8$ with 1 degree of freedom). Considering the Akaike information criterion (AIC ; Akaike 1974), an AIC value of 12.4 is obtained while fitting a power law with an exponential cutoff to the data, which is 12.2 when a power law is fit to the data. The relative likelihood defined as $\exp((\text{AIC}_\text{min} - \text{AIC}_\text{max})/2)$ shows that the power-law model is sufficient to describe the data. The resulting cutoff energy is quite high, exhibiting large errors ($E_c = 19^{+60}_{-10}$ TeV). A cutoff energy lower than 8 TeV can be excluded at a 95% confidence level (CL). The energy cutoff value is based on the statistical analysis and does not take into account the H.E.S.S. systematic error in the energy reconstruction of $\sim 15\%$. A broken power-law fit to the joint Fermi/H.E.S.S. data yields values (Figure 2.3 right) of the break energy between 8 GeV and 140 GeV, with a best-fit value of 24 GeV, and it is as likely as a simple power law fit (1.5σ, $\Delta\chi^2 = 4.0$ with 2 degrees of freedom, and an AIC value of 12.2). These lower and upper bounds were established by fitting the data with a fixed value for the energy break until a $\Delta\chi^2 = 1$ was reached (68% CL), leaving all other parameters free.

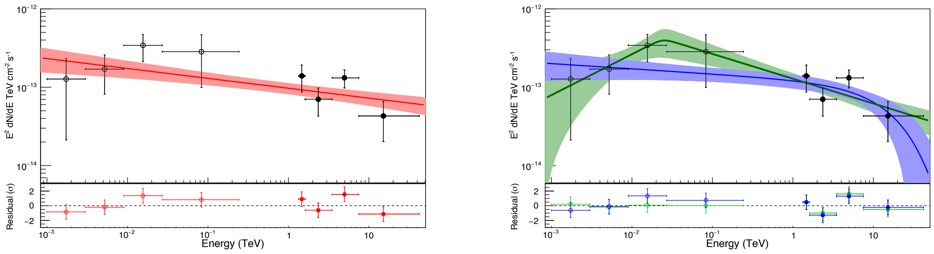

FIGURE 2.3 – Left : *Fermi*-LAT (open circles) and H.E.S.S (dots) combined spectrum fit with a power law. Right : *Fermi*-LAT and H.E.S.S combined spectrum fit with a power law with an exponential cutoff (blue) and a broken power law (green). For both Figures, the best-fit functions are shown with 68 % error bars in the shaded region, as well as residuals compared to the fit. The flux point error bars represent the statistical uncertainties. The fit parameters are reported in Table 2.1.

2.3.2 Morphology in the VHE gamma-ray band

The position of the VHE gamma-ray source was obtained from a two-dimensional fit of the H.E.S.S. so-called ON map consisting of gamma-ray-like events in the source region and a background map, using the gamma-ray events selected in the OFF region multiplied by a scaling factor map in order to reach the source exposure level.

Data	χ^2/ndof	Γ	Φ_0 (1 TeV) $\times 10^{-14}\mathrm{TeV}^{-1}\mathrm{cm}^{-2}\mathrm{s}^{-1}$	E_c/E_b
H.E.S.S. PL	3.9/2	2.32 ± 0.22	13.1 ± 4.3	–
Fermi-LAT + H.E.S.S PL	8.2/6	2.13 ± 0.05	9.7 ± 1.6	–
Fermi-LAT + H.E.S.S ECPL	6.4/5	2.08 ± 0.06	12.3 ± 2.9	$E_c = 19^{+60}_{-10}$ TeV
Fermi-LAT + H.E.S.S BPL	4.2/4	1.47 ± 0.43 2.31 ± 0.14	12.8 ± 2.9	$E_b = 24^{+116}_{-16}$ GeV

Table 2.1 – Spectral fit parameters for the H.E.S.S. and *Fermi*-LAT plus H.E.S.S. data sets. PL stands for "power law", ECPL for "power law with an exponential cutoff" , and "BPL" for "broken power law" (see text for details).

The fit was performed using the *Sherpa* package (Freeman et al. 2001), with a log-likelihood approach (Cash statistic; Cash 1979) and the Levenberg-Marquardt algorithm (Moré 1978). To obtain the source position, a Gaussian source was convolved with the H.E.S.S. analysis PSF ($0\overset{\circ}{.}06$) multiplied by the exposure map to take any asymmetry in the exposure across the analyzed sky region into account, and with the background amplitude fixed to 1. As there is no evidence for an extension, a point source assumption was used by fitting the two-dimensional Gaussian profile with a width of $\sigma = 0\overset{\circ}{.}005$. The fit results in a best-fit position of RA $5^{\mathrm{h}}24^{\mathrm{m}}47^{\mathrm{s}} \pm 6.9^{\mathrm{s}}_{\mathrm{stat}}$ and Dec $-69°38'50'' \pm 29''_{\mathrm{stat}}$ at about $1'$ from the X-ray source position. The uncertainty of the telescope pointing leads to a systematic error of $\sim 20''$ per axis. The systematic error arising from the asymmetrical exposure is negligible. The best-fit position and the confidence region are shown in Figure 2.1 and are consistent with the center of N132D as seen in X-rays within $\sim 1.2\ \sigma$.

Given the diameter of N132D in X-rays of $1.6'$ and the presence of a nearby molecular cloud at a distance of $\sim$ 2 arcminutes, it is likely that the gamma-ray source has a structure on the arcminute scale. With the reported data, a two-dimensional fit with a Gaussian profile centered on the best-fit position provides only a 99% CL upper limit on the source extension in gamma rays corresponding to $\sigma_{\mathrm{2D,Gauss}} = 3.3'$ (49 pc). Because the PSF is $3.6'$, the localization of the emitting region is inside this radius.

2.4 Modeling the multiwavelength spectrum

The results were analyzed in the context of the multiwavelength studies of N132D. Radio observations at wavelengths 3 cm and 6 cm by Dickel & Milne (1995) with the Australia Telescope Compact Array (ATCA), and nonthermal X-ray upper limits in the 0.2 to 4 keV band (Hughes et al. 1998) and in the 2-10 keV band provided by Bamba et al. (2018) were added to the gamma-ray spectrum. This led to a multiwavelength spectrum spanning 15 orders of magnitude (see Figure 2.4). Radio and nonthermal X-ray emission can be related to gamma-ray emission based on two different scenarios. The leptonic scenario assumes that a single population of CR electrons generates synchrotron emission in the radio to X-ray range and inverse Compton emission in gamma rays. Alternatively, in the hadronic scenario, CR electrons are only responsible for the synchrotron radio and X-ray emissions, while CR hadrons produce gamma-ray emission through neutral pions that decay into two photons. In this case, a ratio of $n_{\mathrm{e}}/n_{\mathrm{p}}$ for CRs is one of the parameters, for which the canonical value is 1/100, based on the ratio of electron-to-proton CRs measured near the Earth (see, e.g., Longair 2011; Katz & Waxman 2008). However, the $n_{\mathrm{e}}/n_{\mathrm{p}}$ ratio at Earth may not reflect the ratio in SNRs, and there may be variations in SNRs. Here these radiation processes were modeled using theoretical frameworks developed by Aharonian et al. (2010) for the synchrotron radiation, by Khangulyan et al. (2014) for the inverse Compton mechanism, by Baring et al. (1999) for bremsstrahlung emission, and by Kafexhiu et al. (2014) for the pion decay. To model the multiwavelength spectrum of N132D for the two scenarios, the Naima package was employed (Zabalza 2015b). We used a single-zone model. In reality, emission may arise from a number of regions, such as the shocked ejecta, the main shell of the shocked ambient medium, or even, as we discuss below, from cosmic rays interacting with nearby molecular clouds.

2.4.1 Purely leptonic model

The multiwavelength data can be reasonably well modeled with a purely leptonic model assuming synchrotron emission with a magnetic field of 20 μG and inverse Compton emission with two background radiation components, corresponding to the cosmic microwave background (CMB) radiation with an energy density of 0.26 eV cm^{-3} and an IR component intrinsic to the remnant itself with a temperature of 145 K and an energy density of 1 eV cm^{-3} (see Abramowski et al. 2015b). The latter component is due to dust emission from and around the SNR. The model assumes an electron distribution following a power law with an exponential cutoff. Figure 2.4 shows the model, and the corresponding parameters are reported in Table 2.2. For this model, the required total electron energy is W$_e$($>$ 1 GeV) $=$ 4.50 $\times$ 10^{49} erg, which is significantly higher than observed in other well-studied SNRs (as discussed in Section 2.5.2). Even if an initial released energy higher than the canonical value is considered, for instance, $\sim$5$\times$10^{51} erg (see, e.g., Bamba et al. 2018), then 10 % of this energy can be transmitted to CR protons, which would imply a maximum electron energy of W$_e \simeq 5 \times 10^{48}$ erg if $n_e/n_p = 0.01$ is assumed.

Diffusive shock acceleration should lead to an initial particle distribution that is a power law in momentum (e.g., Malkov & Drury 2001). This means that the energy distribution breaks around the rest-mass energy of the particles. Hence, diffusive shock acceleration produces an electron spectrum that is expected to continue as an unbroken power law to energies well below 1 GeV (e.g. Asvarov et al. 1990; Vink 2008a), unlike the hadronic CR distribution. For example, if a lower limit at 10 MeV is considered, then W$_e$($>$ 10 MeV) $= 1.3 \times 10^{50}$ erg, which suggests that an implausibly high fraction of $>$ 2% of the explosion energy would be contained in relativistic electrons.

The value of 20 μG for the magnetic field strength required by the leptonic model is similar to what was inferred by Abramowski et al. (2015b) and Bamba et al. (2018). Although some 1000–3000 yr old SNRs do have similar magnetic fields (Bamba et al. 2005; Helder et al. 2012; Zeng et al. 2019), such a magnetic field strength is surprisingly low for a radio source as luminous as N132D ($\sim$38 times more luminous at 1 GHz than the $\sim$1835 yr old SNR RCW 86, which is a VHE gamma-ray source), and this would imply that the magnetic field energy density is far out of equipartition with relativistic particle energy density. The equipartition magnetic field strength can be derived from the minimum energy principle, which minimizes the total energy of the nonthermal particles plus the magnetic field energy for a given radio luminosity. The magnetic field strength thus derived, B_{min}, is close to the equipartition value (Burbidge 1956). It leads to the following relation for B_{min} (for a review, see Longair 2011; Vink 2020) : $B_{min}(\mathrm{G}) = 9.3 \times 10^3 \left(\frac{\eta L_\nu}{V}\right)^{2/7} \nu^{1/7}$, with L_ν, the radio luminosity in erg s^{-1} Hz^{-1} at a frequency ν in Hz, V corresponds to 25% of the volume in cm^3 of a sphere with the diameter of N132D (28 pc), and η is a parameter taking into account the ratio of the energy present in CR nuclei versus electrons ($1< \eta <100$). Considering the radio luminosities reported by Dickel & Milne (1995) ($L_\nu = 4.3 \times 10^{24}$ erg s^{-1} Hz^{-1} at 5 GHz) and the volume corresponding to a diameter of 28 pc, $B_{min} \approx 35\,\mu$G is obtained for $\eta = 1$ (the relativistic electron density equals that of CR nuclei), and 134 μG for $\eta = 100$.

Figure 2.7 shows the purely leptonic model with bremsstrahlung in addition to the synchrotron and inverse Compton emission for the electron distribution following a power law with an exponential cutoff as described above. For the bremsstrahlung component to be important, the density of the proton targets has to be as high as $n_\mathrm{p} = 3$ cm^{-3}. At this high density, the pion decay process will play a considerable role, which violates the assumption of a pure leptonic model. In a purely leptonic scenario, bremsstrahlung emission cannot explain the data if the proton density remains low. In the case of a mixed lepto-hadronic model as described in the next Section, a hadronic component would require a lower energy for the protons and electrons, leading to a higher magnetic field value. Then bremsstrahlung emission is marginal and not needed to explain the data. It can be concluded here that a purely leptonic model is unrealistic for the HE-VHE gamma-ray emission considering the extreme total energy in electrons required to explain the measured spectra, and a dominant component of hadronic origin is required.

MODEL	$W_e(> 1$ GeV) erg	Γ	$E_{c_{elec}}$ TeV	B μG	$W_p(> 1$ GeV) erg	n_p cm^{-3}	$E_{c_{prot}}$ TeV
Leptonic	4.5×10^{49}	2.2	8	20	–	–	–
Hadronic	4×10^{48}	2.1	2.5	100	4×10^{50}	10	120

Table 2.2 – Parameters for the proposed models of the N132D multiwavelength spectrum. For details, see text.

2.4.2 Hadronic model

The HE-VHE gamma-ray spectrum can be well fit with a pion decay model, assuming a proton distribution following a power law with an exponential cutoff. The

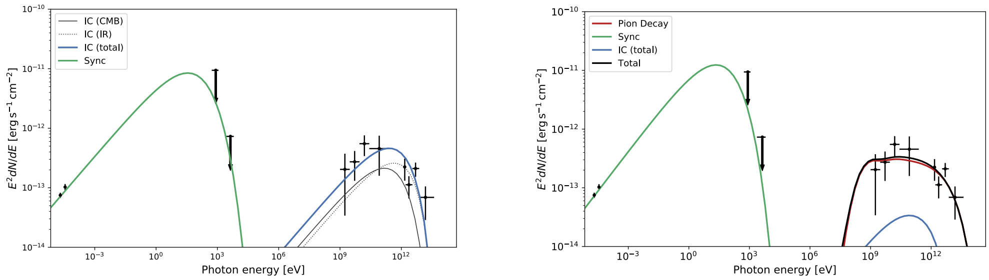

Figure 2.4 – Left : Leptonic model considering an electron distribution following a power law with an exponential cutoff. The parameters are described in Table 2.2 and the IR photon density is 1 eV cm^{-3}. Right : Hadronic model considering a proton distribution following a power law with an exponential cutoff. The parameters are described in Table 2.2.

model requires an ambient proton density of $n_{\rm p}$ = 10 cm^{-3} (Hughes et al. 1998), a total CR proton energy W$_p$(>1 GeV) = 4 × 10^{50} erg, a power-law spectral index Γ = 2.1, and a cutoff energy of E_c =120 TeV (Table 2.2). The cutoff energy value is remarkably high : a lower limit is set at E_c =45 TeV with 95 % CL, which is much higher than the cutoff in the proton spectrum for Cas A, which is estimated to be at ∼10 TeV by Ahnen et al. (2017). The total energy in CR protons, W_p(>1 GeV) = 4 × 10^{50} erg, is high but not unrealistic because the energy released in the explosion is thought to exceed 10^{51} erg (e.g., Dickel & Milne 1995), 10% of which can be transferred to hadronic CRs. The pion decay fit can be achieved with a lower CR proton energy and a higher ambient proton density, for example, W_p(>1 GeV) = 1 ×10^{50} erg and n_p = 40 cm^{-3}, but higher proton densities would necessitate additional target material, other than the SNR itself, for the hadronic interaction to take place, for example, a nearby molecular cloud.

Radio and X-ray data were fit with a synchrotron emission model assuming that the electron energy distribution follows a power law with an exponential cutoff, the normalization being constrained by a total electron energy W_e(>1 GeV) = 4 × 10^{48} erg, assuming 1/100 of the proton energy. The model requires a high magnetic field strength in order to make the leptonic gamma-ray emission subdominant, set here to B = 100 μG, with a cutoff in the electron distribution at E$_c$(100μG) $\leqslant$ 3.5 TeV, in order to fit the radio data points and ensure that the X-ray synchrotron component does not exceed the X-ray upper limits. For the spectrum presented in Figure 2.4, E$_c$ = 2.5 TeV was chosen (see parameters in Table 2.2). In this model, a cutoff energy in the proton distribution is significantly higher than that in the electron distribution.[4]

Our model is compatible with similar models in the literature, such as those proposed for Cas A by Abeysekara et al. (2020), and to some extent, the model for

---

[4] In reality, the electron spectrum may even have a break well below 2.5 TeV as a cooling break is expected at ∼ 0.5 TeV for t = 2500 yr and B = 100 μG (see Section 13.3 Vink 2020).

RX J1713.7-3946 (see Abdalla et al. 2018d), both of which normalize the electron distribution to the radio and X-ray synchrotron emission. The chosen magnetic field strength is close to the equipartition value of 135 μG. The W_e/W_p ratio depends on the electron-to-proton (n_e/n_p) ratio, but also on the respective volumes for integrating proton and electron densities, leading to total energy values. CR electrons can fiducially be considered to emit synchrotron radiation within the SNR volume.

If gamma-ray emission from both CR electrons and protons originates within the SNR, then the assumption of $\mathrm{W}_e/\mathrm{W}_p = n_e/n_p = 1/100$ is reasonable. However, if gamma-ray emission is mainly produced by escaped CR protons interacting with a molecular cloud, then the W_e $/\mathrm{W}_p$ ratio can have a different value.

2.5 Discussion

The analysis of 252 hours of H.E.S.S. observations of N132D confirms the previously published result that N132D is an exceptionally luminous SNR in the VHE band. The well-determined distance to the LMC makes our luminosity estimation robust ; it is therefore worthwhile to compare the gamma-ray SED of N132D to the SEDs of the most luminous SNRs in gamma rays. We found that only one Galactic SNR, G338.3-0.0, is firmly established to show a VHE luminosity that is comparable to that of N132D (see Appendix 2.8 for details). G338.3-0.0 is a composite SNR identified with the VHE source HESS J1640-465, but it is not clear whether the VHE emission comes predominantly from the central PWN or the SNR shell (Abdalla et al. 2018c).

Another important and new result of the analysis presented here is that no clear cutoff has been found in the gamma-ray spectrum, which extends up to 15 TeV. The last bin of the spectrum presented in Figure 2.3 corresponds to gamma rays with energies of about 10 TeV or beyond, which is remarkable for such a distant SNR. The spectra of only a few SNR shells reach such a high energy, and they are younger and more nearby sources than N132D. Assuming a hadronic origin for the gamma-ray emission from N132D, this implies that protons are present in N132D with energies of at least one hundred TeV.

The extremely high VHE luminosity and the extension of the high-energy power-law tail to 15 TeV are two observational properties that need to be examined in the context of the physics of SNRs and their environment. For this purpose, the VHE gamma-ray properties of N132D were compared with those of SNRs with similar physical properties, such as age, shock speed, and circumstellar structure (stellar wind bubbles and vicinity of molecular clouds).

2.5.1 Comparison of properties among SNRs

Supernova remnants are thought to be efficient accelerators during time intervals when the shock speed is high and they transit from the ejecta-dominated phase to the Sedov phase. SNR RX J1713.7-3946 is one of the brightest VHE-emitting SNR and is often considered as a prototypical CR accelerator. It is younger (1600-2100 yr, e.g., Tsuji & Uchiyama 2016) than N132D and it is a nearby source (at 1 kpc). It has a high shock speed of ∼3500 km s^{-1}, therefore the conditions are fulfilled for rapid diffusive shock acceleration. Due to its gamma-ray brightness, its spectrum is measured well beyond 10 TeV, and it exhibits a cutoff at $E_c = 12.9 \pm 1.1$ TeV (Abdalla et al. 2018d). For this source, the leptonic scenario is as plausible as the hadronic one. For a hadronic scenario, the cutoff in the parent proton distribution is estimated at $E_c = 88$ TeV, which is similar to our results. With an age of about 2500 yr, N132D is about an order of magnitude more luminous in the VHE band than SNR RX J1713.7-3946. Thus, even if the age of SNRs is one of the factors making N132D a source with a high CR energy content, other factors should also play a role in making this source so luminous. The X-ray emission from RX J1713.7-3946 is dominated by synchrotron radiation from 10-100 TeV electrons, whereas there is no evidence for X-ray synchrotron emission from N132D, whose X-ray emission is dominated by thermal radiation. Figure 2.5 shows the differential luminosities for five SNRs demonstrating that N132D is one of the two most luminous SNRs, together with HESS J1640-465. In all these VHE sources, only the distant but luminous N132D and the nearby RX J1713.7-3946 exhibit flux points above 10 TeV.

The gamma-ray emission properties of SNRs have recently been compared by Zeng et al. (2019) and Suzuki et al. (2020) using large SNR samples. A comparison of these results to the properties of N132D presented here confirms the exceptional nature of N132D. In particular, the inferred gamma-ray cutoff energy of $E_c \gtrsim 8$ TeV is higher than those of the SNRs in Figure 5b in Suzuki et al. (2020), who used a spectral model comparable to the one used by us. Similar conclusion can be drawn from Figure 3 of Zeng et al. (2019), however, care should be taken wherever a lower limit to the cutoff energy is provided for spectra with a broken power-law shape, as this is an additional model complexity.

N132D belongs to the small class of oxygen-rich SNRs (see Vogt & Dopita 2011), together with Cas A and Puppis A. These SNRs are characterized by elevated abundances of oxygen, neon, and other heavy elements, indicating that this material has its origin within the helium-burned layers of massive progenitor stars. For the progenitor of N132D, different values for its mass have been suggested, for instance, $> 35 M_\odot$ (France et al. 2009) and $15 \pm 5\, M_\odot$ (Sharda et al. 2020), while the progenitors of Cas A and Puppis A have masses in the range of $15 - 25 M_\odot$ (Young et al. 2006; Hwang et al. 2008). The comparison of N132D with Cas A shows that the two remnants have similar properties in the radio and X-ray bands, and bright oxygen emission. The distance of Cas A is measured to be 3.4 kpc (Reed et al. 1995), and its age is ≃340 years (Thorstensen et al. 2001). N132D is therefore much older than Cas A. However, Figure 2.5 clearly shows that N132D is much more luminous than its younger sibling. As already mentioned, the Cas A spectrum exhibits a cutoff at 3.5 TeV that is absent

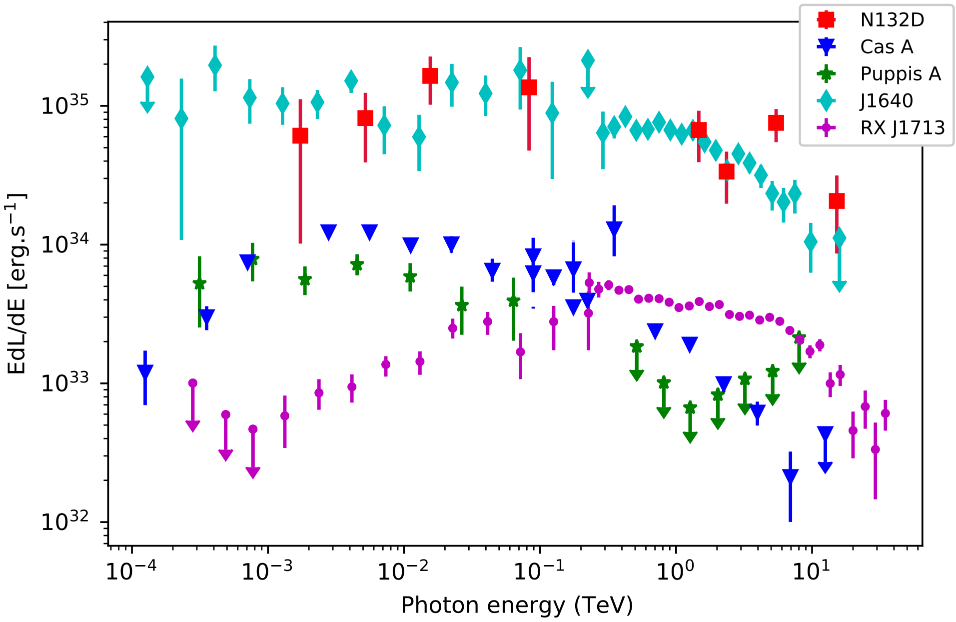

Figure 2.5 – Comparison of differential luminosities, EdL/dE, for VHE bright SNRs. Luminosities are computed using the differential flux data points and estimated distances in the following references : N132D, this work, d = 50 kpc ; Cas A, Ahnen et al. (2017), $d = 3.4$ kpc ; Puppis A , Abramowski et al. (2015a), $d = 2.2$ kpc ; HESS J1640-465, Lemoine-Goumard et al. (2014), $d = 10$ kpc ; and RX J1713.7-3946, Abdalla et al. (2018d), $d = 1$ kpc. The different shapes of the individual SEDs probably reflect the different emission mechanisms (leptonic or hadronic) and evolutionary stages. See the original references for detailed spectral models.

in the N132D spectrum. Puppis A is an older oxygen-rich SNR with an age estimated to be 4450 ± 750 years and a distance of 2.2 ± 0.3 kpc. It is very similar to N132D in terms of chemical composition and age, but it is 30 times closer. Puppis A has not been detected in VHE gamma rays (Abramowski et al. 2015a), and its GeV emission is thought to be due to the interaction with a nearby molecular cloud. A recent study concluded that there is a spectral break at GeV energies, which could explain the absence of VHE emission (Xin et al. 2017). In this regard, Puppis A could be similar to the mature SNRs W44 or IC443, whereas, as demonstrated by Bamba et al. (2018), N132D could be in the transition from being young to a intermediate-age SNR. These facts show that there is significant variation in the observational gamma-ray properties among the members of the oxygen-rich SNR class.

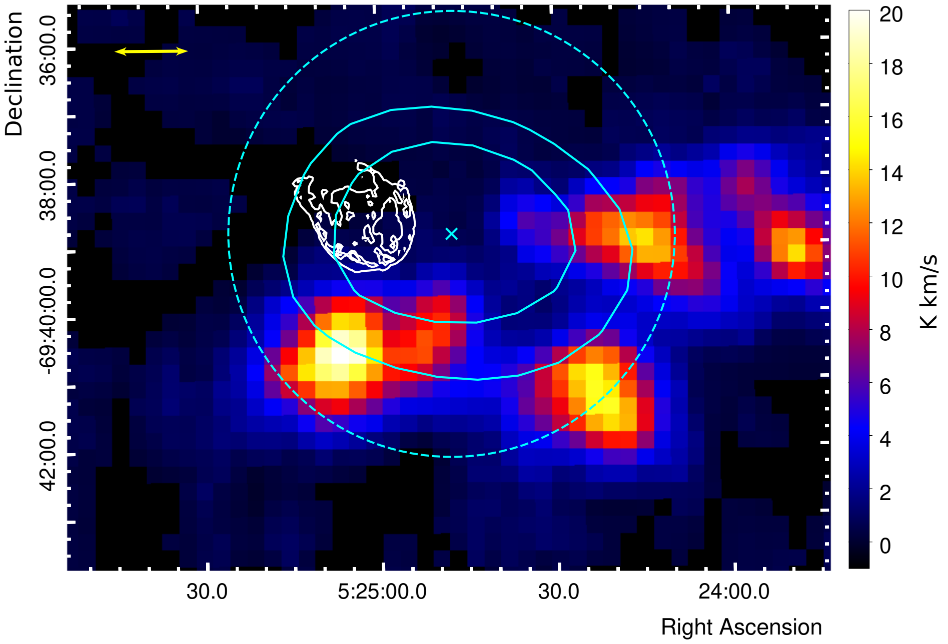

Figure 2.6 – Molecular clouds in the vicinity of N132D. The image shows the CO emission (color scale in K km/s) from the MAGMA survey (`https://www.atnf.csiro.au/research/MAGMA/DR1/`) (Wong et al. 2011). White contours denote *Chandra* X-ray emission from N132D (`https://chandra.harvard.edu/photo/openFITS/`) (Borkowski et al. 2007). The best-fit position of the gamma-ray emission is denoted by the cross, and the elliptical contours are the confidence regions of the position at 2σ and 3σ. The dashed circle illustrates the 99% CL UL on the extension established at $3.3'$. The scale bar indicates $1'$.

2.5.2 Interstellar environment

For hadronic emission, the VHE luminosity is determined by the total energy in CRs above $\sim$ 10 TeV and the local gas density. The high TeV gamma-ray luminosity of N132D may therefore reflect a combination of a high energy in CRs, perhaps caused by a relatively high explosion energy for this SNR, and a high gas density. Two possible locations of a dense gas are discussed below, including the shell of a wind-blown cavity and a massive molecular cloud near N132D. Our multiwavelength modeling indeed suggests that the gamma-ray emission most likely has a hadronic origin. In the case of a leptonic scenario, the required total energy in the electrons is high compared with other observed SNRs (see also Bamba et al. 2018). For example, a leptonic model for the gamma-ray emission from SNRs with a low GeV-to-TeV flux ratio, RX J1713.7-3946 and RX J0852.0-4622 (e.g., see Figure 3 in Dermer & Powale 2013), implies a total electron energy, $W_\mathrm{e}(\mathrm{E} > 1\mathrm{GeV})$, of 3.1×10^{47} erg (Abdalla et al.

2018d) and 2.24×10^{48} erg (Abdalla et al. 2018e), respectively. For HESS J1640-465, a similar modeling leads to $W_\mathrm{e} = 10^{49}$ erg (Abramowski et al. 2014b). To a lesser extent, the lack of nonthermal X-rays from N132D is also in favor of a hadronic origin, although nonthermal X-ray emission may be hidden below the bright thermal X-ray continuum. An X-ray synchrotron luminosity similar to that of RX J1713.7-3946 cannot be excluded. Moreover, the radio luminosity of N132D suggests a high magnetic field strength, compatible with the 100 μG strength assumed in the hadronic model presented in Section 2.4.2.

For the preferred hadronic scenario for the gamma-ray emission of N132D, a high gas density is required, and the question arises where most of these gamma rays are coming from : from CRs within the densest portions of the SNR shell, or from CRs that have escaped the shell and are interacting with the massive molecular cloud near N132D (Banas et al. 1997; Sano et al. 2020). While the GeV luminosities of SNRs interacting with molecular clouds are higher than those of SNRs without nearby molecular clouds, this tendency does not hold for VHE gamma rays (e.g., Fernandez et al. 2013). The VHE luminosity enhancement for N132D and its hard gamma-ray spectrum at VHE energies can be interpreted under the assumptions that (1) the shock accelerates protons until the highest possible energy is reached, and at this point, the shock can no longer confine the protons, and (2) the most energetic protons escape then into the interstellar medium (ISM). The gamma-ray emission created by the interactions of these escaped protons with a gas cloud will be strong and hard (Aharonian & Atoyan 1996; Gabici & Aharonian 2007; Moskalenko et al. 2008). The hadronic scenario requires a high density of the target material. These high densities can be found in molecular clouds. SNRs such as W28 or W44 show gamma-ray emission originating in nearby molecular clouds (see, e.g., Abramowski et al. 2008; Cardillo et al. 2014; Makino et al. 2019), indicating that protons accelerated in the SNR bombard the molecular cloud. N132D is interacting with a molecular cloud as well, which has recently been shown by Sano et al. (2020). Furthermore, the X-ray emission is brightest in the southwestern part, where the SNR is interacting with dense matter.

The molecular clouds near N132D as traced by the CO emission are shown in Figure 2.6. The velocity of the clouds, $+264$ km s^{-1}, agrees with that of N132D, $+268$ km s^{-1} (Banas et al. 1997). The best-fit position of the gamma-ray emission (elliptical contours in Figure 2.6) is consistent with the position of the SNR itself and with parts of the molecular cloud. Therefore these two regions are potential sites of gamma-ray emission. If the VHE gamma-ray emission comes from these molecular clouds, a diffusion coefficient of $D \simeq 2 \times 10^{29}\,(t/2500\ \ \mathrm{yr})^{-1}$ cm^2 s^{-1} for multi-TeV CRs is required. To determine the spatial origin of the gamma-ray emission, a higher sensitivity and a finer angular resolution are needed. Nevertheless, the spectrum with an unbroken power law from GeV to TeV energies could be taken as evidence for a single population of emitting particles. This would be difficult to reconcile with illumination of MCs by CRs originating from the shell. In that case, the low-energy gamma rays would likely come from the shell because only the highest-energy CRs would penetrate the MC and cause gamma-ray radiation at VHE. In addition to the molecular clouds shown in Figure 2.6, Sano et al. (2020) reported smaller clouds that interact with the SNR, as indicated by the ratio of CO $J = 3-2$ versus $J = 1-0$ line emission. These cloudlets are situated in the south and near the center of the SNR. They might also be locations of enhanced hadronic emission, but then directly associated with the SNR itself.

A hadronic scenario involving a wind-blown cavity is also possible. As suggested by Chen et al. (2003), in case of a very massive progenitor, a low-density bubble is formed (see also Weaver et al. 1977). When the SN occurs, the shock propagates with a high velocity ($v \sim$ 5000-10000 km s^{-1}) into the bubble. When the shock wave reaches the high-density shell of swept-up material, it heats the dense shell, and the SNR appears most luminous, but the shock velocity rapidly decreases. A wind-blown bubble model was considered for G338.3-0.0 in order to explain the high VHE luminosity of HESS J1640-465 (Abramowski et al. 2014b). Under the assumptions that the SNR shock freely expands up to the radius of the wind-blown bubble, and with average shock speeds between 5000 km s^{-1} and 10000 km s^{-1}, the authors proposed that the age of SNR G338.3-0.0 could be 1000-2000 yr in this case, and at least younger than 5000-8000 yr (Slane et al. 2010).

The wind-blown bubble model also fits the properties of N132D, given the inconsistency between its kinematic age (2500 yr) and its Sedov dynamical age (6000 yr), indicating that the supernova explosion occurred within a cavity in the interstellar medium (Hughes 1987). In addition to the VHE luminosity enhancement, it is conceivable that this model can also explain the presence of sub-PeV protons to some extent because an SNR expanding into a preexisting stellar wind can accelerate protons to a higher energy than SNRs expanding in a uniform circumstellar medium (Völk & Biermann 1988). Because the gamma-ray spectrum of G338.3-0.0/HESS J1640-465 has an exponential cutoff at 6 TeV, it is unclear so far whether the luminosity enhancement and the increase in a maximum CR energy are expected to be observed simultaneously.

Two other SNRs in the LMC, N63A and N49B, have also been proposed to have evolved in wind-blown cavities (Hughes et al. 1998). Because N63A and N49B were detected with *Fermi*-LAT (Campana et al. 2018) and have massive progenitors, it is possible that the luminosity enhancement takes place in these SNRs as well, as suggested, for example, in Sano et al. (2017). This hypothesis can be tested by observations of N63A and N49B, which are located in the northern part of the LMC disk about 4° away from N132D.

In general, the LMC is well suited for studies of SNRs (see Ginzburg 1972) because its projection is almost face-on (inclination of 35°) and the distance to the LMC SNRs is more certain than for some Galactic SNRs, allowing us to accurately derive the VHE luminosity. Galactic PeVatron candidates with hard ($\Gamma \sim 2$) and featureless spectra similar to those derived for N132D in this work can be listed among unresolved H.E.S.S. sources in the Galactic plane (e.g., Spengler 2020). For example, SNR G318.2+0.1, one of the two most luminous Galactic SNRs at VHE, was proposed to be associated with HESS J1457-593 in 2010 (Hofverberg et al. 2010a) and is listed among PeVatron candidates. However, the association of Galactic VHE sources is often complicated by the presence of several possible source candidates for a given region within the Galactic plane.

Because of the lack of evidence for an energy cutoff in the N132D spectrum, N132D remains a PeVatron candidate. Cristofari et al. (2020) suggested that only the remnants of very powerful rare supernova explosions such as the one that produced the N132D remnant can accelerate CR particles to PeV energies. Moreover, the LMC has a significant angular size, allowing a detailed study of individual SNRs resolved in the VHE band. Identifying the origin of CR hadrons is a long-standing problem (Ginzburg 1972), and the establishment of discrete accelerators of CR protons in the LMC, such as N132D, shows that SNRs are viable sources of CRs in the Milky Way and the LMC.

The possible role of molecular cloud interaction on the gamma-ray emission is worth investigating with the next generation of IACTs, in particular, with the Cherenkov Telescope Array (CTA ; Cherenkov Telescope Array Consortium 2019), which will have a sensitivity that is an order of magnitude better than H.E.S.S. and its angular resolution will be higher. Future N132D observations with CTA might therefore establish whether there is a shift between the SNR center and the origin of gamma-ray emission, and moreover, they might help to determine the energy of the spectral cutoff or even establish this enigmatic SNR as a CR PeVatron.

2.6 Conclusion

The LMC SNR N132D is detected with a statistical significance of 5.7 σ above 1.3 TeV on the basis of H.E.S.S. observations with an exposure time of 252 hours, which is 104 hours longer than the exposure used in the previous publication (Abramowski et al. 2015b). The inclusion of new observations results in an unambiguous detection and allowed us to perform a more detailed spectral analysis.

The Fermi-LAT and H.E.S.S. gamma-ray spectrum extends up to 15 TeV and is well described with a power-law index of 2.13 ± 0.05. No cutoff in energy is needed to explain the spectrum, as a power law with an exponential cutoff fit is statistically as valid as a simple power-law model. A 95% CL lower limit on an exponential cutoff is derived at 8 TeV. This lower limit exceeds the cutoff value of 3.5 TeV established for the spectrum of ~340-year-old Cas A by Ahnen et al. (2017), although N132D is ~2500 years old. N132D is the only extragalactic SNR detected in gamma rays so far, and its luminosity is compatible with that of the most luminous Galactic SNR G338.3-0.0. The absence of a clear spectral break and/or cutoff energy and its high gamma-ray luminosity make N132D a very special object. It is one of the oldest and most distant SNRs emitting at VHE.

A purely leptonic model fails to satisfactorily explain the multiwavelength spectrum of N132D. The main argument is that the required total energy of electrons is too high compared to the fraction of explosion energy that is expected to be transferred to leptonic CRs. An additional but less compelling argument is that the magnetic field strength in the case of a purely leptonic scenario is required to be surprisingly low, 20 μG, which is at odds with the radio brightness of this SNR. Finally, the cutoff energy required for the electron distribution is quite low (8 TeV) compared to the absence of a cutoff observed in the gamma-ray spectrum. Our conclusion is that gamma-ray emission from N132D is most likely hadronic in origin.

The hadronic origin of the VHE gamma-ray emission raises the question whether its high luminosity is due to a very efficient acceleration at the SNR shock front, perhaps related to the evolution of the shock inside a wind-blown cavity, or to an interaction of the SNR with the molecular cloud, which could enhance its gamma-ray luminosity. A massive molecular cloud is present in the southwest of the remnant, where enhanced emission in radio, optical, and X-ray bands is observed. These two scenarios are possible given the uncertainties in VHE source position. Even if some of the emission is caused by CR interaction with the molecular cloud, the hard power-law spectrum, together with the lack of evidence for a cutoff energy, makes the gamma-ray SNR very distinct from mature SNRs that are known to interact with molecular clouds, such as IC 443, W44, and W28.

2.7 Appendix A : Supplementary material for the multiwavelength study

See below Figure 2.7.

2.8 Appendix B : Galactic SNRs

The list of luminous (above 20% of the VHE luminosity of N132D) Galactic SNRs available in the literature includes CTB 37A, SNR G318.2+0.1, CTB 37B, SNR G359.1-0.5, SNR G106.3+2.7, SNR G8.7-0.1, and SNR G338.3-0.0, which are sorted here with increasing VHE luminosity. While this list consists of seven SNRs, there are counter-arguments to the high VHE luminosities of five of these objects. (i) The uncertainties in a background model are suggestive of a lower flux of CTB 37A (which are illustrated in Figure 5 of Abdalla et al. (2018c)) than that published in

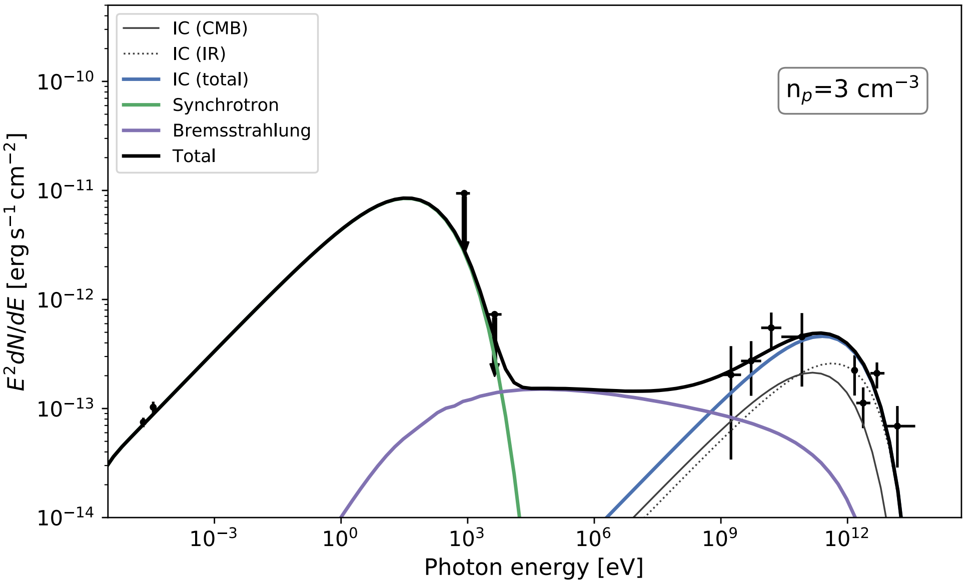

Figure 2.7 – Leptonic model including bremsstrahlung emission. The model considered an electron distribution following a power law with an exponential cutoff. The parameters are described in Table 2.2.

Aharonian et al. (2008a), (ii) the estimated energies of the relativistic particles are too high for the hadronic and leptonic scenarios applied to CTB 37B, suggesting that the distance of 13.2 kpc to this source is an overestimate (Xin et al. 2016), (iii) SNR G359.1-0.5 is likely only to be responsible for a part of the VHE gamma-ray source, HESS J1745-303, given that the solid angle of region A (Aharonian et al. 2008b) that embeds a molecular cloud, as viewed from the center of G359.1-0.5, is about an order of magnitude larger than the angles of the other emitting regions (also Hayakawa et al. 2012), but the contribution from region A to the total flux of HESS J1745-303 is subdominant (Aharonian et al. 2008b), (iv) the distance to SNR G106.3+2.7 is uncertain, and if a distance of 0.8 kpc instead of 12 kpc is adopted, then its estimated VHE luminosity decreases significantly (Acciari et al. 2009), (v) HESS 1804-216 is likely to be dominated by a PWN surrounding the pulsar PSR B1800-21, but not by SNR G8.7-0.1, as demonstrated through the *Fermi*-LAT spectral and spatial analyses (Liu et al. 2019) and on the basis of a comparison of its properties with those of the established VHE PWN (Abdalla et al. 2018b). Finally, SNR G318.2+0.1 is associated with the VHE source HESS J1457-593 and is suggested to be originated from an interaction between G318.2+0.1 and a molecular cloud seen in ^{12}CO data (Hofverberg et al. 2010b), and it therefore cannot be directly compared to SNR N132D. It can also be noted here that in the case of the composite SNR G338.3-0.0 associated with

HESS J1640-465, the scenario in which the VHE emission originates predominantly from the PWN of the subsequently discovered PSR J1640-4631 is highly rated in the context of the VHE PWN population (Abdalla et al. 2018b) ; it remains plausible nonetheless that a significant part of the gamma-ray emission from HESS J1640-465 originates in the SNR shell (Abramowski et al. 2014b).

3

Evidence for gamma-ray emission of Kepler's supernova remnant from deep H.E.S.S. observations

H.E.S.S. collaboration.
Corresponding authors : D.Prokhorov, J.Vink & R.Simoni.

Under Collaboration review - to be submitted

Abstract

Kepler's supernova remnant (SNR) which is produced by the most recent naked-eye supernova in our Galaxy is one of the best studied SNRs, but its gamma-ray detection has eluded us so far. Observations with imaging atmospheric Cherenkov telescopes (IACT) have enlarged the knowledge about nearby SNRs with ages younger than 500 years by establishing Cassiopeia A and Tycho's SNRs as very high energy (VHE) gamma-ray sources and setting a lower limit on the distance to Kepler's SNR. This SNR is significantly more distant than the other two and expected to be one of the faintest gamma-ray sources within reach of the IACT arrays of this generation. We report strong evidence for a VHE signal from Kepler's SNR based on deep observations of the High Energy Stereoscopic System (H.E.S.S.) with an exposure of 152 hours. We further discuss implications of this result for cosmic-ray acceleration in young SNRs.

3.1 Introduction

Since the 1960s supernova remnants (SNRs) have been considered the most likely sources of Galactic cosmic rays (Ginzburg & Syrovatskii 1964), i.e. cosmic rays with energies at least up to 3×10^{15} eV. Although the detection of radio and X-ray synchrotron radiation from SNRs do indeed prove that electrons are accelerated to GeV or even 10 TeV energies (e.g. Helder et al. 2012; Reynolds 2008; Dubner & Giacani 2015; Vink 2020, for reviews), a further insight into the particle acceleration in SNRs comes from gamma-ray astronomy, which inter alia provides a probe of cosmic-ray protons and nuclei through observations of GeV-TeV emission resulting from the decay of secondary neutral pions.

Over the last two decades SNRs have been established as an important population of Galactic gamma-ray sources, both in the high-energy domain (HE ; 100 MeV to 100 GeV) by Fermi-LAT observations (Acero et al. 2016), as well as in the very-high energy domain (VHE ; > 100 GeV) by observations with imaging atmospheric Cherenkov telescopes (IACTs), see Abdalla et al. (2018c) for a population study and Hinton & Hofmann (2009b) for an overview of VHE gamma-ray astrophysics.

VHE spectra are often insufficient by themselves to firmly establish whether the gamma-ray emission is produced by accelerated protons and other atomic nuclei (so-called hadronic cosmic rays) or by accelerated electrons (leptonic cosmic rays). However, in some cases the presence of a characteristic pion-decay feature in the sub-GeV part of the gamma-ray spectrum (the "pion-decay bump") can clearly establish a hadronic origin of the gamma-ray emission. This is for example the case for SNRs IC 433 and W44 (Ackermann et al. 2013). In other cases, due to the fact that hadronic cosmic rays lead to a softer gamma-ray spectrum ($\Gamma \approx 2.2$) in the HE regime than leptonic cosmic rays ($\Gamma \approx 1.5$) the spectral shape indicates the production mechanism of the emission. However, a correspondence between spectral slopes and hadronic/leptonic origin can be more complex if gas clumps are present (Gabici & Aharonian 2014) or in the case of non-linear diffuse shock acceleration (Malkov 1999).

SNRs with ages younger than 2000–3000 yr were established as a class of TeV gamma-ray sources. Many of these young SNRs belong to the class of historical SNRs, i.e. SNRs produced by naked-eye supernovae recorded in history, such as SN 185/RCW 86 (Abramowski et al. 2018), SN 1006 (Acero et al. 2010), and SN 1572/Tycho's SNR (Archambault et al. 2017). The young SNRs RX J1713.7-3946 (RX J1713 for short, Abdalla et al. 2018b), possibly the remnant of SN 393 (Wang et al. 1997), and Cassiopeia A (Cas A, Ahnen et al. 2017; Abeysekara et al. 2020), a nearby 340 yr old SNR for which no reliable eye-witness account has been recorded, are also sometimes added to this class. These SNRs contain both remnants of core-collapse supernovae (RX J1713, Cas A) and thermonuclear (Type Ia) supernovae (SN 185, SN 1006, and SN 1572/Tycho's SNR). Based on the gamma-ray spectral characteristics the gamma-ray emission from Tycho's SNR and Cas A are likely of hadronic origin (Morlino & Caprioli 2012; Ahnen et al. 2017; Abeysekara et al. 2020), whereas for the other, more extended and generally somewhat older SNRs a leptonic origin (e.g. Abdo et al. 2011), i.e. radiation through inverse Compton (IC) scattering, has been suggested. A hadronic scenario for these older TeV gamma-ray emitters is also considered, see for example Berezhko et al. (2012); Inoue et al. (2012); Gabici & Aharonian (2014).

The remnant of the youngest naked-eye supernova (SN), SN 1604 a.k.a. Kepler's SN(R) (Green & Stephenson 2017; Vink 2017), is conspicuously absent from the above list of young SNRs detected in VHE gamma rays. Kepler's SNR is, however, a known X-ray synchrotron emitter (Allen 1999; Nagayoshi et al. 2021), indicating that at least electrons are accelerated up to ~ 10 TeV. Moreover, the relatively high density of its ambient medium (e.g., Williams et al. 2012) makes Kepler's SNR a probable candidate for being a gamma-ray source dominated by hadronic emission. The H.E.S.S. Cherenkov telescopes observed Kepler's SNR in the past, but the previous observations did not result in a detection of the remnant (Aharonian et al. 2008c). This is partially due to the relatively short exposure time compared to other SNRs, as well as the fact that Kepler's SNR is more distant than the historical SNRs listed above.

In this paper, we present the results of deep observations of Kepler's SNR performed with High Energy Stereoscopic System (H.E.S.S.). These results are based on 152 hours of observations, including 122 hours accumulated in 2017-2020, taken with the imaging atmospheric Cherenkov telescopes of H.E.S.S.. This data set is significantly larger than the H.E.S.S. data set with 13 hours of observations published in 2008 (Aharonian et al. 2008c). Kepler's SNR has up to now remained the only historical SNR not detected at TeV energies and these deep observations, therefore, aim at constraining the properties of this potential gamma-ray source. We include the analysis of HE gamma-ray data as a broad gamma-ray SED is important for modeling the entire energy distribution of accelerated particles in the source, and to determine whether the emission is dominated by leptonic or hadronic emission processes. For this reason we also perform an analysis of 10.7 years of *Fermi*-LAT data to study GeV emission from Kepler's SNR.

3.2 Observations and analysis

In this Section, we present analyses of H.E.S.S. and *Fermi*-LAT observations of Kepler's SNR.

3.2.1 H.E.S.S. telescopes

The H.E.S.S. experiment is a hybrid array of five imaging atmospheric Cherenkov telescopes located in the southern hemisphere in Namibia (23°16′18″ S, 16°30′00″ E) at an altitude of 1800 m above sea level (Aharonian et al. 2006b). The H.E.S.S. array consists of four upgraded 12 m-diameter telescopes (Ashton et al. 2020b) placed in a square with 120 m sides and one 28 m-diameter telescope (H.E.S.S. phase II array) in the center of the array. H.E.S.S. employs the stereoscopic imaging atmospheric Cherenkov technique (Daum et al. 1997) and is sensitive to very-high-energy (VHE; > 100 GeV) gamma rays. We performed the dedicated observations of Kepler's SNR

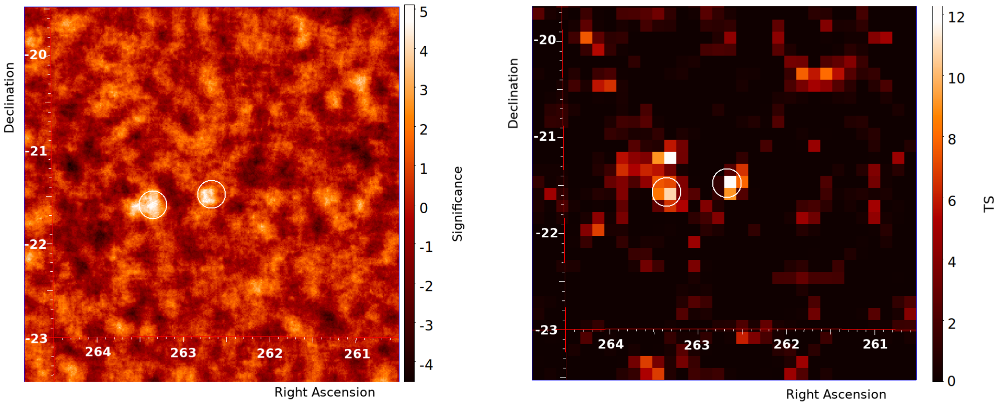

Figure 3.1 – Left panel : H.E.S.S. gamma-ray significance map of Kepler's SNR using an integration radius of 0°.1. Right panel : *Fermi*-LAT TS map in the range of 4.75-300 GeV. The position of Kepler's SNR is in the center of these maps. The circular regions of 0°.15 correspond to Kepler's SNR and SNR G4.8+6.2 (to the east from Kepler's SNR). Both these sources are not present in the 4FGL catalog.

with H.E.S.S. reported in this paper in wobble mode with offsets by 0°.7 in Right Ascension or Declination from Kepler's SNR, allowing a simultaneous measurement of the background in the same field of view (Berge et al. 2007).

Data reduction and analysis

We took data with at least three participating telescopes and in 28 min exposures called runs. We used a standard data quality selection procedure to identify observations with the satisfactory hardware state of the cameras and good atmospheric conditions (Aharonian et al. 2006b; Abdalla et al. 2017). We analyzed 152.2 h of good-quality data recorded during 353 runs. The mean zenith angle of these observations is 26°. Given the age of Kepler's SNR, we consider its VHE gamma-ray emission to be steady during the time interval of 16 years (4% of the age of Kepler's SNR) enclosing the H.E.S.S. observations. This permits a simultaneous spectral fit of both the *Fermi*-LAT and H.E.S.S. data.

We analyzed the H.E.S.S. data using the `Model Analysis` (de Naurois & Rolland 2009, version `HESS_Soft_0-8-34`) and used the analysis configuration that requires a minimum of 60 photo-electrons per image and considers events with an estimated direction reconstruction uncertainty of less than 0°.1. We cross-checked the results with the `Image Pixel-wise fit for Atmospheric Cherenkov Telescope (ImPACT)` analysis (Parsons & Hinton 2014). We defined a circular region-of-interest with a radius of 6′ around the geometrical center of Kepler's SNR (at RA=17h30m40.8s, Dec=-21°29′11″) - hereafter referred to as the source region. Kepler's SNR with 3.5′

diameter is a point-like source for H.E.S.S. and enclosed within the source region.

VHE gamma-ray results

The data analysis yields a number of 1524 gamma-ray-like events from the source region and 23667 gamma-ray-like events from the off-source regions. We estimated the background using the ring background method. We excluded the region around another potential VHE gamma-ray source (SNR G4.8+6.2, see Appendix A) in the field of view from background estimation. The ratio of the on-source exposure time to the off-source exposure time, α, is 0.0569. We computed the number of excess counts by subtracting the number of off-source events multiplied by α from the number of events coming from the source region. The gamma-ray excess is 178 counts above the background. We found the gamma-ray excess of 4.6σ significance by means of equation 17 from Li & Ma (1983). The H.E.S.S. significance map is on the left panel of Figure 3.1. The main and cross-check analyses used in this paper provide compatible results.

We derived the energy spectrum using a reflected region background method (Berge et al. 2007) and a forward-folding technique (Piron et al. 2001). The analysis energy threshold for this data set is 226 GeV given by the energy at which the effective area falls to 15% of its maximum value. The likelihood maximization for a power-law hypothesis yields a photon index of $\Gamma = 2.29 \pm 0.11_{\rm stat} \pm 0.20_{\rm syst}$ and a normalization constant of $N_0 = (9 \pm 1_{\rm stat} \pm 2_{\rm sys}) \times 10^{-14}$ cm^{-2} s^{-1} TeV^{-1}. We binned the spectrum in such a way that spectral points have a minimum significance level of 2.0σ. The spectral analysis resulted in points shown in Figure 3.2. The systematic uncertainties are conservatively estimated to be ±20% on the photon index and ±25% on the normalization coefficient (Aharonian et al. 2006b).

3.2.2 *Fermi*-LAT telescope

The principal instrument on board the *Fermi Gamma Ray Space Telescope* is the Large Area Telescope (LAT ; Atwood et al. 2009), a pair-conversion telescope covering the energy range from about 20 MeV to more than 300 GeV. *Fermi*-LAT has been scanning the entire sky continuously since August 2008.

Data reduction and analysis

For the data analysis, we used the Fermitools package [1] and P8R3_SOURCE_V2 instrument response functions. We selected LAT gamma-ray events with reconstructed energies between 750 MeV and 300 GeV and performed a binned analysis by choosing a $10^\circ \times 10^\circ$ square region centered at RA=17h30m48.7s, Dec=-20°1′55″ (region of interest, ROI). We shifted the central position from that of Kepler SNR by 1.°4 in Declination to reduce systematic effects due to the presence of a molecular cloud, the

---

[1] https://fermi.gsfc.nasa.gov/ssc/data/analysis/software/

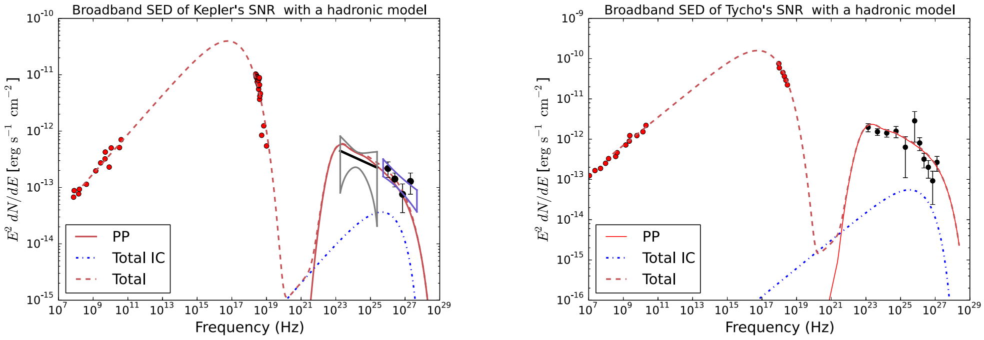

Figure 3.2 – Broadband SEDs of Kepler's SNR (left) and Tycho's SNR (right) with hadronic model fits. SED data points and a butterfly plot for Kepler's SNR as derived from H.E.S.S. and *Fermi*-LAT data, respectively, are shown.

Pipe Nebula, and the Galactic plane in the ROI. For this analysis, we selected events accumulated from 2008 August 4 to 2019 May 16. To reduce the contamination by the gamma-ray emission from the Earth's limb, we selected events with zenith angles $< 90°$. We applied standard quality cuts (`DATA_QUAL>0` && `LAT_CONFIG==1`).

To model the sources within the ROI, we included sources from the 4FGL catalog (Abdollahi et al. 2020) those are within a region of $17\overset{\circ}{.}5$ radius from the center of the ROI. To model the Galactic and isotropic background diffuse emission, we used the standard templates `gll_iem_v07.fits` and `iso_P8R3_SOURCE_V2_v1.txt`. Given the spatial extension of Kepler's SNR in X-rays, we used the point-like source model for its counterpart in HE gamma rays. We applied the binned likelihood analysis on the data by using the `Fermitools` routine, `gtlike`. We binned the data in 25 logarithmically spaced bands in energy and used the spatial binning with a pixel size of $0\overset{\circ}{.}1$. We allowed the normalization and photon index of Kepler's SNR and the normalizations of Galactic and isotropic diffuse sources to vary. We also allowed the normalizations of 4FGL gamma-ray sources within 3° from Kepler's SNR to vary, while held the normalizations of other 4FGL sources fixed. We evaluated the significance of model components or additional parameters using the test statistic, whose expression is $\mathrm{TS} = 2(\log\mathcal{L}\text{-}\log\mathcal{L}_0)$, where $\mathcal{L}_0$ is the likelihood of the reference model without the additional parameter or component (Mattox et al. 1996).

HE gamma-ray results

For the 0.75-300 GeV energy interval, we found that the TS value for Kepler's SNR is 16.8 which corresponds to about 4σ significance. The likelihood maximization yields a photon index of $\Gamma = 2.11 \pm 0.33$ and a power-law prefactor[2], $N_0 =$

---

[2] $\mathrm{d}N/\mathrm{d}E = N_0\,(E/E_0)^{-\Gamma}$

$(0.93 \pm 0.31) \times 10^{-14}$ cm^{-2} s^{-1} MeV^{-1} at E_0=4750 MeV. The TS map based on a source model including only 4FGL sources and generated for the energy range of 4.75-300 GeV is in Figure 3.1. It reveals similarities between the *Fermi*-LAT high-energy TS map and the H.E.S.S. significance map at VHE energies. The positive TS values and significances for KeplerâĂŹs SNR and SNR G4.8+6.2 are present on both these maps in Figure 3.1. The butterfly shaped area shown in Figures 3.2 and 3.3 corresponds to the 68% statistical uncertainty region of the differential flux. The GeV counterpart of Kepler's SNR, if considered together with the corresponding VHE excesses seen with H.E.S.S., provides strong support for identification of Kepler's SNR in the GeV and VHE gamma-ray bands[3].

3.3 Interpretation

3.3.1 Young SNRs as gamma-ray sources

Both Type Ia and core-collapse SNe have similar explosion energies of $\sim 10^{51}$ erg. However, the type of SN does matter for both the ejected mass and the density and structure of the ambient medium. The hadronic scenario—in which the entire gamma-ray emission is produced through the two-photon decay of neutral pions created in hadron collisions of CRs with background gas—results in viable models for both Tycho[4] and Cas A SNRs (Zhang et al. 2013; Ahnen et al. 2017). These two SNRs are comparable in age with Kepler's SNR and this allows investigation into the radiative properties of SNRs at an early stage in their evolution. It is, however, conceivable that the TeV emission detected from the Cas A SNR originates dominantly from the reverse shock instead of from the region heated by the forward shock (e.g., Telezhinsky et al. 2013; Zirakashvili et al. 2014; Helder & Vink 2008). The reverse shock accelerates particles of the ejecta, which in turn colliding with the metal-rich plasma from the SN can lead to strong, hadronic emission on account of the high ejecta density in core-collapse SNRs. This circumstance might hinder a direct comparison of the radiation model for the Cas A SNR with the radiation models for Tycho's and Kepler's SNRs, for which the gamma-ray emission is dominated by forward-shock accelerated particles. For thermonuclear SNe the longer time is required for the system to evolve allowing their progenitors to wander a long distance away from the parent molecular

---

[3] We took the results presented in this Section into account when we made the decision to perform H.E.S.S. observations of Kepler's SNR in 2020. During the internal review of this paper, we became aware of the results of Xiang & Jiang (2021), who derived similar evidence for the GeV excess toward Kepler's SNR from *Fermi*-LAT data.

[4] It is worth noting that the leptonic scenario, in which IC mechanism dominates the VHE emission, is still a viable scenario for Tycho SNR under the assumption that its GeV gamma-ray emission is due to hadronic interactions (Yuan et al. 2012) or in the two-zone approach (Atoyan & Dermer 2012). However, realistic physical models suggest that the gamma-ray emission is primarily due to hadronic processes (Morlino & Caprioli 2012; Slane et al. 2014).

cloud. Thus, the environment in which the remnants of thermonuclear SNe evolve can significantly be different from the environment of core-collapse SNe of massive stars further demarcating a border between their physical models.

Multi-wavelength studies of Kepler's SNR (Vink 2017, for a review) have established that SN 1604 was a Type Ia SN. At a likely distance of 5 kpc (Vink 2017; Ruiz-Lapuente 2017; Sankrit et al. 2016), Kepler's SNR is located 500 pc above the Galactic plane. The relatively high density around Kepler's SNR, in particular in the northwestern part of the SNR, is attributed to mass lost by the progenitor system (Bandiera 1987; Chiotellis et al. 2012; Williams et al. 2012; Toledo-Roy et al. 2014; Burkey et al. 2013b). Apart from its relatively large distance and Kepler's SNR relatively large height above the Galactic plane, Kepler's SNR is best compared to Tycho's SNR located at a distance of about 2.5 kpc : both are Type Ia SNRs and they are of similar age, and develop in a relatively dense ambient medium with $n \approx 1$–$10\ \mathrm{cm}^{-3}$.

3.3.2 SED models

A variety of multi-wavelength data is available for Kepler's SNR. It allows us to construct a characteristic SED for the nonthermal radiation caused by accelerated particles. In addition to the gamma-ray data points described above, we also use radio and X-ray spectral data points of Kepler's SNR from Reynolds & Ellison (1992); Allen et al. (1999), take the WMAP data points at 33 and 41 GHz from Massardi et al. (2009) and the *Swift*-BAT data points at $(4.2, 4.5, 5.3, 7.0, \text{and } 10.0)\times10^{18}$ Hz from Oh et al. (2018). For comparison with the SED of Tycho's SNR, we adopted the data points in the radio and X-ray bands from Kothes et al. (2006); Tamagawa et al. (2009), and selected the gamma-ray data points derived from *Fermi*-LAT and VERITAS (Archambault et al. 2017).

In the framework of a hadronic model, we chose typical values for physical parameters and described both SEDs of Kepler's and Tycho's SNRs by using a modeling package, `Naima` (Zabalza 2015a). The multi-wavelength observation properties of Kepler's and Tycho's SNRs are listed in the appendix B. Our model setup includes : (i) $E_{\mathrm{sn}} = 10^{51}$ erg for the SN Ia explosion energy ; (ii) the distances to Kepler's and Tycho's SNRs of 5.0 kpc (Ruiz-Lapuente 2017) and 2.5 kpc (Zhang et al. 2013; Kozlova & Blinnikov 2018) ; (iii) $n = 0.5\ \mathrm{cm}^{-3}$ for the gas target particle density ; (iv) the CR hadron energy of $E_{\mathrm{CR}}/E_{\mathrm{SN}}$ =13% of the SN Ia explosion energy ; (v) $B = 200\ \mu$G for the interior magnetic field strength[5] ; (vi) the ratio of energy in CR electrons to that in CR hadrons is 0.25%, constrained by fitting the synchrotron SED component ; (vii) $q = 2.3$ for the CR electron and proton spectral indices, $dN_{\mathrm{p,e}}/dE \propto E^{-q}$, assumed to be the same and chosen to provide us with a fit in the radio-frequency band (DeLaney et al. 2002; Kothes et al. 2006) ; and (viii) exponential cut-off energies in the

---

[5] As $B > 80\ \mu$G, the value of 200 μG is somewhat arbitrary, but sufficiently high to suppress the IC emission.

CR proton and electron spectra at 100 TeV and 6.5 TeV, respectively. The radio band to X-ray band SEDs are attributed to the synchrotron radiation of a CR electron population, while the 750 MeV to 10 TeV radiation is attributed to gamma-ray emission driven by the collisions of relativistic CR protons with gas. We assumed the fraction of the SN explosion energy converted into the energy of CRs similar to that given by Berezhko et al. (2006). The conditions (iii), (vi), and (viii) are chosen such that the model matches the SEDs of Kepler's and Tycho's SNRs with a hadronic model. We note that the model is sensitive to the combination $E_{\mathrm{CR}}/E_{\mathrm{SN}} \times n$, rather than these two parameters individually.

We show the fits to the broadband SEDs of Kepler's and Tycho's SNRs with a hadronic model described above on the left and right panels in Figure 3.2, respectively. In the framework of this model, the hadronic gamma-ray component dominates over the gamma-ray component produced by CR electrons.

Comparison of the results presented in Figure 3.2 shows that the same hadronic model scaled with a distance to SNRs explains both the SEDs of Kepler's and Tycho's SNRs. This conclusion supports that these remnants, similar in at least SN type and age, have also similar broadband nonthermal emission properties. However, the single SED model can as well as describe the SEDs of Kepler's and Tycho's SNRs even if they are located at 7 kpc and 3.5 kpc, respectively, keeping the same distance ratio as above (that is 2), but increasing the gas density to $(7/5)^2 \times 0.5 = 1.0$ cm^{-3}. The gas density around Kepler's SNR has a strong gradient, with the southeastern part being more tenuous than the northwestern part. Moreover, the gas appears to be clumpy. Hence, gas densities varies from $n \sim 1$–250 cm^{-3} (Williams et al. 2012), and the average gas density is not well constrained.

Since the proposed similarity in gamma-ray emission properties is most natural for these two SNRs, it makes the future gamma-ray observations of Kepler's SNR relevant to further study this unified model. The Cherenkov Telescope Array (CTA ; Acharya et al. 2015), which provides superior sensitivity and angular resolution in comparison to any existing gamma-ray instrument, will most likely lead to a significant detection of Kepler's SNR in the VHE gamma-ray band allowing precise determination of its spectral and morphological characteristics in the VHE gamma-ray band.

In a leptonic scenario, the gamma-ray emission is produced via IC scattering by energetic electrons off photon fields from the cosmic microwave background (CMB), the infrared photon field emitted by dust in SNRs, and the Galactic infrared photon field. To compute the IC gamma-ray component, we included these three photon fields and took energy densities and spectra of the latter two photon fields from Gomez et al. (2012) and Porter et al. (2006). Given that the electron population emitting synchrotron X-ray radiation is the same as that emitting gamma rays via the IC mechanism, it allows us to constrain the magnetic-field strength by requiring that the model reproduces the observed flux of X-ray emission and does not overproduce the H.E.S.S. SED data points. In case the gamma-ray emission is dominated by hadronic

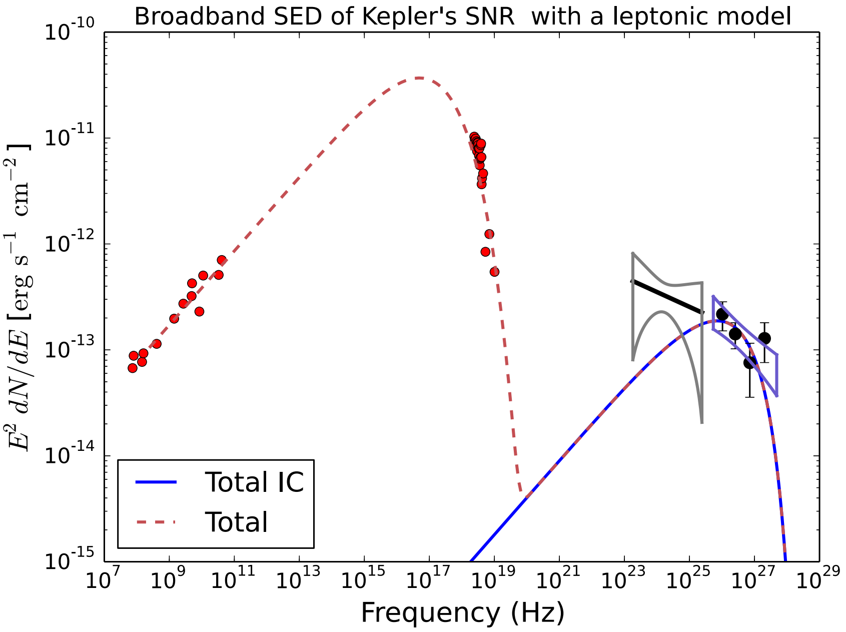

Figure 3.3 – Broadband SED of Kepler's SNR with a leptonic model fit corresponding to the magnetic field of 80 μG.

processes, this constraint should be regarded as a lower limit to the magnetic-field strength. Following the approach by Aharonian et al. (2008c) and considering the gamma-ray observations reported above, we find that for magnetic field values greater than 80 μG the resulting IC flux would be less than the measured gamma-ray flux.

Figure 3.3 illustrates the leptonic model with a magnetic field strength of 80 μG. This magnetic-field strength is somewhat less than the measured downstream magnetic field strength value for Kepler's SNR, which is in the range of 100-200μG (Völk et al. 2005; Helder et al. 2012). The LAT photon index of $\Gamma = 2.12 \pm 0.32$ is softer than that which is expected for the leptonic model, $\Gamma = 1.7$. But in order to better determine which emission model is preferred, we compared the two models using the likelihood ratio test based on the *Fermi*-LAT data with energies between 750 MeV and 300 GeV. The "null" model assumes the emission via IC scattering with a gamma-ray spectrum fit to the H.E.S.S. data, while the alternative model assumes a power-law model with a free flux normalization. The likelihood analysis described in Section 2.2 gives the TS value 5.1 for a comparison of the null and alternative models. Therefore, the leptonic scenario is in 2.3σ tension.

3.4 Conclusions

Gamma-ray observations of young SNRs provide insights into the physical processes of particle acceleration at shock fronts and high-energy photon emission. HE and VHE gamma-ray observations of Tycho's and Cas A SNRs show that remnants younger than 500 years old emit gamma-ray radiation produced likely via the decay of neutral pions created in the proton-proton collisions. Sharing a number of the physical properties with Tycho's SNR, Kepler SNR is an important testbed for models of particle acceleration.

This paper reports the results of 152 hours VHE observations of Kepler's SNR with H.E.S.S. and provides a detailed characterization of the whole data set using advanced analysis methods. Data corresponding to 140 hours, including 122 hours taken with four upgraded 12 m-diameter telescopes in 2017-2020, were accumulated after the previous publication. VHE gamma-ray emission from Kepler's SNR is significant at a 4.6σ statistical level in the entire data set. This paper also includes an analysis of 10.7 years of Fermi-LAT data which provides an indication of the presence of a GeV counterpart of Kepler's SNR. The compatibility of the signals in the HE and VHE gamma-ray bands supports their common origin and association with Kepler's SNR. The SED data are in Figures 3.2 and 3.3.

Although the detection at the 4.6σ level falls short of the gold-standard in the field of VHE gamma-ray astronomy of $> 5\sigma$, our results are based on observations targeting Kepler's SNR directly, and not a blind search. Moreover, Kepler's SNR, being a young SNR and an X-ray synchrotron source, is a priori expected to be a VHE gamma-ray source. These arguments altogether provide a strong reason to endorse Kepler's SNR as a faint HE and VHE gamma-ray source.

The results allow us for the first time to tentatively propose a model of gamma-ray emission describing both the SEDs of Kepler's and Tycho's SNRs. It assumes that both these gamma-ray spectra have a hadronic origin and requires that $\approx 10\%$ of the SN Ia explosion energy to be converted to CR hadron energy and the gas target particle density of 0.5 cm^{-3}. We also derived the lower limit on a magnetic field strength of 80 μG under the assumption that the IC gamma-ray component does not overshoot the H.E.S.S. SED data points.

3.5 Appendix A : SNR G4.8+6.2

The physical properties of SNR G4.8+6.2 are not well known. In the radio band, this SNR has a shell-like morphology and an angular extent of $18'$ at 1.4 GHz (the NRAO VLA Sky Survey). At 2.3 GHz it appears highly polarized with an almost constant orientation of the polarization vectors across the source and with the mean fraction of polarized emission of up to 25% (Duncan et al. 1997). Young SNRs, such as Kepler's SNR, have a much smaller fractional polarization. The excesses coinciding with G4.8+6.2 are present at 3.3σ statistical levels in the H.E.S.S. and *Fermi*-LAT data.

3.6 Appendix B : Tycho's and Kepler's SNRs

In Appendix, we list and compare the observation properties of Tycho's and Kepler's SNRs.

The distances to Tycho's and Kepler's SNRs are estimated to be 2.5 kpc (Zhang et al. 2013; Kozlova & Blinnikov 2018) and 5 kpc (Ruiz-Lapuente 2017), respectively. Their measured forward shock velocities are in excess of ~ 2000 km s^{-1}, see Hwang et al. (e.g., 2002) for Tycho's SNR and Vink (2008b) for Kepler's SNR. The downstream magnetic field strength for these SNRs are in the range of 100-200μG (Völk et al. 2005; Helder et al. 2012). The observed expansion rates of both Tycho's and Kepler's SNRs indicate that these SNRs are still in transition from the early expansion phase to the Sedov phase (Reynoso et al. 1997; Hughes 2000; Vink 2008b). The X-ray spectra of both these SNRs with the presence of large amounts of iron (e.g., Hwang et al. 1998; Kinugasa & Tsunemi 1999) show that they are almost certainly of type Ia and their classification is proven by the spectrum of a scattered-light echo from Tycho's SN (Krause et al. 2008; Rest et al. 2008) and supported by the location of Kepler SNR well above the Galactic plane, respectively. Tycho's SNR located at a Galactic latitude of $1\overset{\circ}{.}4$ was considered to be a sufficiently isolated Type Ia SNR (Tian & Leahy 2011), probably interacting with a semi-closed large molecular shell surrounding the SNR from the north to the east (Ishihara et al. 2010; Zhang et al. 2013), while Kepler's SNR located in a lower density medium has a density gradient with densities in the north greater by an order of magnitude than those in the south (Williams et al. 2012). The single-degenerate binary origin for both Tycho's and Kepler's SNe is supported by the detection of Tycho-G that is the possible companion star surviving the event of Tycho SN (Ruiz-Lapuente et al. 2004; Bedin et al. 2014) and by the presence of a disk-shaped structure near the center of the Kepler SNR possibly created by the collision between SN debris and material expelled by the giant star before the explosion (Burkey et al. 2013c), respectively. The delayed-detonation model for Type Ia SNe (Khokhlov 1991) is the most probable explosion mechanism for both Tycho's and Kepler's SNe (e.g., Badenes et al. 2003; Sun & Chen 2019), resulting in the explosion energy of $E_{\rm SN} = (1.3-1.6)\times 10^{51}$ erg (Gamezo et al. 2005).

4

Upper Limits on Very-High-Energy Gamma-ray Emission from Core-Collapse Supernovae Observed with H.E.S.S.

H.E.S.S. Collaboration.
Corresponding authors : R.Simoni, N.Maxted, M.Renaud & J.Vink.

Astronomy & Astrophysics 2019, 626, A57

Abstract

Young core-collapse supernovae with dense-wind progenitors may be able to accelerate cosmic-ray hadrons beyond the knee of the cosmic-ray spectrum, and this may result in measurable gamma-ray emission. We searched for gamma-ray emission from ten supernovae observed with the High Energy Stereoscopic System (H.E.S.S.) within a year of the supernova event. Nine supernovae were observed serendipitously in the H.E.S.S. data collected between December 2003 and December 2014, with exposure times ranging from 1.4 hours to 53 hours. In addition we observed SN 2016adj as a target of opportunity in February 2016 for 13 hours. No significant gamma-ray emission has been detected for any of the objects, and upper limits on the > 1 TeV gamma-ray flux of the order of $\sim 10^{-13}\,\mathrm{cm^{-2}s^{-1}}$ are established, corresponding to upper limits on the luminosities in the range $\sim 2 \times 10^{39}$ $\mathrm{erg\,s^{-1}}$ to $\sim 1 \times 10^{42}$ $\mathrm{erg\,s^{-1}}$. These values are used to place model-dependent constraints on the mass-loss rates of the progenitor stars, implying upper limits between $\sim 2 \times 10^{-5}$ and $\sim 2 \times 10^{-3}\,\mathrm{M_\odot\,yr^{-1}}$ under reasonable assumptions on the particle acceleration parameters.

4.1 Introduction

Despite more than a century of cosmic-ray (CR) studies, the origin of CRs [1] is still not clear. The bulk of CRs detected at Earth or in space are of Galactic origin, at least for protons up to energies of 3×10^{15} eV (e.g. Ginzburg & Syrovatskii 1964; Strong et al. 2007). Galactic CR sources can only be identified indirectly through the electromagnetic and neutrino emission caused by interactions of CRs with local gas and radiation within their sources of origin. In this respect, gamma-ray observations have proven to be an invaluable tool, as gamma-ray emission is uniquely associated with the presence of highly energetic CR particles. Gamma rays can be detected with sufficient statistics using gamma-ray observatories, either onboard satellites such as NASA's *Fermi* Large Area Telescope (LAT) in the high-energy gamma-ray domain (HE, $0.1 <$ E < 100 GeV), or ground-based Cherenkov telescopes, such as H.E.S.S., VERITAS, MAGIC and HAWC in the very high-energy gamma-ray domain (VHE, i.e. E $\gtrsim 50$ GeV).

These instruments show that the prime candidate sources for Galactic CRs, supernova remnants (SNRs), are indeed gamma-ray sources. Young SNRs, i.e. those SNRs that are a few hundred to a few thousand years of age, emit TeV gamma rays at various stages during their evolution (Hewitt & Lemoine-Goumard 2015). However, there is an ongoing debate as to whether the emission is the result of hadronic CRs interacting with ambient gas or leptonic interactions, usually inverse Compton scattering of ambient photons by relativistic electrons. For some older remnants interacting with dense gas, the gamma-ray emission is clearly associated with hadronic CRs : the gamma-ray spectrum below GeV energies shows the predicted spectral feature of hadronic gamma-ray emission, usually referred to as the "pion bump" (Giuliani et al. 2011; Ackermann et al. 2013). However, there is currently no observational evidence that SNRs contain CR hadrons with energies around 10^{15} eV (=1 PeV) or above, even for the youngest Galactic SNRs such as Cas A (Ahnen et al. 2017). This is somewhat at odds with the fact that Galactic CR hadrons need to be accelerated up to energies of at least 3×10^{15} eV to explain the knee of the CR spectrum.

The energy per supernova (SN) coupled with the Galactic SN rate provides enough power to sustain the CR energy density in the Galaxy (Strong et al. 2004). Moreover, it has been suggested that, for supernova remnants evolving in the winds of their progenitors, the maximum CR energy is reached in the early phase of the SNR development, within days to months after the SN event and not at the time the SNR is several hundred to thousand years old (e.g. Voelk & Biermann 1988; Cardillo et al. 2015; Marcowith et al. 2018). The highest energy CR hadrons are then possibly accelerated in this early phase, at least for a subset of SNe (Bell et al. 2013; Zira-

---

[1] In the manuscript, CR refers to cosmic-ray hadrons, nuclei and electrons when not otherwise specified.

kashvili & Ptuskin 2016). At this early stage, less time is available for acceleration, and the shock surface area is much smaller. Only SNe exploding into sufficiently large circumstellar densities can accelerate sufficient numbers of CR proton up to energies of, or exceeding PeV energies : the number of CR hadrons being accelerated at a given time depends on the local density n by the relation $\dot{N}_{\rm CR} \propto n R_{\rm sh}^2 V_{\rm sh}$, where $R_{\rm sh}$ is the shock radius and $V_{\rm sh}$ is the shock velocity. Furthermore, the maximum energy that can be reached at given time is dependant on the magnetic field and the turbulence as shown by the following relation (e.g. Helder et al. 2012) :

$$\begin{aligned} t &= \eta_{\rm acc}\eta_{\rm g}\frac{cE}{3eBV_{\rm sh}^2} \\ &\approx 1.0\times 10^4 \left(\frac{\eta_{\rm g}\eta_{\rm acc}}{30}\right)\left(\frac{V_{\rm sh}}{10,000~{\rm km\,s^{-1}}}\right)^{-2}\left(\frac{B}{10~{\rm G}}\right)^{-1}\left(\frac{E}{100~{\rm TeV}}\right)~, \end{aligned}$$

with $V_{\rm sh}$ the shock velocity, B is the magnetic field strength, t is the time available for acceleration in seconds, $\eta_{\rm g}$ indicates the ratio of mean free path of the particles and their gyroradius ($\eta_{\rm g} \approx 1$, for a very turbulent magnetic field) and $\eta_{\rm acc} = 8-20$ takes into account the difference in occupancy time of particles upstream and downstream of the shock. This equation shows that in order to reach energies of 100 TeV, typically an acceleration time shorter than a day is sufficient, and for reaching the CR knee at 3×10^{15} eV, an acceleration time of days to weeks is needed provided that the magnetic fields are > 1 G, instead of the $10-100$ μG measured in young SNRs. More detailed calculations that also take into account the expected evolution of the magnetic field strength and escape of the highest energy particles confirm these time scales, see Tatischeff (2009); Marcowith et al. (2018).

Core-collapse (cc-)SNe originating from stellar progenitors with dense winds can fulfil the right conditions for CR acceleration, provided that the shocks are collisionless (Katz et al. 2011; Murase et al. 2011; Bell et al. 2013). First of all, the number density of a stellar wind scales as a function of radius, $n \propto \dot{M} u_{\rm w}^{-1} r^{-2}$ (where $\dot{M}$ is the mass-loss rate and $u_{\rm w}$ is the wind velocity), resulting in a circumstellar medium (CSM) density that is much higher than in the interstellar medium (ISM). As a result the cosmic-ray acceleration rate does not directly depend on the shock radius, but scales as $\dot{N}_{\rm CR} \propto \dot{M} u_{\rm w}^{-1} V_{\rm sh}$. Secondly, the magnetic fields around the shock can be amplified early on to values orders of magnitude larger than in the ISM, by the growth of CR streaming instabilities (Bell 2004). Once CR acceleration begins, it has been argued that magnetic field strengths may be amplified scaling as $B^2 \propto n V_{\rm sh}^2$ (e.g. see Völk et al. 2005; Bell et al. 2013) or even $B^2 \propto n V_{\rm sh}^3$ (Vink 2012; Bell 2004), with shock velocities as fast as 20,000 km s^{-1}. SNe arising from progenitors that exhibit these high-density stellar winds are of type IIP, IIL, IIb, and IIn (see the review in Chevalier & Fransson 2016). Type IIn SNe, in particular, have been observed to eject a considerable mass prior to the explosion (Smith et al. 2008; Ofek et al. 2014; Murase et al. 2014).

Evidence for particle acceleration in cc-SNe is provided by their bright, self-absorbed synchrotron emission at radio wavelengths. These radio observations indicate the presence of relativistic electrons accelerated by strong magnetic fields, and it is thought that relativistic protons and atomic nuclei are present. One prime example is the young type IIb SN 1993J, for which a strong magnetic field, 1-100 G, and shock speeds as high as 20,000 km s^{-1} have been estimated by Fransson & Björnsson (1998) and Tatischeff (2009). Given these estimates and time scales for acceleration to PeV energies, there are good reasons to think that SN 1993J-like SNe can accelerate CR hadrons up to PeV energies within days to a few weeks (see Marcowith et al. 2018, and references therein). However, gamma-ray emission from SNe has not been detected so far, and upper-limits in the GeV domain have been established for type IIn SNe (Ackermann et al. 2015), and superluminous SN candidates (Renault-Tinacci et al. 2018). The possibility of CR acceleration in young SNe motivates the search for signatures of TeV gamma-ray emission. Such a detection could be indicative of pion production (and subsequent decay) arising from acceleration of CR protons and nuclei beyond TeV energies. We analysed H.E.S.S. observations towards nine serendipitously observed cc-SN events and towards the nearby event SN 2016adj, which triggered Target of Opportunity (ToO) observations. The data selection and analysis details are presented in Section 4.2.2. Upper limits on gamma-ray flux from the direction of the CR source candidates are shown in Section 4.2.4 before constraints on the local environment of these SNe are derived in Section 4.3.

4.2 Observations and data analysis

4.2.1 H.E.S.S. observations

H.E.S.S., the High Energy Stereoscopic System, is an array of five imaging atmospheric Cherenkov telescopes (IACTs) located in the Khomas Highland of Namibia at an altitude of 1800 m above sea level. Four 12 m-diameter telescopes (CT1-4) have been operating from December 2003 and a fifth telescope of 28 m-diameter (CT5) became operational in September 2012. In the analysis, the data of at least three telescopes (including CT5 for SN 2016adj) have been utilised. These analysis settings correspond to a field of view of 5°, an angular resolution (68% containment radius) of ∼0.1°, energy threshold values spanning ∼200 GeV to ∼400 GeV and an energy resolution of ∼15%, (Aharonian et al. 2006b). Nine SNe in our sample were in the field of view of other H.E.S.S.-scheduled targets, with a maximal offset of 2.5° from the center of the field of view : the candidate selection is described in Section 4.2.2. The nearby event SN 2016adj (see Section 4.2.2) triggered dedicated observations a few days after the discovery date, in standard wobble mode observations (Aharonian et al. 2006b) with a source offset of ∼0.5°.

Table 4.1 – The list of SN positions tested for H.E.S.S. gamma-ray excess emission. The list was compiled using a system of cuts described in Section 4.2.2. The name, host galaxy, coordinates, estimated distance, SN type and discovery date are given for each SN.

SN Name	Host galaxy	RA [J2000]	DEC [J2000]	Dist. [Mpc]	Type	Disc. date
SN 2004cx	NGC 7755	23h47m52.86s	$-30^\circ 31' 32.6''$	26 ± 5	II	2004-06-26
SN 2005dn	NGC 6861	20h11m11.73s	$-48^\circ 16' 35.5''$	38.4 ± 2.7	II	2005-08-27
SN 2008bk	NGC 7793	23h57m50.42s	$-32^\circ 33' 21.5''$	4.0 ± 0.4	IIP	2008-03-25
SN 2008bp	NGC 3095	10h00m01.57s	$-31^\circ 33' 21.8''$	29 ± 6	IIP	2008-04-02
SN 2008ho	NGC 922	02h25m04.00s	$-24^\circ 48' 02.4''$	41.5 ± 2.9	IIP	2008-11-26
SN 2009hf	NGC 175	00h37m21.79s	$-19^\circ 56' 42.2''$	53.9 ± 3.8	IIP	2009-07-09
SN 2009js	NGC 918	02h25m48.28s	$+18^\circ 29' 25.8\ ''$	16 ± 3	IIP	2009-10-11
SN 2011ja	NGC 4945	13h05m11.12s	$-49^\circ 31' 27.0''$	5.28 ± 0.38	IIP	2011-12-18
SN 2012cc	NGC 4419	12h26m56.81s	$+15^\circ 02' 45.5''$	16.5 ± 1.1	II	2012-04-29
SN 2016adj	NGC 5128	13h25m24.11s	$-43^\circ 00' 57.5''$	3.8 ± 0.1	IIb	2016-02-08

4.2.2 Supernova Selection

Serendipitous sample

The online IAU[2] Central Bureau of Astronomical Telegrams (CBAT) supernova catalogue[3] was used to compile an initial, extensive list of SN candidates.
The NASA/IPAC[4] Extragalactic Database (NED)[5] was then queried for the redshift of each SN host galaxy to compile a short-list of SNe with redshift $z < 0.01$ to ensure that only nearby SNe were considered. If a host galaxy was not stated for a given SN in the CBAT SN catalogue, the SN was discarded from the short-list. The H.E.S.S. database was then queried for observations in the direction of each short-listed SN, within a time range spanning seven days prior to a year after, the SN discovery date. This time range was chosen to account for likely delays between the dates of the discovery and the outburst to be sure to include the peak energy suggested to occur a few days (Marcowith et al. 2014) after the SN event, but potentially lasting months. After reaching this peak emission, the gamma-ray flux is predicted to decline proportionally to $1/t$, as we will discuss later. All H.E.S.S. data taken from December 2003 until the 31st of December 2014 were searched, and all SNe presented on CBAT on the 30th of March 2015 were considered. We removed type Ia and Ic SNe from our sample, because these types are unlikely to occur in a CSM density large enough to accelerate CRs up to TeV energies (see e.g. Smith 2014).

---

[2] International Astronomical Union

[3] www.cbat.eps.harvard.edu/lists/Supernovae.html

[4] Infrared Processing & Analysis Center

[5] ned.ipac.caltech.edu/forms/z.html

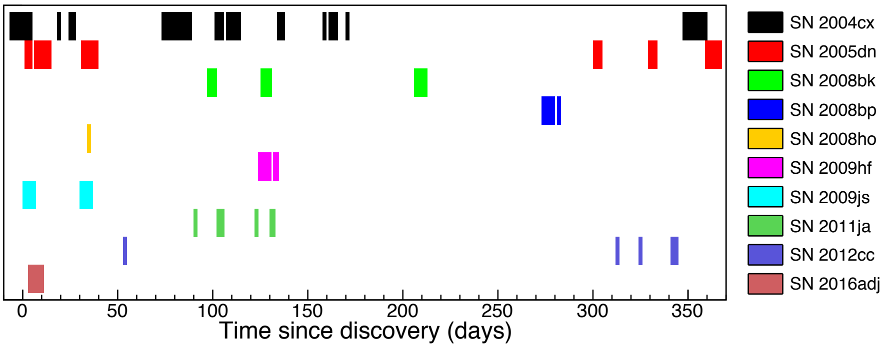

Figure 4.1 – A graphic displaying the H.E.S.S. observation windows for each SN selected for analysis. Time = 0 corresponds to the SN discovery date reported in literature.

SN 2016adj

SN 2016 adj was discovered on the 8th of February in the BOSS Survey [6] (Marples et al. 2016). It appeared in the Centaurus A (Cen A, NGC 5128) galaxy, a few arcminutes from its nucleus, at a distance of ∼3.8 ± 0.1 Mpc (Harris 2010, and references therein). The SN type was soon suggested to be of type IIb by Stritzinger et al. (2016), because of the presence of a Hα line, and later confirmed by Thomas et al. (2016). The proximity and the type of the SN made it a unique and rare event for triggering VHE gamma-ray observations : the last type IIb SN occurring at a similar distance was SN 1993J, and such a nearby cc-SN could be detected at TeV gamma rays with current IACTs as predicted by Marcowith et al. (2014). Cen A itself was detected by H.E.S.S. after a deep observation campaign (Aharonian et al. 2009). Cen A is quite faint at TeV energies and the exposure time of a few hours considered here for SN 2016adj is too short to detect emission from the galaxy itself.
Table 4.1 lists the ten observed SNe along with their corresponding host galaxies, coordinates, distances (ranging between ∼4 and 54 Mpc), types and discovery dates.

4.2.3 Data Analysis

Standard quality cuts were applied to remove bad-quality data from each data set : observation runs with a minimum of three telescopes, a fraction of broken pixels < 10 % and trigger-rate fluctuations < 30 % were kept (see Aharonian et al. 2006b). Then, for each target, the selected data were analysed using the Model analysis framework outlined in de Naurois & Rolland (2009). For a given SN, an ON-region is selected centred on the SN position, and multiple OFF regions are selected at the same offset

---

[6] http ://bosssupernova.com/

as the ON region, using the Reflected Background method (Berge et al. 2007). The ON region radius is 0.1 deg for the serendipitous sample and 0.08 deg for SN 2016adj. Results were confirmed by an independent calibration and analysis chain using the ImPACT framework (Parsons & Hinton 2014) with standard quality cuts and the same Reflected Background method. For each 28-minute observation run which passed the above-mentioned criteria, the gamma-ray excess was computed using $\mathrm{N_{excess}} = \mathrm{N_{on}} - \alpha \mathrm{N_{off}}$, with α being the ratio of the solid angles of on and off regions. The statistical significance for each dataset was established using equation 17 of Li & Ma (1983).

4.2.4 Results

No significant excess is observed for any of the SNe and flux upper limits (ULs) have been derived at the 95% confidence level under the assumption of a power law spectrum ($\mathrm{dN/dE} \propto \mathrm{E}^{-\Gamma}$) with index $\Gamma = 2$. ULs have been computed using a loglikelihood approach as described in De Naurois (2012).

In Table 4.3 we report the relevant statistics of the gamma-ray observations as described in Section 4.2.3. The total livetime, and the observational coverages expressed in days since the SN discovery date are also presented. Given the serendipitous nature of most of the observations, the livetime varies between ~1 and ~50 hours, and the time delay of the first observation since the SN discovery differs between the SNe : for four objects (including SN 2016adj), H.E.S.S. observations started around, or a few days after, the discovery date, while for the other SNe, observations began much later (up to 272 days after the discovery for SN 2008bp). The observational coverage in days after the discovery date are reported in Table 4.3 and the data set for each SN is represented in Figure 4.1.The average time delays, weighted by the exposure of individual observation periods (as represented on Figure 4.1), are also reported in Table 4.3. SN 2016adj was observed every night from day 3 till day 10 after the discovery date, and the average time delay amounts to ~7 days.

In Table 4.2, ULs on the integrated flux above the energy threshold and above 1 TeV are presented. The value of 1 TeV corresponds to the optimal H.E.S.S. sensitivity : it is chosen to compare all results, as the energy threshold depends on observational conditions and varies as indicated in the table. For four SNe (2004cx, 2008bk, 2008bp, 2009js) these ULs supersede previous preliminary results (Lennarz & the H.E.S.S. Collaboration 2013), confirming the non-detections with better sensitivity. In column five of Table 4.2, ULs on the luminosities are presented for each object : these ULs are computed above the energy threshold and above 1 TeV, using the distance to the host galaxy (see Table 4.1). Errors on the distances are not taken into account. The luminosity values above the energy threshold span a range from ~2 $\times 10^{39}$ $\mathrm{erg\,s^{-1}}$ to ~1 $\times$ 10^{42} $\mathrm{erg\,s^{-1}}$. This range is mainly due to the differences in the source distances and to the offset angle with respect to the observation position, observations with large off-center angles having a reduced detection sensitivity. Note that these ULs correspond to a gamma-ray fluence within a year of ∼6 × 10^{46} erg to ∼3 × 10^{49} erg, corresponding to 0.006 - 3 percent of the canonical SN explosion energy of 10^{51} erg. We carefully checked that no significant gamma-ray peak occurred during the duration of the observations. As an example, Figure 4.2 shows the time evolution of the flux above 1 TeV for SN 2016adj, consistent with zero during the observing period. This is the case for all the other SNe (see in Appendix 4.5). The lightcurves presented are binned on a nightly basis and we also checked that no significant emission occurred on a weekly basis for any of the objects. Error bars correspond to 68% confidence levels. This confirms that no significant TeV emission is found towards any of the SNe within one year of the initial explosion.

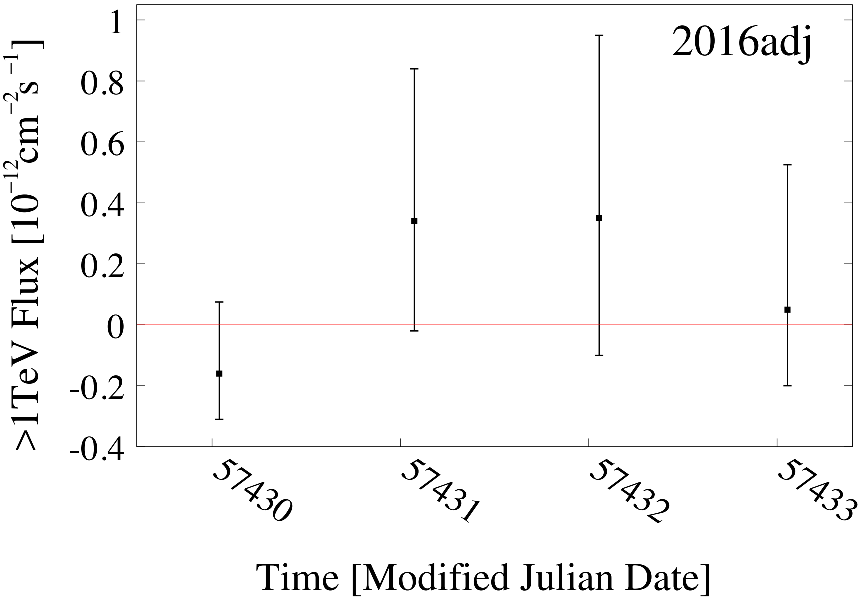

FIGURE 4.2 – Light curve of SN 2016adj. Data points are binned on a nightly basis, the red solid line indicates the zero level.

4.3 Discussion

The serendipitous nature of the observations provided us with a sample with a large diversity in distances, post-explosion delay times and observing conditions. This has to be kept in mind when interpreting the non-detection of TeV emission from these

SNe	E_{Th}	Flux UL	Flux UL	UL on L	UL on L	ULs on $\dot{M}/u_{\mathrm{w}}$	
		$(> E_{\mathrm{Th}})$	$(> 1\mathrm{TeV})$	$(> E_{\mathrm{Th}})$	$(> 1\mathrm{TeV})$	Average time	Fit
	(TeV)	$(10^{-13}\,\mathrm{cm}^{-2}\mathrm{s}^{-1})$		$(10^{40}\ \mathrm{erg\,s}^{-1})$		$(10^{-5}\ \mathrm{M}_{\odot}\ \mathrm{yr}^{-1}\ \mathrm{km}^{-1}\ \mathrm{s})$	
SN 2004cx	0.18	10	1.9	13.0	2.5	6.7	3.2
SN 2005dn	0.21	2.2	0.41	6.2	1.2	3.8	0.26
SN 2008bk	0.21	6.0	4.8	0.18	0.15	1.4	0.4
SN 2008bp	0.21	29	5.5	46.7	8.9	15.9	12.3
SN 2008ho	0.33	16	7.7	52.8	25.4	9.4	5.3
SN 2009hf	0.21	20	5.3	111	29.5	19.9	15.9
SN 2009js	0.63	15	11	7.3	5.4	3.1	0.9
SN 2011ja	0.21	20	5.2	1.1	0.28	1.77	1.6
SN 2012cc	0.72	15	10	11.5	7.7	11.6	3.7
SN 2016adj	0.196	8.8	1.7	0.24	0.05	0.25	0.20

Table 4.2 – Upper limits (ULs) on the integrated flux above the energy threshold and above 1 TeV. These ULs are computed assuming 95% confidence level and a power-law index of 2. The associated ULs on the luminosities are computed using the distances reported in Table 4.1. Upper limits on $\dot{M}/u_{\mathrm{w}}$ are derived from methods using the average time and a fit on the LCs, both using equation 4.3 (see text).

SNe. For instance, two nearby SNe (SN 2008bk, SN 2011ja) have been observed around 100 days after the discovery and we might have missed the periods of maximum TeV emission. By contrast, early and relatively deep observations towards SN 2004cx and SN 2005dn have been performed, but these two SNe are beyond 20 Mpc in distance, and this may explain their non-detection. For SN 2016adj, as already mentioned, the candidate was very promising in terms of distance and time delay, although the duration of observations was not as long as initially planned due to bad weather conditions. Despite the diversity in the observed sample, these H.E.S.S. observations can be used to derive constraints on a key parameter impacting the SN gamma-ray luminosity, namely the mass-loss rate of the progenitor star, which determines the CSM density.

The sample consists mostly of type IIP SNe, the most commonly observed type of cc-SNe, for which the progenitor is a cool red supergiant (RSG) star, like the progenitor found for SN 2003gd (Smartt et al. 2004). Several type IIP SNe show evidence for interaction with dense environments in the form of non-thermal radio emission and X-ray emission (e.g. Chevalier 1982; Pooley et al. 2002). These progenitors are believed to have mass-loss rates of typically $10^{-6} - 10^{-4}\ \mathrm{M}_{\odot}\ \mathrm{yr}^{-1}$. However, some progenitors appear to exhibit mass-loss rates as high as $10^{-4} - 10^{-3}\ \mathrm{M}_{\odot}\ \mathrm{yr}^{-1}$ (Smith 2014). When combined with the relatively slow RSG winds (Chevalier & Fransson 2016), these mass-loss rates may lead to the right circumstances in terms of density for particle acceleration to proceed up to very high energies and for gamma-ray emission to be potentially detectable (e.g. Moriya et al. 2011; Marcowith et al. 2014). Moreover, there is accumulating evidence of enhanced mass-loss rates from progenitors in the last years prior to explosion (e.g. Fuller 2017), which may similarly lead to enhanced CR proton acceleration and gamma-ray emission.

For type IIb SNe, like SN 2016adj, the mass-loss rate is predicted to be typically over 10^{-5} $\mathrm{M}_{\odot}$ yr^{-1} for a wind velocity of $u_{\mathrm{w}} \simeq 10$ km s^{-1}, as estimated for SN 1993J (Tatischeff 2009). However, there is evidence for a sub-type of type IIb SNe depending on the compactness of the progenitor. A more compact, less luminous progenitor with a lower H mass envelope and a high-speed wind, would produce a lower density environment (Chevalier & Soderberg 2010). We will refer to this type of SNe as compact type IIb. Below we will discuss the implications of the obtained H.E.S.S. ULs in terms of the mass-loss rates of the ten observed SNe.

4.3.1 Modelling

To place our flux upper limits into the context of the SN environment, we use a semi-analytical model for cc-SNe described in Dwarkadas (2013). The author predicts a gamma-ray flux of hadronic origin from SNe and young SNRs based on the hydrodynamical evolution described in Chevalier (1982a) and Chevalier & Fransson (1994), and the gamma-ray emissivity formula prescribed by Drury et al. (1994). The model assumes a constant stellar mass-loss rate and wind velocity, usually known as the steady wind scenario (Chevalier 1982a). Under this assumption, the CSM density is given by the continuity of mass equation : $\rho_{\mathrm{amb}} = \dot{M}/4\pi u_{\mathrm{w}} r^{-2}$, which shows that a combination of a high mass-loss rate and a low wind velocity will lead to a high-density CSM. Low wind speeds of ∼10 km s^{-1} are commonly realised in RSG progenitors (e.g. Smith et al. 2009).

For cc-SNe, the model of Dwarkadas (2013) gives the following relation of the expected gamma-ray flux as a function of stellar mass-loss parameters, SN explosion characteristics and time, t, since the explosion :

$$F_{\gamma}(>E_0,\mathrm{t}) = \frac{3q_{\alpha}\xi(\kappa C_1)m^3}{32\pi^2(3m-2)\beta\mu m_{\mathrm{p}}d^2}\left[\frac{\dot{M}}{u_{\mathrm{w}}}\right]^2 t^{m-2}. \tag{4.1}$$

This equation is valid as long as the maximum photon energy $\mathrm{E}_{ph,max}$ (related to the maximum energy of accelerated particles E_{max}) is significantly higher than E_0. As shown by Marcowith et al. (2018), in the case of cc SNe evolving in their dense wind progenitor such as SN 1993J, E_{max} conservatively remains above ∼0.5 PeV (i.e. $\mathrm{E}_{ph,max} \gtrsim 30$ TeV) during the first year after the SN, so that equation 4.1 can be used as is. The variable t is the elapsed time in days since the SN explosion, and the variable d is the distance in Mpc as given in Table 4.1. The variable q_{α} is the gamma-ray emissivity normalised to the hadronic CR energy density, for which values are tabulated in Drury et al. (1994). We use $q_{\alpha}(\geq 1\mathrm{TeV}) = 1.02 \times 10^{-17}$ s^{-1} erg^{-1}

cm^3 (H-atom) $^{-1}$, which corresponds to a gamma-ray spectral index of 2, adopting the value assumed for SN 1993J in Tatischeff (2009). This study clearly shows that the sub shock and total compression ratios both are close to 4, meaning the shock remains weakly modified throughout the SN 1993J time evolution. The potential systematic error introduced by this assumption can be quantified by considering the extreme case of a steep spectral index of 2.4. In such a case, the gamma-ray emissivity would become $q_\alpha(\geq 1\text{TeV}) = 8.1 \times 10^{-19}$ s^{-1} erg^{-1} cm^3 (H-atom) $^{-1}$. This would lower the flux values obtained in equation 4.1 by a factor of ~12. The parameter ξ is the fraction of the shock energy flux that is converted into CR proton energy, and β is the fraction of the total volume, $\mathcal{V}$, that is already shocked and where the density of target protons is high ($\mathcal{V}_{\text{shocked}} = \beta 4\pi R_{\text{sh}}^3/3$). m_{p} is the proton mass, and μ the mean molecular weight of the nuclear targets in the CSM. We set ξ equal to 0.1, β to 0.5 and $\mu = 1.4$ following the parameters chosen for cc-SNe in Dwarkadas (2013). Finally, the parameter κ is the ratio of the forward shock (FS) radius to the contact discontinuity (CD) radius. C_1 is a constant that can be expressed in terms of the geometry of the explosion, as the radius of the FS is defined as $R_{\text{sh}} = \kappa R_{\text{CD}} = \kappa C_1 t^m$.

For this study, we substitute κC_1 with $V_{\text{sh}}/(m\, t^{m-1})$ where V_{sh} is the shock velocity and m is the expansion parameter, leading to the following relation :

$$F_\gamma(E_0, t) = \frac{3 q_\alpha \xi (V_{\text{sh}}) m^2}{32\pi^2 (3m-2)\beta\mu m_{\text{p}}} \left[\frac{\dot{M}}{u_{\text{w}}}\right]^2 \left(\frac{1}{d^2}\right)\left(\frac{1}{t}\right). \tag{4.2}$$

According to the model of Chevalier (1982) for a steady wind scenario, m can be expressed as $m = (n-3)/(n-2)$, where n is the index of the ejecta density profile ($\rho_{\text{ej}} \propto r^{-n}$). For n, Chevalier (1982) has found values between 7 and 12, implying that m lies between 0.8 and 0.9, in agreement with observations of some radio SNe (e.g. Weiler 2006). We adopt here $m = 0.85$, and a shock velocity $V_{\text{sh}} = 10{,}000\,\text{km}\,\text{s}^{-1}$ as fiducial parameters. The dependence on $1/t$ breaks down for $t \to 0$, but particle acceleration does not immediately start at $t = 0$, as the shock first needs to break out of the star, and some time (days-weeks, depending on the B-field value and the turbulence) should be allowed for the particles to be accelerated to high enough energies to produce VHE gamma rays. Note also that $t = 0$ should refer to the time of core collapse, whereas in our analysis we had to use the time of SN detection, which could be several hours or even days after the actual explosion time. Note that within the first week after core collapse the SN may be so bright in the optical band that the gamma-ray emission is strongly attenuated by gamma-gamma interactions, as explained in Section 4.3.3.

Our ULs on the gamma-ray flux above 1 TeV given in Table 4.2 can be converted into an upper value for $\dot{M}/u_{\text{w}}$ by inverting equation 4.2, replacing the constant parameters by their respective values and expressing the mass-loss rate such that $\dot{M} =$

$10^{-5}\ \dot{M}_{-5}\ \mathrm{M}_{\odot}\ \mathrm{yr}^{-1}$ and the wind velocity $u_{\mathrm{w}} = 10\ u_{\mathrm{w},10}\ \mathrm{km\,s^{-1}}$:

$$\left[\frac{\dot{M}_{-5}}{u_{\mathrm{w},10}}\right]^2 \leq \frac{F_{\gamma}(>1\mathrm{TeV})\, d_{\mathrm{Mpc}}^2\, t_{\mathrm{day}}}{5.14\times 10^{-12}}. \tag{4.3}$$

The numerical value of $5.14\times\ 10^{-12}$ is of the same order as that derived in Tatischeff (2009) for SN 1993J (within a factor $\lesssim 2$), and comparable to that obtained by Murase et al. (2014) with the same parameters, within a factor $\lesssim 4$.

To establish the ULs on $\dot{M}/u_{\mathrm{w}}$, we use two methods : the first one simply consists in substituting the variable t by the exposure-weighted average time reported in Table 4.3. A second method consists in fitting with equation 4.3 the nightly binned flux points (cf. Figures 4.2 and 4.5) with their respective dates expressed relatively to the discovery date. For this method, we set the fitting function given in equation 4.3 to zero at t $<$ 5 days, in order to account for the possibly strong gamma-ray attenuation through gamma-gamma interactions during the early stages of the SN evolution (see Section 4.3.3). The goodness of the fit is estimated by a χ^2 test. Fitting the lightcurves in order to constrain the mass-loss parameter is very sensitive to the gamma-ray flux immediately following the SN explosion, whereas using the exposure-weighted time t is more sensitive to the average measured flux. Results and methods are discussed in the next Section.

4.3.2 Derived upper limits on the wind properties

Upper limits representing a 2σ level of the $\dot{M}/u_{\mathrm{w}}$ ratio, derived from the two methods described in the previous Section, are given in Table 4.2. The constraints on $\dot{M}$, assuming $u_{\mathrm{w}} = 10\ \mathrm{km\,s^{-1}}$, are shown in Figure 4.3.

In general, more constraining ULs are obtained through the fit to the lightcurves, as compared to the method using the time-average flux limits : this is the case for SN 2004cx, and SN 2005dn, for which fluxes are determined shortly after the SN explosion dates, as well as as observation spanning the whole year. For 2005dn, the value obtained with the fit method seem to favor the first sets of flux points mostly negatives with small errors, compared to late observations taken after a gap which are showing more positive values. The same case seems to happen for SN 2008bk, for which observations were all taken ~ 100 days after the discovery but are spanning over several months. For SNe observed only during a short time span, like SN 2009hf, SN 2011ja and SN 2016adj, the two methods give similar ULs, as expected. The method using a fit to equation 4.3 gives more weight to the early observations, as this is where the highest fluxes are expected and relies on the assumption that the gamma-ray flux evolution follows exactly the $1/t$ scaling. In reality, the progenitor mass loss history may be more complicated, and there is also some uncertainty regarding the onset of particle acceleration and the effect of gamma-gamma attenuation. As such, the time-average flux method gives perhaps a less precise but more conservative constraints on $\dot{M}/u_{\mathrm{w}}$.

For the nine SNe of the serendipitous sample, both methods give ULs lying between $\sim 2.0 \times 10^{-5}$ $\mathrm{M_\odot}$ $\mathrm{yr^{-1}}$ and $\sim 2.0 \times 10^{-3}$ $\mathrm{M_\odot}$ $\mathrm{yr^{-1}}$, and are consistent with predictions for type IIP SNe with a RSG progenitor having a mass-loss rate in the range $10^{-6} - 10^{-4}$ $\mathrm{M_\odot}$ $\mathrm{yr^{-1}}$. These constraints show large values in $\dot{M}/u_{\mathrm{w}}$, but still within the range of expected mass-loss rates for some RSGs.

For SN 2016adj, the mass-loss rate UL, confirmed by both methods, is reaching $\sim 2.5 \times 10^{-5}$ $\mathrm{M_\odot}$ $\mathrm{yr^{-1}}$, as the SN occurred in the nearby Cen A galaxy and has been observed very early : it is of the same order as the value estimated for the well-studied SN 1993J ($\dot{\mathrm{M}} = 3.5 \times 10^{-5}$ $\mathrm{M_\odot}$ $\mathrm{yr^{-1}}$ for $u_w = 10$ $\mathrm{km\,s^{-1}}$, Tatischeff 2009), both SNe being of Type IIb occurring at similar distances. We note that the expansion parameter of SN 1993J near the time of discovery is estimated to be high, $m = 0.919 \pm 0.09$, as implied by early radio observations (Bartel et al. 2002). Apart from this difference, given that the TeV gamma-ray flux from SN 1993J was predicted to be at the level of sensitivity of current IACTs (Marcowith et al. 2014), TeV emission from SN 2016adj could have been detected with H.E.S.S. if it were to share the same environmental properties as SN 1993J.

4.3.3 Opacity due to gamma-gamma absorption.

At short timescales after the explosion, when the SN is near maximum optical peak luminosity, the VHE gamma-ray emission may be suppressed due to electron-positron pair-production, arising from the interaction of TeV photons with low-energy photons from the SN photosphere. This gamma-gamma absorption critically depends on the photosphere properties of each object, and no complete model exists so far. First attempt to quantify this effect in SN 1993J has been carried out by Tatischeff (2009) under the assumption of isotropic interactions with photospheric photons. More recently, preliminary calculations of this time-dependent absorption accounting for the geometrical effects have been performed by Marcowith et al. (2014) in the case of SN 1993J for which the parameters of the SN hydrodynamical evolution and photosphere are well known. While the absorption is expected to be very large during the first week, the attenuation amounts to a factor of a few at t $\sim$ 10-20 days before gradually decreasing at the level of $\sim$ 10-20% on a month timescale. Thus, pair-production may have an impact on the detectability of gamma-ray emission from the SNe in the first week after the explosion, depending on the luminosity evolution of a given SN. Given the large spread in the distribution of time delays between the H.E.S.S. observations and the SN discoveries for the SN serendipitous sample, this opacity can, in general, be ignored.

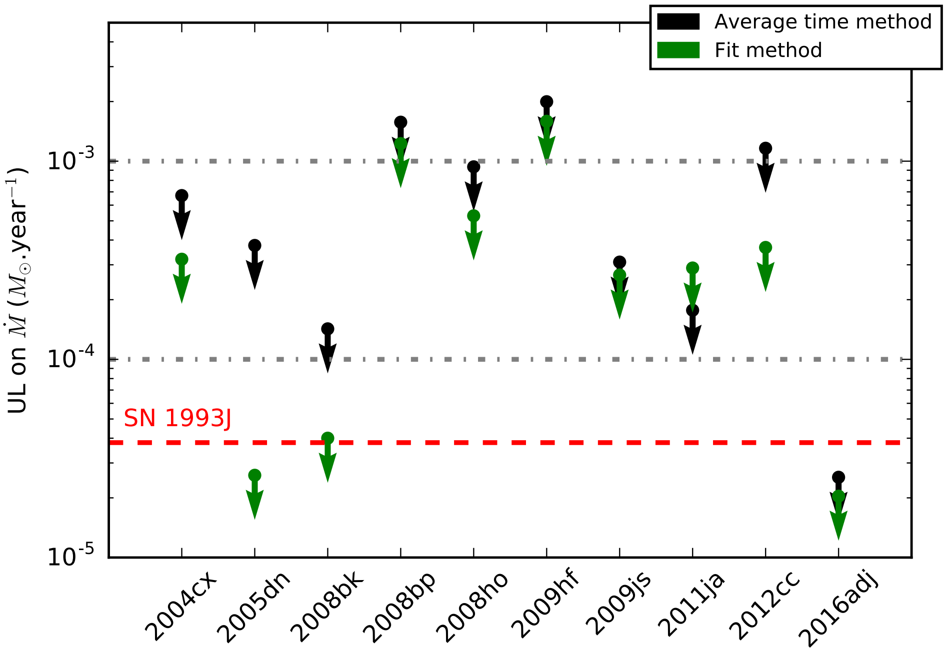

Figure 4.3 – Upper limits on progenitor mass-loss rates, $\dot{M}$, assuming $u_{\mathrm{w}} = 10\ \mathrm{km\,s^{-1}}$ for the ten cc-SNe investigated in this study, derived with two methods (see text). The mass-loss rate for SN 1993J, derived by Tatischeff (2009), is also shown.

The only object for which this attenuation should be considered is SN 2016adj, whose ToO observations are clustered at short time delays. If the attenuation of TeV photons is at a similar level as that estimated in SN 1993J, the expected VHE gamma-ray flux would be much lower during a large part of the H.E.S.S. observation time window and this would explain the non-detection of any excess towards SN 2016adj. In other words, constraints on the VHE gamma-ray flux could not be directly translated into limits on the mass-loss rate until the above-mentioned parameters regarding the evolution of the SN shock and photosphere are better known. SN 2016adj occurred very close to the center of Cen A, so it may well be that the local environment led to an additional gamma-gamma absorption and this could also explain the non-detection.

4.3.4 Discussion on the SNe environment in perspective of other observations.

There may be another explanation for the non-detection of SN 2016adj, for which the ULs are near or below the predicted gamma-ray flux, namely that this interesting candidate does not present the right environmental properties. This could be the case if SN 2016adj was a compact type IIb SN (cIIb), as opposed to SN 1993J, which is known to have been an extended type IIb (eIIb, Chevalier & Soderberg 2010). For type cIIb SNe, the wind velocity is probably higher ($u_\mathrm{w} \gtrsim 100$ km s^{-1}), implying a lower density CSM. Under the hypothesis that SN 2016adj is of type cIIb, assuming $u_\mathrm{w} = 100\,\mathrm{km\,s^{-1}}$, the upper limit on the mass-loss rate would increase by a factor of 10 (see equation 4.3), i.e. $\dot{\mathrm{M}} < 3.0 \times 10^{-4}\ \mathrm{M_\odot\ yr^{-1}}$, and could better accommodate the H.E.S.S. non-detection of this apparent SN 1993J twin. Van Dyk et al. (2016) proposed that SN 2016adj originated from a progenitor with a lower luminosity than the SN 1993J progenitor, suggesting that the explosion might be of compact IIb-type. This claim, however, was later disfavoured by Sugerman & Lawrence (2016). Further multi-wavelength observations will weigh in on the nature of this object, and an analysis of radio and X-ray data is forthcoming (Hajela at al. in prep.). For the rest of the sample, in addition of being Type II SNe (mostly IIP), the nine selected candidates did not have any strong indication of the conditions necessary for significant early CR acceleration. Several of the SNe have been studied at various levels of detail, with results consistent with our study. Radio and X-ray observations are of prime interest to check the consistency of our result, as they can provide additional constraints on the wind parameters. The literature reports radio and X-ray observations for only one SNe in our sample, namely for the rather close-by object SN 2011ja. Chakraborti et al. (2013) suggest that the measured SN 2011ja radio and X-ray fluxes are consistent with an expansion into a low-density bubble and interaction with an inhomogeneous circumstellar medium formed by a RSG ($\sim$12 $\mathrm{M_\odot}$). The corresponding progenitor mass-loss rate was estimated to be of the order of $\sim 10^{-6}\ \mathrm{M_\odot\ yr^{-1}}$, consistent with the constraint of $< 1.6 \times 10^{-4}\ \mathrm{M_\odot\ yr^{-1}}$ derived from our non-detection at TeV gamma rays.

SN 2008bk was observed to have a progenitor mass of $\sim$8 $\mathrm{M_\odot}$ and a luminosity of $\log(L/L_\odot) \sim 4.5$ (Davies & Beasor 2018) after its post-explosion disappearance was confirmed by Mattila et al. (2013) and Van Dyk (2013). By applying the de Jager et al. (1988) prescription (see also Mauron & Josselin 2011), the observed luminosity implies a pre-SN progenitor mass-loss rate of $\sim 10^{-6.3}\ \mathrm{M_\odot\ yr^{-1}}$, consistent with our model-dependent constraint of $< 1.4 \times 10^{-4}\ \mathrm{M_\odot\ yr^{-1}}$.

We further mention a study of the spectral evolution of 122 nearby SNe including post-explosion spectral line observations of SN 2008bp at wavelengths 4000-9500 Å at 12, 40 and 47 days (Gutiérrez et al. 2017). The authors noted SN 2008bp to be the only event to not have Fe-group and H_γ line-blending in early stages of evolution. This characteristic might suggest that the circumstellar medium of SN 2008bp was less dense than that of the rest of the sample. Outlier behaviour was also discovered for SN 2009js. Gandhi et al. (2013) found the event to be subluminous, suggesting a low ejecta mass and explosion energy. It follows that the environments of SN 2008bp and SN 2009js are not likely conducive to the TeV gamma-ray detection sought in our study, but are consistent with the mass-loss rate upper-limits of $\sim 1.6 \times 10^{-3}$ and

$\sim$3.1 × $10^{-4}\,M_\odot$ yr^{-1}, respectively, as derived from the H.E.S.S. observations.

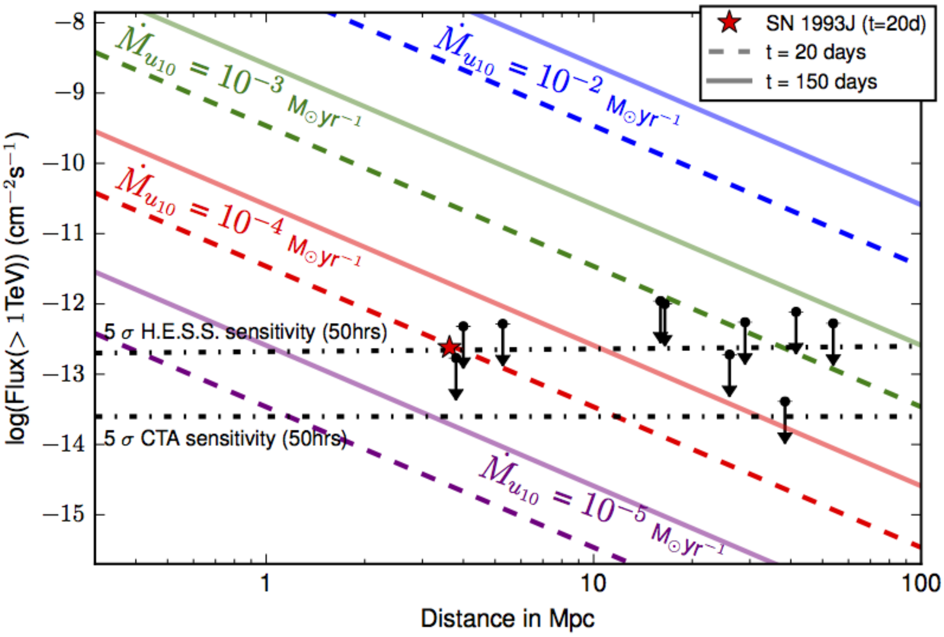

FIGURE 4.4 – Predicted flux above 1 TeV using equation 4.1 as a function of the distance to the source. Mass-loss rates are given in units of $M_\odot$ yr^{-1} assuming $u_w = 10$ km s^{-1} and the parameters described in Section 4.3.1, for $t = 20$ days (solid lines) and $t = 150$ days (dashed lines) after the SN explosion. The Mass-loss rate is given for each pair of lines of the same color. The expected flux for SN 1993J is computed using equation 4.1 and $t = 20$ days. The CTA sensitivity for a 50 hr long observation is taken from Acharya et al. (2013). The ten ULs on the flux above 1 TeV derived in this study are also shown (see text).

4.3.5 Prospects for future observations

In order to put the flux ULs derived in this work in perspective, Figure 4.4 shows the gamma-ray flux computed with equation 4.2 as a function of the distance for different values of the pre-SN mass-loss rate, together with the typical fiveσ point-source sensitivities of H.E.S.S. and of the next generation of IACTs, the Cherenkov Telescope Array (CTA, Acharya et al. 2013). For comparison our upper limits are shown, which, as expected, are close to the 50 h H.E.S.S. sensitivity, $\simeq 2 \times 10^{-13}$ cm^{-2}s^{-1} (Aharonian et al. 2006b), bearing in mind the exposure times. Parameters are chosen as described in Section 4.3.1, with q_α corresponding to a flat spectral index. Two different values for the time delay since the SN explosion are considered : $t = 150$ days corresponds to a value that is representative of our sample, whereas $t = 20$ days roughly corresponds to the optical peak luminosity of a SN. As seen in Figure 4.4, the VHE gamma-ray flux at $t = 20$ days from a SN 1993J-like event is within reach with current IACTs like H.E.S.S., and would clearly be detected by CTA. At $t = 150$ days, and for mass-loss rates higher than 10^{-4} $M_\odot$ yr^{-1}, CTA may detect cc-SNe as far out as the Virgo cluster (16 Mpc).

Mass-loss rates above 10^{-4} $M_\odot$ yr^{-1} are not uncommon, but are usually confined to Type IIb and IIn SNe. Each of these types represent, respectively, ∼10% and ∼8 % of the total cc-SN rates according to Smith et al. (2011). The number of cc-SNe occurring in a year can roughly be expressed as a function of the total available stellar mass in 10^{10} $M_\odot$ units. In our Galaxy, this implies a cc-SN rate of about two per century (see e.g. Li et al. 2011). A galaxy cluster in the local Universe, as the Virgo cluster, has a total stellar mass of the order of 10^{13} $M_\odot$ (see e.g. O'Sullivan et al. 2017), which would bring the number of cc-SNe up to ∼10 per year in a near radius of 16 Mpc. This number is very similar to the number of objects predicted by Horiuchi et al. (2011) for a volume of radius $\lesssim$10 Mpc. Another example is given by Smartt et al. (2009), who identified 5 type IIP SNe in 1999 within ∼18 Mpc, which may represent 60-70% (see e.g. Smartt et al. 2009; Smith et al. 2011) of the whole sample of cc-SNe of that year. Note that type II objects can also exhibit enhanced pre-SNe mass-loss rates above 10^{-3} $M_\odot$ yr^{-1} (e.g. Das & Ray 2017; Arcavi et al. 2017), and other studies have shown that such high mass-loss rates are not so rare among type IIb SNe (Fuller 2017; Ouchi & Maeda 2017). It is then reasonable to expect ∼1 to 2 cc-SNe with $\dot{M} > 10^{-4}$ $M_\odot$ yr^{-1} occurring per year, within a radius of 18 Mpc, whatever the sub-type. Such nearby cc-SN events offer a great opportunity for the detection of gamma rays using IACT observations triggered by observations at optical wavelengths. Such a ToO program to observe cc-SNe as distant as 10 Mpc is currently in place within the H.E.S.S. collaboration. For the expected gamma-ray luminosities of supernovae, the wide-field TeV observatories as HAWC (Abeysekara et al. 2013) and in the future LHAASO Vernetto & LHAASO (2016) are less ideally positioned for detecting gamma-ray emission below 100 TeV, as they require relatively long integration times of up to a year to reach the required sensitivity, whereas the gamma-ray flux is declining on shorter time scales. However, their all-sky monitoring capabilities could lead to early detection of unexpectedly bright gamma-ray SNe events.

4.4 Conclusion

We selected a sample of nine type II SNe that were observed by chance with H.E.S.S. within one year after the SN event, and in addition we triggered ToO observations on SN 2016adj. No significant gamma-ray signal has been detected from any of these ten SNe and we derived flux upper limits of the order of 10^{-13} TeV cm^{-2} s^{-1}.

This result is amending previous efforts (Lennarz & the H.E.S.S. Collaboration 2013) and complements other recent non-detections, namely the Fermi-LAT studies of type IIn SNe at GeV energies (Ackermann et al. 2015), the upper limit at TeV energies established by the MAGIC collaboration for the closest type Ia SN 2014J (Ahnen et al. 2017), and a recent search for GeV emission from super luminous SNe using Fermi-LAT data by Renault-Tinacci et al. (2018). Concerning SN 2016adj, the H.E.S.S. UL is the first constraint derived on this nearby SN event in the gamma-ray domain. The lack of gamma-ray detection reported here, however, does not necessarily indicate that the early phase of SN evolution is not generally conducive to CR acceleration. Instead, the non-detection suggests that it does not occur in this subset of the SNe, which have CSM that are not likely to be dense enough for particle acceleration.

Using the model developed in Dwarkadas (2013), we expressed our ULs in terms of constraints on the mass-loss rates of the SN progenitors, which turn out to be a few times higher than, or of the same order as, the estimated mass-loss rate for the close-by radio-bright SN 1993J. With the same model, we predicted that objects with a mass-loss rate of the order of 10^{-4} M$_\odot$ yr^{-1} and distance of ∼10 Mpc could be detected very early after the outburst by the current generation of telescopes and a fortiori by the next generation, namely the Cherenkov Telescope Array, CTA (Acharya et al. 2013). In our study, we did not observe candidates with the required properties for the detection of gamma rays with H.E.S.S., but our model-dependent investigation suggests that core-collapse SNe will be detected by Cherenkov arrays in the future.

4.5 Appendices : Statistics and Lightcurves

SNe	N_{on}	N_{off}	α	N_{excess}	Sig	Livetime (hrs)	Obs. Cov. (days)	Av. time (days)
SN 2004cx	169	10387	0.015	8.7	0.7	40	-6 - 359	180
SN 2005dn	571	11452	0.053	-39	-1.5	53	-3 - 364	120
SN 2008bk	50	3652	0.018	-18	-2.3	9.6	98 - 211	136
SN 2008bp	32	1860	0.017	1.1	0.2	4.7	272 - 282	282
SN 2008ho	9	369	0.030	-2.3	-0.7	1.4	34 - 34	34
SN 2009hf	43	1404	0.029	3.3	0.5	4.0	124 - 134	133
SN 2009js	14	711	0.015	3.4	1	4.8	1 - 35	17.5
SN 2011ja	37	620	0.053	4.51	0.75	3.4	91 - 131	111
SN 2012cc	7	660	0.013	-1.9	-0.7	3.0	53 - 343	255
SN 2016adj	624	8573	0.070	22	0.9	13	3 - 10	7

Table 4.3 – Observed statistics for each SN (see text). Sig stands for significance , Obs. Cov. stands for Observation coverage and gives the number of days since the SN discovery date for the first - last observation run. The average time is the exposure-weighted mean time in days since the discovery date.

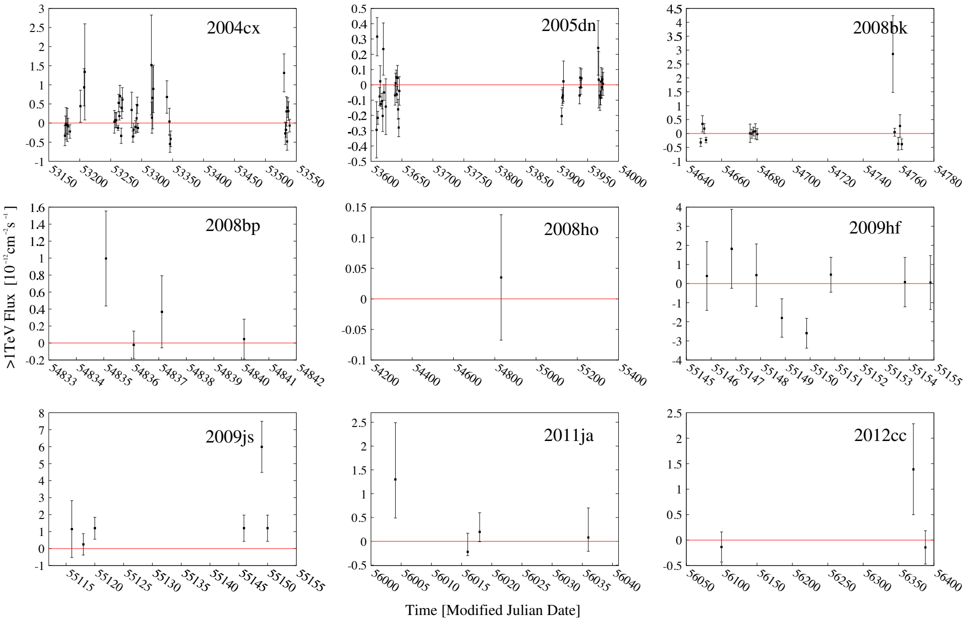

Figure 4.5 – Time evolution binned on a nightly basis of the integrated flux above 1 TeV as measured with H.E.S.S. towards the nine serendipitously observed SNe considered in this study. The red line outlines the zero level.

5

H.E.S.S. ToO program on nearby core-collapse Supernovae : search for very-high energy gamma-ray emission towards the SN candidate AT2019krl in M74

N.Komin, M.Renaud, R.Simoni & S.Ryder on behalf of the H.E.S.S. Collaboration

Proceedings of Science PoS(ICRC2021), 2021, 809

Abstract

While the youngest known supernova remnants, such as Cassiopeia A, have been proven to be able to accelerate cosmic rays only up to $\sim 10^{14}\,\mathrm{eV}$ at their present evolutionary stages, recent studies have shown that particle energies larger than a few PeV ($10^{15}\,\mathrm{eV}$) could be reached during the early stages of a core-collapse Supernova, when the high-velocity forward shock expands into the dense circumstellar medium shaped by the stellar progenitor wind. Such environments, in particular the type IIn SNe whose progenitors may exhibit mass-loss rates as high as $10^2 M_\odot\,\mathrm{yr}^1$ Smith (2014), could thus lead to gamma-ray emission from π^0 decay in hadronic interactions, potentially detectable with current Cherenkov telescopes at very-high energies. Such a detection would provide direct evidence for efficient acceleration of CR protons/nuclei in supernovae, and hence new insights on the long-standing issue of the origin of Galactic Cosmic Rays. In that context, the High Energy Stereoscopic System (H.E.S.S.) has been carrying out a Target of Opportunity program since 2016 to search for such an early very-high-energy gamma-ray emission towards nearby core-collapse supernovae and supernova candidates (up to $\sim$ 10 Mpc), within a few weeks after discovery. After giving an overview of this H.E.S.S. Target of Opportunity

program, we present the results obtained from the July 2019 observations towards the transient AT2019krl, originally classified as a type IIn supernova, which occurred in the galaxy M74 at $\sim 9.8\,\mathrm{Mpc}$. Although its nature still remains unclear, the derived H.E.S.S. constraints on this transient are placed in the general context of the expected VHE gamma-ray emission from core-collapse supernovae.

5.1 Introduction : probing particle acceleration in core-collapse supernovae

Among the gamma-ray emitting supernova remnants (SNRs), no indisputable evidence for the presence of PeV Cosmic Ray (CR) particles being accelerated at their shock fronts has been found yet. Cassiopeia A (Cas A), with an age of about 350 years one of the youngest Galactic SNRs, has long been considered as the best candidate to accelerate particles up to the CR knee (∼3 PeV). Its high-energy/very-high-energy (HE/VHE) gamma-ray spectrum measured with *Fermi*-LAT Yuan et al. (2013); Ahnen et al. (2017), VERITAS Kumar (2015) and MAGIC Ahnen et al. (2017) is better explained by hadronic interactions owing to the turnover seen below 1 GeV, reminiscent of the characteristic π^0 decay signature. The latest combined *Fermi*-LAT/VERITAS spectrum clearly shows an exponential cutoff of the gamma-ray spectrum at ∼2-3 TeV Abeysekara et al. (2020). This demonstrates that the maximum energy of the accelerated particles is below 20 TeV, regardless of the details of the broadband spectral modeling of Cas A Abeysekara et al. (2020). Such a low value points towards the idea that PeV CRs could be accelerated at the shock front much earlier than previously thought during the SNR evolution. Recent studies of the diffusive shock acceleration (DSA) mechanism have shown that particle energies larger than a few PeV could actually be reached when the supernova (SN) shock is propagating at high velocity ($v_{\mathrm{sh}} \gtrsim 10^4$ km s^{-1}) into a dense ($n \gtrsim 10^{7-9}$ cm^{-3}) circumstellar medium (CSM) Tatischeff (2009); Bell et al. (2013); Schure & Bell (2013); Murase et al. (2014); Cardillo et al. (2015); Bykov et al. (2018); Marcowith et al. (2018). Such an environment is formed by the wind from the stellar progenitor prior to explosion, whose density profile is commonly assumed to be steady : $n(R_{\mathrm{sh}}) = \frac{\dot{M}}{4\pi u_{\mathrm{w}} \mu m_H R_{\mathrm{sh}}^2} \sim 3 \times 10^7 \frac{\dot{M}_{-5}}{u_{\mathrm{w},10}} R_{\mathrm{sh},15}^{-2}$ cm^{-3} (for a mean mass per particle $\mu = 1$) with a mass-loss rate $\dot{M} = 10^{-5} \dot{M}_{-5} M_{\odot}$ yr^{-1}, a wind velocity $u_{\mathrm{w}} = 10 u_{\mathrm{w},10}$ km s^{-1} and a shock radius $R_{\mathrm{sh}} = 10^{15} R_{\mathrm{sh},15}$ cm. Tatischeff Tatischeff (2009) has shown that the extensive spectro-morphological radio observations of the synchrotron emission from the nearby, and well-monitored, type IIb SN 1993J can be described by a detailed model coupling the non-linear DSA with self-similar solutions for the SN hydrodynamics. The magnetic field was found to be strongly amplified shortly after the explosion at the level of $\sim 50\ (t/1\mathrm{day})^{-1}$ G [1], most likely due to the CR resonant and nonresonant instabilities operating in the shock precursor (but see Björnsson & Keshavarzi (2017) for a different interpretation). Protons and nuclei would then be accelerated to PeV energies within the first few days after the explosion (see Marcowith et al. (2018)), with a total CR energy $E_{\mathrm{CR}} \sim 7 \times 10^{49}$ erg over the first ∼8 yr. From the best-fit values of the relevant parameters obtained by Tatischeff (2009), the hadronic gamma-ray flux from SN 1993J amounts to

$$F_\gamma(E > E_{\mathrm{TeV}}) \ \sim\ 2\ \times 10^{-12}\ E_{\mathrm{TeV}}^{-1}\ d_{\mathrm{Mpc}}^{-2} \left(\frac{\dot{M}_{-5}}{u_{\mathrm{w},10}}\right)^2 t_{\mathrm{day}}^{-1}\ \ \mathrm{cm}^{-2}\ \mathrm{s}^{-1}. \tag{5.1}$$

Similar calculations have been performed Dwarkadas (2013); Murase et al. (2014); Zirakashvili & Ptuskin (2016); Fang et al. (2019) in the case of the superluminous type IIn SNe, thought to be powered by the interaction between the ejecta and a very dense CSM Gal-Yam (2012). Once the collisionless shock propagates in the wind, efficient CR acceleration has been shown to take place Katz et al. (2011); Murase et al. (2011), and these SN events could thus be privileged source candidates to explain (part of) the very-high-energy neutrinos detected with IceCube Zirakashvili et al. (2014). The expected gamma-ray flux derived in Murase et al. (2014), once applied on SN 1993J, is compatible with equation 5.1 within a factor of $\lesssim 2$.

In the GeV domain, gamma-rays are expected to be mostly unaffected by photon fields from the source Murase et al. (2014), so that these flux estimates can be readily used to estimate the visibility of these SNe with current HE instruments such as *AGILE* and *Fermi*-LAT. The analysis of *Fermi*-LAT data towards an ensemble of 147 type IIn SNe in different time windows has not revealed any significant excess Ackermann et al. (2015). Only for the brightest and closest type IIn events ($d \lesssim$ 20 Mpc) do the derived upper limits start to constrain the theoretical expectations Renault-Tinacci et al. (2018). Nevertheless, two recent studies based on *Fermi*-LAT data have reported marginally significant variable HE emission towards the peculiar H-rich super-luminous SN iPTF14hls at ∼150 Mpc Yuan et al. (2018) and the nearby (∼3.5 Mpc) type IIP SN 2004dj Xi et al. (2020). The latest search for gamma-rays from SNe by means of a variable-size sliding-time-window analysis of the *Fermi*-LAT data has confirmed the variable signal in the direction of iPTF14hls and revealed two new excesses in the direction of the SN candidates AT2019bvr and AT2018iwp, with a flux increase within six months after the discovery date Prokhorov et al. (2021). In the TeV domain, the pair production process $\gamma + \gamma \rightarrow e^+ + e^-$ in the radiation field from the SN photosphere is expected to be effective. While Tatischeff Tatischeff (2009) has overestimated the opacity $\tau_{\gamma\gamma}$ for SN 1993J by assuming an *isotropic* source of

---

[1] at least two orders of magnitude higher than the equipartition value of a Red SuperGiant (RSG) progenitor wind, in line with several previous studies Fransson & Björnsson (1998); Martí-Vidal, I. et al. (2011).

UV/optical photons, the full opacity calculations, including temporal and geometrical effects due to the *anisotropic* gamma-gamma interaction, have recently been applied to SN 1993J Cristofari et al. (2020). The resulting gamma-ray flux, shown to be sensitive to the photospheric properties and SN hydrodynamics, is then strongly attenuated during the first ~ 10 days.

One should note that all these calculations are subject to large uncertainties in the different parameters highlighted above, as most of them are estimated through indirect means, once multi-wavelength (MWL) observations have been carried out. First of all, many details impacting the particle acceleration capability of these SNe are still poorly constrained (e.g. the magnetic field geometry, the nature and growth timescale of the instabilities and the particle injection). Moreover, the characteristics of cc-SN light-curves and spectra, the properties of the stellar progenitors (impacting the time evolution of the photospheric parameters $R_{\rm sh}$, $u_{\rm sh}$) and their stellar winds (mass-loss rate, wind velocity and structure [2]) are very diverse and are still the topic of intense investigation Smartt (2009); Smith (2014). Also, the time of the SN's explosion is usually not known at the time of its discovery until detailed analyses of pre- and post-explosion data are performed. Nevertheless, high-cadence UV/Optical/NIR observations [3] allow for a determination of the SN subclass within a few days and provide important insights on the SN photosphere, the stellar progenitor and on the ejecta chemistry and kinematics (e.g. Nagao et al. (2019); Bose et al. (2021)). Finally, radio observations provide a probe of the magnetic fields in core-collapse supernovae (cc-SNe), as well as the mass-loss rate and the density distribution of the CSM produced by the pre-SN stellar wind (e.g. Bietenholz et al. (2021) and references therein).

5.2 H.E.S.S. Target of Opportunity program on cc-SNe

Based on the above-mentioned calculations from Tatischeff Tatischeff (2009) and Cristofari et al. Cristofari et al. (2020), a H.E.S.S. Target of Opportunity (ToO) program has been set up towards nearby cc-SNe in order to probe early VHE gamma-ray emission. Since progenitor mass-loss rates and wind velocities do greatly vary among the different cc-SN sub-classes, with no univocal relationship with the stellar progenitor and the SN type (see e.g. Smartt (2009)), the most representative values

---

[2] Recent observations show that some type Ibn/IIn SN progenitors (possibly Luminous Blue Variables) experience some episodic mass-loss outbursts during the latest phases before explosion, resulting in a complicated CSM Smith et al. (2017) made of shell-like structures Nyholm, A. et al. (2017).

[3] ASAS-SN (`http://www.astronomy.ohio-state.edu/~assassin/`) and DLT40 (`http://dark.physics.ucdavis.edu/dlt40/DLT40`) projects are yielding the cadence necessary to ensure that nearby southern cc-SNe can be caught within <3 days after the explosion.

have been considered as follows : $(\dot{M}_{-5}/u_{\mathrm{w},10})$ = (1,2,2,5,20) for type (II-P,Ib/c,II-L,IIb,IIn) SNe, respectively Nymark, T. K. et al. (2006); Mauron & Josselin (2011); Kiewe et al. (2012); Taddia, F. et al. (2013); Smith (2014). By assuming the same $\gamma-\gamma$ opacity and CR acceleration efficiency as in SN 1993J, the corresponding horizons of detectability at 5 σ with H.E.S.S., at day 10 after the SN explosion and for $T_{\mathrm{obs}} = 10$ h, have been derived to be (1,1,1,2,8) Mpc[4]. Owing to the uncertainties in defining meaningful trigger criteria as described in the previous Section, (lower-rank) H.E.S.S. ToO observations may also be triggered towards any cc-SN or SN candidate occurring at less than 10 Mpc if there is some interesting MWL information. Given a predicted rate of 1−2 cc-SNe per year at < 10 Mpc Smartt et al. (2009), the expected trigger rate does certainly not exceed 2 yr^{-1}. This on-going ToO program has been enriched by the implementation of several partnerships with groups dealing with MWL observations of cc-SNe. In particular, one of us (S. Ryder) has been leading a radio ToO program with ATCA at 1-20 GHz towards nearby ($d \lesssim 40$ Mpc), southern (Dec. $<$ -40°) cc-SNe. Since 2020, several members of the DLT40 and ASAS-SN optical surveys are also involved in this H.E.S.S. ToO program. Thus, the H.E.S.S. Collaboration can get informed about the properties of any nearby cc-SN event within a few days in order to make a reliable trigger decision.

So far, H.E.S.S. has serendipitously observed nine nearby cc-SNe within a year after their discovery date and triggered ToO observations on one cc-SN a few days after discovery : SN 2016adj, a (possibly compact)[5] type IIb SN in Cen A. No significant excess has been found towards any of these cc-SNe. The analysis and interpretation of the H.E.S.S. data towards these cc-SNe have been published Abdalla, H. et al. (2019). That study provides interesting upper limits on the CSM density under several assumptions on the acceleration efficiency (among other parameters as described in the case of SN 1993J), in particular on SN 2016adj, even though most of the data set spreads over timescales longer than what is considered here. In the following these results will be complemented with ToO observations of AT2019krl, originally classified as a type IIn SN candidate, in the galaxy M74.

5.3 AT2019krl in M74

5.3.1 Discovery and multi-wavelength observations

On 6th July 2019 a transient originally named ZTF19abehwhj was discovered by ZTF (later renamed as AT2019krl) in the M74 galaxy at ∼9.8 Mpc McQuinn et al.

---

[4] The first three values, originally estimated to amount to 0.4-0.8 Mpc, have been rounded to 1 Mpc, below which there is no major star-forming galaxy visible from the Southern Hemisphere except the LMC/SMC.

[5] Type IIb SNe are thought to have more compact and less luminous stellar progenitor with faster and lower-density wind Chevalier & Soderberg (2010)

(2017). On 9th July AT2019krl was shown to have a type IIn SN optical spectrum, exhibiting narrow and intermediate H-α emission lines, although several types of CSM-interacting SNe, a Luminous Blue Variable (LBV) in outburst, or other intermediate-luminosity transients could not be ruled out at that stage (ATel #12913). Following these reports, a H.E.S.S. ToO was triggered on this (possibly very young) type IIn SN candidate on 11th July (see details below). Then, on 12th July, the analysis of the Spitzer archival data to look at the mid-IR pre-discovery evolution of the transient revealed a quiescent source at the location of AT2019krl showing a moderate brightening between December 2018 and April 2019, while the transient became a very bright mid-IR source in mid-May 2019, i.e. about 50 days before the transient has been discovered by ZTF (ATel #12934). The mid-IR brightness measured at this last epoch suggested that AT2019krl is rather a SN than a LBV outburst, whose final explosion likely occurred between 21st April and 17th May.

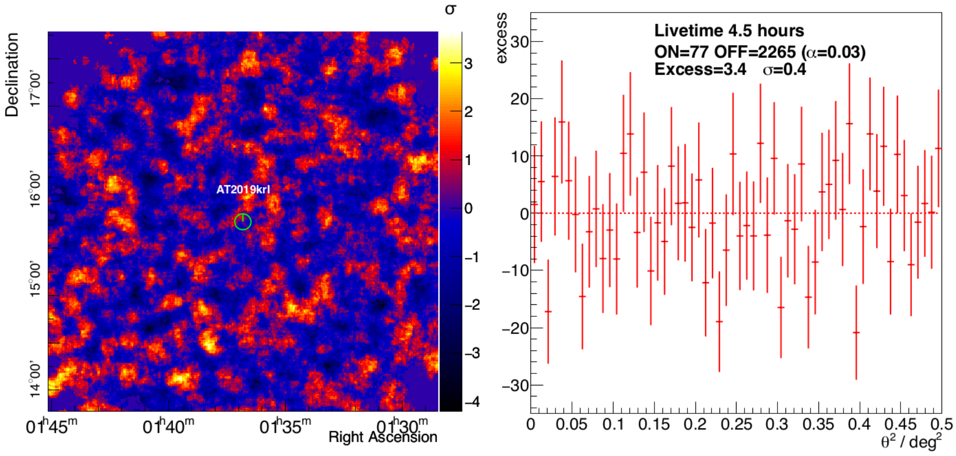

Figure 5.1 – Significance map (left) and radial distribution of the excess at the source position, in θ^2 as described in Aharonian et al. (2006b) (right). The reported statistics are explained in the text. The significance of the emission is 0.4 σ.

5.3.2 Observations and data analysis

Observations were conducted with the High Energy Stereoscopic System (H.E.S.S.), an array of five imaging atmospheric Cherenkov telescopes (IACTs) located in the Khomas Highland of Namibia at an altitude of 1800 m above sea level. AT2019krl was observed with the full array, the four 12 m-diameter telescopes (CT1-4, operating since December 2003) and the fifth 28 m-diameter telescope (CT5, operating since September 2012). The analysis performances are thus the ones of the "H.E.S.S.-II-phase" as described in van Eldik et al. (2016). The data were taken in an "hybrid mode", selecting events triggering at least 3 telescopes including CT5, which allows for a lower energy threshold of 180 GeV compared to 210 GeV for the CT1-4 array. AT2019krl was observed on three consecutive nights, from 11th to 13th July 2019. These observations were made in wobble mode (Aharonian et al. 2006b) with a mean offset angle of 0.5 deg around the source and organized in 28-minute exposures called runs. A total of 10 calibrated runs passing the standard quality criteria (see Hahn et al. 2014) were analysed using the ImPACT reconstruction (Parsons & Hinton 2014), with hybrid configuration and standard cuts. This led to 4.5 hours of livetime with a mean zenith angle of 47.2 deg. The background for the sky map was obtained from rings around each sky bin, applying the ring background method Berge et al. (2007). For the spectral extraction an ON-region (with a radius of 0.086 deg) was defined at the SN position, and multiple OFF regions were selected with the same angular distance from the camera centre as the ON region, using the reflected background method Berge et al. (2007). The gamma-ray excess was computed using $N_{\mathrm{excess}} = N_{\mathrm{on}} - \alpha N_{\mathrm{off}}$, with α the ON to OFF exposure ratio. The statistical significance was estimated using (Li & Ma 1983, eq. 17). The results were confirmed by an independent data calibration and analysis chain using the Model++ framework (de Naurois & Rolland 2009) with standard quality cuts and the same reflected background method.

5.3.3 Results

After 4.5 h of observations no significant excess has been found. As shown in Figure 5.1, the significance map is isotropic, and the photon counts as a function of the θ^2 distance to the source exhibit no excess above the background level. Flux upper limits (ULs) have thus been derived at the 95% confidence level under the assumption of a power law spectrum ($dN/dE \propto E^{-\Gamma}$) with a photon index $\Gamma = 2$ and 2.4. Integrated ULs at $E > 1$ TeV have been computed in order to compare with ULs previously derived towards cc-SNe Abdalla, H. et al. (2019) using a log-likelihood approach Rolke & Lopez (2001). For $\Gamma = 2$ [2.4], UL($E > 1$ TeV) = 3.85 [2.95] $\times 10^{-13}$ cm^{-2} s^{-1}. Assuming a distance to M74 of 9.8 Mpc McQuinn et al. (2017), these flux ULs above 1 TeV translate into luminosity ULs of 3.25 [1.56] $\times 10^{40}$ erg s^{-1}.

5.4 Discussion and Conclusion

Figure 5.2 shows that the upper limit on the VHE gamma-ray flux from AT2019krl is at a comparable level as the other cc-SNe studied in Abdalla, H. et al. (2019). The absence of significant gamma-ray emission from AT2019krl suggests in a hadronic model a low density of the target material. The target density can be estimated with the model of Tatischeff (2009) and using equation (5.1) assuming a distance of d = 9.8 Mpc and no pair-production effect. Considering t = 1 week and Γ=2, the

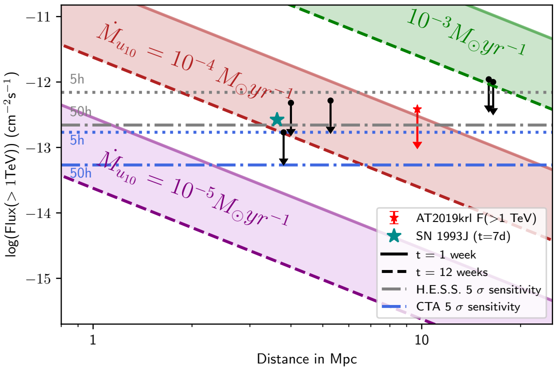

FIGURE 5.2 – Predicted flux above 1 TeV as a function of the distance to the source based on Tatischeff (2009). u_w is set to 10 km s^{-1}. Fluxes are computed for $t = 1$ (solid lines) and 12 (dashed lines) weeks after the SN explosion. The expected flux from SN 1993J is computed assuming $\dot{M}_{-5} = 3.5$ Tatischeff (2009) and $t = 7$ days. H.E.S.S. (CT1-4) and CTA integrated sensitivities for 50 h long observations are taken from Aharonian et al. (2006b) and Cherenkov Telescope Array Consortium (2019), from which those for t= 5 h are derived. In black, ULs on the flux above 1 TeV derived in Abdalla, H. et al. (2019) are also shown (see text).

UL on the CSM density ($\dot{M}/u_\mathrm{w}$) amounts to ~6.3 × 10^{15} g cm^{-1}, equivalent to a progenitor mass-loss rate of ∼ 10^{-4} (10^{-3}) $M_\odot$ yr^{-1} for u_w = 10 (100) km s^{-1}, as shown in Fig. 5.2. Such a constraint is at the same level as the lowest wind densities required to make a type IIn SN Smith et al. (2017), knowing that most of the well-studied type IIn events exhibit typical mass-loss rates higher by a factor of ~10 Smith et al. (2017), for u_w between 10 and 1000 km s^{-1}. Since the absence of gamma-ray emission suggest a low density wind, AT2019krl must either be an atypical SN IIn, or point to a problem with the gamma-ray emission model. For example, the absence of detectable gamma-ray emission can also indicate a strong attenuation due to the pair-production process with UV/optical photons from the SN photosphere, which is particularly important during the first week after the explosion. Bearing in mind that the date of the explosion of AT2019krl is poorly constrained, if the SN occurred on 21st April (i.e. t = 12 weeks before the H.E.S.S. ToO) as suggested by the analysis of Spitzer archival data (ATel #12934), the UL on the CSM density increases to ~2.2 × 10^{16} g cm^{-1} but still falls in the lower part of the estimated values for known type IIn SNe (see Fig. 3 in Smith et al. 2017). Finally, AT2019krl may not have been a SN explosion at all. Indeed, based on extensive archival HST, Spitzer and LBT observations, it has recently been suggested that AT2019krl is either a SN 2008S-like transient due to a Blue SuperGiant (BSG) eruption or an LBV outburst Andrews et al. (2021). In this case, the model discussed here cannot be applied. Irrespective of the non-detection of gamma-ray emission and the disputed nature of AT2019krl the study presented here shows that gamma-ray emission from a type IIn SN at a distance of about 10 Mpc could be detectable with current Imaging Air Cherenkov Telescopes like H.E.S.S., provided that the nuclear interaction losses in such high-density CSM are not limiting the acceleration of PeV CRs (see Marcowith et al. 2018, for detailed calculation). The observation of such emission would be a clear proof of efficient particle acceleration during the early stages of a cc-SN, once the progenitor's parameters are known thanks to multi-wavelength observations.

Estimating the date of the SN explosion is necessary to chose the optimal time window to trigger VHE gamma-ray observations. While shortly after the explosion the gamma-ray emission is absorbed, several weeks later the emission may have declined to a level undetectable by current instruments. The type of the SN explosion is important to estimate the horizon of detectability with IACTs in the TeV domain. Only type IIn SNe can provide a sufficiently dense CSM to produce detectable gamma-ray emission at a distance of about 10 Mpc while the other types could be detectable at ∼1 Mpc. The detection of a good candidate might necessitate observations longer than considered here, of a few tens of hours. The H.E.S.S. ToO program on cc-SNe is ongoing, allowing for a few ToO observations to be triggered each year. A non-detection by H.E.S.S. of a nearby cc-SNe can provide important constraints on the ability of such very young SNe to accelerate CRs to PeV energies. The future Cherenkov Telescope Array (CTA, Cherenkov Telescope Array Consortium (2019)), with a higher sensitivity than H.E.S.S., will be able to probe the VHE gamma-ray emission from cc-SNe at a much lower level.

6

Search for gamma-ray emission at the edge of the Fermi Bubbles with H.E.S.S. using PKS2155-304 Observations

R.Simoni, N. Komin, D. Berge & J. Vink on behalf of the H.E.S.S. collaboration

Internal report. No journal submission

Abstract

We searched for VHE emission for the edge of the Fermi Bubbles located in the five degrees field of view of observations dedicated to the blazar PKS2155-304. Data-set consists of 303.7 hours of good quality data. We observe no significant emission and derive differential upper limits on the flux of the order of $\sim 2 \times 10^{-9}$ TeV $\mathrm{cm^{-2}s^{-1}sr^{-1}}$ at energies of ~ 1 TeV. These results complete the multi-wavelength spectrum at large b at TeV energies, from *Fermi*-LAT upper energy range and the HAWC lower one. No model is constrained; systematic errors are addressed and discussed along with predictions for further observations.

6.1 Introduction

The Fermi Bubbles (FB) are gigantic,$\sim$ 10 kpc sized, diffuse gamma-ray lobes, which seem to "bubble out" of the Galactic center (GC). They were discovered in the *Fermi*-LAT data, by Su et al. (2010), who reported two remarkable symmetric oval-shaped structures extending in Galactic latitude up to $|b| \sim 55°$ above and below the Galactic plane, having a maximal width of $l \sim 40°$ in Galactic longitude. The FBs cover about one steradian of the sky, which makes them one of the biggest identifiable structures in the diffuse Galactic gamma-ray sky. The study established a gamma-ray spectrum of $dN/dE \sim E^{-2}$ (1 - 100 GeV)—harder than the diffuse Galactic plane emission—relatively sharp edges, and an enhanced emission in the southeast side of the FB called the cocoon (see also Su & Finkbeiner 2012).

Large structures that are probably associated with the FBs have been observed at other wavelengths : the WMAP's "microwave haze" (Dobler & Finkbeiner 2008; Ade et al. 2013), radio lobes discovered by the Parkes radio telescope (Carretti et al. 2013), and in X-rays, the very recent discovery of the "eROSITA bubbles" (Predehl et al. 2020). These diffuse X-ray structures are similar in shape to the FB and twice bigger, extending up to $|b| \sim 80°$. In the northeast quadrant, the eROSiTA bubbles coincide with the North Polar spur structure (Snowden et al. 1997; Kataoka et al. 2013; Tahara et al. 2015), although the spur is believed to be much closer than the Galaxy, and not associated with the FB (Das et al. 2020). There is a lack of observational evidence for any shock structure, as Non thermal X-ray emission was not observed in the FB (Kataoka et al. 2013). UV spectroscopy observations were performed in the field of view of the gamma-ray and X-ray bubbles (Fox et al. 2015), studying the properties of swept up gas venting into the FB. This study estimate an age of the FBs of $\sim$ 2.5-4 Myr, which value was confirmed by a study using 2D hydrodynamical modeling compared to OVI and OVIII observations (Sarkar et al. 2017).

The origin of the FB gamma-ray emission is still debated. Two main scenarios explaining the FBs' formation, as well as the origin of their gamma-ray emission have been proposed : (a) the first scenario suggests the FB results from jets produced by the supermassive black hole of the center of our Galaxy, Sgr A *, similar to AGN outflows ; (b) the second scenario considers CR acceleration taking place in the outflow powered by a starburst driven wind that could have been produced in the Galactic Bulge, which is an active star formation region.

The first scenario is supported by the symmetry of FBs, the sharp edge, with cocoon shapes, which are bright in the South and fainter in the North(Su & Finkbeiner 2012; Yang & Ruszkowski 2017; Guo & Mathews 2012; Zubovas & Nayakshin 2012). A similar shape is observed, for example, in Centaurus A (e.g Prokhorov & Colafrancesco 2019) or in M31 (Pshirkov et al. 2016). The main caveat of the "jet-like" scenario is that very little softening of the spectrum with the latitude is observed. However, this would be expected based on the principle of volumetric emissivity from a main central source at the GC, and radiative cooling of relativistic particles, based on a leptonic scenario. Moreover, the study of the FB at low latitudes ($b < 10°$), near the GC, presents an asymmetry (Ackermann et al. 2017; Storm et al. 2017) with a displacement of the emission in negative longitudes, disfavouring the origin at the supermassive black hole.

The star-forming region hypothesis is preferred by some authors (e.g. Crocker & Aharonian 2011; Crocker 2012; Crocker et al. 2014; Lacki 2014; Herold & Malyshev 2019), and is supported by the asymmetry observed at the base of the FBs. Unified modeling using a shock-reverse shock structure provides a plausible description of the multi-wavelength data (Crocker et al. 2015), especially with the discovery of the eROSITA bubbles, which could mark a termination shock (Predehl et al. 2020), with the edge of the FBs marking the contact discontinuity. A supernova (SN) driven wind hypothesis is also preferred for explaining the similarly shaped bubbles in the star-forming regions of the Circinus galaxy (Hayashida et al. 2013; Ebrahim et al. 2020), or in M82 (Abdo et al. 2010; Pedlar et al. 2003, e.g). However, the star-forming region hypothesis is at odds with the fact the edge does not exhibit any shock structure. It cannot easily explain the cocoon shape in the South Bubble. There is also no brightening observed at the edge in the radio data, as observed for example for Circinus A (Ebrahim et al. 2020), that would support the presence of a shock. Multi-wavelength observations do not provide the definitive proof for either hypothesis : the eROSITA bubbles can be explained by both scenarios, assuming a luminosity of 10^{41} erg s^{-1}, which is similar to the value derived in previous works (e.g. Sarkar et al. 2017).

The spectrum of the FB at large latitude (b>10°) presents a clear peak at $\sim$ 10 GeV and a softening above $\sim$ 100 GeV It could be well fitted with both leptonic or hadronic models. In the case of the leptonic scenario, the gamma-ray emission is due to inverse Compton emission of a population of electrons. In the hadronic scenario, the decay of neutral pions, produced by the collision of cosmic-ray nuclei with the ambient medium, leads to the gamma-ray emission. There are more phenomenological arguments in favor of the leptonic origin of the GeV gamma-ray seen by *Fermi*-LAT in both the AGN and SNR wind scenarios, given the low density in the Galactic halo Ackermann et al. (2017); Cheng et al. (2015b). However, the hadronic origin stays plausible (Yang et al. 2014; Giacinti & Taylor 2017; Cheng et al. 2015a; Fujita et al. 2014).

The *Fermi*-LAT collaboration published two deep studies on the FBs, aiming to characterize the FBs' morphology and spectrum : analyzing 4.2 years of data Ackermann et al. (2014) presented a gamma-ray spectrum exhibiting an energy cut-off at 110±50 GeV, that could be well fitted with both hadronic or leptonic models. Ackermann et al. (2017) provided a deeper insight into the GeV emission (6.5 years of data), with new modeling methods, aiming to study the GC excess. This analysis confirmed that the spectrum at large latitude (b >10 °) exhibits an energy cut-off, although the emission near GC extends to 1 TeV without any evidence for a cut-off. HAWC, a water tank Cherenkov observatory monitoring the whole sky, observed the emission of the FB in the northern hemisphere : no detection was found, and upper limits (ULs) on the flux above 3 TeV were reported (Abeysekara et al. 2017). HAWC ULs ruled out some hadronic models predicting PeV gamma-rays, and also limit the possibility of detecting any neutrino emission from the FB by current observatories (Razzaque & Yang 2018; Hallmann et al. 2017; Sherf et al. 2017). However, HAWC ULs were not sufficiently stringent to improve upon the cut-off energy established by Ackermann et al. (2017). Observations at TeV energies are thus crucial to bring insight into the behavior of the spectrum, especially the energy cut-off, that could help to disentangle between the leptonic or hadronic origin of the gamma-ray emission.

Here we report on our study of a particular region near the edge of the southern FB to constrain the TeV emission with H.E.S.S. H.E.S.S. is an imaging atmospheric Cherenkov telescopes (IACT) array located in the southern hemisphere. The observation conditions towards the southern hemisphere and the Galactic center being optimal, H.E.S.S. is a good observatory to provide insight into the TeV emission of the South bubble. Furthermore, the H.E.S.S. sensitivity is optimized at 1 TeV. Thus H.E.S.S.'s observation of the FBs could enlighten the FBs gamma-ray spectrum, in the 0.8-4 TeV range in which *Fermi*-LAT and HAWC are not sensitive enough. Despite its relatively small field of view (FoV) of 5° and its design optimized for point source observation, H.E.S.S. was used to observe diffuse gamma-ray observation in the Galaxy (Abdalla et al. 2018a; Abramowski et al. 2014a). These analyses used observation campaigns scanning large fields and employing non-standard background subtraction methods. Very recently, the H.E.S.S. collaboration provided interesting flux constraints on the base of the FB with the Inner Galaxy Survey (Moulin et al. 2021). This analysis gathered 546 hrs of observations scanning a region in the North, from $b \sim 0°$ to $b \sim 4°$ and in latitude from $l \sim -4°$ to $l \sim 4°$.

We present here an analysis aiming to characterize the FBs spectrum at large b with H.E.S.S., concentrating on the edge of the South bubble, using deep observation of the blazar PKS2155-304, which happens to be located just outside the FB. These observations are not optimized for detecting emission from the FB, and, therefore, provide technical challenges to obtain measurements of the diffuse emission from the FB at one side of the field of view. On the other hand, the sensitivity for detecting diffuse emission from this region will not be matched any time soon, and likely will have to wait until the Cherenkov Telescope Array may be available. In Section 6.2, H.E.S.S. data-set and analysis details are explained. The systematic errors specific to the analysis are discussed in Section 6.2.4. Finally, the derived results are presented and discussed in Section 6.3, a summary is given in Section 6.4.

6.2 Observation and data analysis

A FB template[1] for $|b| > 10°$ was released in Ackermann et al. (2014) and used as a reference for the FB morphology by many publications. The template is built by selecting on the FB significance map : any signal with a level three times the noise level above the model background (a "σ_{3BG} cut") (see Fig.4 & 5 in Ackermann et al. 2014). This motivated our study in 2015, as some parts of the template are coincident with H.E.S.S. observations, especially PKS2155-304, for which we have deep observations.

---

[1] https://www-glast.stanford.edu/pub_data/891/

The source can be assumed to be in the background of the FB ; its distance is of the order of 480 Mpc (z = 0.116) and we assume a distance of about 8 kpc for the FB. If some FB emission extents in the source observations it should be detectable. In our analysis of the PKS2155-304 observation, we use any gamma-ray events but the source, which is excluded.

In this Section, we will briefly present our observatory in Section 6.2.1, detail the data-set in Section 6.2.2, explain the analysis settings in Section 6.2.3 and discuss the uncertainties in Section 6.2.4.

6.2.1 H.E.S.S. Observatory

The H.E.S.S. (High Energy Stereoscopic System) experiment has been operating since June, 2002, in the Khomas Highlands of Namibia (23° 16′ 18″ S, 16° 30′ 1″ E, 1835 m above sea level). It uses the Imaging Air Cherenkov Technique (IACT) which consists in recording the Cherenkov light emitted by secondary particles from the shower created in the atmosphere by very high-energy gamma-rays. In its first phase, the H.E.S.S. array consisted of four telescopes operating in stereoscopic mode. Each telescope has a tessellated 13 m-diameter mirror which focuses the Cherenkov light onto a camera in the focal plane, resulting in a field of view of 5° (Bernlohr et al. 2003; Aharonian et al. 2004b). A 5th telescope of 28 m-diameter became operational in September 2012.

This work uses a data-set taken with 3-4 of the 12 m telescopes, during the "HESSI-phase" which performance is summarized in (Aharonian et al. 2006b). This generally results in an angular resolution (68% containment radius) of ∼0.1°, an energy threshold of ~ 100 GeV, and an energy resolution of $\sim 15\%$.

6.2.2 Data-set

The data-set used in this work consists of archival observations dedicated to the blazar PKS2155-304. This well-known southern object, classified as a BL-Lac source, has been regularly observed by H.E.S.S. since the beginning of operations, allowing detailed studies of the source variability (Abramowski et al. 2010). It is one of the most studied H.E.S.S. sources and has led to 13 publications since 2005 [2]. Its location in the southern hemisphere at large Galactic latitude ($l = 17.74°$, $b = -52.25°$) makes H.E.S.S. an ideal instrument for its study. It is so bright in TeV gamma-rays, that a 5 σ detection can be achieved with less than one hour of observation in a stereo mode (Aharonian et al. 2005). Even during strong flares (e.g. Abramowski et al. 2012), it appears as a point source in TeV gamma-rays, quite isolated in this part of the sky without any other gamma-ray source within the 5° FoV, leading to a clean sky map. For this reason, PKS2155-304 observations were used to test analysis

---

[2] `https://www.mpi-hd.mpg.de/hfm/HESS/pages/publications/pubs_jour.shtml`

features in H.E.S.S. (e.g Berge et al. 2007) and to conduct beyond-the-standard-model studies (see Abramowski et al. 2011, 2013). In our work, we consider any gamma-ray events in the FoV of PKS2155-304, except those coming from the source itself. We use observations taken between July 2004 and June 2013, organized in 28-minute exposure data-sets called runs. The run selection was done thoroughly, first, by selecting quality criteria (dead time inferior to 30 % of the run duration, trigger rate fluctuation low, and weather conditions acceptable (Aharonian et al. 2006b; Hahn et al. 2014)). This led to a good data quality run list of 735 items. We then created a sub-list of runs corresponding to four different observation positions or "wobble" positions. Indeed, as described in Aharonian et al. (2006b) observations are conducted in "wobble mode", on four positions around the sources with typical offset angles of 0.5-0.7 °. Due to the differences in observation campaigns, offset angles were spanning a large range of values for each wobble position : we selected runs with offset angles of 0.5 ± 0.05° on each position. For clarity we will call this subsets of data :"East", "South","North","West". The four wobble observation positions are shown in Figure 6.1. The final data set consists of 690 runs, corresponding to a total exposure of 304 hours (see Table 6.1). Zenith angle values are spanning 7 to 65°, and azimuth angle values are spanning 120 to 250°.

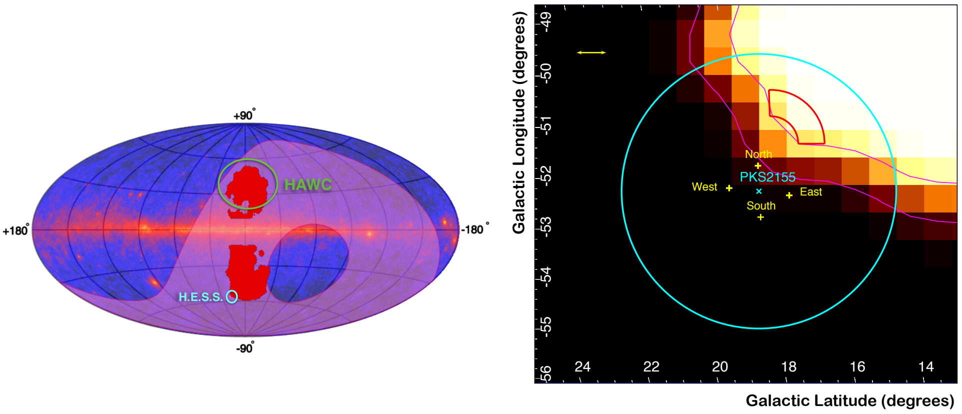

FIGURE 6.1 – Schematic maps showing the Fermi Bubble template (Ackermann et al. 2014). Left : the template is overlaid on the *Fermi*-LAT Galactic map. H.E.S.S. FoV is indicated in magenta. HAWC and H.E.S.S.(this work) observations of the FB are schematized with circles. Right : the template in the region of observation. PKS2155-304 position is shown in yellow, with a circle of radius 2.5° schematizing the H.E.S.S. FoV. The four wobble observation positions are represented in cyan. The edge is smoothed with a Gaussian of radius 1°. The magenta contours are produced with the smoothed template : the outer contour selects pixels with level > 0.7, the inner contour with level > 0.3 (white has a level 1). The source region used to extract the FB signal is shown in red. The yellow arrow indicates 0.5 °

.

6.2.3 H.E.S.S. Data analysis

Each selected run was analyzed using HAP (HESS analysis package) software, with standard cuts, selecting events with a minimum of 60 photo-electrons. The full enclosure configuration was used, suited for large source analysis. We use a larger FoV : normally it is limited to an offset angle of 2.5°, but for this analysis, it was set to an offset angle of 3°. The analysis is using a boosted decision tree-based event classification algorithm to discriminate gamma-ray events from the charged particle background (Ohm et al. 2009), and acceptance is generated from a data-base of extra-galactic runs (see Berge et al. 2007). A source region for the FB is selected with two constraints : we make the extraction region as large as possible, but still fitting within the H.E.S.S. FoV and being reliably within the FB. To give us a safety margin we generate two contours from the template provided in Ackermann et al. (2014) smoothed with a Gaussian of 1° : the white pixels having a level of 1, and the black ones a zero level, we choose the innermost contour (towards PKS2155-304) with a level of 0.3, and the outermost with a level of 0.7. We select the source region inside the outermost contour and the exclusion region to encompass most of the inner contour. The chosen source region is an arc of circle centered on l =17.08°, b= -51.30° with an inner radius of 0.5°, an outer radius of 0.98°, and spanning an angle of $\sim$ 90° (-9 ° to 88° from the trigonometric origin). This region has an area of 0.55 deg^2, which is $\sim$50 times bigger than the usual source region for point sources with a radius of 0.07°. ON events are selected from this region. Figure 6.1 shows the source region on the *Fermi*-LAT template.

To select the background (and OFF events) we first exclude PKS2155-304 and the FB from the FoV, with respectively a circle of radius 0.35°, and a 5° radius arc of a circle centered on l =17.57°, b= -51.70°, spanning 145°. Background regions are selected in the rest of the FoV symmetrically centered on the pointing position compared to the FB source region. This is done with the reflected-region background method as described in Berge et al. (2007). The central symmetry ensures consistency in offset for the source and background which can be treated with the same effective area lookup tables. This procedure is applied to each subset of data resulting in different offset angles for the source and background regions. ON, and OFF events maps as well as exclusion regions are shown for each wobble observation in Figure 6.5.

The excess is computed using $N_{excess} = N_{on} - \alpha N_{off}$, α correcting for the difference of solid angle in the OFF and ON extraction regions. In the case of the reflected-region background method, the α value is equivalent to the inverse of the number of the background region. For the whole data set a mean value of α is computed weighted by the ratio of OFF events in sub-sets compared to OFF events in the whole data-set. Significance is derived using Equation 17 of Li & Ma (1983). No significant excess is observed and an upper limit on the flux is therefore computed. The spectral statistics in the energy range of our interest (0.4 - 4 TeV) are reported in Table 6.1, for each wobble sub-set, and for the whole data-set. Spectra are binned in three energy ranges as described in Table 6.1 : these bins correspond to three logarithmic intervals between the last *Fermi*-LAT point and the first HAWC UL. Differential upper limits (UL) are computed with the method described in Rolke & Lopez (2001), with index 2 and 95 %CL, and considering a zero level in case negative excess. The provided UL is thus conservative and could be considered as a statistical error for the expected UL in case of a negative excess. Results were cross-checked using an independent calibration and analysis chain described (de Naurois & Rolland 2009) with the exact same data-set, the same regions, and the reflected-region background method with standard cuts.

Results reported in Table 6.1 reveal a negative excess, that could be due to a statistical fluctuation, but is not seen in the cross-checked analysis. This is particularly the case in the wobble modes observed at small offset (wobble East, and North) and amplified in the complete data-set. Our UL corrects for this negative excess by considering a zero level, nevertheless, we report an explanation on the possible source for this effect in the next Section.

6.2.4 Systematic errors

The systematic uncertainties due to the instrument and analysis are difficult to estimate : the main source of errors in the atmospheric conditions, which variation can not be well modeled by Monte Carlo simulation, especially seasonal variation that can affect data-set spanning many years. "HESSI" standard analysis generally leads to systematic errors estimated at $\sim 20\%$ on the norm value for the spectrum (Aharonian et al. 2006b). This value is considered in our results. In is important to note here that in standard analysis, the source is observed from four positions in different directions at a small offset. That "wobble" observation technique corrects naturally for any variation of events in the FoV or asymmetrical effects on the acceptance

Our analysis is non standard, as we search for diffuse emission extracting a large region for the source. In our case, although we use four wobble positions, the analysis is not standard for these main reason :

- The source region is on the same side of the FoV compared to the observation position.
- Observations are made at a larger offsets than is customary for H.E.S.S. analysis.
- Observation are spanning a large range in zenith and azimuth angles.
- PKS2155-304 is such a bright source that some emission could spill over into the exclusion region.

The two first points are related to an observed gradient of events through the FoV, which is more important at large offset. For our analysis, this gradient induces a systematic overestimate in the number of events. The gradient in the background extraction region is evaluated for wobble observation East and North (see Section 6.5) and a correction of $\sim 2 \pm 0.2\%$ is applied to the background level for the data sub-sets. The corrected data sub-set is added together with non-corrected sub-sets for observations West and South leading to a whole data-set corrected for the gradient of events in the FoV.

The corrected excess integrated over 0.4-4 TeV are reported in Table 6.1 : values are less negative, corrected from a -2.5 σ level to -0.3 σ for the whole data-set. The values reported in "UL + Systematics" include the correction for the gradient in the FoV and 20% systematic uncertainties : systematic errors are added quadratically to the ULs established considering a zero level. Some residual emissions from PKS2155-304, can not be excluded, as the source is very bright. A rather big exclusion region is chosen, and no obvious emission is seen on the events maps, but PKS2155-304 is reconstructed as a point source, which is modeled with a 2-dimensional fitting of three Gaussian. That does not take into account any asymmetrical emissions. Some residual emissions in one direction could participate in the negative excess for observations in wobble East and North, for which regions are extracted close to the blazar (see Figure 6.5). This hypothesis is not tested in our work.

Finally, it is important to note that the effective areas are computed for a mean zenith value, although our data-set is spanning a large zenith range. We consider the resulting effect marginal compared to the 20% systematic error and we ignore this potential source of systematic uncertainty.

6.3 Results and discussion

H.E.S.S. ULs are reported in Table 6.1 and shown in Figure 6.2, with systematic errors represented in shaded grey. The reported systematic uncertainties include 20% for the "HESSI" analysis and a correction for the gradient applied to observations towards the East and North (see Section 6.5). The effect of this correction is represented as a grey dashed line. Systematic errors are added quadratically to the ULs computed with a zero level. The correction for the gradient is the main effect, as shown by the dashed line in Figure 6.2. The first UL seems to be dominated by systematics, as the level varies by a factor of ~ 2 with the systematic errors. On the second and third points, the systematic errors have little effect. When correcting for the effect of a gradient in the FoV, the resulting excess of the whole data-set integrated over 0.4-4TeV is positive but in the differential ULs, only the first point exhibits a positive excess. Points above 0.86 TeV correspond to negative excesses down to 1 σ. As in these case, the excess remains negative, we might over-subtract the background at these energies and underestimate the systematic errors. The points are consistent within 1 σ with the results from the independent analysis chain considering the systematic errors.

Figure 6.2 is showing the H.E.S.S. ULs along with *Fermi*-LAT spectrum points for the South Bubble (Ackermann et al. 2014) and HAWC ULs (Abeysekara et al. 2017). The spectrum points are scaled by the surface of the observations : ~0.5 sr for *Fermi*-LAT and HAWC, compared to 0.55 deg^2 for H.E.S.S.. As can be seen, the ULs are a factor ~ 4 above the extrapolation of the average surface brightness found with the *Fermi*-LAT experiment, and also less constraining than the ULs reported by HAWC. However, it should be noted that for the *Fermi*-LAT the surface brightness is an average over the whole South FB, whereas for H.E.S.S. we report here the surface brightness for a small region in the South, near the edge. Similarly, the HAWC ULs pertain to the Northside of the bubble.

The spectral characteristics of the FB measured with *Fermi*-LAT indicate a steepening of the spectrum above ~ 0.1 TeV. But this steepening may be position-dependent. For example, in case the outer shock wave surrounding the FB is actively accelerating particles, we may expect some edge brightening only in VHE gamma-rays, since cooling of the accelerated electrons further downstream results in a suppression of VHE gamma-rays. This assumes a leptonic scenario for the GeV emission.

The H.E.S.S. ULs are not very constraining if one just extrapolates the peak in the SED with a power-law spectrum of $\propto E^{-2}$, as represented by the green dashed line. However, the ULs are competitive with a scenario in which at the edges the low energy spectrum (below ~ 3 GeV) can be extrapolated to the VHE energy regime, assuming at the edges radiative cooling is not important, unlike for the FB as a whole.

For a purely hadronic scenario radiative cooling is not important, which make it less likely to have large spectral differences across the whole FB, or to expect large edge brightening effects. Moreover, the low-energy spectrum is rather flat ($\Gamma \approx 1.5$), requiring in this scenario a spectral index for the protons of $q \approx 1.5$, which is rather flat for diffusive shock acceleration.

This argument also applies to a mixed scenario, if the low energy part is dominated by leptonic emission, the hadronic radiation component may take over at high energies. But in order to come close to the H.E.S.S. ULs the hadronic spectrum needs to be rather flat ($\Gamma \approx q \approx 1.5$).

Figure 6.2 shows two horizontal lines. The blue, dashed-dotted, line gives the 2σ sensitivity of H.E.S.S. that applies to our analysis[3] at 0.9×10^{-9} TeV s^{-1} cm^{-2}sr^{-1}. This is an estimation, and 2σ is chosen to account for ULs, but it gives an idea about the limits of the analysis : results could not be improved only by a factor of two. The green line shows approximately the peak in the SED of the FB as measured by the *Fermi*-LAT experiment. In order to tighten the H.E.S.S. ULs to that level a total exposure that is four times better than reported here is needed : 1200 hr.

---

[3] This sensitivity is based on the flux level of the extended remnant RCW 86 (Abramowski et al. 2018). RCW86 estimated radius is 0.41°, it was detected with H.E.S.S. at 18.3 σ for 57 hours, reaching a flux level of 3×10^{-12} TeV^{-1} s^{-1} cm^{-2} at 1 TeV. This value, scaled to 2 σ with our area of 0.55 deg^2 (corresponding to a circle with radius 4.2°), and our lifetime, leads to the reported sensitivity.

This is unrealistically long. So in order to put better constraints on the VHE surface brightness of the FB, either more data by HAWC or perhaps LHAASO (LHAASO collaboration 2021) needs to be reported. But these do not cover the southern part of the FB. So for the southern part a much more constraining observation is to be expected from the future generation of IACTs, as CTA (the Cherenkov Telescope Array ; Cherenkov Telescope Array Consortium 2019).

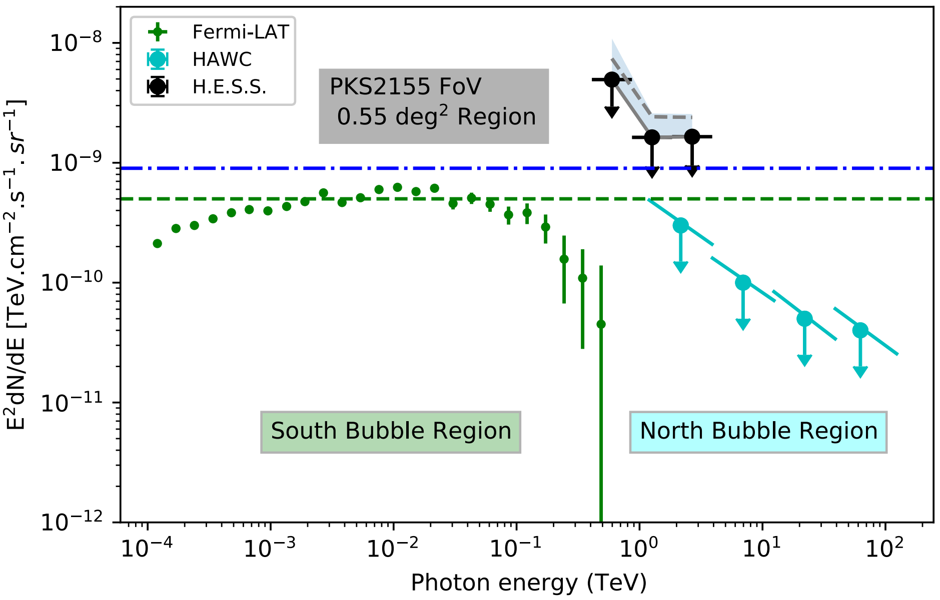

Figure 6.2 – 95 %CL upper limits on the flux of the FB emission in PKS2155-304 observation assuming 20% systematic errors. The shaded area corresponds to systematic errors due to a gradient of events in the FoV.

6.4 Conclusion

We searched for a TeV gamma-ray emission of the southern FB at large latitude, with deep observations taken by H.E.S.S.on the blazar PKS2155-304. We found no signal and establish UL on the flux at 1.3 TeV at 2.77×10^{-13} TeV^{-1} s^{-1} cm^{-2}. These UL scaled to our observation area lead to values of $E^2dN/dE = 3.42 \times 10^{-9}$ TeV s^{-1} cm^{-2} sr^{-1}. These are the first ULs provided around 1 TeV on the signal of the FB at large latitude. This value is one order of magnitude higher than the peak of the flux level reached in the GeV range : it does not provide a constraint

Statistic in the energy range 0.4-4 TeV								Corrected Values	
Data (runs)	Offset (deg)	Livetime (hrs)	N_{on}	N_{off}	α	Excess	Sig(σ)	Excess	Sig(σ)
West (184)	1.7-2.3	85	4370	26225	0.167	-0.83	-0.01	–	–
South (164)	1.8-2.5	70	1692	11830	0.143	2.0	0.05	–	–
East (190)	1.0-2.0	85	6237	32379	0.200	-238	-2.73	-42	-0.5
North (152)	1.0-1.5	64	6031	18378	0.333	-95	-1.05	31	0.28
All	1.0-2.5	304	18330	88812	0.210	-331	-2.43	-20	-0.32

Upper limits ($\times 10^{-9}$ TeV^{-1}cm^{-2}s^{-1} sr^{-1})			
	0.41-0.86 TeV	0.86-1.84 TeV	1.84-3.90 TeV
UL	4.94	1.63	1.65
UL + Systematics	10.61	1.80	1.78

Table 6.1 – Top : Observed statistics for the analysis extracted with the reflected-region method for each wobble position and for the whole data-set in the energy range 0.4-4 TeV. Bottom : 95% CL UL on the flux presented for the whole data-set for three energy bins : UL is computed from a zero level in case of negative excess. The UL values including the systematic errors are also reported (see text for details).

on whether the VHE gamma-ray spectrum is an extrapolation of the GeV spectrum with a power-law of index 2.

The analysis is limited to two factors : the uncertainties in the location of the FB emission in our FoV and the errors raised by the analysis. The non-standard settings are leading to important systematic errors that are partly estimated in this work. Results below 0.9 TeV are dominated by systematic. Above 1 TeV, the statistical level given by the UL assuming a zero level is dominant, and could potentially be improved by adding more observations. A rough estimate of the H.E.S.S. sensitivity for an extended source suggests that the provided ULs are reaching the limit of the analysis settings, especially the size of the extraction region.

Looking at the edge of the FB is may thus not be the right approach, given the many uncertainties. Extracting a bigger area in a brighter zone of the FB zone, and comparing it to the outside background could be more efficient for this faint signal, assuming observations are taken in the same zenith range, and that the systematic are mastered. That would in any case necessitate a lot of dedicated observations, as the area for the FB signal is limited by the H.E.S.S. FoV —thus 30 times bigger than the source region extracted in this work— leading to an sensitivity of the order of $\sim 5 \times 10^{-11}$TeV s^{-1} cm^{-2} sr^{-1} for 300 hours. Another alternative is to conduct analysis by comparing observations inside and outside the FBs similarly to what had been done for the Galactic ridge (Aharonian et al. 2006a). This could be conducted with an archival data-set, although in this case, the zenith range of observation has a bigger impact leading to a shift in the diffuse events with respect to zenith angle, inducing big systematic errors when stacking observations. Some diffuse search by scanning a large area of the FB at large b could be an approach. Note that a recent study using such an approach in the inner galaxy, using more than 600 hrs dedicated to date, could not establish any detection of the base of the FB and provide upper limits (Moulin et al. 2021). Finally, new tools for diffuse gamma-ray emission with a template could be used, such as gammapy (Mohrmann et al. 2019) assuming the systematic errors are mastered.

So far only IACTs could investigate the TeV emission from the FB as HAWC has the dedicated FOV but not the sensitivity. Maybe LHASSO in the future will be able to detect the diffuse gamma-ray emission from FB, although it is optimized for UHE detection. We could still use H.E.S.S. and improve the analysis skills, however the sensitivity should be improved by more than five times to detect such a faint signal. This is a good case for CTA, which could reach the required surface brightness level in 100-200 hr. Moreover, CTA has a larger FoV, which helps to better deal with the observational systematic uncertainties and background subtraction.

6.5 Appendix A : Evaluation of the gradient of events in the FoV

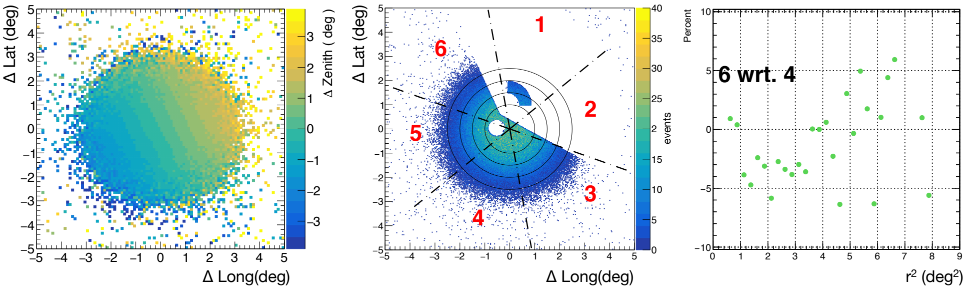

Figure 6.3 – Events distributions for the "wobble North" observations. Left : zenith event map for the whole data-set : zenith value for each event with coordinates relative to the observation coordinates. Middle : event map for the whole data-set, with coordinated relative to the observation coordinates, with six zones to extract events. Right : histogram of the difference of events from zone 6 with respect to zone 4 in percentage, plotted as the distance to the camera in square degrees.

When pointing to an object with a zenith angle θ, the two edges of the FoV present a small discrepancy in the zenith angle equivalent to $\theta \pm 2.5°$. This difference in zenith leads to a gradient of events through the FoV. Indeed fewer gamma-rays are reconstructed at large zenith ; the atmosphere is thicker and absorption and diffusion effects are more important. Even at zenith angle variations of 5°, this is noticeable. Figure 6.3 (left) shows the zenith angle value for each event in the FoV (for wobble North), with respect to the observation position. Near the center this difference is small ($\sim 1°$), although from one side of the FoV to the other it can lead to a zenith variation of $\sim$ 6°. In our analysis, we select ON and OFF events at large offset sometimes on the far edge of the FoV (see Figure 6.5). This leads to an overestimate of OFF events compared to ON events. If no correction is applied, a negative excess is recorded which is our case.

We estimate the systematic errors due to this gradient by evaluating the mean number of events in the FoV, using the different zones represented in Figure 6.3 (middle). The event map is sliced into six zones, with concentric circles at offset angles 1, 1.5, 2, and 2.5°. Events in FB and PKS2155-304 exclusion regions are not included. The FB source region in zone 1 is shown to guide the eye. We are interested in regions 3 to 6, where OFF events are extracted. In Figure 6.5 (right), events of zone 6 are subtracted to events of zone 4 and plotted with respect to squared offset. The percentages are negative for offset angles between 1 and 2°, and positive above. This offset range concerns the background extraction region for wobble East and North. For Wobble South and West, the extraction is taken at a larger offset which could explain the less negative excess. We use such a histogram to estimate differences of

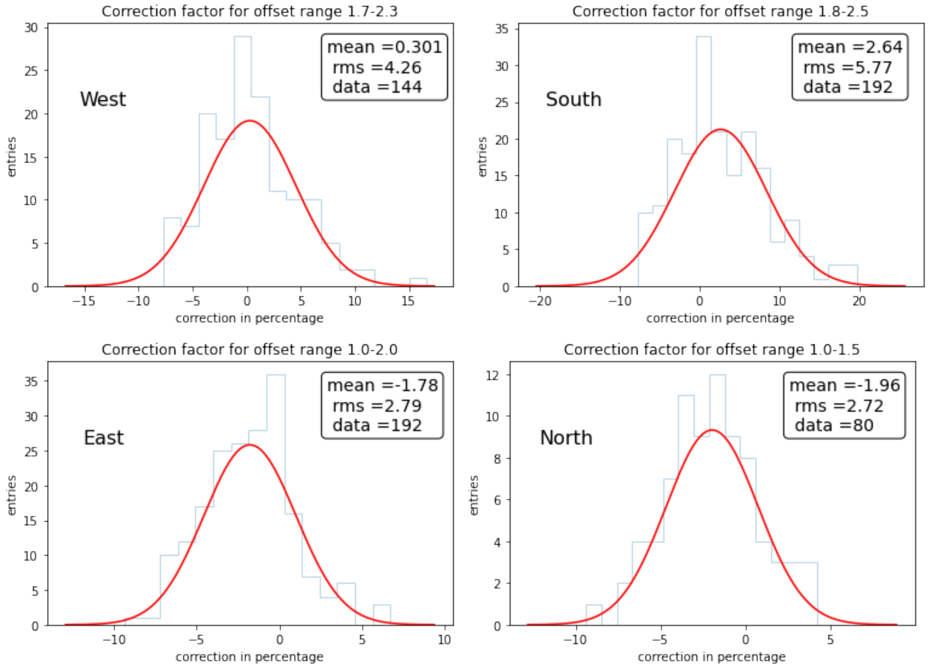

Figure 6.4 – Distribution of events in zone 6,3 compared to zone 4,5 given in percentage. A normal distribution fitted to the data is represented, mean and root mean square (RMS) values are reported. "Data" is the number of points considered to perform the fit. Distribution is regrouped in 15 bins. The four distributions are extracted in offset ranges corresponding to the wobble observations subsets – respectively, West, South, East, North.

events in zone 6 and 3 with respect to zones 5 and 4. This leads to a distribution of a few values ($\sim$ 100) for which a mean and variance can be computed. The mean is the average gradient affecting the background extraction area, the variance is the difference of gradient from 6/5, 6/4, and 3/4, 3/5. We consider the mean as an overall correction to apply to the background level of the considered wobble observations. We apply the correction to the off exposure of the data-set, which has a direct effect on the value of alpha, and correct for the negative excess. The variance could account for some statistical error on the estimation of the background level but is not taken into account in this work.

We checked that no significant variation in the mean and variance values is observed with respect to the zenith angle, neither to the wobble position. A correction is then computed using the whole data-set event map, and selecting the offset range corresponding to each wobble observation mode. The distributions are shown in Figure 6.4.

We correct for wobble East and wobble North for which a negative gradient is found of the order of $\sim 2\% \pm 0.2$. We apply the correction to the considered observations, before adding it to the whole data-set and generate the corresponding UL with the Rolke method. Corrected excess values are reported in Table 6.1. We can note here that another way to correct for the gradient is to include a 2-dimensional correction in the acceptance map and applied it run by run : this is for example implemented in the method used for the crosscheck as described in de Naurois & Rolland (2009).

6.6 Appendix B : Maps by wobble observations

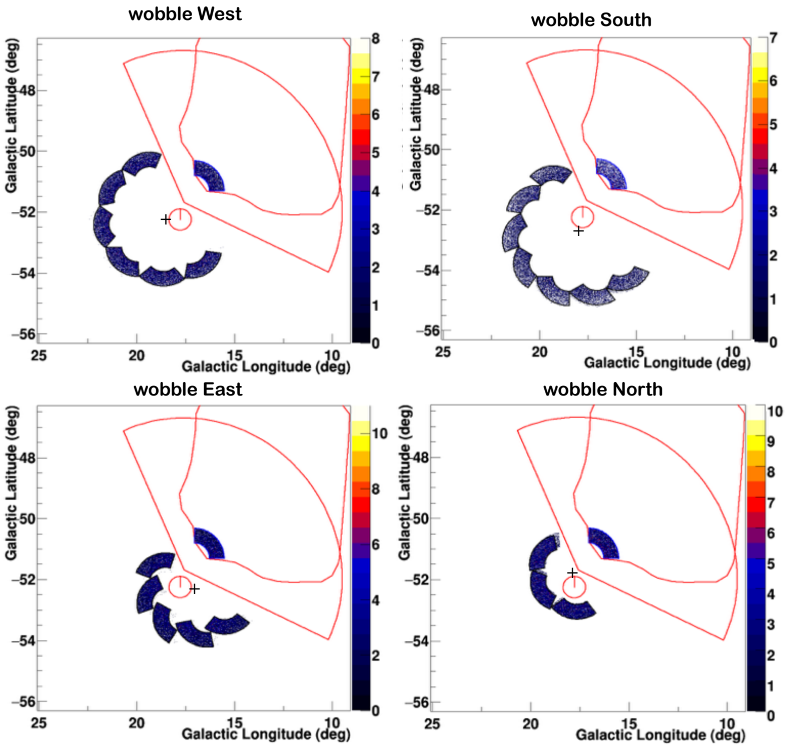

Figure 6.5 – Events maps for sub-set of data for the four wobble observation positions. In red are represented the exclusion regions, as well as the FB template contour. Observation positions are represented with a cross.

Bibliographie

Abdalla, H., Abramowski, A., Aharonian, F., et al. 2017, A&A, 600, A89

Abdalla, H., Abramowski, A., Aharonian, F., et al. 2018a, A&A, 612, A9

Abdalla, H., Abramowski, A., Aharonian, F., et al. 2018b, A&A, 612, A6

Abdalla, H., Abramowski, A., Aharonian, F., et al. 2018c, A&A, 612, A1

Abdalla, H., Abramowski, A., Aharonian, F., et al. 2018d, A&A, 612, A5

Abdalla, H., Abramowski, A., Aharonian, F., et al. 2018b, A&A, 612, A2

Abdalla, H., Abramowski, A., Aharonian, F., et al. 2018c, A&A, 612, A3

Abdalla, H., Abramowski, A., Aharonian, F., et al. 2018d, A&A, 612, A6

Abdalla, H., Abramowski, A., Aharonian, F., et al. 2018e, A&A, 612, A7

Abdalla, H., Abramowski, A., Aharonian, F., et al. 2018e, A&A, 612, A8

Abdalla, H., Abramowski, A., Aharonian, F., et al. 2018f, A&A, 610, L17

Abdalla, H., Adam, R., Aharonian, F., et al. 2019, Nature, 575, 464

Abdalla, H., Aharonian, F., Ait Benkhali, F., et al. 2021, Science, 372, 1081

Abdalla, H., Aharonian, F., Ait Benkhali, F., et al. 2019, A&A, 626, A57

Abdo, A. A., Ackermann, M., Ajello, M., et al. 2011, ApJ, 734, 28

Abdo, A. A., Ackermann, M., Ajello, M., et al. 2010, ApJ, 709, L152

Abdollahi, S., Acero, F., Ackermann, M., et al. 2020, ApJS, 247, 33

Abeysekara, A. U., Alfaro, R., Alvarez, C., et al. 2013, Astropart. Phys., 50-52, 26

Abeysekara, A. U., Albert, A., Alfaro, R., et al. 2017, ApJ, 842, 85

Abeysekara, A. U., Archer, A., Benbow, W., et al. 2020, ApJ, 894, 51

Abeysekara, A. U., Archer, A., Benbow, W., et al. 2020, American Astronomical Society, 894, 51

Abraham, J., Aglietta, M., Aguirre, I., et al. 2004, Nuclear Instruments and Methods in Physics Research Section, 523, 50

Abramowski, A., Acero, F., Aharonian, F., et al. 2012, A&A, 545, L2

Abramowski, A., Aharonian, F., Ait Benkhali, F., et al. 2008, A&A, 481, 401

Abramowski, A., Acero, F., Aharonian, F., et al. 2010, A&A, 520, A83

Abramowski, A., Acero, F., Aharonian, F., et al. 2011, Astropart. Phys., 34, 738

Abramowski, A., Acero, F., Aharonian, F., et al. 2012, A&A, 539, A149

Abramowski, A., Acero, F., Aharonian, F., et al. 2013, Phys. Rev. D, 88, 102003

Abramowski, A., Aharonian, F., Ait Benkhali, F., et al. 2014a, Phys. Rev. D, 90, 122007

Abramowski, A., Aharonian, F., Benkhali, F. A., et al. 2014b, MNRAS, 439, 2828

Abramowski, A., Aharonian, F., Ait Benkhali, F., et al. 2014a, A&A, 562, A40

Abramowski, A., Aharonian, F., Ait Benkhali, F., et al. 2015a, A&A, 575, A81

Abramowski, A., Aharonian, F., Benkhali, F. A., et al. 2015b, Science, 347, 406

Abramowski, A., Aharonian, F., Ait Benkhali, F., et al. 2018, A&A, 612, A4

Abramowski, A. Ostrowski, M., Oya, I., Panter, M., & Parsons. 2014b, MNRAS, 441, 3640

Abramowski, A., Aharonian, F., Ait Benkhali, F., et al. 2015, A&A, 574, A100

Abu-Zayyad, T., Aida, R., Allen, M., et al. 2013, The Astrophysical Journal Letters, 768, L1

Acciari, V. A., Aliu, E., Arlen, T., et al. 2009, ApJ, 703, L6

Acciari, V. A., Aliu, E., Arlen, T., et al. 2011, ApJ, 730, L20

Acciari, V. A., Ansoldi, S., Antonelli, L. A., et al. 2020, A&A, 635, A158

Acciari, V. A., Ansoldi, S., Antonelli, L. A., et al. 2021, ApJ, 908, 90

Acero, F., Aharonian, F., Akhperjanian, A. G., et al. 2010, A&A, 516, A62

Acero, F., Ackermann, M., Ajello, M., et al. 2016, ApJ Supplement Series, 224, 8

Acharya, B., Actis, M., Aghajani, T., et al. 2013, Astropart. Phys., 43, 3 , seeing the High-Energy Universe with the Cherenkov Telescope Array - The Science Explored with the CTA

Acharya, B. S., Aramo, C., Babic, A., et al. 2015, Astropart. Phys., 62, 152

Ackermann, M., Ajello, M., Allafort, A., et al. 2013, Science, 339, 807

Ackermann, M., Albert, A., Atwood, W. B., et al. 2014, ApJ, 793, 64

Ackermann, M., Arcavi, I., Baldini, L., et al. 2015, ApJ, 807, 169

Ackermann, M., Albert, A., Atwood, W. B., et al. 2016, A&A, 586, A71

Ackermann, M., Ajello, M., Albert, A., et al. 2017, ApJ, 840, 43

Ade, P. a. R., Aghanim, N., Arnaud, M., et al. 2013, A&A, 554, A139, publisher : EDP Sciences

Aharonian, F., Akhperjanian, A., Aye, K.-M., et al. 2004a, Astropart. Phys., 22, 109

Aharonian, F., Akhperjanian, A., Barrio, A., et al. 2001, A&A, 370, 112

Aharonian, F., Akhperjanian, A. G., Aye, K.-M., et al. 2004b, A& A, 425, 13âĂŞ17

Aharonian, F., Akhperjanian, A. G., Aye, K. M., et al. 2005, A&A, 430, 865

Aharonian, F., Akhperjanian, A. G., Bazer-Bachi, A. R., et al. 2006a, Nature, 439, 695

Aharonian, F., Akhperjanian, A. G., Bazer-Bachi, A. R., et al. 2006b, A&A, 457, 899

Aharonian, F., Akhperjanian, A. G., Barres de Almeida, U., et al. 2008a, A&A, 490, 685

Aharonian, F., Akhperjanian, A. G., Barres de Almeida, U., et al. 2008b, A&A, 483, 509

Aharonian, F., Akhperjanian, A. G., Barres de Almeida, U., et al. 2008c, A&A, 488, 219

Aharonian, F., Akhperjanian, A. G., Anton, G., et al. 2009, ApJ, 695, L40

Aharonian, F. A., & Atoyan, A. M. 1996, A&A, 309, 917

Aharonian, F. A., Kelner, S. R., & Prosekin, A. Y. 2010, Physical Review D, 82, 043002

Ahnen, M. L., Ansoldi, S., Antonelli, L. A., et al. 2017, MNRAS, 472, 2956

Ahnen, M. L., Ansoldi, S., Antonelli, L. A., et al. 2017, A&A, 602, A98

Ahnen, M. L., Ansoldi, S., Antonelli, L. A., et al. 2019, MNRAS, 485, 356

Akaike, H. 1974, IEEE transactions on automatic control, 19, 716

Albert, A., Alfaro, R., Alvarez, C., et al. 2020, ApJ, 905, 76

Allen, G. 1999, in International Cosmic Ray Conference, Vol. 3, 26th International Cosmic Ray Conference (ICRC26), Volume 3, 480

Allen, G. E., Gotthelf, E. V., & Petre, R. 1999, in International Cosmic Ray Conference, Vol. 3, 26th International Cosmic Ray Conference (ICRC1999), 480

Amenomori, M., Bao, Y. W., Bi, X. J., et al. 2021a, Phys. Rev. Lett., 126, 141101

Amenomori, M., Bao, Y. W., Bi, X. J., et al. 2021b, Nat Astron, 5, 460, bandiera_abtest : a Cg_type : Nature Research Journals Number : 5 Primary_atype : Research Publisher : Nature Publishing Group Subject_term : High-energy astrophysics ;Particle astrophysics Subject_term_id : high-energy-astrophysics ;particle-astrophysics

Anderson, C. D. 1932, Science, 76, 238

Anderson, C. D., & Neddermeyer, S. H. 1936, Phys. Rev., 50, 263, publisher : American Physical Society

Andrews, J. E., Jencson, J. E., Dyk, S. D. V., et al. 2021, American Astronomical Society, 917, 63

Arcavi, I., Hosseinzadeh, G., Brown, P. J., et al. 2017, ApJ, 837, L2

Archambault, S., Archer, A., Benbow, W., et al. 2017, ApJ, 836, 23

Ashton, T., Backes, M., Balzer, A., et al. 2020a, Astropart. Phys., 118, 102425

Ashton, T., Backes, M., Balzer, A., et al. 2020b, Astropart. Phys., 118, 102425

Asvarov, A. I., Guseinov, O. H., Kasumov, F. K., & Dogel', V. A. 1990, A&A, 229, 196

Atoyan, A., & Dermer, C. D. 2012, ApJ, 749, L26

Atwood, W. B., Abdo, A. A., Ackermann, M., et al. 2009, ApJ, 697, 1071

Baade, W., & Zwicky, F. 1934a, Proceedings of the National Academy of Science, 20, 259

Baade, W., & Zwicky, F. 1934b, Proceedings of the National Academy of Science, 20,

254
Badenes, C., Bravo, E., Borkowski, K. J., & Domínguez, I. 2003, ApJ, 593, 358
Balzer, A. 2010, Master's thesis, U. Erlangen-Nuremberg (main)
Balzer, A. 2014, doctoralthesis, Universität Potsdam
Balzer, A., Füßling, M., Gajdus, M., et al. 2014, Astropart. Phys., 54, 67
Bamba, A., Yamazaki, R., Yoshida, T., Terasawa, T., & Koyama, K. 2005, The Astrophysical Journal, 621, 793
Bamba, A., Ohira, Y., Yamazaki, R., et al. 2018, ApJ, 854
Banas, K. R., Hughes, J. P., Bronfman, L., & Nyman, L.-A. 1997, ApJ, 480, 607
Bandiera, R. 1987, ApJ, 319, 885
Baring, M. G., Ellison, D. C., Reynolds, S. P., Grenier, I. A., & Goret, P. 1999, ApJ, 513, 311
Bartel, N., Bietenholz, M. F., Rupen, M. P., et al. 2002, ApJ, 581, 404
Bedin, L. R., Ruiz-Lapuente, P., González Hernández, J. I., et al. 2014, MNRAS, 439, 354
Behar, E., Rasmussen, A. P., Griffiths, R. G., et al. 2001, A&A, 365, L242
Bell, A., Schure, K., Reville, B., & Giacinti, G. 2013, MNRAS, 431, 415
Bell, A. R. 1978a, MNRAS, 182, 147
Bell, A. R. 1978b, MNRAS, 182, 443
Bell, A. R. 2004, MNRAS, 353, 550
Berezhko, E. G. 1996, Astropart. Phys., 5, 367
Berezhko, E. G., Ksenofontov, L. T., & Völk, H. J. 2006, A&A, 452, 217
Berezhko, E. G., Ksenofontov, L. T., & Völk, H. J. 2012, ApJ, 759, 12
Berge, D., Funk, S., & Hinton, J. 2007, A&A, 466, 1219
Bernlöhr, K. 2008, Astropart. Phys., 30, 149
Bernlohr, K., Carrol, O., Cornils, R., et al. 2003, Astropart. Phys., 20, 111
Bi, B., Barcelo, M., Bauer, C., et al. 2021, PoS, ICRC2021, 743
Bietenholz, M. F., Bartel, N., Argo, M., et al. 2021, ApJ, 908, 75
Björnsson, C. I., & Keshavarzi, S. T. 2017, ApJ, 841, 12
Blandford, R., & Eichler, D. 1987, Phys. Rep., 154, 1
Bolmont, J., Corona, P., Gauron, P., et al. 2014, Nuclear Instruments and Methods in Physics Research A, 761, 46
Borkowski, K. J., Hendrick, S. P., & Reynolds, S. P. 2007, ApJ, 671, L45
Bose, S., Dong, S., Kochanek, C. S., et al. 2021, MNRAS, 503, 3472
Braiding, C., Wong, G. F., Maxted, N. I., et al. 2018, Publications of the Astronomical Society of Australia, 35, e029
Burbidge, G. R. 1956, ApJ, 124, 416
Burkey, M. T., Reynolds, S. P., Borkowski, K. J., & Blondin, J. M. 2013a, ApJ, 764, 63
Burkey, M. T., Reynolds, S. P., Borkowski, K. J., & Blondin, J. M. 2013b, ApJ, 764, 63

Burkey, M. T., Reynolds, S. P., Borkowski, K. J., & Blondin, J. M. 2013c, ApJ, 764, 63

Bykov, A. M., Ellison, D. C., Marcowith, A., & Osipov, S. M. 2018, Space Sci. Rev., 214, 41

Campana, R., Massaro, E., & Bernieri, E. 2018, Ap&SS, 363, 144

Cao, Z., Aharonian, F. A., An, Q., et al. 2021, Nature, 594, 33

Cardillo, M., Amato, E., & Blasi, P. 2015, Astropart. Phys., 69, 1

Cardillo, M., Tavani, M., Giuliani, A., et al. 2014, A&A, 565, A74

Carretti, E., Crocker, R. M., Staveley-Smith, L., et al. 2013, Nature, 493, 66

Cash, W. 1979, ApJ, 228, 939

Chakraborti, S., Ray, A., Smith, R., et al. 2013, ApJ, 774, 30

Chalme-Calvet, R., de Naurois, M., & Tavernet, J. P. 2014, Muon efficiency of the H.E.S.S. telescope, arXiv:1403.4550 [astro-ph.IM]

Chen, Y., Zhang, F., Williams, R. M., & Wang, Q. D. 2003, ApJ, 595, 227

Cheng, K. S., Chernyshov, D. O., Dogiel, V. A., & Ko, C. M. 2015a, ApJ, 799, 112

Cheng, K. S., Chernyshov, D. O., Dogiel, V. A., & Ko, C. M. 2015b, ApJ, 804, 135

Cherenkov Telescope Array Consortium. 2019, Science with the Cherenkov Telescope Array (WORLD SCIENTIFIC), https://www.worldscientific.com/doi/pdf/10.1142/10986

Chevalier, R. A. 1982, ApJ, 259, 302

Chevalier, R. A. 1982a, ApJ, 258, 790

Chevalier, R. A., & Fransson, C. 1994, ApJ, 420, 268

Chevalier, R. A., & Fransson, C. 2016, ArXiv e-prints, arXiv:1612.07459 [astro-ph.HE], ads

Chevalier, R. A., & Soderberg, A. M. 2010, ApJ, 711, L40

Chiotellis, A., Schure, K. M., & Vink, J. 2012, A&A, 537, A139

Cornils, R., Bernlöhr, K., Heinzelmann, G., Hofmann, W., & Panter, M. 2005, in International Cosmic Ray Conference, Vol. 5, 29th International Cosmic Ray Conference (ICRC29), Volume 5, 171

Cristofari, P., Blasi, P., & Amato, E. 2020, Astropart. Phys., 123, 102492

Crocker, R. M. 2012, MNRAS, 423, 3512

Crocker, R. M., & Aharonian, F. 2011, Phys. Rev. Lett., 106, 101102

Crocker, R. M., Bicknell, G. V., Carretti, E., Hill, A. S., & Sutherland, R. S. 2014, ApJ, 791, L20, arXiv : 1312.0692

Crocker, R. M., Bicknell, G. V., Taylor, A. M., & Carretti, E. 2015, ApJ, 808, 107

Das, K. K., Zucker, C., Speagle, J. S., et al. 2020, MNRAS, 498, 5863

Das, S., & Ray, A. 2017, The Astrophysical Journal, 851, 138

Daum, A., Hermann, G., Heß, M., et al. 1997, Astropart. Phys., 8, 1

Davies, B., & Beasor, E. 2018, MNRAS, 474, 2116

Davies, J. M., & Cotton, E. S. 1957, Solar Energy, 1, 16

De Angelis, A., Giglietto, N., & Stramaglia, S. 2010, arXiv e-prints, arXiv:1002.2888 de Jager, C., Nieuwenhuijzen, H., & van der Hucht, K. A. 1988, A&AS, 72, 259

De Naurois, M. 2012, Habilitation à diriger des recherches, Université Pierre et Marie Curie - Paris VI

de Naurois, M., & Rolland, L. 2009, Astropart. Phys., 32, 231

DeLaney, T., Koralesky, B., Rudnick, L., & Dickel, J. R. 2002, ApJ, 580, 914

Dermer, C. D., & Powale, G. 2013, A&A, 553, A34

Devin, J., Bregeon, J., Vasileiadis, G., & Gallant, Y. 2019, in European Physical Journal Web of Conferences, Vol. 197, European Physical Journal Web of Conferences, 01001

Dickel, J. R., & Milne, D. K. 1995, The Astronomical Journal, 109, 200

Dobler, G., & Finkbeiner, D. P. 2008, ApJ, 680, 1222, publisher : IOP Publishing

Drury, L. O., Aharonian, F. A., & Voelk, H. J. 1994, A&A, 287, 959

Dubner, G., & Giacani, E. 2015, A&A Rev., 23, 3

Duncan, A. R., Stewart, R. T., Haynes, R. F., & Jones, K. L. 1997, MNRAS, 287, 722

Dwarkadas, V. V. 2013, MNRAS, 434, 3368

Ebrahim, R., Chen, A., Prokhorov, D., et al. 2020, in Proceedings of 7th Annual Conference on High Energy Astrophysics in Southern Africa âĂŤ PoS(HEASA2019), 018

Fang, K., Metzger, B. D., Murase, K., Bartos, I., & Kotera, K. 2019, ApJ, 878, 34

Fermi, E. 1949, Phys. Rev., 75, 1169

Fernandez, D., Hahn, J., Marandon, V., et al. 2013, in International Cosmic Ray Conference, Vol. 33, International Cosmic Ray Conference, 2682

Fox, A. J., Bordoloi, R., Savage, B. D., et al. 2015, ApJ, 799, L7

France, K., Beasley, M., Keeney, B. A., et al. 2009, ApJ, 707, L27

Fransson, C., & Björnsson, C.-I. 1998, ApJ, 509, 861

Freeman, P., Doe, S., & Siemiginowska, A. 2001, in Astronomical Data Analysis, ed. J.-L. Starck & F. D. Murtagh, Vol. 4477, International Society for Optics and Photonics (SPIE), 76

Fujita, Y., Ohira, Y., & Yamazaki, R. 2014, ApJ, 789, 67

Fuller, J. 2017, MNRAS, 470, 1642

Gabici, S. 2017, in American Institute of Physics Conference Series, Vol. 1792, 6th International Symposium on High Energy Gamma-Ray Astronomy, 020002

Gabici, S., & Aharonian, F. A. 2007, ApJ, 665, L131

Gabici, S., & Aharonian, F. A. 2014, MNRAS, 445, L70

Gabici, S., Aharonian, F. A., & Casanova, S. 2009, MNRAS, 396, 1629

Gal-Yam, A. 2012, Science, 337, 927

Gamezo, V. N., Khokhlov, A. M., & Oran, E. S. 2005, ApJ, 623, 337

Gandhi, P., Yamanaka, M., Tanaka, M., et al. 2013, ApJ, 767, 166

Giacinti, G., & Taylor, A. M. 2017, ArXiv e-prints, arXiv:1710.11082

Ginzburg, V. L. 1972, Nature Physical Science, 239, 8

Ginzburg, V. L., & Syrovatskii, S. I. 1964, The Origin of Cosmic Rays (Oxford, New

York, Pergamon Press)

Giuliani, A., Cardillo, M., Tavani, M., et al. 2011, ApJ, 742, L30

Gomez, H. L., Clark, C. J. R., Nozawa, T., et al. 2012, MNRAS, 420, 3557

Gottschall, D. 2018, PhD thesis, Universität Tübingen

Green, D. A. 2019, Journal of Astrophysics and Astronomy, 40, 36

Green, D. A., & Stephenson, F. R. 2017, Possible and Suggested Historical Supernovae in the Galaxy (Springer, Cham), 179

Guo, F., & Mathews, W. G. 2012, ApJ, 756, 181, arXiv : 1103.0055

Gutiérrez, C. P., Anderson, J. P., Hamuy, M., et al. 2017, ApJ, 850, 90

Hahn, J., de los Reyes, R., Bernlöhr, K., et al. 2014, Astropart. Phys., 54, 25

Hallmann, S., Eberl, T., & KM3NeT collaboration. 2017, Journal of Physics: Conference Series, 888, 012102

Harris, G. L. H. 2010, PASA, 27, 475

Hayakawa, T., Torii, K., Enokiya, R., Amano, T., & Fukui, Y. 2012, PASJ, 64, 8

Hayashida, M., Stawarz, Ł., Cheung, C. C., et al. 2013, ApJ, 779, 131

Heck, D., Knapp, J., Capdevielle, J. N., Schatz, G., & Thouw, T. 1998, CORSIKA : a Monte Carlo code to simulate extensive air showers.

Helder, E. A., & Vink, J. 2008, ApJ, 686, 1094

Helder, E. A., Vink, J., Bykov, A. M., et al. 2012, Space Sci. Rev., 173, 369

Helfand, D. J., & Becker, R. H. 1987, ApJ, 314, 203

Herold, L., & Malyshev, D. 2019, A&A, 625, A110

H.E.S.S. Collaboration, Abdalla, H., Aharonian, F., et al. 2019, A& A, 626, A57

H.E.S.S. Collaboration, Abdalla, H., Aharonian, F., Ait Benkhali, F., et al. 2021, A& A, 655, A7

Hewitt, J. W., Grondin, M.-H., Lemoine-Goumard, M., et al. 2012, ApJ, 759, 89

Hewitt, J. W., & Lemoine-Goumard, M. 2015, Comptes Rendus Physique, 16, 674

Hillas, A. M. 1982, Journal of Physics G Nuclear Physics, 8, 1475

Hillas, A. M. 1984, ARA&A, 22, 425

Hillas, A. M. 1985, in ICRC, Vol. 3, [Proc.(ICRC19), Volume 3, 445

Hillas, A. M. 2006, arXiv e-prints, astro

Hinton, J. A., & HESS Collaboration. 2004, New A Rev., 48, 331

Hinton, J. A., & Hofmann, W. 2009a, ARA&A, 47, 523

Hinton, J. A., & Hofmann, W. 2009b, ARA&A, 47, 523

Hofverberg, P., Chaves, R. C. G., Fiasson, A., et al. 2010a, in 25th Texas Symposium on Relativistic Astrophysics, 196

Hofverberg, P., Chaves, R. C. G., Fiasson, A., et al. 2010b, in 25th Texas Symposium on Relativistic Astrophysics, 196

Holder, J. 2012, Astropart. Phys., 39, 61

Horiuchi, S., Beacom, J. F., Kochanek, C. S., et al. 2011, ApJ, 738, 154

Hughes, J. P. 1987, ApJ, 314, 103

Hughes, J. P. 2000, ApJ, 545, L53

Hughes, J. P., Hayashi, I., & Koyama, K. 1998, ApJ, 505, 732

Hwang, U., Decourchelle, A., Holt, S. S., & Petre, R. 2002, ApJ, 581, 1101

Hwang, U., Hughes, J. P., & Petre, R. 1998, ApJ, 497, 833

Hwang, U., Petre, R., & Flanagan, K. A. 2008, ApJ, 676, 378

IceCube Collaboration, Aartsen, M. G., Ackermann, M., et al. 2018, Science, 361, eaat1378

Čerenkov, P. A. 1937, Phys. Rev., 52, 378

Inoue, T., Yamazaki, R., Inutsuka, S.-i., & Fukui, Y. 2012, ApJ, 744, 71

Ishihara, D., Kaneda, H., Furuzawa, A., et al. 2010, A&A, 521, L61

Jogler, T., & Funk, S. 2016, The Astrophysical Journal, 816, 100

Kafexhiu, E., Aharonian, F., Taylor, A. M., & Vila, G. S. 2014, Physical Review D, 90, 123014

Kataoka, J., Tahara, M., Totani, T., et al. 2013, ApJ, 779, 57, publisher : American Astronomical Society

Katz, B., Sapir, N., & Waxman, E. 2011, Proceedings of the International Astronomical Union, 7, 274

Katz, B., & Waxman, E. 2008, J. Cosmology Astropart. Phys., 2008, 018

Kelner, S. R., Aharonian, F. A., & Bugayov, V. V. 2006, Phys. Rev. D, 74, 034018

Khangulyan, D., Aharonian, F. A., & Kelner, S. R. 2014, ApJ, 783, 100

Khokhlov, A. M. 1991, A&A, 245, 114

Kiewe, M., Gal-Yam, A., Arcavi, I., et al. 2012, ApJ, 744, 10

Kinugasa, K., & Tsunemi, H. 1999, PASJ, 51, 239

Kothes, R., Fedotov, K., Foster, T. J., & Uyanıker, B. 2006, A&A, 457, 1081

Koyama, K., Petre, R., Gotthelf, E. V., et al. 1995, Nature, 378, 255

Kozlova, A. V., & Blinnikov, S. I. 2018, in Journal of Physics Conference Series, Vol. 1038, Journal of Physics Conference Series, 012006

Krause, O., Tanaka, M., Usuda, T., et al. 2008, Nature, 456, 617

Kumar, S. 2015, arXiv preprint arXiv :1508.07453

Lacki, B. C. 2014, MNRAS, 444, L39

Lagage, P. O., & Cesarsky, C. J. 1983, A&A, 125, 249

Lattes, C. M. G., Occhialini, G. P. S., & Powell, C. F. 1947, Nature, 160, 453

Lemoine-Goumard, M., & Ballet, J. 2021, PoS, ICRC2021, 594

Lemoine-Goumard, M., Grondin, M.-H., Acero, F., et al. 2014, ApJ, 794

Lennarz, D., & the H.E.S.S. Collaboration. 2013, ArXiv e-prints, arXiv:1307.7727 [astro-ph.HE], ads

LHAASO collaboration. 2021, arXiv e-prints, arXiv:2101.03508

Li, T.-P., & Ma, Y.-Q. 1983, ApJ, 272, 317

Li, T.-P., & Ma, Y.-Q. 1983, The Astrophysical Journal, 272, 317

Li, W., Chornock, R., Leaman, J., et al. 2011, MNRAS, 412, 1473

Liu, B., Yang, R.-z., Sun, X.-n., Aharonian, F., & Chen, Y. 2019, ApJ, 881, 94

Longair, M. S. 2011, High Energy Astrophysics (University of Cambridge)

Maggi, P., Haberl, F., Kavanagh, P. J., et al. 2016, A&A, 585, A162

Makino, K., Fujita, Y., Nobukawa, K. K., Matsumoto, H., & Ohira, Y. 2019, PASJ, 71, 78

Malkov, M. A. 1999, ApJ, 511, L53

Malkov, M. A., & Drury, L. O. 2001, Reports on Progress in Physics, 64, 429

Marcowith, A., Dwarkadas, V. V., Renaud, M., Tatischeff, V., & Giacinti, G. 2018, MNRAS, 479, 4470

Marcowith, A., Dwarkadas, V. V., Renaud, M., Tatischeff, V., & Giacinti, G. 2018, MNRAS, 479, 4470

Marcowith, A., Renaud, M., Dwarkadas, V., & Tatischeff, V. 2014, Nuclear Physics B Proceedings Supplements, 256, 94

Mariaud, C. 2018, Phdthesis, Université Paris-Saclay

Marples, P., Bock, G., & Parker, S. 2016, The Astronomer's Telegram, 8651, ads

Martí-Vidal, I., Pérez-Torres, M. A., & Brunthaler, A. 2011, A&A, 529, A47

Massardi, M., López-Caniego, M., González-Nuevo, J., et al. 2009, MNRAS, 392, 733

Mathewson, D. S., Ford, V. L., Dopita, M. A., et al. 1983, ApJ Supplement Series, 51, 345

Mattila, S., Fraser, M., Smartt, S. J., et al. 2013, MNRAS, 431, 2050

Mattox, J. R., Bertsch, D. L., Chiang, J., et al. 1996, ApJ, 461, 396

Mauron, N., & Josselin, E. 2011, A&A, 526, A156

McQuinn, K. B. W., Skillman, E. D., Dolphin, A. E., Berg, D., & Kennicutt, R. 2017, AJ, 154, 51

Minkowski, R. 1957, in Radio astronomy, ed. H. C. van de Hulst, Vol. 4, 107

Mohrmann, L., Specovius, A., Tiziani, D., et al. 2019, A&A, 632, A72

Moré, J. J. 1978, in Numerical analysis (Springer), 105

Mori, M. 1997, ApJ, 478, 225

Moriya, T., Tominaga, N., Blinnikov, S. I., Baklanov, P. V., & Sorokina, E. I. 2011, MNRAS, 415, 199

Morlino, G., & Caprioli, D. 2012, A&A, 538, A81

Moskalenko, I. V., Porter, T. A., Malkov, M. A., & Diamond, P. H. 2008, in International Cosmic Ray Conference, Vol. 2, International Cosmic Ray Conference, 763

Moulin, E., Montanari, A., Malyshev, D., & Malyshev, D. 2021, arXiv e-prints, arXiv:2108.10028

Murase, K., Thompson, T. A., Lacki, B. C., & Beacom, J. F. 2011, Phys. Rev. D, 84, 043003

Murase, K., Thompson, T. A., & Ofek, E. O. 2014, MNRAS, 440, 2528

Nagao, T., Cikota, A., Patat, F., et al. 2019, MNRAS: Letters, 489, L69

Nagayoshi, T., Bamba, A., Katsuda, S., & Terada, Y. 2021, PASJ, 73, 302

Nyholm, A., Sollerman, J., Taddia, F., et al. 2017, A&A, 605, A6

Nymark, T. K., Fransson, C., & Kozma, C. 2006, A&A, 449, 171

Ofek, E. O., Sullivan, M., Shaviv, N. J., et al. 2014, ApJ, 789, 104

Oh, K., Koss, M., Markwardt, C. B., et al. 2018, ApJS, 235, 4

Ohm, S., van Eldik, C., & Egberts, K. 2009, Astropart. Phys., 31, 383

O'Sullivan, E., Ponman, T. J., Kolokythas, K., et al. 2017, MNRAS, 472, 1482

Ouchi, R., & Maeda, K. 2017, ApJ, 840, 90

Parsons, R., Murach, T., & Gajdus, M. 2015, in International Cosmic Ray Conference, Vol. 34, 34th International Cosmic Ray Conference (ICRC2015), 826

Parsons, R. D., & Hinton, J. A. 2014, Astropart. Phys., 56, 26

Pedlar, A., Muxlow, T., & Wills, K. A. 2003, in Revista Mexicana de Astronomia y Astrofisica Conference Series, Vol. 15, Revista Mexicana de Astronomia y Astrofisica Conference Series, ed. J. Arthur & W. J. Henney, 303

Pietrzyński, G., Graczyk, D., Gallenne, A., et al. 2019, Nature, 567, 200

Piron, F., Djannati-Atai, A., Punch, M., et al. 2001, A&A, 374, 895

Pooley, D., Lewin, W. H. G., Fox, D. W., et al. 2002, The Astrophysical Journal, 572, 932

Porter, T. A., Moskalenko, I. V., & Strong, A. W. 2006, ApJ, 648, L29

Prandini, E. 2017, arXiv e-prints, arXiv:1706.01670

Predehl, P., Sunyaev, R. A., Becker, W., et al. 2020, Nature, 588, 227

Prokhorov, D. A., & Colafrancesco, S. 2019, MNRAS, 483, 3444

Prokhorov, D. A., Moraghan, A., & Vink, J. 2021, MNRAS, 505, 1413

Pshirkov, M. S., Vasiliev, V. V., & Postnov, K. A. 2016, MNRAS, 459, L76

Raab, C. 2021, Phdthesis, Université libre de Bruxelles, http ://hdl.handle.net/2013/ULB-DIPOT :oai :dipt.ulb.ac.be :2013/325215

Razzaque, S., & Yang, L. 2018, Galaxies, 6, 47

Reed, J. E., Hester, J. J., Fabian, A. C., & Winkler, P. F. 1995, ApJ, 440, 706

Renault-Tinacci, N., Kotera, K., Neronov, A., & Ando, S. 2018, A&A, 611, A45

Rest, A., Welch, D. L., Suntzeff, N. B., et al. 2008, ApJ, 681, L81

Reynolds, S. P. 2008, ARA&A, 46, 89

Reynolds, S. P., & Ellison, D. C. 1992, ApJ, 399, L75

Reynoso, E. M., Moffett, D. A., Goss, W. M., et al. 1997, ApJ, 491, 816

Rochester, G. D., & Butler, C. C. 1947, Nature, 160, 855

Rolke, W. A., & Lopez, A. M. 2001, Nuclear Instruments and Methods in Physics Research, 458, 745

Ruiz-Lapuente, P. 2017, ApJ, 842, 112

Ruiz-Lapuente, P., Comeron, F., Méndez, J., et al. 2004, Nature, 431, 1069

Sankrit, R., Raymond, J. C., Blair, W. P., et al. 2016, ApJ, 817, 36

Sano, H., Fujii, K., Yamane, Y., et al. 2017, in American Institute of Physics Conference Series, Vol. 1792, 6th International Symposium on High Energy Gamma-Ray Astronomy, 040038

Sano, H., Plucinsky, P. P., Bamba, A., et al. 2020, ApJ, 902, 53

Sarkar, K. C., Nath, B. B., & Sharma, P. 2017, MNRAS, 467, 3544, arXiv : 1610.00719

Schure, K. M., & Bell, A. R. 2013, MNRAS, 435, 1174

Schure, K. M., Bell, A. R., O'C Drury, L., & Bykov, A. M. 2012, Space Sci. Rev., 173, 491

Seok, J. Y., Koo, B.-C., & Onaka, T. 2013, ApJ, 779, 134

Sharda, P., Gaetz, T., Kashyap, V., & Plucinsky, P. 2020, arXiv e-prints, arXiv:2004.07366

Sherf, N., Keshet, U., & Gurwich, I. 2017, ApJ, 847, 95

Shklovskii, I. 1953, DOKLADY AKADEMII NAUK SSSR, 91, 475

Slane, P., Castro, D., Funk, S., et al. 2010, ApJ, 720, 266

Slane, P., Lee, S. H., Ellison, D. C., et al. 2014, ApJ, 783, 33

Smartt, S. J. 2009, ARA&A, 47, 63

Smartt, S. J., Eldridge, J. J., Crockett, R. M., & Maund, J. R. 2009, MNRAS, 395, 1409

Smartt, S. J., Maund, J. R., Hendry, M. A., et al. 2004, Science, 303, 499

Smith, N. 2014, ARA&A, 52, 487

Smith, N. 2014, Annual Review of Astronomy and Astrophysics, 52, 487

Smith, N., Alsabti, A., & Murdin, P. 2017, Handbook of Supernovae

Smith, N., Chornock, R., Li, W., et al. 2008, ApJ, 686, 467

Smith, N., Hinkle, K. H., & Ryde, N. 2009, AJ, 137, 3558

Smith, N., Li, W., Filippenko, A. V., & Chornock, R. 2011, MNRAS, 412, 1522

Snowden, S. L., Egger, R., Freyberg, M. J., et al. 1997, The Astrophysical Journal, 485, 125

Spengler, G. 2020, A&A, 633, A138

Storm, E., Weniger, C., & Calore, F. 2017, J. Cosmology Astropart. Phys., 2017, 022

Stritzinger, M., Hsiao, E. Y., Morrell, N., et al. 2016, The Astronomer's Telegram, 8657, ads

Strong, A. W., Moskalenko, I. V., & Ptuskin, V. S. 2007, Annual Review of Nuclear and Particle Science, 57, 285

Strong, A. W., Moskalenko, I. V., Reimer, O., Digel, S., & Diehl, R. 2004, A&A, 422, L47

Su, M., & Finkbeiner, D. P. 2012, ApJ, 753, 61

Su, M., Slatyer, T. R., & Finkbeiner, D. P. 2010, The Astrophysical Journal, 724, 1044

Sugerman, B., & Lawrence, S. 2016, The Astronomer's Telegram, 8759, ads

Sun, L., & Chen, Y. 2019, ApJ, 872, 45

Suzuki, H., Bamba, A., Yamazaki, R., & Ohira, Y. 2020, PASJ, 72, 72

Taddia, F., Stritzinger, M. D., Sollerman, J., et al. 2013, A&A, 555, A10

Tahara, M., Kataoka, J., Takeuchi, Y., et al. 2015, ApJ, 802, 91, publisher : IOP Publishing

Tamagawa, T., Hayato, A., Nakamura, S., et al. 2009, PASJ, 61, S167

Tamm, I., & Frank, I. 1937, Dokl. Akad. Nauk SSSR, 14, 107

Tappe, A., Rho, J., Boersma, C., & Micelotta, E. R. 2012, ApJ, 754, 132

Tappe, A., Rho, J., & Reach, W. T. 2007, ApJ, 659, 1794

Tatischeff, V. 2009, A&A, 499, 191

Telezhinsky, I., Dwarkadas, V. V., & Pohl, M. 2013, A&A, 552, A102

Thomas, A., Tucker, B. E., Childress, M., et al. 2016, The Astronomer's Telegram, 8664, ads

Thorstensen, J. R., Fesen, R. A., & van den Bergh, S. 2001, AJ, 122, 297

Tian, W. W., & Leahy, D. A. 2011, ApJ, 729, L15

Toledo-Roy, J. C., Esquivel, A., Velázquez, P. F., & Reynoso, E. M. 2014, MNRAS, 442, 229

Tsuji, N., & Uchiyama, Y. 2016, PASJ, 68, 108

Van Dyk, S. D. 2013, AJ, 146, 24

Van Dyk, S. D., Ascenso, J., Wu, Y.-L., et al. 2016, The Astronomer's Telegram, 8693, ads

van Eldik, C., Holler, M., Berge, D., et al. 2016, in The 34th International Cosmic Ray Conference, Vol. 236, SISSA Medialab, 847

Vernetto, S., & LHAASO, C. 2016, Journal of Physics: Conference Series, 718, 052043

Vink, J. 2008a, A&A, 486, 837

Vink, J. 2008b, ApJ, 689, 231

Vink, J. 2012, The Astronomy and Astrophysics Review, 20, 49

Vink, J. 2017, Supernova 1604, Kepler's Supernova, and its Remnant (Cham, Switzerland : Springer International Publishing), 139

Vink, J. 2020, Physics and Evolution of Supernova Remnants (Springer, Cham)

Voelk, H. J., & Biermann, P. L. 1988, ApJ, 333, L65

Vogt, F., & Dopita, M. A. 2011, Astrophysics and Space Science, 331, 521âĂŞ535

Völk, H. J., Berezhko, E. G., & Ksenofontov, L. T. 2005, A&A, 433, 229

Völk, H. J., & Biermann, P. L. 1988, ApJ, 333, L65

Wagner, S. J., & H. E. S. S. Collaboration. 2021, The Astronomer's Telegram, 14844, ads

Wang, Z. R., Qu, Q. Y., & Chen, Y. 1997, A&A, 318, L59

Weaver, R., McCray, R., Castor, J., Shapiro, P., & Moore, R. 1977, ApJ, 218, 377

Weekes, T. C., Cawley, M. F., Fegan, D. J., et al. 1989, ApJ, 342, 379

Weiler, K. 2006, in KITP Conference: Supernova and Gamma-Ray Burst Remnants

Williams, B. J., Borkowski, K. J., Reynolds, S. P., et al. 2012, ApJ, 755, 3

Williams, B. J., Borkowski, K. J., Reynolds, S. P., et al. 2006, ApJ, 652, L33

Wong, T., Hughes, A., Ott, J., et al. 2011, ApJS, 197, 16

Xi, S.-Q., Liu, R.-Y., Wang, X.-Y., et al. 2020, ApJ, 896, L33

Xiang, Y., & Jiang, Z. 2021, ApJ, 908, 22

Xin, Y.-L., Guo, X.-L., Liao, N.-H., et al. 2017, ApJ, 843, 90

Xin, Y.-L., Liang, Y.-F., Li, X., et al. 2016, ApJ, 817, 64

Yang, H. Y. K., & Ruszkowski, M. 2017, ApJ, 850, 2

Yang, R.-z., Aharonian, F., & Crocker, R. 2014, A&A, 567, A19

Young, P. A., Fryer, C. L., Hungerford, A., et al. 2006, ApJ, 640, 891

Yuan, Q., Liao, N.-H., Xin, Y.-L., et al. 2018, ApJ, 854, L18

Yuan, Q., Liu, S., & Bi, X. 2012, The Astrophysical Journal, 761, 133

Yuan, Y., Funk, S., Jóhannesson, G., et al. 2013, ApJ, 779, 117

Zabalza, V. 2015a, in International Cosmic Ray Conference, Vol. 34, 34th International Cosmic Ray Conference (ICRC2015), 922

Zabalza, V. 2015b, Proc. of International Cosmic Ray Conference 2015, 922

Zatsepin, G. T., & Kuzmin, V. A. 1966, Soviet Journal of Experimental and Theoretical Physics Letters, 4, 78

Zeng, H., Xin, Y., & Liu, S. 2019, ApJ, 874, 50

Zhang, X., Chen, Y., Li, H., & Zhou, X. 2013, MNRAS, 429, L25

Zirakashvili, V. N., Aharonian, F. A., Yang, R., Oña-Wilhelmi, E., & Tuffs, R. J. 2014, ApJ, 785, 130

Zirakashvili, V. N., & Ptuskin, V. S. 2016, Astropart. Phys., 78, 28

Zubovas, K., & Nayakshin, S. 2012, MNRAS, 424, 666

Zyla, P., et al. 2020, PTEP, 2020, 083C01

Contribution from co-authors

This page summarizes Rachel Simoni's contributions, chapter by chapter, and the publication details, if applicable.

Publications by the H.E.S.S. collaboration allows a maximum of five corresponding authors, including the person responsible for the analysis and the one responsible for the analysis crosscheck. Co-authors are involved in the interpretation of the results and the writing. The collaboration discusses the publications through several internal review steps before being submitted to a scientific journal. These review steps involve a review of the data analysis, checking the consistency between the two analysis chains, an internal review by two senior members of the collaboration, iterating on the draft, and a collaboration review including all H.E.S.S. members . which again may lead to a final iteration of the manuscript.

Four projects in this thesis have gone through the collaboration validation steps, including Chapter 5, as this conference proceeding is the final publication for this observational result. In addition, chapter 5 has been reviewed by co-authors.

Chapter 2 : LMC N132D : A mature supernova remnant with a power-law gamma-ray spectrum extending beyond 8 TeV

H.E.S.S. Collaboration : H. Abdalla, F. Aharonian, et al
corresponding authors **R.Simoni**, D.Prokhorov, J.Vink & N.Komin

Astronomy & Astrophysics, 2021, 655, A7

R. Simoni : overall coordination, writing and HAP analysis. D. Prokhorov : M++ cross-analysis, co-writer. J. Vink and N. Komin : interpretation input.

Chapter 3 : Evidence for gamma-ray emission of Kepler's supernova remnant from deep H.E.S.S. observations

H.E.S.S. Collaboration
corresponding authors : D.Prokhorov, J.Vink, **R.Simoni**

under internal review from the H.E.S.S. Collaboration

D. Prokhorov : overall coordination, writing M++ analysis and modelling section. R.Simoni : HAP cross-analysis and co-writer, J. Vink : interpretation input.

Chapter 4 : Upper Limits on Very-High-Energy Gamma-ray Emission from Core-Collapse Supernovae Observed with H.E.S.S

H.E.S.S. Collaboration : H. Abdalla, F. Aharonian, et al
corresponding authors : R.Simoni, N.Maxted, M.Renaud & J.Vink

Astronomy & Astrophysics 2019, 626, A57

R. Simoni : overall coordination, writing, HAP analysis, interpretation with the use of theoretical model. N.Maxted : Selection of the sample, M++ cross-analysis, co-writer. M. Renaud and J. Vink : interpretation input, co-writer.

Chapter 5 : H.E.S.S. ToO program on nearby core-collapse Supernovae : search for very-high energy gamma-ray emission towards the SN candidate AT2019krl in M74

N.Komin, M.Renaud, **R.Simoni** & S.Ryder on behalf of the H.E.S.S. Collaboration.

Proceedings of Science PoS(ICRC2021), 2021, 809

R.Simoni : main analysis with HAP, writting –Results part and co-writing the discussion part–. N.Komin : M++ cross-analysis, writing the Discussion part. M.Renaud : PI of the ToO program, writing the first part of the proceeding.

Chapter 6 : Search for gamma-ray emission at the edge of the Fermi Bubbles with H.E.S.S. using PKS2155-304 Observations

R.Simoni, N. Komin, D. Berge & J. Vink on behalf of the H.E.S.S. Collaboration.

Internal report. No journal submission

R.Simoni overall coordination, writing HAP analysis. Nukri Komin crosschecked the results with M++. J. Vink and D.Berge : interpretation input.

Publications

Co-authored articles, main corresponding author

1. H.E.S.S. Collaboration et al. (2019)
   Astronomy & Astrophysics A57 (2019)
   Upper Limits on Very-High-Energy Gamma-ray Emission from Core-Collapse Supernovae Observed with H.E.S.S
2. H.E.S.S. Collaboration et al. (2021)
   Astronomy & Astrophysics 655, A7 (2021)
   LMC N132D : A mature supernova remnant with a power-law gamma-ray spectrum extending beyond 8 TeV

Conference proceedings

1. Rachel Simoni, Nigel Maxted, Mathieu Renaud and Jacco Vink on behalf of the H.E.S.S. Collaboration
   Proceedings of the International Astronomical Union , Volume 12 , Symposium S331 : Supernova 1987A :30 years later - Cosmic Rays and Nuclei from Supernovae and their aftermaths , February 2017 , pp. 325 - 328
   Upper Limits on Gamma-ray Emission from Supernovae Serendipitously Observed with H.E.S.S.
2. Rachel Simoni, Nigel Maxted, Mathieu Renaud, Jacco Vink, Luigi Tibaldo, on behalf of the H.E.S.S. Collaboration
   Proceedings of the 35th International Cosmic Ray Conference 2017, 711
   Upper limits on gamma-ray emission from Supernovae serendipitously observed with H.E.S.S.
3. Nukri Komin, Matthieu Renaud, Rachel Simoni, Stuart Ryder on behalf of the H.E.S.S. Collaboration

Proceedings of the 37th International Cosmic Ray Conference, 2021, 809
H.E.S.S. ToO program on nearby core-collapse Supernovae : search for very-high energy gamma-ray emission towards the SN candidate AT2019krl in M74

4. Jacco Vink, Rachel Simoni, Nukri Komin, Dmitry Prokhorov on behalf of the H.E.S.S. Collaboration
   Proceedings of the 37th International Cosmic Ray Conference, 2021, 778
   LMC N132D : a mature supernova remnant with a youthful gamma-ray spectrum
5. Dmitry Prokhorov, Jacco Vink, Rachel Simoni, Nukri Komin, Stefan Funk, Denys Malyshev, Lars Mohrmann, Stefan Ohm, Gerd Pühlhofer, Heinrich J. Völk on behalf of the H.E.S.S. Collaboration
   Proceedings of the 37th International Cosmic Ray Conference, 2021, 805
   Deep observations of Kepler's SNR with H.E.S.S

Summary

Energetic charged particles of cosmic origins (protons, electrons/positrons, nuclei) are constantly bombarding Earth: they were identified and named cosmic-rays (CRs) in the 1910s. This natural phenomenon is recorded on Earth, but the charged CRs can not trace back their sources, instead neutral "messengers" undeflected by magnetic fields, such as gamma-rays need to be used. CR particles accelerated at supernova remnants shock front can produce gamma-rays at TeV energies via two mechanisms. According to the so-called "leptonic scenario" CR leptons experience inverse Compton scattering on ambient photons, which will be boosted to TeV energies. In the "hadronic scenario" the inelastic collisions of CR hadrons with ambient gas leads to the production of a neutral pion that will decay quickly into TeV gamma-rays. The clear signature for a hadronic origin of gamma-rays produced by two mature SNRs, IC443, and W44 confirmed confirmed SNRs as sources of CRs.

SNRs are believed to be responsible for the bulk of Galactic CRs, but their gamma-ray emission was observed, only up to tens of TeV, not beyond. That corresponds to CR particles with energies of the order of 10^{14} eV, so SNRs can not be considered responsible for CRs above 10^{15} eV.

Among the $\sim$26 SNRs observed at TeV energies, some observational observational trends can be deduced: young SNRs ($\lesssim$ 1000 years) are bright at TeV, and mature SNRs ($\gtrsim$ 3000 years), are brighter at GeV energies, but not at TeV energies, as if their CR "fuel" gauge is lower. Indeed the shock velocity has dropped, and the high-energy CRs have escaped. Mature SNR seen at TeV energies seems to interact with nearby dense matter such as molecular clouds. In this case, it is believed that the CR hadrons escape and interact with surrounding proton and nuclei, leading to neutral pion production and subsequent gamma-ray emission. The work reported in chapters 2-5 of this thesis presents analyses related to TeV gamma-ray emission for SNR and supernovae, using data taken with the High Energy Stereoscopic System (H.E.S.S.).

H.E.S.S., the instrument used for the work presented here, is an array of five Cherenkov telescopes located in Namibia. The detection technique is indirect and consists in recording the Cherenkov light emitted by the relativistic particles of the atmospheric shower induced by the cosmic gamma-ray. The Cherenkov light detection is possible only with ultra-fast cameras, triggering in nanoseconds. Reconstruction of the incoming gamma-ray relies on Monte Carlo simulations for the Air shower and the atmosphere and the instrument response. The analyses are background-dominated: first, the hadrons-induced showers must be rejected. Then the gamma-ray background is estimated in the same field of view than the source, and excess is computed comparing source and background signals.

Chapter 2 concerns the "middle-aged" SNR N132D, which is quite particular in regard to CR acceleration. This $\sim$ 2500 years old remnant located in the LMC ($\sim$ 50 kpc) is, so far, the only extra-galactic SNR observed in gamma-rays. SNR N132D belongs to the small class of oxygen-rich SNR, along with the young Cassiopeia A ($\sim$ 340 yrs old), to which it is often compared.We report a 5.7 σ detection for this remnant. A joint analysis of the H.E.S.S. and Fermi-LAT spectra shows that the gamma-ray spectrum is well-fitted with a single power-law distribution. The lack of a clear cut-off in the spectrum below 10 TeV is remarkable, given that the much younger Galactic SNR Casssiopeia A exhibits an energy cut-off around 3.5 TeV. The multi-wavelength modeling shows that a pure leptonic scenario is not excluded but would imply unlikely high energy taken by the CRs electrons. On the other hand, a dominantly hadronic scenario for the gamma-ray emission of the remnant is plausible. The hadronic origin of the gamma-ray is supported by the SNR interacting with dense matter in the southeast. However, this interaction can not be enlightened in our analysis.

The remnant of the youngest naked-eye supernova SN 1604, better known as Kepler's SNR, was the only historical SNR not detected in gamma-rays. This young type Ia SNR is among the best-studied SNRs across the electromagnetic spectrum. It is, however, more distant than the other historical SNRs ($\sim$ 5 kpc), among which its sibling Type Ia Tycho's SNR ($\sim$ 2.5 kpc), to which it can be compared to many regards. In chapter 3 we present the results of deep observations of Kepler's SNR performed with H.E.S.S. based on 152 hours of observations. We report strong evidence for a VHE signal from Kepler's SNR at a statistical level of 4.6 σ. This excess, as well as a reported 4.4σ signal at GeV energies with *Fermi*-LAT, indicates that Kepler's SNR is a VHE gamma-ray source and confirms the presence of particles accelerated to TeV energies.

Chapters 4 and 5 are treating the possible TeV emission at the earlier stage of SNR, the supernova (SN) itself. In the search for cosmic-ray sources, young (a few months to a few years) SNe should not be overlooked. Some models predict a TeV to PeV gamma-ray emission for type IIp, IIb, and IIn SNe. These SNe are embedded in a dense circumstellar medium (CSM) due to the high-mass loss rates and slow wind speeds of their progenitor stars. A population of CR hadrons from such an environment may leave a signature of gamma-ray emission as proton-proton interactions occur within the surrounding dense CSM, and the heavy CSM ionization eases the particle acceleration process. The possibility of a brief period of high gamma-ray flux from young SNe offers the H.E.S.S telescope a window to search for signatures of particle acceleration beyond TeV energies. We analyzed data towards nine objects serendipitously observed with H.E.S.S. and from two nearby SN2016apj and AT2019krl, which triggered dedicated observations. No significant excess is observed for any of the eleven objects. Upper limits on the flux are derived and translated into constraints on the supernova environment.

Chapter 6 reports a search for a TeV gamma-ray emission for the Fermi Bubbles. The Fermi Bubbles are gigantic diffuse gamma-ray lobes, symmetrical, extending on both parts of the galactic plane up to $|b| = 40^\circ$ in Galactic latitude. They are the biggest feature in the gamma-ray sky, but their nature and origin remain unknown. It is still debated whether its formation is caused by energetic jets originating from the supermassive black hole in the center of the Milky Way or by a past episode of star formation in the Galactic center. We searched for VHE emission for the edge of the Fermi Bubbles located in the five degrees field of view of deep observations dedicated to PKS2155-304. We observed no significant emission and derived differential upper limits on the flux completing the multiwavelength spectrum at large b at TeV energies. No model was constrained by the results. Systematic errors are addressed and discussed, along with predictions for further observations.

Nederlandse Samenvatting

Energetische, geladen deeltjes van kosmische oorsprong bombarderen voortdurend de aarde: zij werden in de jaren 1910 geïdentificeerd en kosmische-straling genoemd. Dit natuurlijke verschijnsel wordt op aarde waargenomen, maar richting van waaruit de geladen kosmische deeltjes komen wijzen niet terug naar hun bron van oorsprong; in plaats daarvan moet gebruik worden gemaakt van neutrale "boodschappers", zoals gammastraling, die niet door magnetische velden worden afgebogen. Kosmische deeltjes die aan het schokfront van supernova restanten ("Supernova remnants", SNRs in het vervolg) worden versneld, produceren gammastralen met TeV-energieën via twee stralingsmechanismen. Volgens het zogenoemde "leptonische scenario" veroorzaken kosmische leptonen (elektronen/positronen) inverse Compton-verstrooiing van alom aanwezige fotonen. Die verstrooiing zwiept de fotonen op tot tot TeV-energieën. In het "hadron-scenario"leiden de inelastische botsingen van kosmische hadronen (protonen en atoomkernen) met omgevingsgas wat leidt tot de productie van neutrale pionen, deeltjes die snel vervallen in twee fotonen, wat leidt TeV-gammastraling als de oorspronkelijk hadronen energetisch genoeg zijn. De duidelijke gamma-stralings signatuur voor zo'n hadron-oorsprong is gedetecteerd voor twee relatief oude SNRs, IC443, en W44, wat bevestigt dat SNRs bronnen zijn van hadron kosmische-straling.

SNRs worden verondersteld verantwoordelijk te zijn voor het grootste deel van de Galactische kosmische-straling, maar hun gammastraling werd slechts waargenomen tot energieën van tientallen TeV, en niet daarboven. Dat komt overeen met kosmische deeltjes met energieën in de orde van 10^{14} eV, zodat SNR's niet verantwoordelijk kunnen worden geacht voor kosmische-stralen boven 10^{15} eV.

Onder de $\sim$26 SNRs die bij TeV-energieën zijn gedetecteerd, kunnen enkele observationele trends worden afgeleid: jonge SNRs ($\lesssim$ 1000 years) zijn helder bij TeV, en volwassen SNRs ($\gtrsim$ 3000 jaar), zijn helderder bij GeV-energieën, maar niet bij TeV-energieën, alsof hun kosmische-"brandstof"-meter lager is. De schoksnelheid is inderdaad afgeremd, en de hoogenergetische deeltjes zijn grotendeels ontsnapt. Oudere SNRs die bij TeV-energieën worden waargenomen lijken in interactie te zijn met omgevingsgas van hoge dichtheid, zoals moleculaire wolken. In dit geval wordt aangenomen dat de kosmische hadronen ontsnapt zijn en interactie aangaan met de protonen en atoomkernen in het omliggende gas. Dit leidt tot neutrale pion productie, resulterend in de productie van gammastraling. Het werk dat in de hoofdstukken 2–5 van dit proefschrift wordt beschreven presenteert analyses met betrekking tot TeV gammastraling van SNRs en supernovae, waarbij gebruik is gemaakt van gegevens die zijn verzameld met het High Energy Stereoscopic System (H.E.S.S.).

H.E.S.S., het instrument dat voor het hier gepresenteerde werk is gebruikt, is een array van vijf Cherenkov-telescopen die in Namibië staan. De detectietechniek is indirect en bestaat uit het registreren van het Cherenkov licht dat wordt uitgezonden door een cascade van relativistische deeltjes in de atmosfeer, veroorzaakt door een interactie van gammastralingsfotonen met de atmosfeer. De detectie van dit Cherenkovlicht is alleen mogelijk met ultrasnelle camera's, die in nanoseconden triggeren. Reconstructie van de eigenschappen van het oorspronkelijke gammastralingsfoton berust op Monte Carlo-simulaties van de vorming van de deeltjescascade in de atmosfeer, en de respons van het instrument. De gegevens zijn achtergrond gedomineerd: eerst moeten de door kosmische straling veroorzaakte cascades worden verwijderd. Vervolgens wordt de achtergrond van de gammastraling geschat in hetzelfde gezichtsveld als de bron, en aan de hand daarvan wordt berekend welke fractie van de gammastraling toegeschreven kan worden aan de bron.

Hoofdstuk 2 betreft de SNR van "middelbare leeftijd"N132D, die nogal bijzonder is wat betreft de kosmische-stralings versnelling. Deze 2500 jaar oude restant in de Grote Magelhaense Wolk (50 kpc) is tot nu toe de enige extragalactische SNR die in gammastraling is waargenomen. SNR N132D behoort tot de kleine klasse van zuurstofrijke SNRs, samen met de jonge Cassiopeia A ($\sim$ 340 jaar oud), waarmee hij vaak wordt vergeleken. Wij melden een gammastralingsdetectie met een significantie 5.7 σ voor N132D. Een gezamenlijke analyse van de H.E.S.S. en Fermi-LAT spectra laat zien dat het gammastralingsspectrum goed past bij een enkele machtswet verdeling. Het ontbreken van een duidelijke afkapping in het spectrum onder 10 TeV is opmerkelijk, gezien het feit dat de veel jongere Galactische SNR Casssiopeia A een energie afkapenergie van rond de 3.5 TeV vertoont. De multigolflengte modellering toont aan dat een puur leptonisch scenario niet uitgesloten is, maar dat dit wel een onwaarschijnlijk hoog energiebudget van de kosmische elektronen zou impliceren. Anderzijds is een overwegend hadronisch scenario voor de gammastraling van de overblijfselen aannemelijk. De hadron-oorsprong van de gammastraling wordt ondersteund door de interactie van de SNR met dichte materie in het zuidoosten. Deze interactie kan echter niet worden opgehelderd in onze analyse.

Het overblijfsel van de jongste, met het blote oog waargenomen supernova SN 1604, beter bekend als de SNR van Kepler, was de enige historische SNR die niet in gammastralen is waargenomen. Deze jonge type Ia SNR is een van de best bestudeerde SNRs in het elektromagnetische spectrum. Hij is echter verder weg dan de andere historische SNRs (∼5 kpc), waaronder de gerelateerde Type Ia SNR Tycho (het restant van SN1572) (∼2.5 kpc), waarmee hij in veel opzichten kan worden vergeleken. In hoofdstuk 3 presenteren we de resultaten van diepe waarnemingen van Kepler's SNR uitgevoerd met H.E.S.S. op basis van 152 uur waarnemingen. We beschrijven sterke aanwijzingen voor een TeV signaal van Kepler's SNR op een statistisch niveau van 4.6 σ. Dit signaal, samen met een gerapporteerd signaal van 4.4 σ bij GeV-energieën met het *Fermi*-LAT instrument, wijst erop dat Kepler's SNR een TeV-gammastralingsbron is en bevestigt de aanwezigheid van deeltjes die versneld zijn tot TeV-energieën.

De hoofdstukken 4 en 5 behandelen de mogelijke TeV-emissie in het vroegste stadium van een SNR, namelijk kort na de supernova explosie. Bij het zoeken naar kosmische stralingsbronnen mogen jonge (enkele maanden tot enkele jaren) supernovae niet over het hoofd worden gezien. Sommige modellen voorspellen een TeV tot PeV gammastraling type IIp, IIb, en IIn SNe. Deze supernovae zijn ingebed in een dicht circumstellair medium (CSM) ten gevolge van het hoge massaverlies in de vorm van een stellaire wind van de moederster, en de trage snelheden van die wind.Een populatie van kosmische hadronen in zo'n omgeving zal gammastraling veroorzaken omdat proton-proton interacties plaatsvinden in het omringende CSM van hoge dichtheid, en de sterk ionisatie van het CSM het deeltjesversnellings proces vergemakkelijkt. De mogelijkheid van een korte periode van hoge gammastralingsflux van deze jonge SNe biedt de H.E.S.S telescoop een venster om te zoeken naar tekenen van deeltjesversnelling voorbij TeV energieën. We hebben de gegevens geanalyseerd van negen SNe die bij toeval met H.E.S.S. zijn waargenomen, en van twee nabije SN2016apj en AT2019krl, die aanleiding waren voor specifieke waarnemingen. Voor geen van de elf objecten is significante gammastraling waargenomen. Bovengrenzen aan de flux zijn berekend en hieruit is afgeleid wat dit betekent voor eigenschappen van het CSM rond deze SNe.

In hoofdstuk 6 wordt verslag gedaan van een zoektocht naar TeV gammastraling vanuit de Fermi Bubbles. De Fermi Bubbles zijn gigantische diffuse, symmetrische gammastraling lobben, die zich uitstrekken aan beide zijden van het galactische vlak tot $b = 40°$ in Galactische breedtegraad. Zij zijn het grootste verschijnsel aan de gammastralingshemel, maar hun aard en oorsprong zijn onbekend. Er wordt nog steeds over gediscussieerd of de vorming ervan wordt veroorzaakt door energetische jets afkomstig van het superzware zwarte gat in het centrum van de Melkweg of door een voorbije episode van stervorming in het Galactische centrum. Wij hebben gezocht naar TeV-emissie aan de rand van de Fermi Bubbles in het vijf-graden-brede beeldveld van diepe waarnemingen aan de bron PKS2155-304. We hebben geen significante emissie waargenomen en leidden differentiële bovengrenzen af voor de flux die het spectrum het multigolflengte spectrum van de Fermi Bubbles aanvult tot TeV-energieën voor een grote galactische breedte b. De bovengrenzen zijn niet in conflict met bestaande modellen voor gammastraling van de Fermi Bubbles. Systematische fouten worden behandeld en besproken, samen met voorspellingen voor verdere waarnemingen.

Résumé

Des particules énergétiques d'origine cosmique bombardent constamment la Terre: elles ont été identifiées et nommées rayons cosmiques ("cosmic-rays") vers 1912. Ce phénomène naturel est capté par des observatoires terrestres, mais les particules cosmiques sont chargées (protons, électrons/positrons, ions) et ne permettent pas de remonter à leur source, car déviées par les champs magnétiques dans l'éspace. Pour explorer les sources de rayons cosmiques, en partie inconnues, on utilise des "messagers" neutres comme les rayons gamma.

Les particules cosmiques accélérées par l'onde de choc des vestiges de supernova ("Supernovae remnants", SNR dans le reste du texte) peuvent produire des rayons gamma dits de très hautes énergies, (atteignants des énergies du TeV, soit 10^{12}eV). Les rayons gamma TeV sont le signal utilisé dans les travaux de cette thèse pour l'étude des SNR en tant que sources de rayons cosmiques.

Les rayons gamma sont produits via deux mécanismes:
1) selon le "scénario leptonique", les électrons/positrons cosmiques subissent une diffusion Compton inverse sur les photons ambiants, et leur transfèrent une énergie qui peut atteindre les TeV,
2) dans le "scénario hadronique", les collisions inélastiques de protons et ions cosmiques avec le gaz ambiant conduisent à la production d'un pion neutre qui se désintégre rapidement en rayons gamma d'énergies TeV.

La signature d'une origine hadronique des rayons gamma produits par deux SNRs "matures", IC443, et W44, a confirmé les SNRs comme sources de rayons cosmiques. On pense donc que les SNRs sont responsables de la majeure partie des rayons cosmiques galactiques observés sur Terre, mais leur émission en rayons gamma n'a été observée que jusqu'à des dizaines de TeV, pas au-delà.

Parmi les $\sim$26 SNRs observés aux énergies TeV, certaines tendances observationnelles apparaissent: les jeunes SNRs ($\lesssim$ 1000 ans) sont lumineuses en signal TeV, et les SNRs matures ($\gtrsim$ 3000 ans), sont moins lumineuses aux énergies TeV, comme si leur jauge de "carburant" était plus faible. Ceci est dû au fait qu'avec le temps, la vitesse du choc a baissé, et les rayons cosmiques de haute énergie se sont échappés. On a montré que l'émission TeV observée pour les SNR matures, provient certainement d'une interaction avec de la matière dense du milieu inter-stellaire, comme les nuages moléculaires. Lors de cette interaction, les hadrons cosmiques s'échappent et interagissent avec les protons et ions environnants, entrainant la production de pions neutres et une émission en rayons gamma.

Le travail rapporté dans les chapitres de cette thèse présente des analyses liées à l'émission de rayons gamma dans le domaine TeV pour les SNR et les supernovae, et utilise des données prises avec le système stéréoscopique à haute énergie (H.E.S.S.).

H.E.S.S., est un observatoire composé de cinq télescopes Cherenkov et situé en Namibie. La technique de détection est indirecte et consiste à enregistrer la lumière Cherenkov émise par les particules relativistes de la gerbe atmosphérique induite par les rayons gamma venant de l'éspace. La détection de la lumière Cherenkov n'est possible qu'avec des caméras ultra-rapides, se déclenchant en quelques nanosecondes. La reconstruction des rayons gamma repose sur des simulations Monte Carlo pour les gerbes atmosphériques, la composition de l'atmosphère, et pour la réponse des instruments. Les analyses sont dominées par le bruit de fond : il faut d'abord rejeter les gerbes induites par des protons. Ensuite, le fond de rayons gamma est estimé dans le même champ de vue que la source, et un excès est calculé en comparant les signaux de la source et du fond.

Le chapitre 2 concerne la SNR N132D "d'âge moyen", qui est particulière en ce qui concerne l'accélération des rayons cosmiques. Cette SNR de $\sim$ 2500 ans située dans le grand nuage de Magellan ($\sim$ 50 kpc) est, à ce jour, la seule SNR extra-galactique observée en rayons gamma. SNR N132D appartient à la petite classe des SNRs riches en oxygène, comme la jeune SNR Casssiopeia A ($\sim$ 340 ans), auquelle elle est souvent comparée. Nous rapportons une détection de 5.7 σ pour ce vestige de supernova. Une analyse conjointe des spectres H.E.S.S. et Fermi-LAT montre que le spectre des rayons gamma est bien ajusté avec une distribution unique de type loi de puissance. L'absence d'une coupure en énergie dans le spectre au-delà de 10 TeV est remarquable, étant donné que la SNR galactique Casssiopeia A, beaucoup plus jeune, présente une coupure d'énergie autour de 3.5 TeV. La modélisation multi-longueur d'onde montre qu'un scénario purement leptonique n'est pas exclu mais impliquerait une énergie improbablement élevée pour les électrons cosmiques. Par contre, un scénario à dominante hadronique pour l'émission de rayons gamma du vestige est plausible. L'origine hadronique des rayons gamma est par ailleurs soutenue par l'interaction de la SNR avec de la matière dense dans le sud-ouest. Cette interaction ne peut être cependant mise en évidence dans notre analyse.

Le vestige de la plus jeune supernova observée à l'oeil nu, SN 1604, plus connue sous le nom de Kepler's SNR, est la seule SNR historique non détectée en rayons gamma. Cette jeune SNR de type Ia fait partie des SNRs les mieux étudiées dans le spectre électromagnétique. Elle est plus distante que les autres SNR historiques ($\sim$ 5 kpc), parmi lesquelles sa "soeur" de type Ia la SNR de Tycho ($\sim$ 2,5 kpc), auquelle elle peut être comparée à bien des égards. Dans le chapitre 3, nous présentons les résultats des observations de la SNR de Kepler réalisées avec H.E.S.S. sur une base de 152 heures d'observations. Nous rapportons une évidence pour un signal de la SNR de Kepler à un niveau statistique de 4.6 σ. Cet excès, ainsi qu'un signal de 4.4 σ aux énergies de GeV avec *Fermi*-LAT, indique que la SNR de Kepler est une source de rayons gamma VHE et confirme la présence de particules accélérées à des énergies TeV.

Les chapitres 4 et 5 traitent de l'émission possible au stade antérieur d'une SNR, la supernova elle-même. Dans la recherche de sources de rayons cosmiques, les supernovae restent des candidats possibles. En effet certains modèles prédisent une émission de rayons gamma jusqu'à 1000 TeV pour les supernovae de type IIp, IIb et IIn. Ces supernovae évoluent dans un milieu circumstellaire dense (CSM), produit par l'importante perte de mass de leurs étoiles progénitrices, avant l'explosion de la supernova.Une population de hadrons cosmiques provenant d'un tel environnement peut laisser une signature en rayons gamma car des interactions proton-proton se produisent dans le CSM dense, et la forte ionisation du CSM facilite le processus d'accélération des particules. La possibilité d'une brève période de flux en rayons gamma provenant de jeunes supernovae (de quelques jours à un mois) permet une recherche avec le télescope H.E.S.S. Nous avons analysé les données de neuf objets observés par hasard avec H.E.S.S. et de deux supernovae, SN2016apj et AT2019krl, qui ont déclenché des observations dédiées. Aucun excès significatif n'est observé pour aucun des onze objets. Des limites supérieures sur le flux sont dérivées et traduites en contraintes sur l'environnement des supernovae.

Le chapitre 6 rapporte la recherche d'une possible émission de rayons gamma TeV pour les bulles de Fermi. Les bulles de Fermi sont de gigantesques lobes symétriques d'émission gamma, s'étendant sur les deux parties du plan galactique jusqu'à $|b| = 40°$ en latitude galactique. Elles constituent le plus grand élément du ciel gamma, mais leur nature et leur origine restent inconnues. On ne sait toujours pas si leur formation est dûe à des jets énergétiques provenants du trou noir supermassif au centre de la Voie lactée, ou à un épisode antérieur de formation d'étoiles dans le centre galactique. Nous avons cherché un possible signal TeV sur les bord des bulles de Fermi. Nous n'avons observé aucune émission significative et avons dérivé des limites supérieures différentielles sur le flux complétant le spectre multi-longueur d'onde aux énergies TeV. Ces limites sont trop élevées pour apporter une quelconque information, et sont discutées au regard des limites en sensitivité, des erreurs systématiques, et de prédictions pour des observations futures.

Acknowledgements

During my PhD, I have met many great people and got a lot of support. My situation was particular as I worked in two institutes at API in Amsterdam, and at IIHE in Brussels, and I was feeling at home to both. I'm also part of the H.E.S.S. collaboration, which has more than 200 members.So...I have so many people to thank!

Let me then start from the very beginning: this thesis could not have happened without the input of few people; I will mention them chronologically and with a mix of French and English.

First of all I want to thank my partner, Federico, without who this crazy life would not have been possible, as he took care of our kids when I was away. Federico, sans toi cette vie de fou n'aurait pas été possible. Je sais, cela n'a pas été facile mais on y est arrivés! Mille mercis, je t'aime!

Marianne Van Leeuw Koplewicz, c'est toi qui a déclenché mon retour à la physique. Tu m'as soutenue tout du long, lors de mes études et de mon PhD avec de nombreuses visites à Amsterdam avec Hosnie: bien sûr tu avais raison sur toute la ligne et je vais essayer de continuer en recherche fondamentale le plus loin possible. Spéciale dedicace à toi et à Hosnie!

Laurent Favart, un très grand merci: un soutien comme le tien c'est de l'or. Tu m'as acceuillie et soutenue dans le cadre de ma reprise d'étude à l'ULB. Tu m'as supervisée pour un master sur le Z+jets, et j'ai pris goût à la physique experimentale. J'ai appris énormement et cela m'a certainement permis de continuer en physique des Astroparticules. Pendant mon PhD, j'ai été acceuillie à l'IIHE, avec un statut de guest, ce qui m'a permis de concilier thèse et vie de famille. Cela a été une aide précieuse et je ne l'oublierai pas. On garde contact!

Jacco Vink, how could I thank you for all these years of passionate PhD? I mean, let's go backward: first, thanks for hiring me. Secondly, when I announced my (first) pregnancy and my wish to work partly from Brussels, we were just at the renewing period: you had to decide to keep on with the pressure that I could fail. Honestly, I was not sure myself I would manage to do it. More importantly, you are such

a supernova remnant specialist and passionate! That is automatically contagious. It was great to learn from your tremendous knowledge of supernova remnants, in all possible observations and perspectives, as your book can testify. Your scientific intuition is impressive: almost all of your ideas were confirmed for the works we did together. You supervised me perfectly through the projects with H.E.S.S. in the cosmic-ray perspective, even with the Fermi Bubbles project, for which I was blocked, and that you did not initiate. Each of the projects took a long time to complete, but we were discovering how it works in the H.E.S.S. collaboration. In the last years, you took a leading role in H.E.S.S., in which you are doing very well, always bringing up exciting science.

Dmitry Prokhorov, your arrival at API saved my PhD. No doubt that without you, I would not have made it. As we are dealing with two different software chains for H.E.S.S., we could crosscheck each other's analysis; that was the perfect team and quite exciting. I'm very grateful that you considered me a colleague in our discussions, taking all my comments into account. You were always available for any concern I was bothered with. Even if the H.E.S.S. group in Amsterdam was reduced to three people, we all can be proud of what the Amsterdam group has achieved with H.E.S.S. data analysis. This was only possible with your hard work. Merci beaucoup.

David Berge, I really enjoyed the dynamic of our H.E.S.S. group in Amsterdam. Your left API to join DESY, and that was a kind of shock, although I was super happy for you. Your input was more than precious concerning H.E.S.S. data analysis. Thanks for inviting me to Berlin and to find someone to help with my specific analysis. Your advice about showing enthusiasm has stuck with me to this very day.

Ralph Wijers, as API director, you always supported me, both on the scientific and the financial level. This latter was not a detail, and it has not escaped your notice. As a co-supervisor of the thesis, you were regularly present, and in the last steps, you found the right words to keep me going. That was perfect timing.

Nukri Komin, you are co-author on all almost all the thesis Chapters; that means a lot. You agreed to cross-check the Fermi Bubbles complex analysis and carry the AT2019krl project to ICRC. It was super easy to communicate with you. I'm happy we met and did great science together. Thank you very much for your support. Matthieu Renaud, Nigel Maxted, you invited me to join the supernova project, which boosted my PhD. Nigel, you had great ideas, that really helped the project. Matthieu, you have such a clear vision and strong knowledge of the possible gamma-ray emission of supernovae at TeV energies. We managed to defend that we should keep observing, despite seeing nothing. I'm pretty convinced and proud of our work, to which also participated Alexandre Marcowith. And a huge thank to you, Matthieu, for organizing the Symposium IAUS331 in La Réunion: it certainly marked the minds of all the participants. Dmitry Malyshev, thank you for the hard work for the Fermi Bubble Task Group and for your comments on the Fermi Bubbles Chapter of my thesis. On the Fermi Bubbles project, I would also like to thank Roland Crocker for quite an

interesting discussion.

Back in the days I began my PhD, we had a bigger H.E.S.S. group at API, which was a great time. Arnim Balzer, thanks for setting everything up with the H.E.S.S. software, HAP, and introducing me to the H.E.S.S. collaboration. You are such a good developer – guess what, nobody managed to help me with my VMware virtual machine when it crashed! Heike Prokhov, thanks for explaining our complex detection technique and the beers! Marc Bryan, you were my H.E.S.S. PhD mate, although I was not super present. You helped me a lot "digging in the HAP code", which I kept doing along. I was not helping much with motivation for your PhD., but nowadays, that doesn't matter much. Just see how long it took me to finish mine! David Salek, Felicia Kraus, Maurice Stefan, that was a pleasure to meet you all.

In H.E.S.S. I met right away great colleagues, among which Vincent Marandon and Dan Parsons. They constantly answered my questions about HAP analysis and software since October 2014 and till the very end of the thesis completion. Guys, you were answering all my messages; that is invaluable. On top of that, Dan, you helped a lot dealing with the Fermi Bubbles analysis, that was so helpful. In the end, you provided me with these fantastic plots on the ImPACT performance versus the multiplicity; thanks again. I wish you both all the best in your career. H.E.S.S./CTA should never let you go!

In the DESY Group, I want to thank Stefan Ohm and Stefan Klepser for a lot of input on my projects. Andrew Taylor, it was a pleasure to meet you. Maria Haupt, we shared concerns about upper limits and motherhood. You seem to deal with it so easily; I'm really impressed. Also, thank you for the last-minute advice on UL implementation in HAP. I have no doubt you will pursue a career in research as you wish.

On the H.E.S.S. French side I would like to thank the APC team in Paris, especially Bruno Khelifi. Thank you for welcoming me few days in Paris to work with you. Bruno, you taught me a lot on HAP, merci! Arache and Jacek, we had a great time watching some World Cup games in Berlin. Francois Brun, Sami Caroff, that was always a pleasure to meet you and chat. Thanks for organizing the H.E.S.S. school. Sami, thanks for the analysis review on N132D. Fabian Schlússer, thanks for pushing through the AT2019krl analysis. Mathieu de Naurois, thanks again for your "habilitation" and your tutorial at the H.E.S.S. school; it made it all clear. Christian Mariaud, we both went into this adventure late, but you were a hare, and I was a snail. I was happy to meet you. I really appreciated the birth gift for my daughter. Karl Kosack, thanks for sharing your former analysis on the Fermi Bubbles and your useful routines on the hd cluster. Alison Mitchell thanks for answering my concerns in English. Justine Devin, Yves Gallant, Ryan Chaves, I will forever remember the IAUS331. Yves, your comments on my work were always relevant; thanks for that.

The SNR group at API has been an inspiring place to share results: Vladimir, Maria, Dimitris, Ping, Fabio Acero, Orestis, Nelson Rozeena I'm happy to have met you all. To the -rather- news members, Amael, Emmanuele, I wish you a lot of fun! Ping, Vladimir, and Dimitris, thanks for all your help, and answering my alert messages on Slack. Vlad, you were constantly kindly asking for news, thanks guy, that was cheerful.

At API, although I was part-time, I always felt welcomed. First, thank the excellent secretary team: ladies, you really input the institute's spirit. Susan, honestly, you are doing such a great job supporting us all. You always has a kind word, and you dealt with my administrative stuff so quickly, thank you. Milena – 74 are the best– I wish I have 5% of your energy. Renee, always joyful, a special thanks for sending birth presents to Brussels. Lucas, thanks for dealing with administrative work in my particular situation. Martin, I know, I was never around, but admit we had good discussions and a lot of beers. Thanks for all your efforts to keep API's active social life. My PhD/PD mates from my begin at API, I will never forget you: Macla, Alice, Kaustubh, Lucia, Bertrand, Oscar, Ylva, Daniele, Amruta, Gullo, Mathieu Renzo, Manos, Adam Ingram, Smirti and Alicia, Nina, Mark... You all made me feel like I was part of the API. The little I was there, I had fun. Ylva, my friend, you deserve more than a thank you: you were welcoming me to your home for more than a year. I have so many good memories with you and Santiago. I'm sure we'll meet again. Of course, I haven't forgotten you all, who welcomed me to oversleep at their place, that was allways great moments, and super kind from you: Ping, Smirti and Alicia, Mathieu, Gullo, Nina and Rick.

I loved to work at the IIHE in Bruxelles. Thanks, To Audrey, Marleen, Sophie for the excellent secretary work but also for being so friendly. Thanks to the whole IT team and Samir and Abdel! Alexandre Leonard, you helped me so much with root. I'm full of gratitude. IceCube group, thanks for welcoming me to your meetings and the great discussions: Nick van Eindhoven, Kael Hanson, Krijn de Vries, Catherine De Clercq, Juan Antonio Aguilar Sánchez , Simone Toscano, Elisa Pinat, Jan Kunnen, Lionel Brayeur, and all actual and past members that I met. Thanks also to CMS members for great discussions in the coffee room, Pascal, Barbara, Gilles, and many others. And finally, a big up to all my great office mates: Thomas Lenzi, David and Thomas, Chris, Gwen, Simon, and finally Denise, and Alexander. Christophe Raab, compagnon de thèse à L'ULB, we shared a desk and our PhD doubts. With no surprise, you did great at your defense, and your advices were more than welcome concerning the thesis printing; thank you! I wish you a lot of happiness in your life.

To the people from the Fermi Summer School: Jamie Holder, Liz Hays, Julie Mc Enery, your school was great! I really appreciated to be un-anonymous later when we met around at conferences. Micky, that was great to follow the school with you.

And now it is time to thank my family and friends, who provided tremendous support to my crazy life. First, let's drop a few dates on the timeline: I began the PhD in October 2014, my daughter was born on 6 October 2015, and my son on 20 November 2018. In 2016-2018 I managed to come 5 days to API almost every two weeks. My partner, mother, and sister were visiting me many times in Amsterdam with my daughter –who doesn't remember it... That was so important to have them all around. From 2019 onward, I mainly stayed in Brussels, regularly commuting to API for one day or two. Maman, mille fois merci. Tu en as fait des kilomètres! Tu es toujours là quand j'ai besoin d'aide. Sarah, merci pour mon installation à Amsterdam, et pour ce voyage de fou à Berlin, cétait super! Reb, évidemment, merci aussi, pour tous les coups de main à distance. Katia, c'était un plaisir de partager l'appartement avec toi. Eve, Fil, François, Valene, Aline, Jo, Céline et Facundo, Géraldine et Guillaume, depuis 2014 nous avons vu grandir nos enfants ensemble, et c'est génial. Merci pour tous les anniveraires, les gardes, les repas, les trajets!

More recently, I completed my thesis at home during the pandemic, and by then, friends welcomed me to work at their place when university was closed. I got a permanent office at Carine and Pieter's home: merci à vous, cétait top! Merci aussi à Raf et mon cousin Alex. Moreover, friends helped with taking care of the kids while my partner was away and that was a great relief: merci à Andrea, Nico et Ellen, Raf et lola, Arnould, Valene, Céline! Cécile, Gaétane, merci pour votre soutien, de Bruxelles à Briançon, we keep in touch, je vous aime les filles! Ben, merci pour les encouragements, les corrections et conseils de rédactions, mais surtout, merci d'être ma copine! Et je suis sûre que j'oublies plein de monde, merci à toutes et tous!

Rachel Simoni,
19 December 2021

The analyses presented in this thesis are using H.E.S.S. observations, thanks to many institutions. It is thus important to report the following H.E.S.S. acknowledgments:
The support of the Namibian authorities and of the University of Namibia in facilitating the construction and operation of H.E.S.S. is gratefully acknowledged, as is the support by the German Ministry for Education and Research (BMBF), the Max Planck Society, the German Research Foundation (DFG), the Helmholtz Association, the Alexander von Humboldt Foundation, the French Ministry of Higher Education, Research and Innovation, the Centre National de la Recherche Scientifique (CNRS/IN2P3 and CNRS/INSU), the Commissariat Ãă l'ńergie atomique et aux ńergies alternatives (CEA), the U.K. Science and Technology Facilities Council (STFC), the Knut and Alice Wallenberg Foundation, the National Science Centre, Poland grant no.2016/22/M/ST9/00382, the South African Department of Science and Technology and National Research Foundation, the University of Namibia, the National Commission on Research, Science & Technology of Namibia (NCRST), the Austrian Federal Ministry of Education, Science and Research and the Austrian Science Fund (FWF), the Australian Research Council (ARC), the Japan Society for the Promotion of Science and by the University of Amsterdam. We appreciate the excellent work of the technical support staff in Berlin, Zeuthen, Heidelberg, Palaiseau, Paris, Saclay, Tübingen, and in Namibia in the construction and operation of the equipment. This work benefited from services provided by the H.E.S.S. Virtual Organisation, supported by the national resource providers of the EGI Federation. J. Vink and D. Prokhorov are partially supported by funding from the European Union's Horizon 2020 research and innovation program under grant agreement No 101004131 and by the Netherlands Research School for Astronomy (NOVA).

Chi va piano va sano e va lontano.

Italian proverb